
Electronic Thesis and Dissertation Repository

8-10-2022 2:30 PM

Solid Electrolytes and Interface Design for High-Performance All-Solid-State Batteries

Shumin Zhang, *The University of Western Ontario*

Supervisor: Xueliang Sun, *The University of Western Ontario*

Co-Supervisor: Tsun-Kong Sham, *The University of Western Ontario*

A thesis submitted in partial fulfillment of the requirements for the Doctor of Philosophy degree in Mechanical and Materials Engineering

© Shumin Zhang 2022

Follow this and additional works at: <https://ir.lib.uwo.ca/etd>

 Part of the [Materials Chemistry Commons](#), and the [Other Materials Science and Engineering Commons](#)

Recommended Citation

Zhang, Shumin, "Solid Electrolytes and Interface Design for High-Performance All-Solid-State Batteries" (2022). *Electronic Thesis and Dissertation Repository*. 8699.
<https://ir.lib.uwo.ca/etd/8699>

This Dissertation/Thesis is brought to you for free and open access by Scholarship@Western. It has been accepted for inclusion in Electronic Thesis and Dissertation Repository by an authorized administrator of Scholarship@Western. For more information, please contact wlsadmin@uwo.ca.

Abstract

All-solid-state batteries (ASSBs), in which solid superionic conductors are used as electrolytes to transport ions between cathode and anode, have been regarded as one of the most promising candidates for the next-generation energy storage technologies in electric vehicles (EVs), grid applications, etc. The advances of ASSBs over conventional lithium-ion batteries (LIBs) come from their inherent safety and high energy density, which benefits from the use of nonflammable solid electrolytes (SEs) to potentially enable metal anodes (such as Li metal or Na metal) and high-voltage cathode active materials (CAM) in ASSBs. Since that, the research and design of SEs have been a hot topic to accelerate the development of ASSBs. At the same time, a good compatibility (e.g., chemical stability, electrochemical stability, and mechanical compatibility) between SEs and metal anodes/high-voltage cathodes are essential for achieving high-energy-density ASSBs with long cycle life.

In this dissertation, the research towards SEs development and SE/electrodes interfacial protection have been studied. First, several new superionic conductors ($\text{Li}_{x-3}\text{YI}_x$, $x\text{Li}_2\text{O-TaCl}_5$, and $x\text{Li}_2\text{O-HfCl}_4$) with considerable Li-ion conductivity over $10^{-3} \text{ S cm}^{-1}$ are developed, some of which are feasible in ASSBs with stable cycling performances. The novel structures those solids behave have been firstly discovered, deepening the fundamental understandings for ionic conductors. Then, by rational modifying an existing SE to possess high practical anodic limit, the stability between SE and high-voltage cathode can be achieved for high-voltage ASSBs. Finally, the concerns associated with active Na anode and SEs are addressed via applying functional molecular layer deposition (MLD) coatings. The results on SE synthesis, interfacial engineering, and mechanism studies in this dissertation shall pave the way to achieve high-performance all-solid-state Li-ion batteries, as well as guide the development for the beyond lithium battery technologies.

Keywords

All-solid-state batteries; solid electrolytes; halides; cathode-electrolyte interface; Na Metal anode

Summary for Lay Audience

All-solid-state batteries (ASSBs) are types of advanced batteries which use solid electrolytes (SEs) to replace the conventional liquid electrolytes. The main advantages of ASSBs over conventional batteries are high safety and energy density, which make ASSBs become attractive energy storage devices for portable electronics and electric vehicles (EVs). SE is a core component of ASSB, which is a solid ionic conductor between the cathode and anode. A promising SE should essentially possess good ionic conductivity (over $10^{-3} \text{ S cm}^{-1}$), anodic stabilities ($>4.5 \text{ V vs. Li/Li}^+$), and good metal anode compatibility. However, there has been few SEs that can simultaneously show those properties. Besides, driven by the concerns of lithium scarce in the earth, fundamental understandings as well as established technologies should be applied to support the development of the beyond lithium batteries (such as all-solid-state Na-ion batteries).

In this dissertation, the improvements of SEs in terms of good ionic conductivities and anodic stabilities are accessed. Besides, referring to the coating technologies in conventional liquid batteries, the instability between active Na anode and SEs is addressed. In specific, several inorganic ionic conductors are developed with an attractive Li-ion conductivity around $10^{-3} \text{ S cm}^{-1}$. Some of them also show good cathode compatibility and anodic stability, which enables the use of 4 V class cathode active materials (CAMs) in ASSBs even high-voltage ASSBs with stable cycling. Second, the developed molecular layer deposition (MLD) coating strategy is adopted to solve the instability issues between active Na anode and SEs. The solutions and understandings in this thesis shall provide some guidance for developing high-performance ASSBs.

Co-Authorship Statement

1.

Title: Novel Iodide Superionic Conductors: Reviving of $\text{Li}_{x-3}\text{YI}_x$

Manuscript to be submitted.

Authors: Shumin Zhang, Feipeng Zhao, Jianwen Liang, Jiamin Fu, Minsi Li, Sandamini H Alahakoon, Lo-Yueh Chang, Graham King, Mohsen Shakouri, Yining Huang, Tsun-Kong Sham, Xueliang Sun

Contributions: Shumin Zhang: conceptualization, methodology, formal analysis, writing-original draft, investigation; Feipeng Zhao and Jianwen Liang: conceptualization, methodology; Minsi Li, Lo-Yueh Chang, Graham King, and Mohsen Shakouri: synchrotron data collection; Sandamini H. Alahakoon: NMR measurements; Tsun-Kong Sham and Xueliang Sun: supervision; all authors participated in the reviewing and editing of the manuscript.

2.

Title: New superionic lithium oxychloride glasses

Manuscript to be submitted.

Authors: Shumin Zhang, Feipeng Zhao, Jiatang Chen, Jiamin Fu, Jing Luo, Sandamini H Alahakoon, Lo-Yueh Chang, Jianwen Liang, Renfei Feng, Yang Zhao, Xiaona Li, Le He, Yining Huang, Tsun-Kong Sham, Xueliang Sun

Contributions: Shumin Zhang: conceptualization, methodology, formal analysis, writing-original draft, investigation; Feipeng Zhao: conceptualization, methodology; Jiatang Chen, Jiamin Fu, Lo-Yueh Chang, Renfei Feng, and Tsun-Kong Sham: synchrotron data collection and discussion; Sandamini H. Alahakoon: NMR measurements; Tsun-Kong Sham and

Xueliang Sun: supervision; all authors participated in the reviewing and editing of the manuscript.

3.

Title: Advanced High - Voltage All - Solid - State Li - Ion Batteries Enabled by a Dual - Halogen Solid Electrolyte

The final version of this manuscript has been published in *Adv. Energy Mater.* **2021**, *11*, 2100836.

Authors: Shumin Zhang, Feipeng Zhao, Shuo Wang, Jianwen Liang, Jian Wang, Changhong Wang, Hao Zhang, Keegan Adair, Weihan Li, Minsi Li, Hui Duan, Yang Zhao, Ruizhi Yu, Ruying Li, Huan Huang, Li Zhang, Shangqian Zhao, Shigang Lu, Tsun-Kong Sham, Yifei Mo, Xueliang Sun

Contributions: Shumin Zhang: conceptualization, methodology, formal analysis, writing-original draft, investigation; Feipeng Zhao and Jianwen Liang: conceptualization, methodology; Feipeng Zhao and Jian Wang: synchrotron data collection; Hao Zhao: XRD refinement; Shuo Wang: simulations; Tsun-Kong Sham and Xueliang Sun: supervision; all authors participated in the reviewing and editing of the manuscript.

4.

Title: Gradiently Sodiated Alucone as an Interfacial Stabilizing Strategy for Solid - State Na Metal Batteries

The final version of this manuscript has been published in *Adv. Funct. Mater.* **2020**, *30*, 2001118

Authors: Shumin Zhang, Yang Zhao, Feipeng Zhao, Long Zhang, Changhong Wang, Xiaona Li, Jianwen Liang, Weihan Li, Qian Sun, Chuang Yu, Jing Luo, Kieran Doyle - Davis, Ruying Li, Tsun-Kong Sham, Xueliang Sun

Contributions: Shumin Zhang: conceptualization, methodology, formal analysis, writing-original draft, investigation; Yang Zhao and Feipeng Zhao: conceptualization, methodology; Tsun-Kong Sham and Xueliang Sun: supervision; all authors participated in the reviewing and editing of the manuscript.

Acknowledgments

This Ph.D. work was supervised by Professor Xueliang (Andy) Sun in Department of Mechanical and Materials Engineering (MME) and Professor Tsun-Kong Sham in Department of Chemistry. Undertaking the Ph.D. role has been a quite challenging experience in my whole life. I could never have explored the depths and finished my Ph. D. study smoothly without the help, support, guidance, and efforts of a lot of people.

First, I would like to express my sincerest gratitude to my supervisor Prof. Xueliang (Andy) Sun for his invaluable help. Prof. Sun provides me an excellent opportunity and an incredible platform where I can explore the mysteries in the sea of battery science and synchrotron radiation analysis. He also teaches me how to plan the career and deal with multi tasks at the same time. Meanwhile, I would also like to show my deepest gratitude to my co-supervisor Prof. Tsun-Kong Sham for his careful guidance. Prof. Sham is a role model for me in term of his enthusiasm and attitude in science, insightful knowledge, and endless patience to students. Their prospective vision and the personal charisma have made a profound impact on me.

I would like to thank my advisory committee members, Dr. Robert J Klassen and Dr. Aaron Price. They have carefully tracked my progresses and gave me valuable comments since my comprehensive report. I deeply appreciate their advices and discussions toward the completion of this Ph.D. thesis.

I must give my special thanks to our lab manager Mrs. Ruying (Kathy) Li, Prof. Le He from Soochow University, Dr. Yang Zhao and Dr. Yun-Mui You from Western University. They help me overcome many crisis situations in both my research and daily lives.

Undoubtedly, I appreciate many past and current members in Prof. Sun's lab. I feel much enjoyed working with them. I would like to thank Dr. Jianwen Liang, Dr. Feipeng Zhao, Dr. Weihan Li, Dr. Jiatang Chen, Dr. Xiaona Li, Dr. Changhong Wang, Dr. Yulong Liu, and Dr. Zhiqiang Wang, for giving me constructive suggestions and support when I felt confused in conducting my research. I am greatly indebted to Dr. Jing (Erica) Luo, Dr. Minsi Li, and Mr. Jiamin Fu, for all their assistance, intellectual stimulation, and lasting friendship. I am grateful to my colleagues and neighbors: Dr. Yipeng Sun, Dr. Xia Li, Dr. Changtai Zhao, Dr.

Xiaofei Yang, Dr. Xuejie Gao, Ms. Lu Yao, Dr. Xiaoting Lin, Dr. Sixu Deng, Dr. Wei Xia, Ms. Xiaoge Hao, Ms. Bingyu (Caroline) Dong, Mr. Xuchun Wang, Mr. Zhi-Liang (Tony) Dong, Mr. Justin Kim, Mr. Yingjie Gao, Mr. Yang Hu, and Mr. Matthew Zheng. I would also acknowledge the substantial influence on this dissertation by other group members: Dr. Ruizhi Yu, Dr. Hui Duan, Dr. Junjie Li, Dr. Keegan Adair, and Mr. Kieran Doyle Davis.

I would like to take this opportunity to thank Dr. Lo-Yueh Chang from National Synchrotron Radiation Research Center in Taiwan, and all the beam scientists at SGM, SXRMB, SM, BXDS-WHE and VESPERS beamlines from Canadian Light Source (CLS) for their collaborations in synchrotron data collection. I deeply appreciate Mrs. Sandamini H. Alahakoon and Prof. Yining Huang for their help in collecting and analyzing NMR data. I benefit a lot from their help and the powerful characterization techniques. My thanks also go to Dr. Shuo Wang and Prof. Yifei Mo from University of Maryland for their help in simulations.

Most importantly, none of this would have been possible without the love and patience of my family. I would like to express my heart-felt gratitude to my parents Jianfeng Zhang and Rong Deng, and my brother Zhaoxing Zhang. They give me their infinite love, cherish, encouragement, and support. There are no beautiful words can fully express my love for them. My deepest appreciation also goes to my husband, Feipeng Zhao, who not only cares my daily life and guides me step-by-step in my research career, but also lights me up mentally and spiritually. He gives me the strongest support and encouragement, endless patience and care in my bad motion and hard times. Most of my happiness, joy, enrichment, and confidence are related to him.

Finally, I would like to take the opportunity to thank all persons who have ever helped me before.

Shumin Zhang

May 8th, 2022, at London, ON, Canada

Table of Contents

Abstract.....	ii
Summary for Lay Audience.....	iii
Co-Authorship Statement.....	iv
Acknowledgments.....	vii
Table of Contents.....	ix
List of Tables.....	xiii
List of Figures.....	xiv
List of Appendices.....	xxii
List of Abbreviations.....	xxiii
Chapter 1.....	1
1 Introduction to this thesis.....	1
1.1 From conventional battery to all-solid-state battery.....	1
1.2 Challenges for the development of all-solid-state batteries.....	3
1.3 Thesis objectives.....	4
1.4 Thesis organization.....	5
1.5 References.....	7
Chapter 2.....	10
2 Literature review.....	10
2.1 Inorganic solid electrolytes (ISEs).....	11
2.1.1 Fundamentals of ion migration in ISEs.....	12
2.1.2 Oxide ISEs.....	17
2.1.3 Sulfide ISEs.....	19
2.1.4 Halide ISEs.....	22
2.2 Electrolytes and electrodes interfaces in ASSBs.....	38

2.2.1	Electrochemical stability of ISEs.....	38
2.2.2	Cathode-SE interface (CEI).....	39
2.2.3	Anode-SE interface.....	41
2.2.4	Interfacial stability strategies.....	42
2.3	References.....	44
Chapter 3	54
3	Experimental apparatus and characterization techniques.....	54
3.1	Experimental apparatus.....	54
3.1.1	Ball milling machine.....	54
3.1.2	Ampules.....	55
3.1.3	Molecular layer deposition (MLD).....	55
3.2	Characterization techniques.....	56
3.2.1	Scanning electron microscope (SEM).....	56
3.2.2	Time-of-Flight Secondary Ion Mass Spectrometry (ToF-SIMS).....	57
3.2.3	X-ray photoelectron spectroscopy (XPS).....	58
3.2.4	Lab X-ray diffraction (XRD).....	59
3.2.5	Raman.....	60
3.2.6	Solid-state nuclear magnetic resonance (SS-NMR).....	60
3.2.7	Synchrotron radiation (SR).....	61
3.3	Electrochemical evaluations.....	66
3.3.1	Cell configuration.....	66
3.3.2	Electrochemical working station.....	67
3.3.3	Batter testing system.....	68
Chapter 4	70
4	Novel Iodide Superionic Conductors: Reviving of $\text{Li}_{x-3}\text{YI}_x$	70
4.1	Introduction.....	71

4.2	Experimental section.....	72
4.3	Results and discussion	74
4.4	Conclusion	82
4.5	Acknowledgments.....	83
4.6	References.....	83
4.7	Supporting information.....	86
Chapter 5.....		91
5	New superionic lithium oxychloride glasses.....	91
5.1	Introduction.....	92
5.2	Experimental section.....	93
5.3	Results and Discussion	96
5.4	Conclusion	109
5.5	Acknowledgements.....	109
5.6	References.....	110
5.7	Supporting information.....	115
Chapter 6.....		128
6	Advanced high-voltage all-solid-state Li-ion batteries enabled by a dual-halogen solid electrolyte.....	128
6.1	Introduction.....	129
6.2	Experimental Section	130
6.3	Results and discussion	136
6.4	Conclusion	148
6.5	Acknowledgments.....	149
6.6	References.....	149
6.7	Supporting Information.....	152
Chapter 7.....		160

7	Gradiently Sodiated Alucone as an Interfacial Stabilizing Strategy for Solid-State Na Metal Batteries	160
7.1	Introduction.....	161
7.2	Experimental section.....	162
7.3	Results and Discussion	165
7.4	Conclusion	175
7.5	Acknowledgments.....	176
7.6	References.....	176
7.7	Supporting information.....	178
	Chapter 8.....	184
8	Conclusions and Perspectives	184
8.1	Conclusions.....	184
8.2	Contributions to this field	186
8.3	Perspectives.....	188
	Appendices.....	191
	Curriculum Vitae	193

List of Tables

Table 5.1 Structural parameters of $x\text{Li}_2\text{O}-\text{TaCl}_5$ ($x = 1.2, 1.4, 1.6$ and 1.8) glasses extracted from Ta L_3 -edge EXAFS fittings.	104
Table 6.1 Phase equilibria and minimum decomposition energies of the $\text{Li}_3\text{InCl}_{4.8}\text{F}_{1.2}$, Li_3InCl_6 , LiF , LiInF_4 , and Li_3InF_6 materials at the interface with LiCoO_2 cathode materials under charged and discharged status.....	147

List of Figures

Figure 2.1 (a) categories of SEs and (b) the potential applications of ASSBs. ³	12
Figure 2.2 (a) Schematics of ion diffusion and energy barrier in solid electrolytes and liquid electrolytes. ⁵ (b) Three typical ion migration mechanisms in crystalline solids: vacancy, direct interstitial and correlated interstitial involving a single or multiple sites. ⁷ (c) Arrhenius plot for Ag ₂ SO ₄ , in which all the compositions are found to obey the Arrhenius law in both the α and β phases. ⁸ (d) Complex impedance plot for pure Ag ₂ SO ₄ at 250°C. ⁸	14
Figure 2.3 (a) Li-ion migration pathways in hcp-type anion lattices. ¹⁰ (b) Schematic of the influence of the width of the diffusion pathway. ¹¹ (c) A softer anionic sublattice in iodides compared chlorides leads to larger vibrational amplitudes and lower activation barriers. ¹² (d) Schematic two-dimensional representation of tetrahedrally coordinated silica glass. ¹⁵ (e) Simplified pictorial view of the ionic conduction energy based on the Anderson and Stuart model. ¹⁶	16
Figure 2.4 (a) Crystal structure of cubic perovskite. ³² (b) Schematic representations of the rhombohedral NASICON. ³³ (c) Crystal structure of cubic Li ₇ La ₃ Zr ₂ O ₁₂ ³⁴ (d) Amorphous LiPON structure of composition Li _{2.94} PO _{3.50} N _{0.31} obtained from Ab initio molecular dynamics (AIMD) simulations. Li (green), P (gray), O (red), N (blue); P (O,N) ₄ tetrahedra are drawn. ³⁵	19
Figure 2.5 (a) XRD patterns and Raman spectroscopy of 70Li ₂ S-30P ₂ S ₅ in (a) glass state, (b) glass-ceramic state, (c) crystals ⁴⁶ . (b) Crystal structures of Li ₆ PS ₅ X with X = Cl, Br, I; The free S ²⁻ anions and the corner of the PS ₄ ³⁻ tetrahedra derived from Frank–Kasper polyhedral, where shows three Li ⁺ conduction pathways. ⁵⁰ (c) Local structure of Na ₃ SbS ₄ ⁵⁵ (left) and Na _{2.88} Sb _{0.88} W _{0.12} S ₄ ⁵⁴ (right). (d) Framework structure of Li ₁₀ GeP ₂ S ₁₂ ⁵² (left) and Li _{9.54} Si _{1.74} P _{1.44} S _{11.7} Cl _{0.3} ⁵³ (right).....	22
Figure 2.6 (a) The measured XRD patterns of mechanochemically synthesized low-crystalline-LYC and annealed high-crystalline-LYC. ⁵⁸ The crystal structures of LYC obtained after Rietveld refinement, superimposed with a calculated BVSE-based lithium-ion potential map. The yellow surface corresponds to the ionic conduction path, and the regions	

enclosed with red surfaces correspond to the stable lithium-ion positions. (b) Structure of annealed-LIC, showing two kinds of InCl_6^{3-} octahedra with different occupations of In^{3+} (red wine) and vacancies (V'' , white); orange balls are Cl^- . Arrhenius plots of ball-milled and annealed Li_3InCl_6 samples.⁵⁹ (c) XRD patterns of $\text{Li}_3\text{Y}_{1-x}\text{In}_x\text{Cl}_6$ ($x = 0, 0.1, 0.2$) and ($x = 0.3-1.0$), respectively.⁶¹ 24

Figure 2.7 (a) Structural features within the unit cell, showing face-sharing ErCl_6^{3-} octahedra with Li^+ in chains along the c-axis.⁶² Arrhenius plot showing the room-temperature conductivities and activation barriers for ionic motion. (b) Phase evolution of $\text{Li}_3\text{M}_{1-x}\text{Zr}_x\text{Cl}_6$ ($\text{M} = \text{Er}, \text{Y}$) upon Zr substitution.⁶⁴ 26

Figure 2.8 Diffusion mechanism of the $\text{Li}_x\text{ScCl}_{3+x}$ SEs: (a) Li^+ probability density marked by yellow isosurfaces;⁶⁵ (b) Li^+ migration pathways in ccp-anion stacking sublattice of Li_3ScCl_6 structure;⁶⁵ (c) Li^+ probability density of $\text{Li}_x\text{ScCl}_{3+x}$ ($x = 1, 1.8, 3, \text{ and } 5$) structures;⁶⁵ (d) blocking effect of Sc^{3+} in Li^+ diffusion; and (e) Arrhenius plot of Li^+ diffusivity in $\text{Li}_x\text{ScCl}_{3+x}$ from simulations.⁶⁵ (f) Structure of spinel Li_2MgCl_4 from single crystal X-ray diffraction, depicting a possible Li^+ ion diffusion pathway⁶⁶. (g) Structure of disordered spinel $\text{Li}_2\text{Sc}_{2/3}\text{Cl}_4$ from powder neutron diffraction, demonstrating that it is related to spinel Li_2MgCl_4 but with different site occupancies⁶⁶. (h) Structure of disordered spinel $\text{Li}_2\text{Sc}_{2/3}\text{Cl}_4$ only showing Li^+ -containing polyhedron that represent a 3D Li^+ ion diffusion pathway⁶⁶. (i) Nyquist plots of $\text{Li}_2\text{Sc}_{2/3}\text{Cl}_4$ at room temperature.⁶⁶ 28

Figure 2.9 (a) Cuts through the unit cell of Na_3ErCl_6 showing the highly interconnected MCl_6 polyhedra.⁶⁷ (b) Representative Nyquist plot of a room-temperature impedance measurement and (c) Arrhenius plots from the temperature dependent Measurements.⁶⁷ (d) XRD of the $\text{Na}_{3-x}\text{Y}_{1-x}\text{Zr}_x\text{Cl}_6$ compositions and the corresponding room temperature conductivity values⁶⁸. (f) Arrhenius plot of $\text{Na}_{2.25}\text{Y}_{0.25}\text{Zr}_{0.75}\text{Cl}_6$ from experimental measurements.⁶⁸ (g) Arrhenius plots and XRD patterns of BM- Na_2ZrCl_6 and HT- Na_2ZrCl_6 and h) their corresponding crystalline structure⁶⁹. 32

Figure 2.10 (a) Conductivity of Li_3InBr_6 against $1/T$. Second and third runs are shown by circles and triangles, respectively.⁷⁰ (b) Conductivity of LiInBr_4 against $1/T$.⁷⁰ (c) The measured XRD patterns of mechanochemically synthesized lc-LYB and annealed hc-LYB.⁵⁸ (d) The crystal structures of LYB obtained after Rietveld refinement, superimposed with a

calculated BVSE-based lithium-ion potential map. The yellow surface corresponds to the ionic conduction path, and the regions enclosed with red surfaces correspond to the stable lithium-ion positions.⁵⁸ (e) The Arrhenius plots of lithium ion conductivities of *BM*-LYB and AN-LYB, respectively.⁵⁸ (f) Crystal structure of AN-LYB with *fcc*-type anion lattice. The light purple, red and cyan balls represent Li, Br, and Y atoms respectively.⁵⁸ 34

Figure 2.11 (a) Representative Nyquist plots for the ball-milled and annealed samples and (b) calculated Arrhenius plots of the total ionic conductivity and their corresponding activation energies.¹² (c) Possible lithium diffusion pathways obtained by a bond valence sum calculation. The blue sections show the strongly interconnected lithium sites in the *ab*-plane, possibly leading to a fast in-plane diffusion.¹² (d) Schematic of how a softer anionic sublattice in Li_3ErCl_6 compared to Li_3YCl_6 leads to larger vibrational amplitudes and lower activation barriers.¹² (e) Unit cells of Li_3MI_6 ($\text{M} = \text{Sc}, \text{Y}, \text{and La}$) crystal (in the C2 space group).⁷² (f) Calculated temperature-dependent formation energies (Helmholtz free energies) of Li_3YI_6 and Li_3LaI_6 materials.⁷² 36

Figure 2.12 (a) Schemes show process 1 and process 2 uses a conversion reaction between ALD-made AlF_3 and the lithium precursors to deposit Li_3AlF_6 .⁷³ (b) Schematic synthesis of Li_3GaF_6 . Li_2CO_3 is firstly dissolved in ionic liquid Li source and gallium nitrate hydrate as Ga source is then added to the solution to hydrolyze $\text{C}_{10}\text{mimBF}_4$ to releases free F^- .⁷⁴ (c) Ga^{3+} , Li^+ and F^- combine together to form Li_3GaF_6 deposit crystal structures of $\beta\text{-Li}_3\text{GaF}_6$ viewed along direction.⁷⁴ (d) Arrhenius plots of Li_3GaF_6 (annealed at 60°C and 120°C) with activation energies of 0.41eV and 0.46 eV respectively.⁷⁴ 37

Figure 2.13 Calculated thermodynamics intrinsic electrochemical win-dows of Li-M-X ternary fluorides, chlorides, bromides, iodides, oxides, and sulfides.⁷⁷ 39

Figure 2.14 (a) scheme of cathode and ISE contact in ASSBs⁸⁴ (b) SEMs of a given cell after 50 full battery cycles in the discharged state. The NMC particles shrink during delithiation (charge) and lose contact with the SE⁸⁵ (c) Reaction energies (left) and volume changes (right) for electrode/SE pairs.⁸⁶ (d) Initial charge/discharge curves and Nyquist plots of the EIS spectra of ASSBs with LYC, LYB and $\text{Li}_6\text{PS}_5\text{Cl}$ cathode electrolytes, respectively.⁵⁸ (e) The mutual reaction energy and the total reaction energy (dashed lines) at the SE-LCO

interfaces under applied potential f in a 2–5V range. ⁸¹ (f) Na ₃ PS ₄ cathode composite before and after being fully charged/discharged ⁸⁷	41
Figure 2.15 (a) reactive and mixed conducting interphase; (b) reactive and metastable solid-electrolyte interphase. ⁸⁸ (c) Scheme of the dendrite growth mechanism in ISE. ⁹⁰	42
Figure 2.16 (a) Scheme about the electrochemical window and the Li chemical potential profile (black line) in the ASSBs. (b) ESW of commonly used coating layer materials and the change of Li chemical potentials and the electrochemical potentials across the interface between the ISE and the cathode material. ⁹⁸ (c) Benefits associated with the employment of a suitable cathode coatings. ⁹⁹ (d) Electrochemical window of ISEs and other materials and the change of Li chemical potentials and the electrochemical potentials across the interface between the anode and the ISEs. ⁹⁸ (e) Plating and stripping of Na with Na ₃ SbS ₄ and hydrated Na ₃ SbS ₄ . ⁹⁴	43
Figure 3.1 PM200 two-station planetary ball mill produced by Retsch	54
Figure 3.2 (a) The equipment for quartz tube encapsulation. (b) Muffle furnace for heating the ampules	55
Figure 3.3 The Gemstar-8 ALD system as well as the connected glove box.	56
Figure 3.4 The Hitachi S-4800 SEM, equid with EDS.....	57
Figure 3.5 The ToF-SIMS station at Surface Science Western ¹	58
Figure 3.6 The Bruker D8 Advance Diffractometer XRD system.	59
Figure 3.7 The HORIBA Scientific LabRAM HR Raman spectrometer	60
Figure 3.8 The ss-NMR spectrometer with computers.....	61
Figure 3.9 One SGM endstation area ²	62
Figure 3.10 STXM endstation at SM beamline ³	63
Figure 3.11 The distribution of SXRMB ⁴	63

Figure 3.12 The experimental station high energy wiggler beamline at Brockhouse ⁵	65
Figure 3.13 The XANES/EXAFS experimental station at TPS 44A ⁶	66
Figure 3.14 A model cell with the internal parts and the shell	67
Figure 3.15 The VMP3 working station with a programmable thermal chamber.	68
Figure 3.16 The Land 2001A Battery Test System.	69
Figure 4.1 (a) Lab-based XRD patterns of the prepared $\text{Li}_{x-3}\text{YI}_x$ powders ($x = 12, 7, 6,$ and 5) and their corresponding magnified regions at 24.7° to 26.3° , 28.7° to 30.3° , and 41.7° to 43.3° ; (b) Normalized impedance spectra of the $\text{Li}_{x-3}\text{YI}_x$ pellets. (c) Arrhenius plots of $\text{Li}_{x-3}\text{YI}_x$ SEs and LiI. (d) Comparison of RT ionic conductivities and activation energies of $\text{Li}_{x-3}\text{YI}_x$ SEs and LiI.	76
Figure 4.2 Rietveld refinement of the SXRD pattern for (a) $\text{Li}_9\text{YI}_{12}$ and (c) Li_4YI_7 . The experimental profile is shown in blue crosses; the green line denotes the calculated pattern; the difference of profile is shown in cyan, and calculated positions of the Bragg reflections is LiI. Crystal structure of (b) $\text{Li}_9\text{YI}_{12}$ and (d) Li_4YI_7 , respectively.	78
Figure 4.3 (a) I L_2 -edge XANES spectra for LiI, $\text{Li}_{x-3}\text{YI}_x$ ($x = 6, 7,$ and 12), and YI_3 . (b) PDF $G(r)$ and fitting results for Li_4YI_7 . (c) Fitting results of the k^3 -weighted FT spectra of Li_4YI_7 at Y K -edge, showing the experimental data (grey circle) and Feff modeling (grey line) in terms of magnitude of FT and the real part of FT experimental data (red circle) and Feff ²⁹ modeling (red line) traces. The R factor for this fitting is 0.003 and S_0^2 is set as 0.81. (d) ^6Li MAS NMR spectra of Li_4YI_7 and LiI.	80
Figure 4.4 (a) Temporal EIS spectra of Li-Li symmetric cells using Li_4YI_7 ; (b) Cycling performance of Li/ Li_4YI_7 /Li symmetric cell at 0.1 mA cm^{-2} and 0.1 mAh cm^{-2} ; (c) Critical current density testing from 0.1 to 1.1 mA cm^{-2} ; (d) Li 1s, (e) Y 3d, and (f) I 3d XPS spectrum of the lithium metal side after long cycling.....	82
Figure 5.1 Powder XRD diffraction patterns for the as-prepared (a) $x\text{Li}_2\text{O-TaCl}_5$ ($1 \leq x \leq 2$) and (c) $x\text{Li}_2\text{O-HfCl}_4$ ($0.8 \leq x \leq 2$) samples. Synchrotron-based 2D diffraction patterns of selected (b) $x\text{Li}_2\text{O-TaCl}_5$ ($x = 1.8, 1.6,$ and 1.1) and (d) $x\text{Li}_2\text{O-HfCl}_4$ ($x = 2, 1.5,$ and 1.4)	

samples. The 2D diffraction data were recorded on a Pilatus 1M detector with a photon energy of 13 keV (0.9537 Å) at the VESPERs beamline of Canadian Light Source (CLS). 97

Figure 5.2 Comparison of RT ionic conductivities for selected (a) $x\text{Li}_2\text{O}-\text{TaCl}_5$ and (c) $x\text{Li}_2\text{O}-\text{HfCl}_4$ samples; extracted activation energy (E_a) from Arrhenius plots for (b) $x\text{Li}_2\text{O}-\text{TaCl}_5$ and (d) $x\text{Li}_2\text{O}-\text{HfCl}_4$ samples. (e) Static ^7Li motional narrowing spectra of $1.6\text{Li}_2\text{O}-\text{TaCl}_5$ and $1.5\text{Li}_2\text{O}-\text{HfCl}_4$ between 293–443 K; temperature-dependent ^7Li SLR NMR rates for (c) $1.6\text{Li}_2\text{O}-\text{TaCl}_5$ and (f) $1.5\text{Li}_2\text{O}-\text{HfCl}_4$ samples measured in the laboratory frame of the reference. The Larmor frequency was 155.248 MHz. 99

Figure 5.3 (a) XANES, (b) EXAFS, and (c) FT-EXAFS of $x\text{Li}_2\text{O}-\text{TaCl}_5$ ($x = 1.2, 1.4, 1.6, 1.8$) glasses, as well as Ta_2O_5 and TaCl_5 referential samples at Ta L_3 -edge. WT spectra of (d) Ta_2O_5 and TaCl_5 , (e) $1.2\text{Li}_2\text{O}-\text{TaCl}_5$, (f) $1.4\text{Li}_2\text{O}-\text{TaCl}_5$, (g) $1.6\text{Li}_2\text{O}-\text{TaCl}_5$, and (h) $1.8\text{Li}_2\text{O}-\text{TaCl}_5$ at Ta L_3 -edge with a k^2 weighting. (i) Schematic figure of the reaction route to form superionic $x\text{Li}_2\text{O}-\text{TaCl}_5$ glasses. The local structures are also displayed with coordination and possible geometry (bond angle is not accurate). (j) One possible connection of the smallest local structure unit in $x\text{Li}_2\text{O}-\text{TaCl}_5$ glasses..... 103

Figure 5.4 Room-temperature electrochemical performance of Li-In| Li_3YCl_6 | $1.6\text{Li}_2\text{O}-\text{TaCl}_5$ |NMC83 and Li-In| Li_3YCl_6 | $1.5\text{Li}_2\text{O}-\text{HfCl}_4$ |NMC83 ASSLIBs: (a) and (c) are charge-discharge curves at different C rates; (b) and (d) are rate performances; (e) and (f) are the long-term cycling performance..... 106

Figure 5.5 Low-temperature electrochemical performance of Li-In|LGPS| $1.6\text{Li}_2\text{O}-\text{TaCl}_5$ |LCO and Li-In//LGPS – $1.5\text{Li}_2\text{O}-\text{HfCl}_4$ //LCO ASSBs at -10°C : (a) and (d) are rate performances; (b) and (e) are charge-discharge curves at 1st, 10th, 50th, and 100th; (c) and (f) are long cycling performances at 0.2 C (1 C = 140 mAh g⁻¹). 108

Figure 6.1 (a-1) SXRD ($\lambda=0.729293\text{Å}$) patterns of the prepared $\text{Li}_3\text{InCl}_{4.8}\text{F}_{1.2}$ BM, $\text{Li}_3\text{InCl}_{4.8}\text{F}_{1.2}$, and Li_3InCl_6 powders and their corresponding magnified regions ((a-2) 6° to 8° and (a-3) 15° to 17°). (b) SEM images of pelletized (b-1) $\text{Li}_3\text{InCl}_{4.8}\text{F}_{1.2}$ DHSE and (b-2) Li_3InCl_6 SE, scale bar: 5 μm . (c) EDS elemental mapping of In, Cl, and F in the powder $\text{Li}_3\text{InCl}_{4.8}\text{F}_{1.2}$ sample, scale bar: 4 μm . (d) Nyquist plots of Li_3InCl_6 and $\text{Li}_3\text{InCl}_{4.8}\text{F}_{1.2}$ SEs at room temperature (RT). (e) The Li-ion migration pathways in the anion sublattice of

Li_3InCl_6 (upper) and $\text{Li}_3\text{InCl}_{4.8}\text{F}_{1.2}$ (lower) structure, and (f) corresponding energy profiles of Li-ion migration. 138

Figure 6.2 (a) Crystal structure of $\text{Li}_3\text{InCl}_{4.8}\text{F}_{1.2}$ from the view that is parallel to a axis and b axis, respectively. (b) F K-edge XAS spectra at $\text{Li}_3\text{InCl}_{4.8}\text{F}_{1.2}$ and standard samples (LiF and InF_3). First-principles calculations results: (c) $\text{Li}_3\text{InCl}_{4.8}\text{F}_{1.2}$ unit cells with (c-1) high-energy and (c-2) low-energy In-F sublattice. (d) Calculated formation energy of two In-F disordering in $\text{Li}_3\text{InCl}_{4.8}\text{F}_{1.2}$ versus the structure ordering which is referenced to the lowest-energy structure unit cell. (e) In-In pair correlation function $g(r)$ for (e-1) high-energy and (e-2) low-energy structures. 140

Figure 6.3 (a) LSV analysis of the Li_3InCl_6 SE and $\text{Li}_3\text{InCl}_{4.8}\text{F}_{1.2}$ DHSE from open circuit voltage (OCV) to 7 V. The dashed area represents the integral spectrum intensity of each material. (b) Phase equilibria of $\text{Li}_3\text{InCl}_{4.8}\text{F}_{1.2}$ DHSE at different Li/Li⁺ potentials based on the first principles computation. (c) The calculated thermodynamics electrochemical stability windows of $\text{Li}_3\text{InCl}_{4.8}\text{F}_{1.2}$, LiF, LiInF_4 , In_3InF_6 , Li_3InCl_6 , and LiCl. 142

Figure 6.4 Electrochemical performance of the full cells using $\text{Li}_3\text{InCl}_{4.8}\text{F}_{1.2}$ and Li_3InCl_6 cathode SE. (a) the first three discharge/charge curves of $\text{Li}_3\text{InCl}_{4.8}\text{F}_{1.2}$ cathode SE cell. (b) Cycling performance of $\text{Li}_3\text{InCl}_{4.8}\text{F}_{1.2}$ and Li_3InCl_6 cathode SE cells in the voltage range of 2.6 – 4.47 V (vs. Li/Li⁺) (first 5 cycles at 0.063 mA cm⁻²). (c) Charge-discharge profiles of $\text{Li}_3\text{InCl}_{4.8}\text{F}_{1.2}$ (upper) and Li_3InCl_6 (lower) cathode SE cells at 1st, 10th, and 20th cycles in the voltage range of 2.6 – 4.8 V (vs. Li/Li⁺). (d) Cycling performance of $\text{Li}_3\text{InCl}_{4.8}\text{F}_{1.2}$ cathode SE cell charged at 4.8 V (vs. Li/Li⁺) (first 5 cycles at 0.063 mA cm⁻²). 144

Figure 6.5 Synchrotron spectroscopic analyses for standard LiF, $\text{Li}_3\text{InCl}_{4.8}\text{F}_{1.2}$, LCO/ $\text{Li}_3\text{InCl}_{4.8}\text{F}_{1.2}$ cathode composites after 1st, 10th, and 50th cycling processes: (a) F K-edge XAS (the E_0 of standard LiF is marked by the black vertical line) and (b) first derivative absorption spectra. (c) X-ray ptychography and (d) STXM mapping images of a single 50-cycle LCO particle at 688.5 eV, pixel size: 5.7 nm. (e) F K-edge XAS at 7 marked positions (a-g) in (c) compared with that of the standard LiF. (f) The periodic EIS results during a constant-voltage charging (CVC) test process at 4.47 V, time scale indicates the time of CVC processes. 146

Figure 7.1 (a) Schematic diagram of the reactive Na/sulfide-based SSEs interface and stable Na@alucone/sulfide-based SSEs interface; (b) ToF-SIMS secondary ion images of Na@alucone anode before Cs⁺ consecutive sputtering; (c) 3D rendering models based on the depth scan of Na@mld150C anode by ToF-SIMS. 167

Figure 7.2 Comparison of Na plating/stripping behavior of Na symmetric cells at a current density of 0.1 mA cm⁻² with an areal capacity of 0.1 mAh cm⁻²: a) 50 cycles alucone (mld50C) versus bare Na; b) 150 cycles alucone (mld150C) versus bare Na; c) 300 cycles alucone (mld300C) versus bare Na..... 170

Figure 7.3 Top-side SEM images of the cycled Na|Na₃SbS₄|Na using (a) bare Na and (b) Na@mld150C electrodes; ToF-SIMS depth profile of the cycled (c) bare Na electrode and (d) Na@mld150C electrode, respectively..... 172

Figure 7.4 (a) Presumed schematic diagram of Na@mld150C/Na₃SbS₄ interface after symmetric cell cycles; (b) High-resolution XPS spectra of S 2p, Sb 3d, Al 2p and C 1s. The Sb 3d spectra indicate Sb⁵⁺. The peaks of Al 2p and C 1s represent the existence of alucone; XPS depth profile of Na 1s (c) and Al 2p (d) of the cycled Na@mld150C/Na₃SbS₄ interface. The metallic Na (bottom curve) and interlayer 1 (top two curves) were identified in different sputtering depths, and the interlayer 2 was identified by the chemical valence changes of Na and Al..... 174

Figure 7.5 (a) CV curves of all-solid-state Na@mld150C/Na₃SbS₄/TiS₂ battery. (b) The charge and discharge profiles of Na@mld150C/Na₃SbS₄/TiS₂ cell performed at room temperature with a current density of 0.11 mA cm⁻² (c) cycling stability and coulombic efficiency of Na/Na₃SbS₄/TiS₂ and Na@mld150C/Na₃SbS₄/TiS₂ cells. 175

List of Appendices

Appendix A: Permission from John Wiley and Sons for Published Article on <i>Advanced Energy Materials</i>	191
Appendix B: Permission from John Wiley and Sons for Published Article on <i>Advanced Functional Materials</i>	192

List of Abbreviations

A

ALD: atomic layer deposition

AN: annealing

AIMD: Ab initio molecular dynamics

ASSB: all-solid-state battery

ASSLB: all-solid-state lithium battery

ASSLIB: all-solid-state lithium-ion battery

ASSMBs: All-solid-state metal batteries

ASSSMBs: All-solid-state Na metal batteries

ASSLMBs: All-solid-state Li metal batteries

B

BXDS: Brockhouse Diffraction Sector Beamlines

Bcc: body-centered-cubic

BM: ball milling

C

CV: cyclic voltammetry

CPE: composite polymer electrolyte

CCP: cubic-close-packed

CEI: cathode-electrolyte interface

CLS: Canadian Light Source

CB: carbon black

CN: coordination number

CE: Columbic efficiency

CV: Cyclic voltammetry

D

DFT: density functional theory

DC: direct current

DHSE: dual-halogen solid electrolyte

E

EDS: energy dispersive spectroscopy

EIS: electrochemical impedance spectroscopy

EG: ethylene glycol

EV: electric vehicles

ESW: electrochemical stability window

G

GITT: Galvanostatic intermittent titration technique

H

HRTEM: high-resolution transmission electron microscopy

HXMA: hard X-ray micro-analysis

Hcp: hexagonal closed packing

HT: heat treatment

I

ISE: Inorganic solid electrolyte

IE: liquid electrolyte

L

LCO: lithium cobalt oxide

LMO: lithium manganese oxide

LFP: lithium iron phosphate

LATP: lithium aluminum titanium phosphate

LLZO: lithium lanthanum zirconium oxide ($\text{Li}_7\text{La}_3\text{Zr}_2\text{O}_{12}$)

Lipon: lithium phosphorus oxynitride

LNMO: $\text{LiNi}_{0.5}\text{Mn}_{1.5}\text{O}_4$

LGPS: $\text{Li}_{10}\text{GeP}_2\text{S}_{12}$

LE: liquid electrolyte

LIB: lithium-ion battery

LNO: LiNbO_3

LSV: Linear sweep voltammetry

LZO: lithium zirconium oxide

LYC: Li_3YCl_6

LYB: Li_3YBr_6

LT: low-temperature

M

MAS: magic angle spinning

MLD: molecular layer deposition

N

NMC: lithium nickel-manganese-cobalt oxides

NEB: Nudged Elastic Band Calculations

NCA: lithium nickel cobalt aluminium oxides

NMR: Nuclear Magnetic Resonance

NBO: non-bridging oxygen

O

OCV: Open-circuit voltage

P

PDF: pair distribution function

R

RT: room-temperature

S

SE/SSE: solid(-state) electrolyte

SXRD: synchrotron-based high-resolution powder X-ray diffraction

SS-NMR: solid-state nuclear magnetic resonance

SEI: solid electrolyte interface

SEM: secondary electron microscopy

STXM: Scanning transmission X-ray microscopy

SPE: Solid polymer electrolyte

SGM: Spherical Grating Monochromator

SM: SpectroMicroscopy

SXRMB: Soft X-Ray Microcharacterization Beamline

SLR: spin-lattice relaxation

T

TEM: transmission electron microscopy

TGA-DSC: Thermogravimetric analysis and differential scanning calorimetry

TOF-SIMS: time-of-flight secondary ion mass spectrometry

TMA: trimethylaluminium

TPS: Taiwan Photon Source

V

VEPSERS: Very Sensitive Elemental and Structural Probe Employing Radiation from a Synchrotron

X

XAS: X-ray absorption spectroscopy

XANES: X-ray absorption near edge structure

XPS: X-ray photoelectron spectrometer

XRD: X-ray diffraction

Chapter 1

1 Introduction to this thesis

1.1 From conventional battery to all-solid-state battery

The revolution of battery development was started in the 1990s, when Sony Company firstly reported a commercial Li-ion battery (LIB).¹ LIB is a type of rechargeable battery that uses lithium ions as a key component of its electrochemistry. It shows the primary advantages of high energy density, long cycle life, and environmental friendliness.^{2,3} Due to these advantages, LIBs have been quickly occupied the market of energy storage devices in the past 30 years. They have displaced the traditional nickel-cadmium or nickel-metal-hydrate batteries in portable electronic devices (e.g. smartphones and laptops).⁴ Some of the electrical vehicles (EVs), Nissan Leaf, Tesla Model S, BYD e6, and BMW i4, also use LIBs as their primary fuel source to improve the vehicle performance and reduce emissions.⁵ Additionally, LIBs can store energy from renewable sources, such as solar and wind power. The development of LIBs has laid the foundation of a wireless, fossil fuel-free society, and are of the greatest benefit to humankind. Owing to the technical advances that LIBs have taken to our lives, the 2019 Nobel Prize rewarded the development of LIBs, and the pioneering researchers, John B. Goodenough, M. Stanley Whittingham, and Akira Yoshino, were honored. In the recent years, LIBs are of intense interest from industry, academic institutes, and government funding agencies, and research in this field has abounded.

Conventional LIBs mainly consist of cathode, anode, electrolyte, and separator. Li ions move from the cathode, through the electrolyte, to the anode during charging process and then go back when discharging. Cathode materials for commercialized LIBs are generally constructed from LiCoO_2 (LCO), LiMn_2O_4 (LMO), LiFePO_4 (LFP), $\text{LiNi}_x\text{Co}_y\text{Al}_z\text{O}_2$ (NCA), or $\text{LiNi}_x\text{Mn}_y\text{Co}_z\text{O}_2$ (NMC). The dominant market for commercially used anode is graphite-based materials. The conventional electrolyte is generally a mixture of lithium salt and organic solvents. The separator is in between the cathode and the anode as a safety component. The first-generation LIBs are commonly

made from LCO cathode and graphite anode. A high energy density of 150-190 Wh/kg makes LCO batteries become a decent choice for portable electronics.⁶ Beyond the early demand for the consumer electronics market, LIBs are expected to gradually take the roles of powering EVs. It is forecasted that $\approx 50\%$ of all manufactured LIBs will be used in the EV sector by 2025.⁷ Since that, the design parameters for the next-generation batteries are focused on high safety, low cost, long cycle life, high energy density as well as power density by researchers. While NMC, NCA, and LFP cathodes are cost-effective, and batteries with those cathodes are durable and show improved energy to some extent, LIBs still suffer from safety concerns of overcharging, short-circuits, gas generation, and flammable liquid electrolyte.^{8,9} Besides, enhancing the energy density of LIBs is a long-term goal to meet the high demand for the EV market. Despite conventional LIBs achieve 300 Wh kg⁻¹ to power 500-km EVs at the current research stage, further improving energy density is restricted since conventional liquid electrolytes cannot withstand potentials higher than 4.3 V vs Li/Li⁺ and will be oxidized if used with high-voltage cathodes.¹⁰ Meanwhile, research on alternative, beyond lithium technologies should be developed to avoid the overreliance on scarce Li-based resources.⁶

Technological breakthrough for next-generation battery is the use of solid electrolyte (SE) to replace the conventional liquid electrolyte and separator, which is called all-solid-state battery (ASSB). ASSBs are promising to address the issues related to the conventional batteries. First, SEs show distinct advantages of safety, mechanical and thermal stability, wide electrochemical stability window, low flammability, and high power density, avoiding the issues related to liquid counterparts.^{11, 12, 13} Second, the self-supporting SEs compactly contact with electrodes, eliminate the use of separator, and simplify the packaging process of battery, which allows the reach of gravimetric and volumetric energy densities high enough to support EVs with long drive.¹⁴ Finally, SEs are possibly compatible with metal anode (like Li metal with a specific capacity of 3860 mAh g⁻¹ and a reduction potential of -3.04 V vs standard hydrogen electrode), by which the energy density of ASSB can be enhanced greatly, and the formation of dendrites can be restrained to prevent the internal short circuit.¹⁵

1.2 Challenges for the development of all-solid-state batteries

Despite the large-scale production and commercialization of ASSBs are very promising, the development of high-performance ASSBs is not straightforward, and mature techniques for conventional LIBs are not commonly applicable for developing ASSBs.

One of the major challenges is the ionic conductivity of SEs is lower compared to that of the liquid electrolytes. Solid polymer electrolyte (SPE) suffers from the low ionic conductivity of $10^{-5} \text{ S cm}^{-1}$ thus restricted to room-temperature (RT) applications.¹⁶ Inorganic solid electrolyte (ISE), including oxides (e.g. $\text{Li}_7\text{La}_3\text{Zr}_2\text{O}_{12}$), sulfides (e.g. $\text{Li}_{5.5}\text{PS}_{4.5}\text{Cl}_{1.5}$ ¹⁷, $\text{Li}_{6+x}\text{M}_x\text{Sb}_{1-x}\text{S}_5\text{I}$ ($\text{M} = \text{Si}, \text{Ge}, \text{Sn}$)¹⁸, $\text{Li}_{10}\text{GeP}_2\text{S}_{12}$ ¹⁹, $\text{Li}_{9.54}\text{Si}_{1.74}\text{P}_{1.44}\text{S}_{11.7}\text{Cl}_{0.3}$ ²⁰, and $\text{Na}_{2.88}\text{Sb}_{0.88}\text{W}_{0.12}\text{S}_4$ ²¹, and Na_3SbS_4 ²²), and halides (e.g. Li-M-Cl system^{23, 24, 25, 26}; $\text{M} = \text{Y}, \text{In}, \text{Sc}$) show decent RT ionic conductivities of 10^{-4} to $10^{-2} \text{ S cm}^{-1}$, but which is still insufficient to make ISE competitive with liquid electrolytes.

Another challenge is the fundamentals of local structure and ion transport in ISEs remains ununified. Despite most of the published literatures are focused on discussing the crystalline SEs, the relation between ionic conductivity and crystal structure, especially the roles of different cations and anions, is still a controversial topic. Besides, most of the research has been focused on crystalline SE exploration; yet for glassy ones, the structure modeling and ion conduction have been not fully established.

Moreover, there are always interfacial compatibility between SEs and electrodes. To achieve high energy density, metal anodes (such as Li and Na) with high capacity and low discharge potential as well as high-voltage cathodes with high charge potential should be applied. However, there is few high ionic conductive SEs that can directly match high-voltage cathode and metal anode simultaneously. Sulfides show narrow electrochemical stability window (1.5 - 2.5 V vs Li/Li⁺), problematically contacting with cathode and metal anode without coating or interlayer protection. Halides show improvements towards cathode compatibility, while which are severely reactive with

metal anode. Besides, poor physical contact between ISE and electrolytes is a major barrier to hinder ion transport.

1.3 Thesis objectives

To prompt the development of ASSBs, there are three aspects which need to be further explored and improved. From a mechanism perspective, understand and unify the fundamentals of Li/Na-ion conduction in SEs. From a practical perspective, design new solid-state superionic conductors with good chemical and electrochemical stability, easy processibility, and feasibility in ASSBs at different operating temperatures. Last, address the interfacial issues related to high-voltage cathode and metal anode to improve the performance of ASSBs. This thesis will investigate ASSB from SE design and interfacial protection. The main objectives are list below:

1. To fully reveal the halogen chemistry for developing future halide SE with fast Li ion transports and good stabilities, a new group of conducting iodides, $\text{Li}_{x-3}\text{YI}_x$, are synthesized for proper evaluation. The mechanism related to structure and Li-ion conductivity will be conducted. The improvement of $\text{Li}_{x-3}\text{YI}_x$ compared with Li_3YCl_6 and Li_3YBr_6 will be exhibited.
2. Other than the halogens, chalcogens make a great contribution to form SEs in both crystalline and amorphous state. To investigate the synergistic effect of mixed anions in SE, a family of oxychloride SEs $x\text{Li}_2\text{O-MCl}_y$ glassy SEs (M = Hf or Ta) are prepared. The stoichiometric ratio of starting materials will be optimized to yield the highest ionic conductive compounds. Li-ion conductive behavior and local structure will be also explored to understand the fundamentals of glassy SEs. Using as SEs in ASSBs, various C-rates and temperature ranges will be set to realize their practical applications in ASSBs.
3. To achieve the use of high-voltage cathodes in ASSBs, fluorinating halide SE (Li_3InCl_6) is attempted since lithium fluorides are reported showing wide electrochemical stability window and high oxidation limit. The fluorine (F) doping content as well as the resulted structure will be explored. The electrochemical stability, high-voltage cathode compatibility, and performance in full cells will also be demonstrated. Furthermore, the mechanism of high-voltage

$\text{Li}_3\text{InCl}_{6-x}\text{F}_x$ against oxidation will be studied and characterized by simulations, synchrotron radiation analysis, and etc.

4. To realize the use of metal anode in ASSBs, the active Na metal and its compatibility with popular sodium-based sulfides are investigated. Representative sodium-based sulfide SEs will be prepared firstly. Then, interfacial issues between Na metal and sulfide SEs will be explored. Interfacial stabilization methods will be evaluated by testing Na/Na symmetric cell and Na metal full cell performance.

1.4 Thesis organization

This thesis is composed of 8 chapters (one introductory chapter, one chapter of literature review, one chapter of experimental and characterization details, four chapters of research projects, and one conclusion and perspective chapter). The manuscript for each research project will be submitted or already accepted as a research article to peer-reviewed journals. The chapters are organized according to the requirements on Integrated-Article form as outlined in the Thesis Regulation Guide by the School of Graduate and Postdoctoral Studies (SGPS) of the University of Western Ontario. Specially, the contents of the thesis chapters are organized as following:

Chapter 1 gives the brief introduction of the battery revolution, especially from conventional liquid-based batteries to ASSBs. The technological challenges hindering the development of ASSBs are also discussed. After that, the research objectives and the thesis structure are stated.

Chapter 2 provides a comprehensive literature review on the development of solid-state electrolytes (SEs) and the strategies for interfacial stabilization. The review of SEs is mainly focused on the inorganic sulfide and halide SEs in term of the fundamentals of ion conduction, classification, research progress, and challenges. From the perspective of interfaces, the issues between SEs and high-voltage, SEs and metal anodes are discussed respectively. Corresponding solutions, especially SE modification and interlayer, are then reviewed.

Chapter 3 outlines the experimental apparatus and characterization techniques. The synthesis methods for solid electrolyte and relevant instruments are listed. Various characterization techniques, such as XRD, SEM, XPS, Raman, ToF-SIMS and etc, are also listed for the analysis of the chemical, electrochemical, and physical properties of materials and batteries. Importantly, synchrotron radiation (SR) techniques are included and introduced in detail.

Chapter 4 reports novel superionic iodide SEs: $\text{Li}_{x-3}\text{YI}_x$. The highest ionic conductivity for Li_4YI_7 can reach to $1.04 \times 10^{-3} \text{ S cm}^{-1}$ at RT. The Li-ion conduction behavior and structure are systematically explored. This material shows cubic-type structure with high structural symmetry. The direct rock salt structure of high ionic conductive Li_4YI_7 is characterized from different dimensions. The average crystal structures and local defects are studied by Rietveld refinement against synchrotron-based X-ray diffraction (SXRD) patterns and pair distribution function (PDF) analysis. The electrochemical performance shows that Li_4YI_7 possesses a low cathodic limit, stable electrochemical Li plating/stripping for over 1000 h.

Chapter 5 reports a family of new glassy SEs: $x\text{Li}_2\text{O-MCl}_y$ ($M = \text{Hf}$ or Ta). One-step ball-milling method yields the desired products in an amorphous state. The optimized $x\text{Li}_2\text{O-TaCl}_5$ glass possesses a higher ionic conductivity of $6.6 \times 10^{-3} \text{ S cm}^{-1}$ at RT among all the other developed glasses. Such a high value can be maintained within the glassy formation region in which Li_2O content (mole ratio) changes from 52.4% to 64.3%. The optimized $x\text{Li}_2\text{O-HfCl}_4$ glass also exhibits a decent ionic conductivity of $1.97 \times 10^{-3} \text{ S cm}^{-1}$ at RT. The local structures of high ionic conductive $x\text{Li}_2\text{O-TaCl}_5$ SEs are studied via Nuclear Magnetic Resonance (NMR), Extended X-ray Absorption Fine Structure (EXAFS), and Raman spectroscopy. In addition, $x\text{Li}_2\text{O-MCl}_y$ match with various cathode materials and the corresponding full cells performances are demonstrated at different C-rate and operating temperatures.

Chapter 6 investigate the compatibility between high-voltage cathode and halide SEs. Here, we report a fluorinating halide SE ($\text{Li}_3\text{InCl}_{4.8}\text{F}_{1.2}$) which shows decent ionic conductivity of 10^{-4} S/cm and high practical oxidation limit over 6 V (vs. Li/Li^+). The

mechanism of $\text{Li}_3\text{InCl}_{4.8}\text{F}_{1.2}$ showing good oxidation stability is explored via simulations, electrochemical characterizations, and SR-based microscopy. The as-prepared $\text{Li}_3\text{InCl}_{4.8}\text{F}_{1.2}$ is matched with high-voltage LCO to show the electrochemical performance of full cells.

Chapter 7 investigate the compatibility between active Na metal and Na-based sulfide SEs. Representative sulfide SEs, Na_3PS_4 and Na_3SbS_4 , are prepared and their compatibility with Na metal are tested. Al_2O_3 thin film by atomic layer deposition (ALD) and alucone layer by molecular layer deposition (MLD) are used as interlayer between sulfide SEs and Na metal, respectively. The protection mechanism is investigated by Na/Na symmetric cell and full cell performances.

Chapter 8 summarizes the results, conclusions, and contributions of the thesis work. In addition, the author provides perspectives for the development of high-performance ASSBs in the future.

1.5 References

1. Li, M., Lu, J., Chen, Z. W., Amine, K. 30 Years of Lithium-Ion Batteries. *Advanced Materials* **30**, 1800561 (2018).
2. Janek, J., Zeier, W. G. A solid future for battery development. *Nature Energy* **1**, 1-4 (2016).
3. Nitta, N., Wu, F. X., Lee, J. T., Yushin, G. Li-ion battery materials: present and future. *Materials Today* **18**, 252-264 (2015).
4. Zubi, G., Dufo-Lopez, R., Carvalho, M., Pasaoglu, G. The lithium-ion battery: State of the art and future perspectives. *Renewable & Sustainable Energy Reviews* **89**, 292-308 (2018).
5. Yong, J. Y., Ramachandramurthy, V. K., Tan, K. M., Mithulananthan, N. A review on the state-of-the-art technologies of electric vehicle, its impacts and prospects. *Renewable & Sustainable Energy Reviews* **49**, 365-385 (2015).
6. Chayambuka, K., Mulder, G., Danilov, D. L., Notten, P. H. L. From Li-Ion Batteries toward Na-Ion Chemistries: Challenges and Opportunities. *Advanced Energy Materials* **10**, 2001310 (2020).

7. Kavanagh, L., Keohane, J., Garcia Cabellos, G., Lloyd, A., Cleary, J. Global Lithium Sources—Industrial Use and Future in the Electric Vehicle Industry: A Review. *Resources* **7**, 57 (2018).
8. Cheng, Z. W., Liu, T., Zhao, B., Shen, F., Jin, H. Y., Han, X. G. Recent advances in organic-inorganic composite solid electrolytes for all-solid-state lithium batteries. *Energy Storage Materials* **34**, 388-416 (2021).
9. Lou, S. F., *et al.* Interface Issues and Challenges in All-Solid-State Batteries: Lithium, Sodium, and Beyond. *Advanced Materials* **33**, 2000721 (2021).
10. Tan, S., Ji, Y. J., Zhang, Z. R., Yang, Y. Recent progress in research on high-voltage electrolytes for lithium-ion batteries. *Chemphyschem* **15**, 1956-1969 (2014).
11. Fan, L., Wei, S. Y., Li, S. Y., Li, Q., Lu, Y. Y. Recent Progress of the Solid-State Electrolytes for High-Energy Metal-Based Batteries. *Advanced Energy Materials* **8**, 1702657 (2018).
12. Chen, Z., *et al.* 4-V flexible all-solid-state lithium polymer batteries. *Nano Energy* **64**, 103986 (2019).
13. Kato, Y., *et al.* High-power all-solid-state batteries using sulfide superionic conductors. *Nature Energy* **1**, 1-7 (2016).
14. Liu, Y. J., He, P., Zhou, H. S. Rechargeable Solid-State Li-Air and Li-S Batteries: Materials, Construction, and Challenges. *Advanced Energy Materials* **8**, 1701602 (2018).
15. Hou, W. R., Guo, X. W., Shen, X. Y., Amine, K., Yu, H. J., Lu, J. Solid electrolytes and interfaces in all-solid-state sodium batteries: Progress and perspective. *Nano Energy* **52**, 279-291 (2018).
16. Liang, J., *et al.* Stabilizing and understanding the interface between nickel-rich cathode and PEO-based electrolyte by lithium niobium oxide coating for high-performance all-solid-state batteries. *Nano Energy* **78**, 105017 (2020).
17. Adeli, P., *et al.* Boosting Solid-State Diffusivity and Conductivity in Lithium Superionic Argyrodites by Halide Substitution. *Angewandte Chemie-International Edition* **58**, 8681-8686 (2019).

18. Zhou, L. D., Assoud, A., Zhang, Q., Wu, X. H., Nazar, L. F. New Family of Argyrodite Thioantimonate Lithium Superionic Conductors. *Journal of the American Chemical Society* **141**, 19002-19013 (2019).
19. Kamaya, N., *et al.* A lithium superionic conductor. *Nature Materials* **10**, 682-686 (2011).
20. Kato, Y., *et al.* High-power all-solid-state batteries using sulfide superionic conductors. *Nature Energy* **1**, (2016).
21. Hayashi, A., *et al.* A sodium-ion sulfide solid electrolyte with unprecedented conductivity at room temperature. *Nature Communications* **10**, 1-6 (2019).
22. Banerjee, A., *et al.* Na₃SbS₄: A Solution Processable Sodium Superionic Conductor for All-Solid-State Sodium-Ion Batteries. *Angewandte Chemie-International Edition* **55**, 9634-9638 (2016).
23. Asano, T., Sakai, A., Ouchi, S., Sakaida, M., Miyazaki, A., Hasegawa, S. Solid Halide Electrolytes with High Lithium-Ion Conductivity for Application in 4 V Class Bulk-Type All-Solid-State Batteries. *Advanced Materials* **30**, 1803075 (2018).
24. Li, X. N., *et al.* Water-Mediated Synthesis of a Superionic Halide Solid Electrolyte. *Angewandte Chemie-International Edition* **58**, 16427-16432 (2019).
25. Zhou, L. D., Kwok, C. Y., Shyamsunder, A., Zhang, Q., Wu, X. H., Nazar, L. F. A new halospinel superionic conductor for high-voltage all solid state lithium batteries. *Energy & Environmental Science* **13**, 2056-2063 (2020).
26. Zhou, L. D., *et al.* High areal capacity, long cycle life 4 V ceramic all-solid-state Li-ion batteries enabled by chloride solid electrolytes. *Nature Energy* **7**, 83-93 (2022).

Chapter 2

2 Literature review

In this chapter, the development of ISEs will be reviewed. Besides, the interfacial strategies between ISEs and electrodes (anode and cathode) will be presented.

2.1 Inorganic solid electrolytes (ISEs)

SEs are generally divided into SPEs, ISEs, and composite polymer electrolytes (CPEs) (**Figure 2.1**). Specifically, while SPEs are deformable to provide intimate contact with electrodes, they show drawbacks of poor mechanical strength, poor thermal dimensional stability, narrow operating temperature range, narrow electrochemical window, and relatively low conductivity.¹ Research interest has been stimulated recently to use SPEs as a framework in CPEs, which can display the advantages of their respective components and compensate each other regarding their drawbacks.² In comparison, ISEs with solid nature show increased safety and thermal stability. They can also enable and support battery operation at low and high temperatures in which conventional liquid electrolytes (LEs) would freeze, boil or decompose.³ Moreover, no bulk polarization is expected in solid materials resulting from immobility of the anionic framework.⁴ The favorable properties that SEs possess widen the application of ASSBs in tailorable and penetrable batteries, portable electronics, electric vehicles, and photoelectric space stations, making our lives safer, more convenient and more efficient. Herein, the fundamentals, current progress, challenges, and potential of ISEs will be comprehensively summarized below.

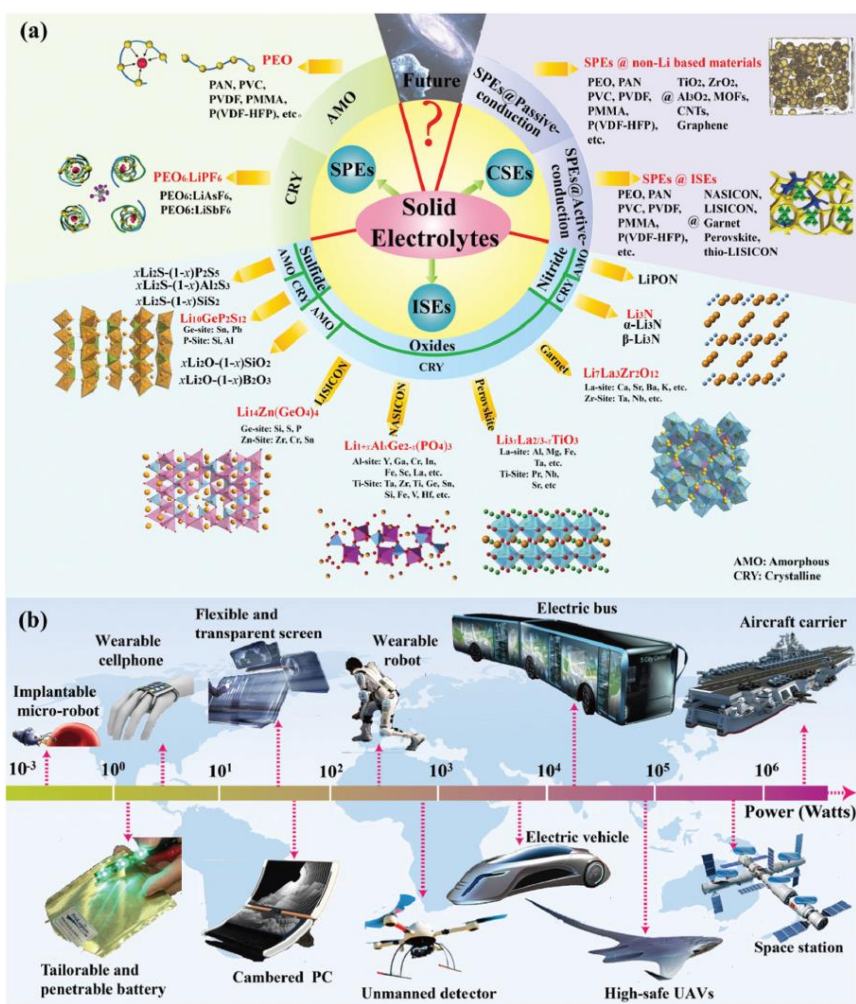


Figure 2.1 (a) categories of SEs and (b) the potential applications of ASSBs.³

2.1.1 Fundamentals of ion migration in ISEs

ISEs consist of mobile ions as well as metal and nonmetal ions which form polyhedra with ligands that create the skeleton of the crystal structure.⁵ Generally, cations from IA Group (H^+ , Li^+ , Na^+ , K^+), Mg^{2+} , Al^{3+} , Cu^{2+} , and Ag^+ , as well as anions like O^{2-} , F^- , and Cl^- in are regarded as mobile ions in solids. A large number of metals from groups IIA and IIIA, part of (post)transition metals, rare-earth metals and some reactive nonmetals (e.g., Si, P, Se and S) are the core cations in a polyhedral to form skeletons of ISE, while chalcogens, halogens, and nitrogen are used as ligands. As shown in **Figure 2.2a**, the ion-conduction mechanisms in ISEs are totally different from those in LEs. Take Li^+/Na^+

transport as an example, in LEs, there are moving solvated lithium ions in the solvent medium. The Li/Na-ion conductivity in LEs can be enhanced 1) by increasing salt/ion dissociation in solvents with greater dielectric constants, and 2) promoting the mobility of solvated ions by lowering the viscosity of solvents.⁶ The fast charge transfer of ions/molecules in solvent results in flat potential energy profile of mobile Li ions in LEs. In sharp contrast, Li⁺/Na⁺ diffuse in solids can be treated as ion hopping along favorable migration pathways, while they have to pass through periodic energetic barrier that separates the two local minima (**Figure 2.2a**). The energy barrier greatly influences ionic mobility and ionic conductivity, where low migration energies lead to high ionic mobility and conductivity. The sites and their energies are mainly defined by their local bonding environment.

In crystalline solids, other than mobile ions, cationic vacancies or interstitials are also perceived as the mobile charged species. As depicted in **Figure 2.2b**, there are generally three principal diffusion mechanisms: (1) vacancy directly hopping; (2) interstitial directly hopping; (3) interstitial knock-off.⁶ The ion diffusion and ionic conductivity in solids can be related by Nernst-Einstein relation since they both related to charge and mass transport. Therefore, the ionic conductivity can be expressed by:

$$\sigma_{\text{ion}} = nq\mu \quad (1)$$

where q is the concentration of charge carriers and μ is their mobility. Based on the modified Arrhenius theory, it should be noted that ion conduction is a thermally activated process affected by the temperatures, which can be described as below:

$$\sigma_{\text{ion}} = AT^m e^{-\frac{E_a}{k_B T}} \quad (2)$$

Where m typically equal to -1 , k_B the Boltzmann constant, T the temperature in degree Kelvin, A is the pre-exponential factor which relates the entropy of migration, the jump distance, and the attempt frequency. E_a a characteristic activation energy for ion conduction, which includes the energy needed to form the mobile defects (E_f) and the energy barrier for their migration (E_m). Taking E_a as a constant the last can be integrated to yield a linear equation to depict Arrhenius plots (**equation 3** and **Figure 2.2c**):

$$\ln(\sigma_{\text{ion}}T) = \ln(A) - E_a/k_B T \quad (3)$$

The ionic conductivity can be determined by testing complex impedance spectroscopy at a wide range of frequency (**Figure 2.2d**). In the complex impedance plot real and imaginary impedance has been plotted as a parametric function of frequency and a trendy behavior, the low frequency intercept of the arc on real axis represents bulk resistance and ionic conductivity can be obtained as equation (4). The detailed discussion of this part will be shown in Chapter 3.

$$\sigma_{\text{ion}} = \frac{l}{R_{\text{bulk}}A} \quad (4)$$

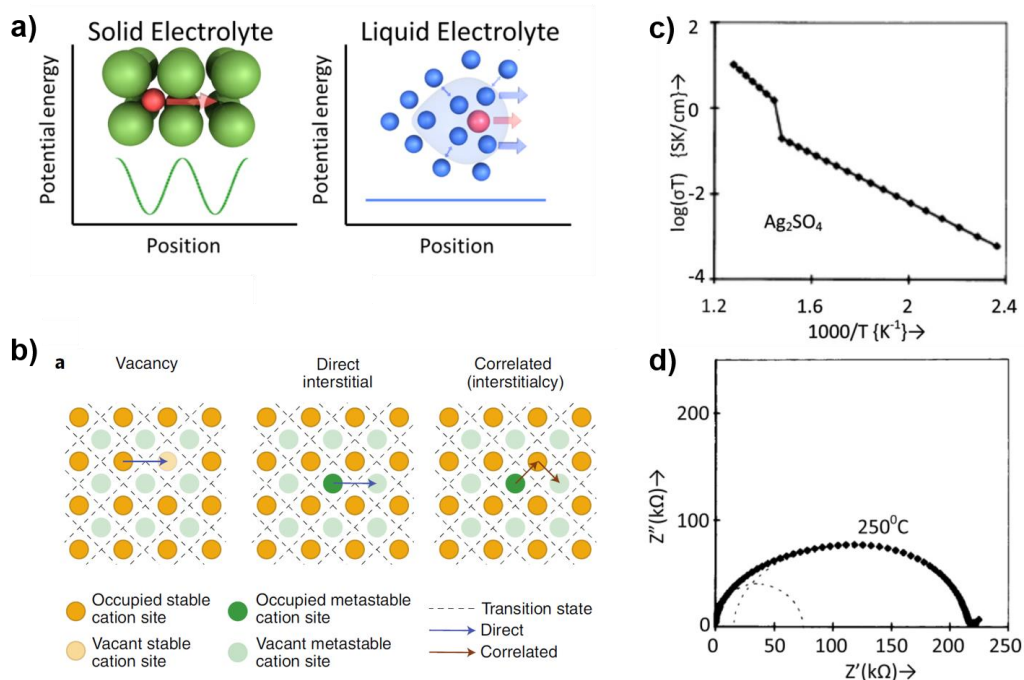


Figure 2.2 (a) Schematics of ion diffusion and energy barrier in solid electrolytes and liquid electrolytes.⁵ (b) Three typical ion migration mechanisms in crystalline solids: vacancy, direct interstitial and correlated interstitial involving a single or multiple sites.⁷ (c) Arrhenius plot for Ag_2SO_4 , in which all the compositions are found to obey the

Arrhenius law in both the α and β phases.⁸ (d) Complex impedance plot for pure Ag_2SO_4 at 250°C.⁸

Based on the above equations, certain requirements for fast ion transport can be derived and are listed⁹: (1) A high dimensionality of the conduction pathways; (2) Optimized carrier density (Li^+/Na^+); (3) A low enthalpy of migration (activation energy). Generally, ionic conductivity is closely related to structural changes of solids. Certain structural requirements and typical approaches to influence the conductivity of pertinent materials can be found in **Figure 2.3**. First, a polyhedral connectivity that allows for lower energy jumps between sites is needed. A typical example of Li-ion conduction in hexagonal-close-packed (hcp) lattice is shown in **Figure 2.3a**.¹⁰ There are tetrahedra (T) and octahedra (O) with various configuration in a hcp lattice. Li ions migrate through T-O-T, O-O, and T-T paths experience different activation barriers. Second, structural changes due to substitutions of cations and anions with different ionic radii can alter the lattice parameters and make ions easily access the ‘bottleneck’ (**Figure 2.3b**).¹¹ Last, the widening of diffusion pathways and the idea that a softer, more polarizable lattice will lead to better ionic transport (such as iodide ligand) (**Figure 2.3c**).¹²

In glassy solids, the ion migration is different since the lack of long-range periodicity in glassy ISEs implies the absence of regular coordination sites and symmetric long-range migration pathways. Taking oxide glasses as an example, oxides glassy ISEs are formed by randomly cross-linked network former (SiO_2 , BO_3 , Al_2O_3 , and etc.), which is broken in some places by the glass modifier Li/Na oxides. The structure has large holes which are available sites for ionic conduction (**Figure 2.3d**). There have been several models to describe the ion conduction behavior in glass. One of them is called Anderson and Stuart model, which suggests that the total activation energy ΔE_a is the combination result of the electrostatic binding energy ΔE_B and the strain energy ΔE_s . ΔE_B describes the Columbic forces acting on the ion as it moves away from its charge-compensating site, and ΔE_s describes the mechanical forces acting on the ion as it dilates the structure sufficiently to allow the ion to move between sites (**Figure 2.3e**).¹³ Despite diligent efforts, a unified

theory for conduction in the amorphous state is not fully established. Nevertheless, elements of the hopping theory mentioned in crystalline solids can still be utilized, but require a statistical treatment, such as considering a distribution of activation energies for hops instead of a discrete one.¹⁴ Ionic conduction in glasses can be identified when a material shows an Arrhenius relationship with temperature. Besides, the manners for improving ionic conductivity, such as increasing Li/Na concentration, cation and anion doping /substitution, can also be applicable in the glass system.

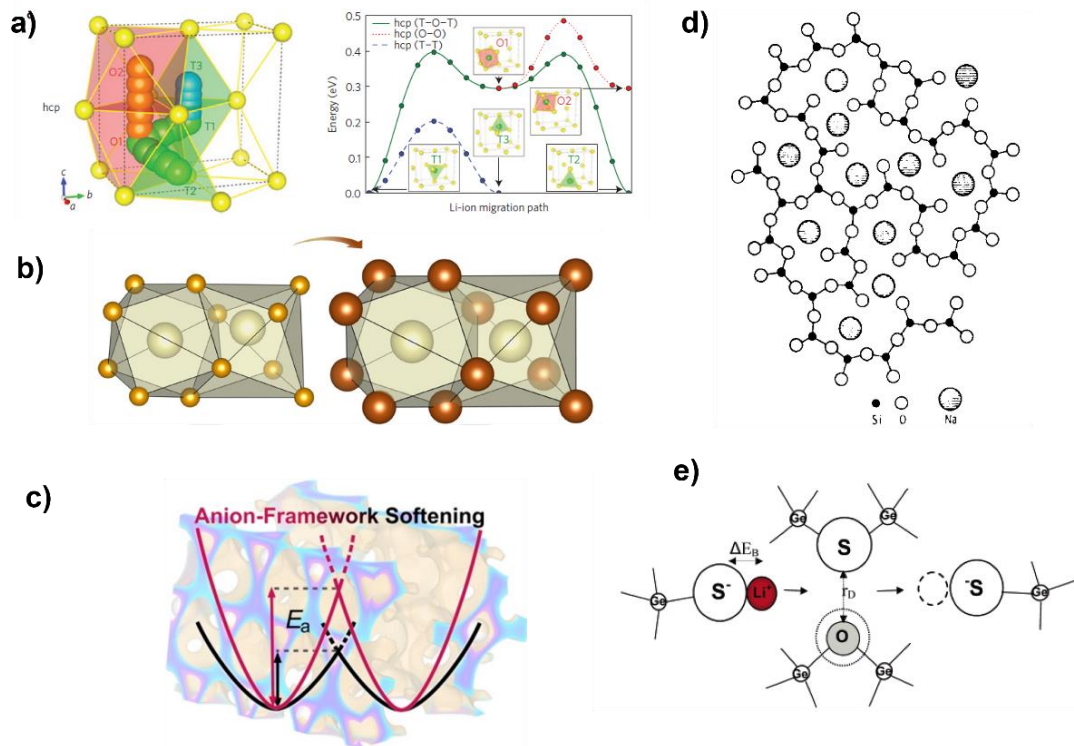


Figure 2.3 (a) Li-ion migration pathways in hcp-type anion lattices.¹⁰ (b) Schematic of the influence of the width of the diffusion pathway.¹¹ (c) A softer anionic sublattice in iodides compared chlorides leads to larger vibrational amplitudes and lower activation barriers.¹² (d) Schematic two-dimensional representation of tetrahedrally coordinated silica glass.¹⁵ (e) Simplified pictorial view of the ionic conduction energy based on the Anderson and Stuart model.¹⁶

2.1.2 Oxide ISEs

Crystalline oxide ISEs mainly include perovskite-type, NASICON-type, LISICON-type ($\text{Li}_{14}\text{Zn}(\text{GeO}_4)_4$), garnet-type, and etc. Bulk ionic conductivity greater than 1 or even 10 mS cm^{-1} has been achieved at RT for perovskite, NASICON, and garnet-type oxide SEs with activation energy of 0.2 eV–0.3 eV.

For perovskite oxides, the general formula is ABO_3 in which A-site ions is occupied by large ionic radius cations (typically alkaline-earth or rare-earth elements) at the corners, B ions (typically transition-metal ions) at the center, and oxygen atoms at the face-center positions (**Figure 2.4a**). Various perovskite-type Li-ion solid electrolytes, including $\text{Li}_x\text{La}_{(2-x)/3}\text{TiO}_3$ (LLTO), and $(\text{Li}, \text{Sr})(\text{B}, \text{B}')\text{O}_3$ ($\text{B} = \text{Zr}, \text{Hf}, \text{Ti}, \text{Sn}, \text{Ga}, \text{etc.}$, $\text{B}' = \text{Nb}, \text{Ta}, \text{etc.}$), have been developed in recent years.¹⁷ Among them, LLTO is more promising since it exhibits a maximum bulk ionic conductivity of $1 \times 10^{-3} \text{ S cm}^{-1}$ at RT at x near 0.3.¹⁸ However, the grain-boundary conductivity of LLTO reach to $10^{-5} \text{ S cm}^{-1}$ at RT, resulting in low total ionic conductivity for a classic polycrystalline microstructure.¹⁹ Moreover, the employment of Ti^{4+} causes low stability against Li metal. Recently, the polymer-LLTO CSEs have been reported to overcome the interface resistance as well as protect the SE from direct contact with Li metal.^{20, 21} Thus, Li-ion batteries consisting of such CSEs are potential candidates for next-generation batteries.

For NASICON oxides, the general molecular formula is $\text{A}_x\text{MM}'(\text{XO}_4)_3$, where A is Li or Na; M and M' is metal includes Fe, Ge, Sn, Hf, Zr, Sc, Y, or In; X is P, Si, or As. The crystal structures of NASICON are mainly rhombohedral and monoclinic even for the same composition (**Figure 2.4b**). The pioneering NASICON compound is $\text{Na}_{1+x}\text{Zr}_2\text{P}_{3-x}\text{Si}_x\text{O}_{12}$ ($0 \leq x \leq 3$).²² Substituting Zr^{4+} by Hf^{4+} results in an improved conductivity of $2.3 \times 10^{-3} \text{ S cm}^{-1}$.²³ Some of the representative NASICON-type Na^+ SEs can also be commercialized and successfully used in Na- O_2 and Na-S batteries.^{24, 25} Besides, NASICON-type Li-ion conductors have been of great interest. The common system is $\text{LiM}_2(\text{PO}_4)_3$, in which M is Ti or Ge. M can be partially substituted by trivalent and divalent cations such as Al, Ga, Sc, and etc.^{26, 27} $\text{Li}_{1+x}\text{Al}_x\text{Ti}_{2-x}(\text{PO}_4)_3$ (LATP) shows

a higher ionic conductivity of $3.4 \times 10^{-3} \text{ S cm}^{-1}$ at RT when x was 0.2 or 0.4²⁸, while they suffer from poor sintering behavior.

Garnet-type SE with the nominal formula $\text{Li}_7\text{La}_3\text{Zr}_2\text{O}_{12}$ (LLZO) is one of the most promising Li-ion conducting oxides. Cubic LLZO (**Figure 2.4c**) is superior to tetragonal phase because of the fast Li-ion conductivity ($10^{-4} - 10^{-3} \text{ S cm}^{-1}$), wide electrochemical window, and high stability against Li metal.²⁹ LLZO can be combined in SE framework for high energy and high power battery applications (such as Li-S and Li-O₂).

The representative amorphous oxide ISEs is lithium phosphorus oxynitride (Lipon) (**Figure 2.4d**). The development of Lipon is the incorporation of N into amorphous Li_3PO_4 to form Lipon simultaneously increases the RT ionic conductivity by over an order of magnitude up to $3 \times 10^{-6} \text{ S cm}^{-1}$ and improves the electrochemical stability of the electrolyte.³⁰ Lipon is the only ISE which can enable an all-solid-state thin film battery with a lithium metal anode and a high-voltage $\text{LiNi}_{0.5}\text{Mn}_{1.5}\text{O}_4$ (LNMO) cathode to achieve a capacity retention of 90% over 10,000 cycles with a Coulombic efficiency over 99.98%.³¹ However, the drawback is that Lipon show poor ionic conductivity and shows difficulty to involve in bulk-type ASSBs.

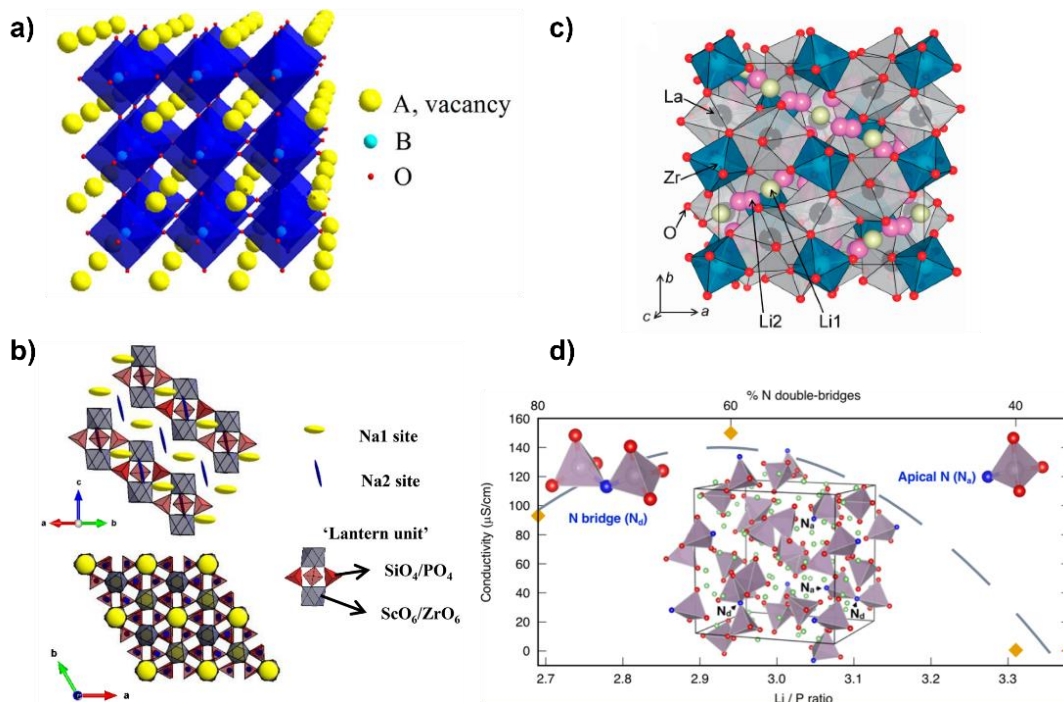


Figure 2.4 (a) Crystal structure of cubic perovskite.³² (b) Schematic representations of the rhombohedral NASICON.³³ (c) Crystal structure of cubic $\text{Li}_7\text{La}_3\text{Zr}_2\text{O}_{12}$ ³⁴ (d) Amorphous LiPON structure of composition $\text{Li}_{2.94}\text{PO}_{3.50}\text{N}_{0.31}$ obtained from Ab initio molecular dynamics (AIMD) simulations. Li (green), P (gray), O (red), N (blue); P (O,N)₄ tetrahedra are drawn.³⁵

2.1.3 Sulfide ISEs

Sulfide SEs can be generally classified as glasses, glass–ceramics, and ceramic SEs based on their crystallinity and preparation process. Sulfide glasses are firstly investigated as ionic conductors. Glassy materials show advantages of low grain boundary resistance, isotropic conduction paths, and easy fabrication. Basic sulfide glasses contain $\text{Li}_2\text{S}/\text{Na}_2\text{S}$ as glass modifier in addition to glass former such as P_2S_5 , SiS_2 , B_2S_3 and etc.³⁶ Both melt-quenching and mechanochemical milling methods can easily yield the desired products in amorphous state. Crystallization of glass usually decreases the conductivity except for $\text{Li}_2\text{S}-\text{P}_2\text{S}_5$ compounds, which show high ionic conductivity up to $10^{-4} \text{ S cm}^{-1}$.^{37, 38, 39} Two common methods have been adopted to improve the conductivity of

glasses. One is adding lithium halides (e.g., LiI or LiCl) to increase the lithium concentration and act as network former coordinating the polyhedra.^{36,40} However, this improvement is often accompanied by narrowing of the electrochemical window due to the decomposition of halides.⁴¹ The other is adding metal oxides or lithium ortho-oxosalt (e.g., Li₄SiO₄ or Li₃PO₄) to create non-bridging oxygen (NBO) which acts as strong ion traps in the structure.^{42,43} Both methods are based on the “mixed-anion effect” where the conductivity of the ion mixture does not change monotonically but reaches a maximum in some property between the two end states at an ideal material composition.⁴⁴

Glass–ceramic sulfides can be regarded as a post-annealing product of glass. Single-step ball milling can be also used to form glass–ceramics. It is defined glass–ceramics are inorganic, non-metallic materials prepared by controlled crystallization of glasses via different processing methods. They contain at least one type of functional crystalline phase and a residual glass. The volume fraction crystallized may vary from ppm to almost 100%.⁴⁵ The mostly researched system is Li₂S–P₂S₅, in which the compound 70Li₂S–30P₂S₅ glass-ceramic show a high ionic conductivity of $3.2 \times 10^{-3} \text{ S cm}^{-1}$ with a low activation energy of 18 KJ mol⁻¹ (**Figure 2.5a** top). The ambient ionic conductivity for 70Li₂S–30P₂S₅ glass is only $5.4 \times 10^{-5} \text{ S cm}^{-1}$. Raman data indicated that the boosted conductivity compared with that of glassy sulfides is attributed to the arrangements of the pyro-thiophosphate anion P₂S₇⁴⁻, which totally appears in crystalline compound by solid-state reaction (**Figure 2.5a** below).⁴⁶ Besides, as the pioneered compounds, Li₃PS₄ and Na₃PS₄ also draw much interest and contribute to the development of sulfide-based SEs.^{47,48}

Crystalline sulfides are one of the promising SE candidates since some of them show high ionic conductivity (10⁻² level) surpassing those of the liquid counterparts. Representative crystalline sulfides include argyrodite Li₆PS₅X (X = Cl, Br, I), Li₁₀GeP₂S₁₂ (LGPS)-type, and NaMM'S-type SEs (M = P or Sb; M' = Sn or W). For argyrodite compounds Li₆PS₅X (X = Cl, Br, I), the general ionic conductivity is over 10⁻³ S cm⁻¹ at RT.⁴⁹ X⁻ anions in Li₆PS₅X form a face-centered-cubic (*fcc*) framework, and nonbonded “free” S²⁻ ions and PS₄³⁻ units occupy the tetrahedral and octahedral voids, respectively (**Figure 2.5b**).⁵⁰ Ionic size differences cause site order/disorder differences,

which means in $\text{Li}_6\text{PS}_5\text{I}$, the Γ^- and S^{2-} anions remain on their two unique crystallographic sites, while for $\text{X} = \text{Br}^-$ and Cl^- , significant site disorder is observed. Benefiting from such an order/disorder local structures, the most recent developed variant $\text{Li}_{6.6}\text{Si}_{0.6}\text{Sb}_{0.4}\text{S}_5\text{I}$ show an excellent ionic conductivity of $14.8 \text{ mS}\cdot\text{cm}^{-1}$ for cold pressed pellet.⁵¹ The nominal LGPS-type SEs are $\text{Li}_{10}\text{GeP}_2\text{S}_{12}$ and $\text{Li}_{9.54}\text{Si}_{1.74}\text{P}_{1.44}\text{S}_{11.7}\text{Cl}_{0.3}$ (**Figure 2.5d**). Their RT ionic conductivities are 12 mS cm^{-1} (cold pressed)⁵² and 25 mS cm^{-1} (hot pressed)⁵³, respectively. The 3D conduction pathways (1D along the c axis and 2D in the ab plane) in LGPS-type structures contribute to the fast Li-ion mobility. The use of LGPS-type SEs in ASSBs show great advantages not only in high energy density but also high powder density.⁵³ In comparison with Li-based counterparts, superionic Na-based sulfides are lately developed since 2012. One of the representative Na-based sulfides is Na_3SbS_4 (**Figure 2.5c**, left). It shows decent ionic conductivity of $1.05 \times 10^{-3} \text{ S cm}^{-1}$ at RT. More importantly, Na_3SbS_4 exhibit air stability without any modification, which makes it special since almost all the sulfides are sensitive to moisture to produce H_2S . Doping with high valence state element such as W^{6+} ($\text{Na}_{2.88}\text{Sb}_{0.88}\text{W}_{0.12}\text{S}_4$) can dramatically increase the ionic conductivity to $3.2 \times 10^{-2} \text{ S cm}^{-1}$ (**Figure 2.5c**, right), which is the highest value among all the developed SEs.⁵⁴ In sodium system, most of the superionic conductors are in cubic structures and Na-ion are favorable to move in 3D frameworks.

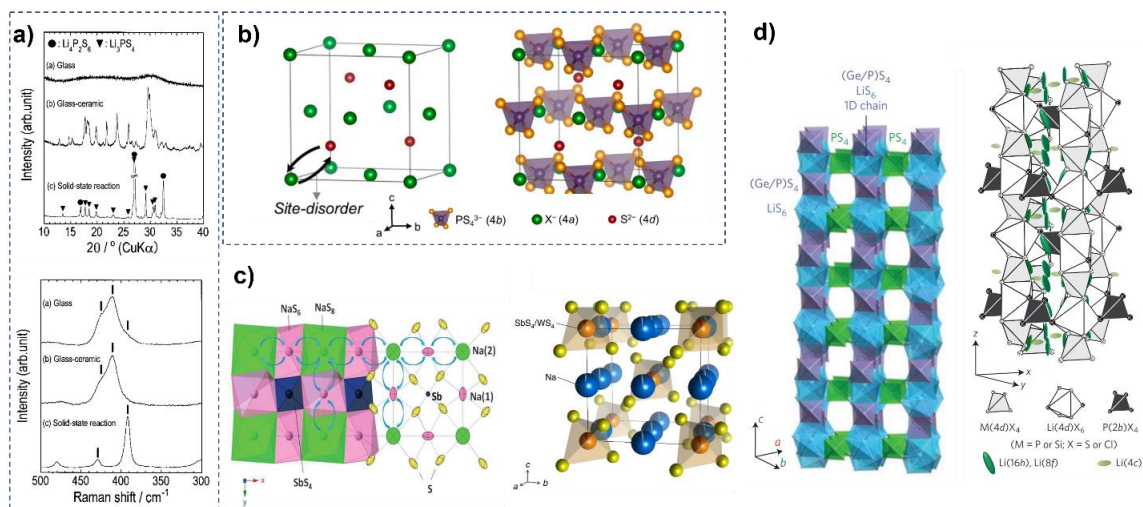


Figure 2.5 (a) XRD patterns and Raman spectroscopy of 70Li₂S-30P₂S₅ in (a) glass state, (b) glass-ceramic state, (c) crystals⁴⁶. (b) Crystal structures of Li₆PS₅X with X = Cl, Br, I; The free S²⁻ anions and the corner of the PS₄³⁻ tetrahedra derived from Frank-Kasper polyhedral, where shows three Li⁺ conduction pathways.⁵⁰ (c) Local structure of Na₃SbS₄⁵⁵ (left) and Na_{2.88}Sb_{0.88}W_{0.12}S₄⁵⁴ (right). (d) Framework structure of Li₁₀GeP₂S₁₂⁵² (left) and Li_{9.54}Si_{1.74}P_{1.44}S_{11.7}Cl_{0.3}⁵³ (right)

2.1.4 Halide ISEs

2.1.4.1 Chloride ISEs

In 1990s, LiAlCl₄ was developed by molten LiCl–AlCl₃, which can be treated as the first chloride SE and possesses an ionic conductivity of 0.35 S/cm at 174 °C.⁵⁶ Generally, LiAlCl₄ dissolving in nonaqueous solvents was used as a soluble cathode or electrolyte in lithium batteries. The ionic conductivity of solid LiAlCl₄ is around 10⁻⁶ S/cm, which can be directly used as thin-filmed SE layer in a thin-film Li_xTiS₂/LiAlCl₄/LiCoO₂ all-solid-state lithium batteries (ASSLB).⁵⁷ A great breakthrough was made in 2018, when Tetsuya Asano et al. synthesized Li₃YCl₆ (LYC) with a Li-ion conductivity of 0.51 × 10⁻⁴ S/cm.⁵⁸ LYC is mechanochemically synthesized from a stoichiometric mixture of binary compound precursors, LiCl and YCl₃. The conductivity of LYC decreased when improving the crystallinity. Different from the lattice structure of other SEs, the

structural framework of these metal halide electrolytes is anionic close-packed structure, the volume and polarity of cation species influence the overall lattice. As shown in **Figure 2.6a**, XRD Rietveld analysis for LYC shows a trigonal (spacegroup of $P-3m1$) structure with an hcp anion sublattice, lithium-ion transport paths along the ab -plane are via tetrahedral interstitial sites, while along the c -axis, the paths are directly connected between neighboring octahedral sites. These pathways of lithium ions in LYC are in contrast to the highly conducting sulfides where lithium ions transport via face-shared distorted tetrahedral sites of a bcc-like anion arrangement.

In the subsequent year, Li_3InCl_6 (LIC) SE was prepared through a ball-milling and annealing method.⁵⁹ XRD results indicate that Li_3InCl_6 is a monoclinic structure with a hcp anion sublattice, which can also be regarded as a distorted LiCl structure as presented in **Figure 2.6b**, with Li^+ , In^{3+} , and a vacancy located in the octahedron formed by Cl^- anions. The ball-milled and annealed Li_3InCl_6 SEs show RT high ionic conductivities of 0.84×10^{-4} and 1.49×10^{-3} S/cm (**Figure 2.6b**). Relatively high crystallinity is good for Li-ion conduction in LIC. Another favorable and desirable advantage of LIC is that it can be synthesized through a water-mediated approach, which shows a high RT ionic conductivity of 2.04×10^{-3} S/cm.⁶⁰ LiCl and InCl_3 directly dissolve into water with a stoichiometric ratio to form $\text{Li}_3\text{InCl}_6 \cdot 2\text{H}_2\text{O}$ intermediates, which are then dehydrated to form the final LIC powders. Besides, the reversible conversion between LIC and its hydrated form can ensure a recoverable structure and ionic conductivity after being exposed to humid air. The water-mediated LIC is also demonstrated showing a monoclinic structure.

As discussed above, we can see that the crystal lattice plays an important role in the intrinsic properties of a SE, such as Li ion transport kinetics, air/humidity tolerance, and the related chemistry. Therefore, the ionic conductivity and humidity stability of a SE can be improved by tuning the crystal sublattice of the material. A typical example is tuning the lattice structure of Li_3YCl_6 by replacing part of the Y^{3+} (90 pm) to In^{3+} (80 pm) to form $\text{Li}_3\text{Y}_{1-x}\text{In}_x\text{Cl}_6$.⁶¹ When the ratio of In^{3+} was increased, a gradual structural conversion from the hcp anion arrangement to cubic-close-packed (ccp) anion arrangement has been traced. As shown in **Figure 2.6c**, without In^{3+} substitution ($x = 0$),

the XRD pattern can be indexed to orthorhombic LYC, while it changed to the trigonal LYC structure (ICSD no. 04-009-8882) when $x = 0.1$. The obvious monoclinic LIC phase starts to evolve at $x \geq 0.3$, with all the XRD patterns being quite similar. Once the ccp anion structure appeared, the ionic conductivities are highly improved to 6.02×10^{-4} S/cm for $\text{Li}_3\text{Y}_{0.8}\text{In}_{0.2}\text{Cl}_6$, and all samples with $x \geq 0.5$ retained high ionic conductivity in the range from 1.09 to 1.42×10^{-3} S/cm. Compared to hcp anion sublattice, the $\text{Li}_3\text{Y}_{1-x}\text{In}_x\text{Cl}_6$ materials with ccp anion sublattice reveals faster Li^+ migration. Besides, $\text{Li}_3\text{Y}_{1-x}\text{In}_x\text{Cl}_6$ processes good humidity tolerance³ due to the introduction of $(\text{Y}/\text{In})\text{Cl}_6^{3-}$ octahedral structures, which guarantees a similar humidity stability of $\text{Li}_3\text{Y}_{1-x}\text{In}_x\text{Cl}_6$ with that of the LIC. This phenomenon is quite different from the previous opinions that ionic conductivity traditionally increases along with the increase in the unit cell volume or reaching an “optimal” size, which plays an important role for understanding the crystal structure and Li-ion conduction mechanism of SEs.

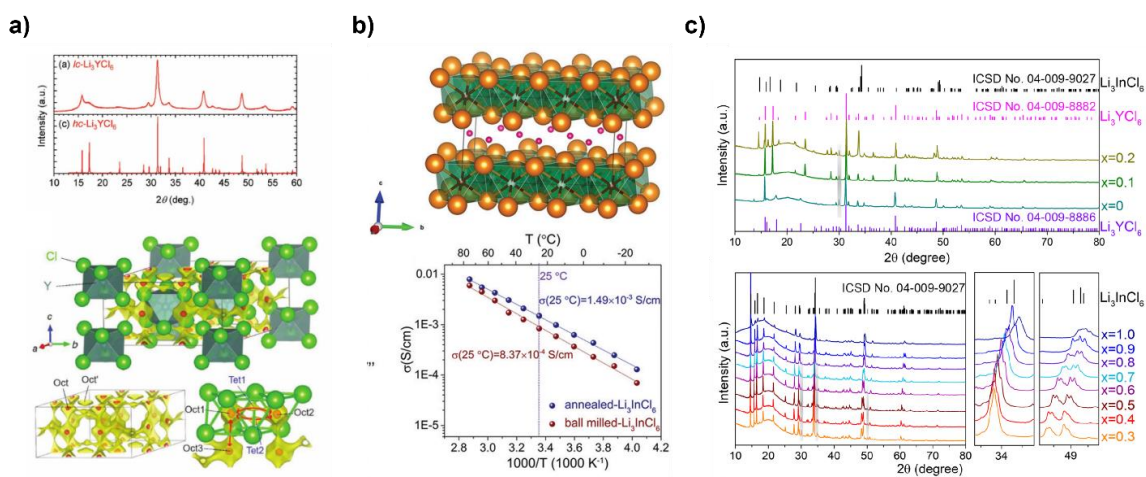


Figure 2.6 (a) The measured XRD patterns of mechanochemically synthesized low-crystalline-LYC and annealed high-crystalline-LYC.⁵⁸ The crystal structures of LYC obtained after Rietveld refinement, superimposed with a calculated BVSE-based lithium-ion potential map. The yellow surface corresponds to the ionic conduction path, and the regions enclosed with red surfaces correspond to the stable lithium-ion positions. (b) Structure of annealed-LIC, showing two kinds of InCl_6^{3-} octahedra with different occupations of In^{3+} (red wine) and vacancies (V'' , white); orange balls are Cl^- .

Arrhenius plots of ball-milled and annealed Li_3InCl_6 samples.⁵⁹ (c) XRD patterns of $\text{Li}_3\text{Y}_{1-x}\text{In}_x\text{Cl}_6$ ($x = 0, 0.1, 0.2$) and ($x = 0.3-1.0$), respectively.⁶¹

In order to identify other new promising Li-ion conductors, high-throughput computational method is adopted to screen 14,000 Li-containing compounds in the Materials Project database using a descriptor based on lattice dynamics. One of 18 predicted promising compounds, Li_3ErCl_6 , is synthesized by ball-milling and annealing the stoichiometric mixture of ErCl_3 and LiCl . The obtained conductivities and activation barriers for Li_3ErCl_6 are 0.3 mS/cm ($E_a = 0.41$ eV) and 0.05 mS/cm ($E_a = 0.48$ eV) for the ball-milled and the crystalline samples, respectively.⁶² The ball-milled sample without subsequent annealing has a noticeably increased conductivity, which is similar with that of the LYC. The structure of Li_3ErCl_6 is shown in **Figure 2.7a**. The chloride atoms build up a hexagonally closed packed lattice with octahedral voids that are partially occupied. Every ErCl_6^{3-} octahedron is surrounded by six LiCl_6^{6-} octahedra. X-ray diffraction was used to characterize the samples and further investigate the structure. The diffraction pattern for the crystalline sample that was collected after subsequent annealing of the ball-milled sample can be indexed to the trigonal space group $P-3m1$. We noticed that the radius of Y^{3+} and Er^{3+} are very similar ($\text{Y}^{3+} = 104$ pm, $\text{Er}^{3+} = 103$ pm), and the resultant crystal structure of LYC and Li_3ErCl_6 belong to tetragonal-hcp (hcp-T) structure with hcp anionic lattice. Other compounds of Li_3MCl_6 (M^{3+} ranges from 106.3 pm (Tb^{3+}) to 102 pm (Tm^{3+})) also show the same ionic conductive properties and crystal structure. Therefore, we can conclude that the radius of M^{3+} ranges from 106.3 pm (Tb^{3+}) to 102 pm (Tm^{3+}), the Li_3MCl_6 can maintain the hcp-T structure.⁶³ And for this category halide Li_3MCl_6 , SE properties like ionic conductivity is related to its crystal structure. Aliovalent substitution or doping of metal ions to optimize vacancies as well as Li^+ concentration in a mobile Li^+ sublattice is an effective strategy to improve the ionic conductivity of SEs. Nazar et al reported $\text{Li}_{3-x}\text{M}_{1-x}\text{Zr}_x\text{Cl}_6$ ($\text{M} = \text{Y}, \text{Er}$) SEs with RT ionic conductivity up to 1.4×10^{-3} S/cm by using the aliovalent substitution strategies.⁶⁴ As shown in **Figure 2.7b**, the substitution of M^{3+} by Zr^{4+} can introduce a large number of vacancies. Meanwhile, the lattice structure will be affected by the radius of different

metal cations in the metal halide electrolyte. The substitution of M^{3+} ion by a smaller radius Zr^{4+} ion is accompanied by an hcp-T to hcp-O transition. Moreover, isovalent substitution is another strategy for improving the ionic conductivity. Although the isovalent substitution of metal ions cannot induce vacancy or Li content, it can distort the local structure or even affect the anion stacked sublattice based on different radii and polarizability of the introduced cation.

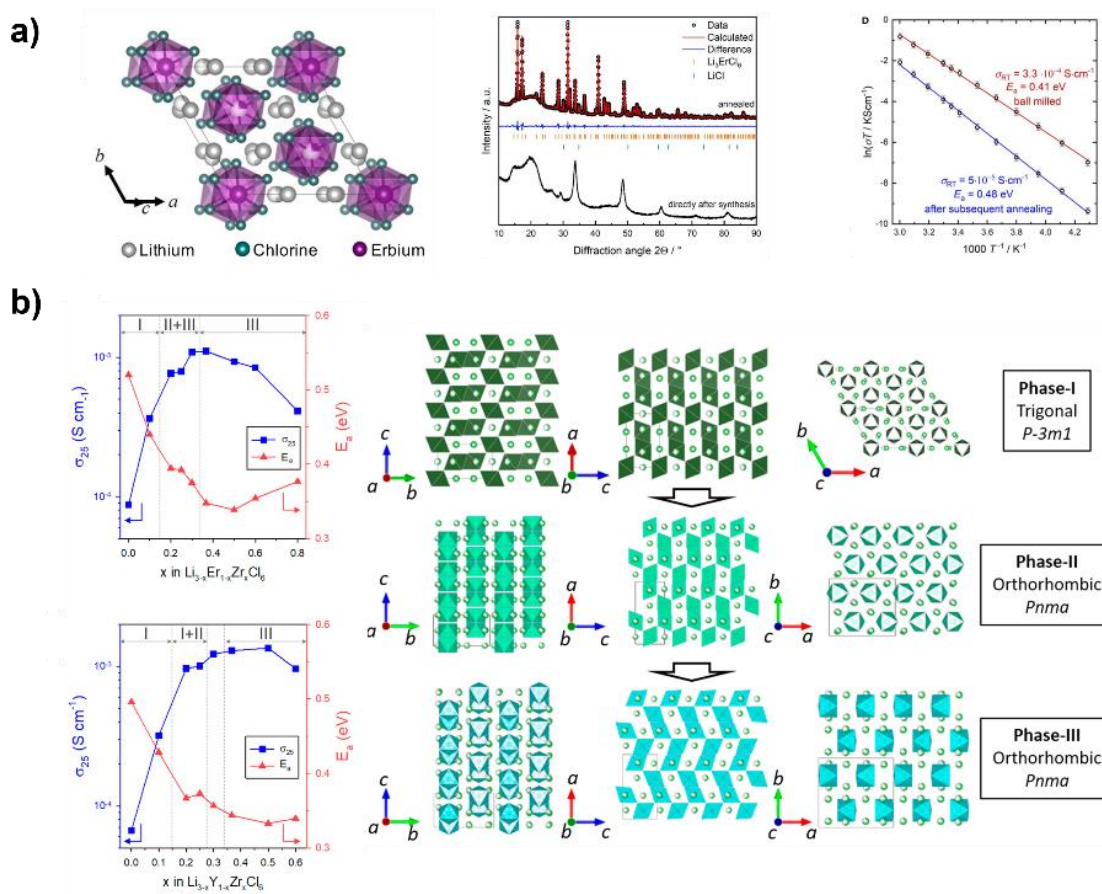


Figure 2.7 (a) Structural features within the unit cell, showing face-sharing $ErCl_6^{3-}$ octahedra with Li^+ in chains along the c -axis.⁶² Arrhenius plot showing the room-temperature conductivities and activation barriers for ionic motion. (b) Phase evolution of $Li_3M_{1-x}Zr_xCl_6$ ($M = Er, Y$) upon Zr substitution.⁶⁴

Another typical example of chloride SEs Li-Sc-Cl. In 2020, a series of $\text{Li}_x\text{ScCl}_{3+x}$ ($2.5 < x < 4$) SEs were synthesized.⁶⁵ The optimized Li^+ conductivity can reach to 3.02×10^{-3} S/cm for Li_3ScCl_6 , in which the Li^+ conducting paths are connected via tetrahedral interstitial sites in all three directions (**Figure 2.8a and b**). All $\text{Li}_x\text{ScCl}_{3+x}$ SEs exhibit a similar monoclinic structure of Li_3ScCl_6 (**Figure 2.8c**). The only difference is their configurational variability and the occupation of Sc^{3+} , Li^+ , and vacancies in the octahedral interstice of Cl^- . By analyzing the Li^+ density probability of all $\text{Li}_x\text{ScCl}_{3+x}$, the blocking effect is proved, which would distort the diffusion channels of Li^+ and result in different Li^+ mobility kinetics (**Figure 2.8c and d**). When increasing the x value in $\text{Li}_x\text{ScCl}_{3+x}$, the Li^+ carrier concentration will be increased, while the opposite trend is observed for the Sc blocking effect and the total vacancy concentration for hopping. A balance is needed to achieve a structure with appropriate Li^+ carrier concentration and vacancy concentration for Li^+ diffusion as well as continuous diffusion channels. The conduction of ions in solids is a complex physical phenomenon and is affected by many factors. Without a comprehensive understanding of the mechanisms in these ion transport processes; the rational design of new fast ionic conductors is not possible. The ionic conductivities and activation energies of the four structures based on AIMD simulation were compared in **Figure 2.8e**. The ionic conductivities of LiScCl_4 ($x = 1$), $\text{Li}_{1.8}\text{ScCl}_{4.8}$ ($x = 1.8$), Li_3ScCl_6 ($x = 3$), and Li_5ScCl_8 ($x = 5$) at 300 K are 0.18, 0.44, 5.1, and 2.4 mS/cm, respectively. The calculated E_a of 0.25 ± 0.04 eV for Li_3ScCl_6 is similar to that of Li_5ScCl_8 (0.26 ± 0.07 eV), while the ionic conductivity of Li_5ScCl_8 is lower than that of Li_3ScCl_6 . This originates from the low rate of the ionic hopping in Li_5ScCl_8 due to the low concentration of vacancies in the structure. The calculated E_a values of LiScCl_4 (0.37 ± 0.07 eV) and $\text{Li}_{1.8}\text{ScCl}_{4.8}$ (0.34 ± 0.07 eV) are higher than that of Li_3ScCl_6 , which is due to the blocking effect of extra Sc occupation in the vacancy Li^+ layer. The allotropicity of Li_3ScCl_6 is developed by Nazar et al in the same year, which is $\text{Li}_2\text{Sc}_{2/3}\text{Cl}_4$.⁶⁶ $\text{Li}_2\text{Sc}_{2/3}\text{Cl}_4$ was indexed in the cubic space group, $Fd-3m$, which is adopted by other spinel materials. A lower Sc^{3+} content leads to increasing amounts of LiCl impurity. A slightly higher Sc^{3+} content leads to lower ionic conductivity and even higher Sc^{3+} content leads to a ScCl_3 impurity. The title composition is therefore optimal. The structure of spinel $\text{Li}_2\text{Sc}_{2/3}\text{Cl}_4$ is somewhat similar to the previously reported spinel

Li_2MgCl_4 . The important difference is that the disordered spinel $\text{Li}_2\text{Sc}_{2/3}\text{Cl}_4$ exhibits four Li sites: Li_2 and Li_3 are new while Li_1 and Li_4 are also present in Li_2MgCl_4 , as shown in **Figure 2.8f**. Li_2MgCl_4 is constructed from edge-sharing (Mg_1/Li_2) Cl_6 octahedra and Li_1 fills the corner-sharing tetrahedral site. In contrast, while Li_2MgCl_4 also contains edge-sharing (Sc_1/Li_4) Cl_6 octahedra, $\text{Li}_{1,2,3}$ occupy the face-sharing octahedral and tetrahedral sites (**Figure 2.8g and h**).

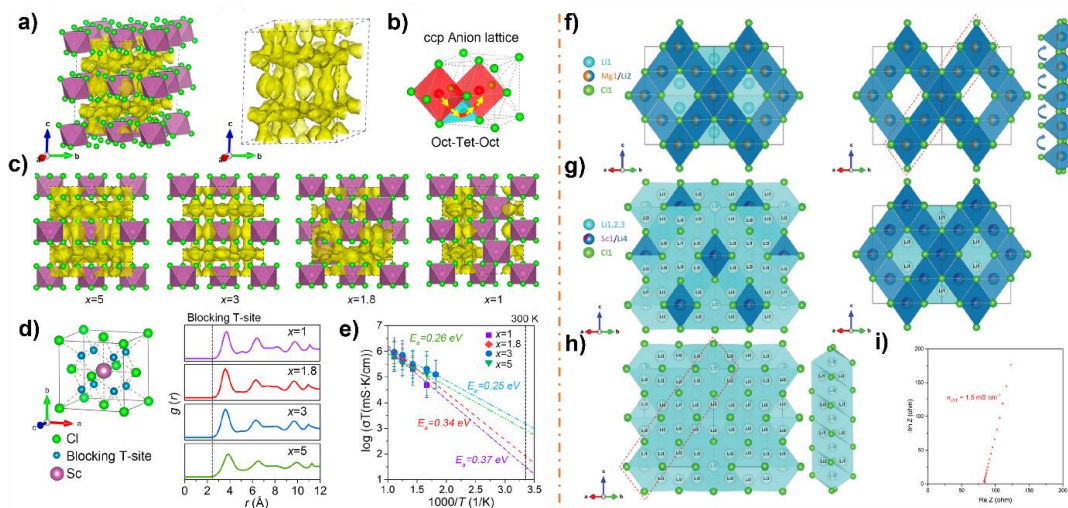


Figure 2.8 Diffusion mechanism of the $\text{Li}_x\text{ScCl}_{3+x}$ SEs: (a) Li^+ probability density marked by yellow isosurfaces;⁶⁵ (b) Li^+ migration pathways in ccp-anion stacking sublattice of Li_3ScCl_6 structure;⁶⁵ (c) Li^+ probability density of $\text{Li}_x\text{ScCl}_{3+x}$ ($x = 1, 1.8, 3, \text{ and } 5$) structures;⁶⁵ (d) blocking effect of Sc^{3+} in Li^+ diffusion; and (e) Arrhenius plot of Li^+ diffusivity in $\text{Li}_x\text{ScCl}_{3+x}$ from simulations.⁶⁵ (f) Structure of spinel Li_2MgCl_4 from single crystal X-ray diffraction, depicting a possible Li^+ ion diffusion pathway⁶⁶. (g) Structure of disordered spinel $\text{Li}_2\text{Sc}_{2/3}\text{Cl}_4$ from powder neutron diffraction, demonstrating that it is related to spinel Li_2MgCl_4 but with different site occupancies⁶⁶. (h) Structure of disordered spinel $\text{Li}_2\text{Sc}_{2/3}\text{Cl}_4$ only showing Li^+ -containing polyhedron that represent a 3D Li^+ ion diffusion pathway⁶⁶. (i) Nyquist plots of $\text{Li}_2\text{Sc}_{2/3}\text{Cl}_4$ at room temperature.⁶⁶

The development of chloride SEs not only focus on the Li-based compounds, but also on the Na-based counterparts. Based on the previous reports, Na_3ErCl_6 crystallizes in a

distorted cryolite type structure with monoclinic space group ($P21/n$).⁶⁷ The crystal structure of Na_3ErCl_6 is shown in **Figure 2.9a** along different crystallographic orientations. The close resemblance of Na_3ErCl_6 with a body-centered-cubic (bcc) structure hints at a possible favorable ionic conduction process in this class of materials. However, the full structure shows its dense polyhedral packing and complexity. The ErCl_6^{3-} polyhedra share edges with the NaCl_6^{5-} prism, indicating an influence of the Er polyhedra on the Na-diffusion pathway. Therefore, aliovalent substitution may be needed to improve the ion transport of Na_3ErCl_6 via substitution of Er with higher valent cations, which hopefully tunes the Na-vacancy density along with diffusion pathway modification. Zr^{4+} ($r = 72$ pm) was selected as a substituent for Er^{3+} ($r = 89$ pm) because of its large ionic radius compared to other tetravalent metal ions. The changes of crystal structure and ionic transport are studied via increasing Zr/Er ratio ($\text{Na}_{3-x}\text{Er}_{1-x}\text{Zr}_x\text{Cl}_6$, $x = 0-1$). Initially, the diffraction patterns of Na_3ErCl_6 and Na_2ZrCl_6 confirm the monoclinic and trigonal crystal structure of the parent compounds, respectively. Upon incorporation of Zr^{4+} , $\text{Na}_{3-x}\text{Er}_{1-x}\text{Zr}_x\text{Cl}_6$ adopts the monoclinic crystal structure of the Na_3ErCl_6 endmember. A minor phase fraction of a NaCl impurity is found, which is unlikely to affect the ionic transport properties. A selected composition of $\text{Na}_{2.8}\text{Er}_{0.8}\text{Zr}_{0.2}\text{Cl}_6$ represents the pathway with a lowest valence mismatch and energy for sodium. Temperature-dependent impedance spectroscopy was used to access the influence of the changing structural features on the transport properties. **Figure 2.9b** shows a representative Nyquist plot of one of the collected room temperature impedance data sets ($\text{Na}_{3-x}\text{Er}_{1-x}\text{Zr}_x\text{Cl}_6$ with $x = 0.2$). A parallel resistor-constant phase element combination that is in series to a second constant phase element is used as the equivalent circuit for fitting the impedance data. The process corresponds to the bulk contribution and ion-blocking behavior of the used steel electrodes, respectively. As bulk and grain boundary contributions cannot be reasonably deconvoluted, even at low temperature up to -40 °C, the here reported conductivities represent total conductivities. The comparison of all obtained Arrhenius plots is shown in **Figure 2.9c**. The ionic conductivity of the pristine Na_3ErCl_6 of 10^{-6} mS/cm (25 °C) can be attributed to the absence of vacant Na^+ site in the structure. Upon Zr^{4+} introduction, the conductivity of $\text{Na}_{3-x}\text{Er}_{1-x}\text{Zr}_x\text{Cl}_6$ increases and

reaches a maximum value of 0.035 mS/cm (25 °C) for Na_{2.8}Er_{0.8}Zr_{0.2}Cl₆, followed by a strong decrease afterward that ends up at 3.5×10^{-7} mS/cm for Na₂ZrCl₆.

Another Zr⁴⁺ doped compounds are Na_{3-x}Y_{1-x}Zr_xCl₆.⁶⁸ The crystalline form of the end members Na₃YCl₆ and Na₂ZrCl₆ exhibit a closed-pack arrangement of [YCl₆]³⁻ and [ZrCl₆]²⁻ polyanions, respectively. With increasing x in Na_{3-x}Y_{1-x}Zr_xCl₆, the unit cell volume increases, which results in a widening of the Na⁺ diffusion channels. Na_{3-x}Y_{1-x}Zr_xCl₆ compounds were synthesized using stoichiometric amounts of NaCl, YCl₃, and ZrCl₄ (see Methods). The room temperature ionic conductivity of Na₃YCl₆ was determined to be 9.5×10^{-8} S/cm via electrochemical impedance spectroscopy (EIS) measurements. With Zr doping, the *P21/n* space group of the parent compound NYC is largely retained up to x = 0.875, suggesting a solid solution in this compositional range. For x ≥ 0.875, additional peaks emerge in the XRD patterns at 2θ = 9.6° and 10.5°, indicating the presence of a second, different phase (**Figure 2.9d**). This particular phase was determined to be crystalline Na₂ZrCl₆. **Figure 2.9e** shows the extracted conductivity values, over the entire Na_{3-x}Y_{1-x}Zr_xCl₆ compositional range at x=0.125 increments. The ionic conductivity for $0.375 \leq x < 1$ is in the range of $2.6\text{--}6.6 \times 10^{-5}$ S/cm, with Na_{2.25}Y_{0.25}Zr_{0.75}Cl₆ exhibiting the highest conductivity of 6.6×10^{-5} S/cm. A drop in conductivity was observed for x ≥ 0.875 compositions, attributed to the formation of a small amount of crystalline Na₂ZrCl₆ phase with a much lower room temperature conductivity of 1.4×10^{-7} S/cm. In addition, crystalline Na₂ZrCl₆ has a relative density of ~79%, which could also contribute to its lower conductivity. Since Na_{2.25}Y_{0.25}Zr_{0.75}Cl₆ exhibited the highest conductivity among all compositions explored herein, the activation energy was measured (**Figure 2.9f**) and found to be 663.6 meV. In addition, the electronic conductivity of Na_{2.25}Y_{0.25}Zr_{0.75}Cl₆ was determined to be 8.89×10^{-9} S/cm via direct-current polarization, i.e., Na_{2.25}Y_{0.25}Zr_{0.75}Cl₆ is an ionic conductor and an electronic insulator.

In 2021, the following end member Na₂ZrCl₆ was prepared by ball-milling (BM) a stoichiometric mixture of NaCl and ZrCl₄ with and without subsequent heat treatment (HT) at 400 °C, respectively.⁶⁹ The Na⁺ conductivities of the cold-pressed pellet samples were measured by the AC impedance method using Na⁺-blocking Ti/SE/Ti symmetric

cells. **Figure 2.9g** shows the Arrhenius plots of the Na⁺ conductivities for BM- and HT-Na₂ZrCl₆. BM-Na₂ZrCl₆ exhibited a Na⁺ conductivity of 1.8×10^{-5} S/cm at 30 °C with an activation energy of 0.40 eV. For the heat-treated sample, a considerably lower Na⁺ conductivity of 6.9×10^{-8} S/cm and a higher activation energy of 0.49 eV were obtained. The drastic change observed in the Na⁺ conductivity upon heat treatment is similar to that observed for LYC. The electron conductivity of BM-Na₂ZrCl₆, measured by chronoamperometry using the Ti/SE/Ti symmetric cell was 2.1×10^{-10} S/cm, which is more than five orders of magnitude lower than the Na⁺ conductivity. Therefore, BM-Na₂ZrCl₆ can be regarded as a good solid electrolyte. The powder X-ray Rietveld refinement profile for HT-Na₂ZrCl₆ is shown in **Figure 2.9g**. All the reflections can be indexed as the trigonal crystal structure with *P-3m1* symmetry that is isostructural with trigonal LYC and Li₃ErCl₆. As shown in **Figure 2.9h**, the lattice framework of Na₂ZrCl₆ is similar to that of previously reported trigonal Li₃ErCl₆ (LYC); however, the Na⁺ ions are fully occupied in one crystallographic Wyckoffsite (6g) for Na₂ZrCl₆, while Li⁺ ions occupy two sites (fully occupied in 6g and half occupied in 6h) for Li₃ErCl₆. The structure similarities between Na₂ZrCl₆ and Li₃ErCl₆ is corresponding to their ionic conductivity trend at various temperatures.

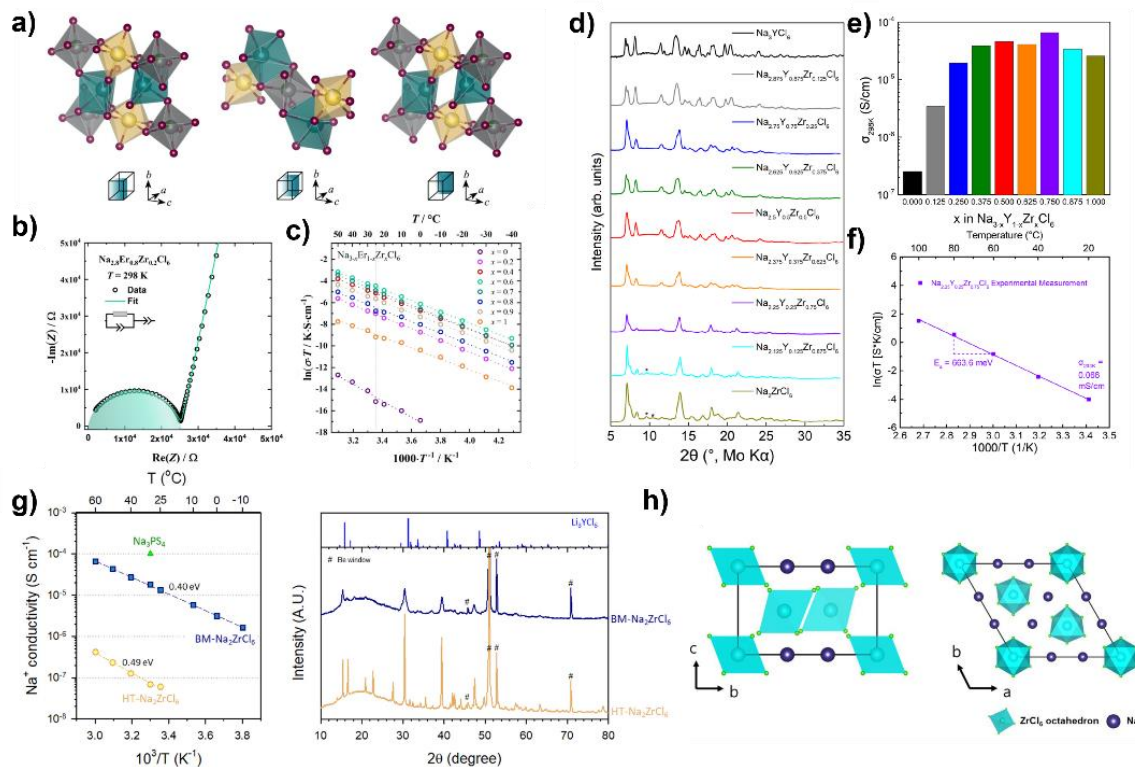


Figure 2.9 (a) Cuts through the unit cell of Na_3ErCl_6 showing the highly interconnected MCl_6 polyhedra.⁶⁷ (b) Representative Nyquist plot of a room-temperature impedance measurement and (c) Arrhenius plots from the temperature dependent Measurements.⁶⁷ (d) XRD of the $\text{Na}_{3-x}\text{Y}_{1-x}\text{Zr}_x\text{Cl}_6$ compositions and the corresponding room temperature conductivity values⁶⁸. (e) Bar chart of $\sigma_{300\text{K}}$ vs composition. (f) Arrhenius plot of $\text{Na}_{2.25}\text{Y}_{0.25}\text{Zr}_{0.75}\text{Cl}_6$ from experimental measurements.⁶⁸ (g) Arrhenius plots and XRD patterns of $\text{BM-Na}_2\text{ZrCl}_6$ and $\text{HT-Na}_2\text{ZrCl}_6$ and (h) their corresponding crystalline structure⁶⁹.

2.1.4.2 Bromide ISEs

The pioneered work of bromide materials is Li-In-Br system.⁷⁰ The as-synthesized Li_3InBr_6 compound exhibits a relatively low RT ionic conductivity of 10^{-7} S/cm. However, it undergoes a phase transition to a superionic phase at 314 K associated with a steep increase of the conductivity ($\sigma = 4 \times 10^{-3}$ S/cm) at 330 K (**Figure 2.10a**). A pseudo ccp of the bromide ions is formed in this phase. Unfortunately, such a high-temperature structure will again degrade and yield significantly reduced ionic conductivity at 260 K,

which makes it not suitable for practical application. The other compound is LiInBr_4 . Similar to Li_3InBr_6 , the as-synthesized LiInBr_4 is also a poor Li^+ conductor while transforms to a superionic phase (HT phase) at 316 K during a heating process (**Figure 2.10b**). The HT phase can be maintained until the temperature down to 260 K. Differently, the structure of HT-phase LiInBr_4 is a defect cubic spinel structure, which is totally different from that of Li_3InBr_6 . Along with the report of LYC, Li_3YBr_6 (LYB) was developed by Tetsuya Asano et al in 2018.⁵⁸ The bromide ion arranges in ccp structure in which lithium-ion conducting paths are connected via tetrahedral interstitial sites in all three directions (**Figure 2.10c and d**). The tetrahedral interstitial sites adjacent to Y^{3+} are blocked by repulsive coulombic interactions between Y^{3+} and Li^+ , which is similar to the case for layered rock-salt cathode materials. After a mechanochemical process by ball-milling LiBr and YBr_3 , the ionic conductivity of LYB is 0.72×10^{-4} S/cm. Interestingly, its ionic conductivity increases to 1.7×10^{-3} S/cm after an annealing process, which means high crystallinity is favorable for Li-ion conduction on LYB. The lithium-ion conductivity of LYB is also tuned by tailoring the milling and annealing parameters to obtain a pure phase with optimized conductivity. BM- Li_3YBr_6 and annealing (AN)- Li_3YBr_6 SEs with ionic conductivities of 0.39 and 3.31 mS/cm at room temperature, respectively, were obtained by mechanical milling and annealing (**Figure 2.10e**). The conductivity measurement showed that the heat treatment process can effectively increase the lithium-ion conductivity. As shown in **Figure 2.10f**, Neutron diffraction at various temperatures suggested that the lattice expansion of AN- Li_3YBr_6 can provide a larger lithium-ion conductivity at higher temperature due to the improved lithium diffusion framework. Lithium nuclear density analysis clarified that the $4g(\text{Li})$ site is more mobile than that of the $4h(\text{Li})$.

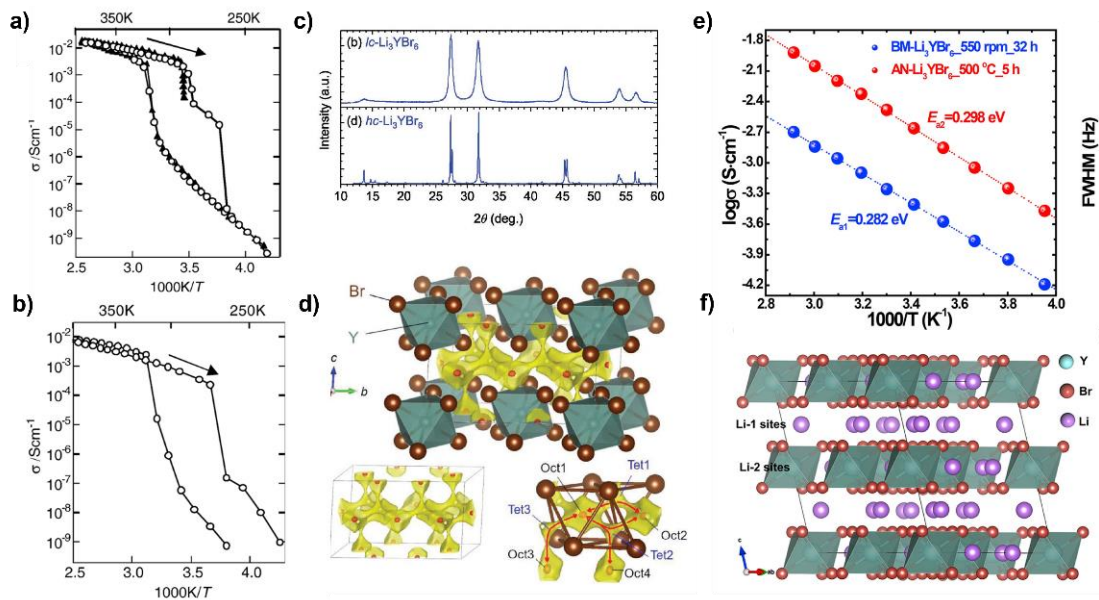


Figure 2.10 (a) Conductivity of Li_3InBr_6 against $1/T$. Second and third runs are shown by circles and triangles, respectively.⁷⁰ (b) Conductivity of LiInBr_4 against $1/T$.⁷⁰ (c) The measured XRD patterns of mechanochemically synthesized *lc*-LYB and annealed *hc*-LYB.⁵⁸ (d) The crystal structures of LYB obtained after Rietveld refinement, superimposed with a calculated BVSE-based lithium-ion potential map. The yellow surface corresponds to the ionic conduction path, and the regions enclosed with red surfaces correspond to the stable lithium-ion positions.⁵⁸ (e) The Arrhenius plots of lithium ion conductivities of *BM*-LYB and *AN*-LYB, respectively.⁵⁸ (f) Crystal structure of *AN*-LYB with *fcc*-type anion lattice. The light purple, red and cyan balls represent Li, Br, and Y atoms respectively.⁵⁸

2.1.4.3 Iodide ISEs

Among the binary lithium compounds (LiX , $\text{X}=\text{Cl}$, Br , I and F), LiI shows a relatively higher value of 10^{-7} S/cm. Thin-film type ASSBs with LiI as the SE were developed at the end of the 1960s and the beginning of the 1970s, such as Li/LiI/I_2 and Li/LiI/AgI , with open-circuit voltages around 2.45–3 V.⁷¹ Compared with other halide anions, iodide can form a softer and more polarizable anion sublattice that is beneficial for ionic transport. The first experimentally reported iodide SE is Li_3ErI_6 . As shown in **Figure**

2.11a and b, temperature-dependent impedance spectroscopy shows low activation energies of 0.37 and 0.38 eV alongside promising ionic conductivities of 0.65 and 0.39 mS/cm directly after ball milling and the subsequently annealed Li_3ErI_6 , respectively.¹² The structural framework can be described as isolated layers of edge-sharing ErI_6^{3-} octahedra in the ab-plane, in which erbium partially occupies two different positions (**Figure 2.11c**). Multiple different possible disorder positions were tested for erbium, because the chlorine and bromine-based compounds in the Li_3MX_6 family have shown a significant rare earth disorder, which has been shown to dramatically affect the ionic transport. The disorder of Li^+ within the Li^+ layer in the ab-plane and Li^+ in the ErI_6^{3-} plane suggests a possible three-dimensional diffusion. Guided by the idea that the iodide anion leads to improved ionic transport as it constitutes a more polarizable lattice framework (**Figure 2.11d**), the lattice dynamics of Li_3ErI_6 are measured and compared to Li_3ErCl_6 . The softer lattice leads to a decreased activation barrier and improved ionic conductivity, showing that even within this class of lithium rare-earth halides the lattice dynamics severely affect the ionic motion. Apart from experimental work, theoretical work also investigated new nonspinel structured lithium ion conducting iodides: Li_3MI_6 ($\text{M} = \text{Sc}, \text{Y}, \text{and La}$), based on density functional theory (DFT) calculations (**Figure 2.11e**).⁷² As shown in **Figure 2.11f**, Li_3LaI_6 is theoretically predicted to meet the requirements of high Li ionic conductivity, deformability, and chemical and electrochemical stability, which can be attributed to its long ionic bond length, high anionic polarizability, high stability of LaI_6^{3-} octahedra, and the beneficial Li conduction channel with considerable cation vacancy sites.

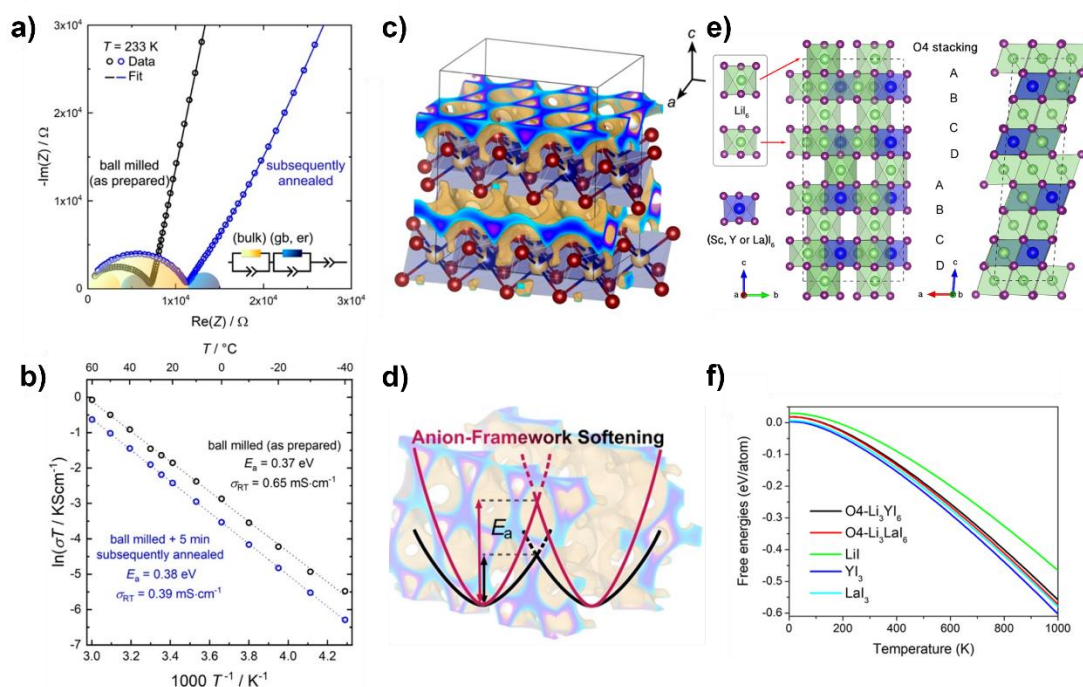


Figure 2.11 (a) Representative Nyquist plots for the ball-milled and annealed samples and (b) calculated Arrhenius plots of the total ionic conductivity and their corresponding activation energies.¹² (c) Possible lithium diffusion pathways obtained by a bond valence sum calculation. The blue sections show the strongly interconnected lithium sites in the ab-plane, possibly leading to a fast in-plane diffusion.¹² (d) Schematic of how a softer anionic sublattice in Li_3ErCl_6 compared to Li_3YCl_6 leads to larger vibrational amplitudes and lower activation barriers.¹² (e) Unit cells of Li_3MI_6 ($M = \text{Sc}, \text{Y}, \text{and La}$) crystal (in the C2 space group).⁷² (f) Calculated temperature-dependent formation energies (Helmholtz free energies) of Li_3YI_6 and Li_3LaI_6 materials.⁷²

2.1.4.4 Fluoride ISEs

Fluoride seems to play a vital role in terms of Li metal consolidation and Li-ion conductor modification. It is less hydrophilic compared with other halide-based compounds. LiF has been well known as an important solid electrolyte interface (SEI) component for Li dendrite suppression. A typical example is the Li–Al–F system⁷³ that can be found in the literature. Li_3AlF_6 , with an orthorhombic structure (space group

Pna21), has been reported to show an ionic conductivity of $\sim 10^{-6}$ S/cm at 200 °C. However, the ionic conductivity can be dramatically increased up to 2×10^{-6} S/cm at 200 °C by mechanically milling Li_3AlF_6 with LiCl in the form of $\text{Li}_3\text{AlF}_6\text{-LiCl}$ (**Figure 2.12a**). In addition, similar to the amorphous LiF-ScF_3 thin film mentioned above, the amorphous LiF-AlF_3 thin film grown by thermal evaporation with a nearly stoichiometric LiAlF_4 composition also shows a higher RT ionic conductivity of 10^{-6} S/cm. However, it should also be noted that the high ionic conductivity is not caused by pure Li^+ migration; protons might be also involved for amorphous LiF-AlF_3 . Another Li-rich fluoride SE is Li_3GaF_6 , which can be synthesized by a low-temperature ionic liquid method and shows nanostructured morphology.⁷⁴ **Figure 2.12b** shows the schematic synthesis of Li_3GaF_6 electrolyte via liquid method. The crystal structure of Li_3GaF_6 derivative from cryolite phase is shown in **Figure 2.12c**. Li_3GaF_6 crystallizes into the monoclinic structure isotypic to $\beta\text{-Li}_3\text{AlF}_6$. It has the lattice parameters of $a = 14.367 \text{ \AA}$, $b = 8.571 \text{ \AA}$, $c = 9.994 \text{ \AA}$, $\beta = 94.78^\circ$ as well as a cell volume of 1226.4 \AA^3 . The characteristic building units are GaF_6 octahedra and the Li atoms are octahedrally, pentahedrally or tetrahedrally coordinated by F. As shown in **Figure 2.12d**, the room temperature ionic conductivity of optimized Li_3GaF_6 is estimated to be 8.8×10^{-5} S/cm and an activation energy of 0.41 eV.

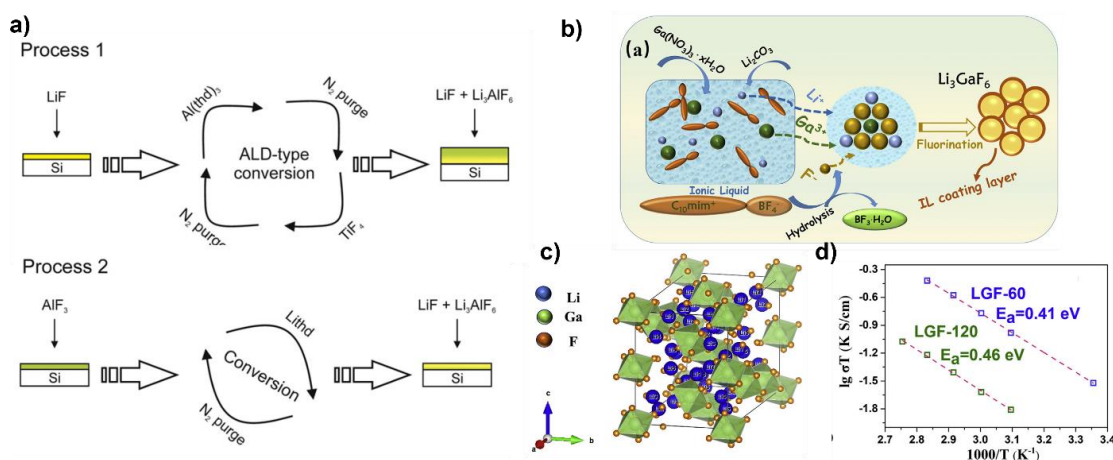


Figure 2.12 (a) Schemes show process 1 and process 2 uses a conversion reaction between ALD-made AlF_3 and the lithium precursors to deposit Li_3AlF_6 .⁷³ (b) Schematic synthesis of Li_3GaF_6 . Li_2CO_3 is firstly dissolved in ionic liquid Li source and gallium

nitrate hydrate as Ga source is then added to the solution to hydrolyze $C_{10}mimBF_4$ to releases free F.⁷⁴ (c) Ga^{3+} , Li^+ and F^- combine together to form Li_3GaF_6 deposit crystal structures of $\beta-Li_3GaF_6$ viewed along direction.⁷⁴ (d) Arrhenius plots of Li_3GaF_6 (annealed at $60^\circ C$ and $120^\circ C$) with activation energies of 0.41 eV and 0.46 eV respectively.⁷⁴

2.2 Electrolytes and electrodes interfaces in ASSBs

2.2.1 Electrochemical stability of ISEs

The electrochemical stability of a SE is closely related to the interface formation in ASSBs. The electrochemical stability window (ESW) of the electrolyte can be defined as the gap between the oxidation and reduction potentials. To ensure thermodynamic stability, the electrochemical potential of the electrodes should be located within the ESW of the electrolyte since an anode with an electrochemical potential above the electrolyte reduction potential could reduce the electrolyte, while a cathode with an electrochemical potential below the electrolyte oxidation potential could oxidize the electrolyte unless a passivation layer prevents continuous electron transfer.^{75, 76} **Figure 2.13** summarize the calculated thermodynamics intrinsic electrochemical windows of ternary fluorides, chlorides, bromides, iodides, oxides, and sulfides. Fluorides show wide ESW but low ionic conductivity. Chlorides strike a balance between reduction and oxidation stability and have a significant advantage in stability over oxides and sulfides.⁷⁷

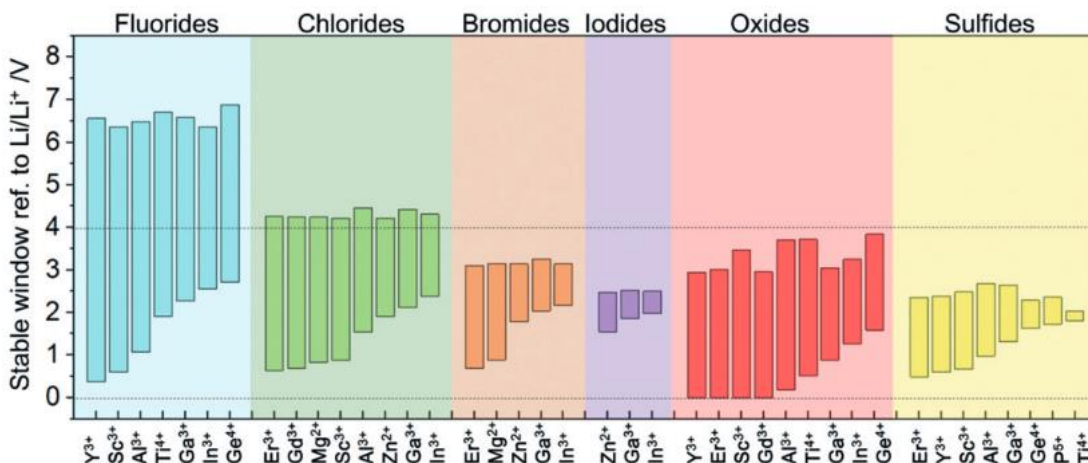


Figure 2.13 Calculated thermodynamics intrinsic electrochemical win-dows of Li-M-X ternary fluorides, chlorides, bromides, iodides, oxides, and sulfides.⁷⁷

2.2.2 Cathode-SE interface (CEI)

In ASSBs, the interfacial compatibility is a big issue to affect a battery's performance. In cathode side, the instability generally arises from inadequate physical contact, chemical reactions, electrochemical reactions, or a space-charge layer.⁷⁸

Inadequate physical contact is caused by the point-to-point contact of solids (**Figure 2.14a**). Moreover, during charge/discharge processes, the lithiation/delithiation-induced phase transition, accompanied by volume change, generates microcracks, lattice dislocations, and defects in the electrode as well as the electrode-SE interface (**Figure 2.14b**). Deformability is an essential aspect as it directly translates to the ability of the SEs to be densified.⁷⁹ For example, oxide ISEs are very stiff and there is a large number of grain boundaries. Glass or ceramic sulfide-based ISEs are more malleable and thus can be densified at RT by simple cold-pressing. From a mechanical and processing perspective, this makes them more promising in terms of generating a favorable interface with electrode materials. One standard method to improve the mechanical contact is by applying high pressure during cell production and cycling, which helps to achieve better

interface contact and decrease the interfacial resistance.⁸⁰ However, too much pressure is able to cause the detrimental shorts in Li/Na-metal ASSBs.

Chemical reactions arise from a chemical potential difference between cathode materials and SEs. They can be identified from thermodynamic computation or experimental techniques. Thermodynamic analysis can provide assumption that cathode and ISE at a heterogeneous interface react to form the most favorable products under full thermodynamic equilibrium.^{81, 82} The most favorable reaction is determined by constructing the pseudobinary phase diagram between the two materials and finding the reaction ratio resulting in the most negative reaction energy. As shown in **Figure 2.14c**, Na-based sulfide and selenide ISEs are unstable with most of the oxide cathode materials. NaTiS₂ cathode shows good compatibility with all sulfide SEs. The poor chemical instability can also be found in most of the Li-based sulfide ISEs and cathode materials. Aside from thermodynamic calculations, electrochemical techniques such as electrochemical charge/discharge profiles and impedance measurements, also be taken into consideration. Halide SEs are experimentally proved to be stable with cathodes such as LCO and NMC. As show in **Figure 2.14d**, the initial charge and discharge curves of LYC/LCO and LYB/LCO indicates that almost no side reactions occur in LCO and these halide materials. Besides, the interfacial resistance between LCO and LYC was only 16.8 $\Omega \text{ cm}^{-2}$ for the LYC-cell and 6.6 $\Omega \text{ cm}^{-2}$ for the LYC/LYB-cell, which are much smaller than that of the sulfide ISE based cell.⁵⁸

Electrochemical reactions will be triggered during a charge/discharge process. Form computation view, the reactions will be predicted by reaching the phase equilibrium of the two materials in contact under an applied potential. As shown in **Figure 2.14e**, the interface between LCO and Li₃PS₄ was found to have poor stability over the entire range of the applied voltage from 2 to 5 V applied potential. The oxide SE-LCO interfaces generally have significantly better stability than the sulfide ISEs over the whole voltage range.⁸¹ In-situ or ex-situ XRD can also give the information about the electrochemical reaction products during cycling processes (**Figure 2.14f**).⁸³

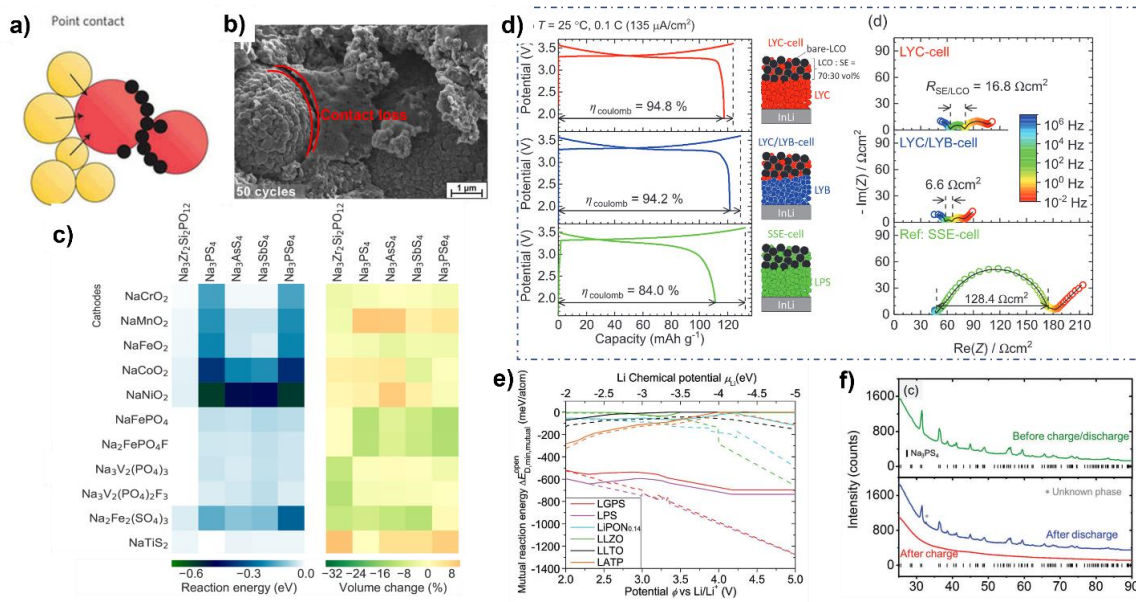


Figure 2.14 (a) scheme of cathode and ISE contact in ASSBs⁸⁴ (b) SEMs of a given cell after 50 full battery cycles in the discharged state. The NMC particles shrink during delithiation (charge) and lose contact with the SE⁸⁵ (c) Reaction energies (left) and volume changes (right) for electrode/SE pairs.⁸⁶ (d) Initial charge/discharge curves and Nyquist plots of the EIS spectra of ASSBs with LYC, LYB and Li₆PS₅Cl cathode electrolytes, respectively.⁵⁸ (e) The mutual reaction energy and the total reaction energy (dashed lines) at the SE–LCO interfaces under applied potential ϕ in a 2–5V range.⁸¹ (f) Na₃PS₄ cathode composite before and after being fully charged/discharged⁸⁷

2.2.3 Anode-SE interface

At anode side, high-capacity Li/Na metal anode is of great interest since Li/Na metal anode can increase the energy density of the ASSB by at least 20%.⁷⁸ However, Li/Na metal is very electropositive and reactive, it will spontaneously react with most SEs at RT to form SEI. There are generally two different transport properties of the formed SEI. One is that the formed products show partial electronic and ionic conductivity (**Figure 2.15a**). In this case, the interphase may steadily grow “into” the ISEs and thereby alter the properties of the whole bulk material. The formation of such a mixed conducting interphase will eventually allow electron transport through the electrolyte and finally lead

to the self-discharge of the battery.^{88, 89} The other case is that the reaction products are electronically non-conductive or the electronic conductivity is low enough to limit the growth of the interphase to a very thin film, which can be regarded as a stable SEI (**Figure 2.15b**). The performance of the battery will then critically depend on the ion conducting properties of such a SEI. Other than that, dendrite growth is a big issue in solid-state Li/Na metal batteries. As shown in **Figure 2.15c**, dendrites prefer to nucleate and grow at the microstructure on the surface, void and defect within the ISE. Grain boundaries can also induce Li/Na propagation inside the ISE. Furthermore, electrons from the residual conductivity, oxygen framework, and pore surface induce the formation of Li cluster inside the ISE.

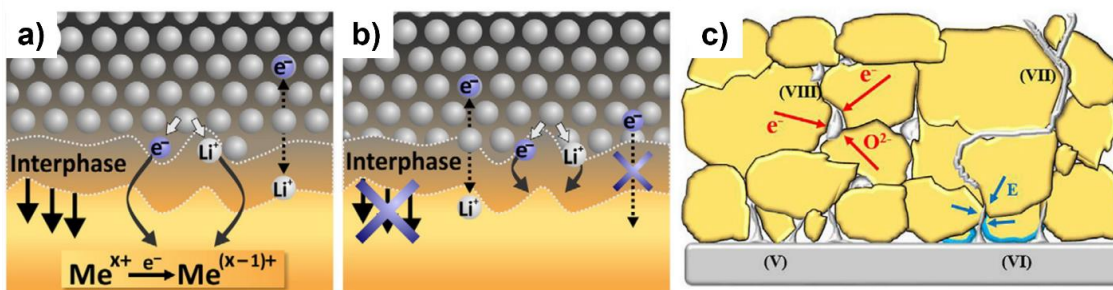


Figure 2.15 (a) reactive and mixed conducting interphase; (b) reactive and metastable solid-electrolyte interphase.⁸⁸ (c) Scheme of the dendrite growth mechanism in ISE.⁹⁰

2.2.4 Interfacial stability strategies

Up to now, there is an independent ISE that possesses both high oxidation and low reduction limits to be directly applied in bulk-type high-voltage all-solid-state Li/Na metal batteries. However, the intrinsic ESW of SE materials plus the electrochemical window provided by the interphases can help to reach an extended practical ESW of SE, enabling the direct contact with high-voltage cathode and Li/Na anode materials (**Figure 2.16a**). There are generally two strategies to achieve interfacial stability. First, modifying developed ISE to make it decompose into favorable interphases at an applied potential. The interphases should show good stability, good ionic conductivity, and poor electronic transport to passivate the ISE. As shown in **Figure 2.16d**, anion doping, such

2.3 References

1. Mindemark, J., Lacey, M. J., Bowden, T., Brandell, D. Beyond PEO-Alternative host materials for Li⁺-conducting solid polymer electrolytes. *Progress in Polymer Science* **81**, 114-143 (2018).
2. Zheng, Y., *et al.* A review of composite solid-state electrolytes for lithium batteries: fundamentals, key materials and advanced structures. *Chemical Society Reviews* **49**, 8790-8839 (2020).
3. Chen, R. J., Qu, W. J., Guo, X., Li, L., Wu, F. The pursuit of solid-state electrolytes for lithium batteries: from comprehensive insight to emerging horizons. *Materials Horizons* **3**, 487-516 (2016).
4. Janek, J., Zeier, W. G. A solid future for battery development. *Nature Energy* **1**, 1-4 (2016).
5. Bachman, J. C., *et al.* Inorganic Solid-State Electrolytes for Lithium Batteries: Mechanisms and Properties Governing Ion Conduction. *Chemical Reviews* **116**, 140-162 (2016).
6. Xu, K. Nonaqueous liquid electrolytes for lithium-based rechargeable batteries. *Chemical Reviews* **104**, 4303-4417 (2004).
7. Famprakis, T., Canepa, P., Dawson, J. A., Islam, M. S., Masquelier, C. Fundamentals of inorganic solid-state electrolytes for batteries. *Nature Materials* **18**, 1278-1291 (2019).
8. Rickert, H. Solid Ionic Conductors - Principles and Applications. *Angewandte Chemie-International Edition in English* **17**, 37-46 (1978).
9. Ohno, S., *et al.* Materials design of ionic conductors for solid state batteries. *Progress in Energy* **2**, (2020).
10. Wang, Y., *et al.* Design principles for solid-state lithium superionic conductors. *Nature Materials* **14**, 1026-1031 (2015).
11. Kraft, M. A., *et al.* Influence of Lattice Polarizability on the Ionic Conductivity in the Lithium Superionic Argyrodites Li₆PS₅X (X = Cl, Br, I). *Journal of the American Chemical Society* **139**, 10909-10918 (2017).

12. Schlem, R., Bernges, T., Li, C., Kraft, M. A., Minafra, N., Zeier, W. G. Lattice Dynamical Approach for Finding the Lithium Superionic Conductor Li_3ErI_6 . *Acs Applied Energy Materials* **3**, 3684-3691 (2020).
13. Martin, S. W. Ionic-Conduction in Phosphate-Glasses. *Journal of the American Ceramic Society* **74**, 1767-1784 (1991).
14. Chandra, A., Bhatt, A., Chandra, A. Ion Conduction in Superionic Glassy Electrolytes: An Overview. *Journal of Materials Science & Technology* **29**, 193-208 (2013).
15. Ravaine, D. Glasses as Solid Electrolytes. *Journal of Non-Crystalline Solids* **38-9**, 353-358 (1980).
16. Panacek, A., *et al.* Silver colloid nanoparticles: Synthesis, characterization, and their antibacterial activity. *Journal of Physical Chemistry B* **110**, 16248-16253 (2006).
17. Sun, Y. D., Guan, P. Y., Liu, Y. J., Xu, H. L., Li, S. A., Chu, D. W. Recent Progress in Lithium Lanthanum Titanate Electrolyte towards All Solid-State Lithium Ion Secondary Battery. *Critical Reviews in Solid State and Materials Sciences* **44**, 265-282 (2019).
18. Stramare, S., Thangadurai, V., Weppner, W. Lithium lanthanum titanates: A review. *Chemistry of Materials* **15**, 3974-3990 (2003).
19. Inaguma, Y., *et al.* High Ionic-Conductivity in Lithium Lanthanum Titanate. *Solid State Communications* **86**, 689-693 (1993).
20. Bi, J. Y., *et al.* A hybrid solid electrolyte $\text{Li}_{0.33}\text{La}_{0.557}\text{TiO}_3/\text{poly}(\text{acrylonitrile})$ membrane infiltrated with a succinonitrile-based electrolyte for solid state lithium-ion batteries. *Journal of Materials Chemistry A* **8**, 706-713 (2020).
21. Bae, J., *et al.* A 3D Nanostructured Hydrogel-Framework-Derived High-Performance Composite Polymer Lithium-Ion Electrolyte. *Angewandte Chemie-International Edition* **57**, 2096-2100 (2018).
22. H.Y-P.Hong. Crystal structures and crystal chemistry in the system $\text{Na}_{1+x}\text{Zr}_2\text{Si}_x\text{P}_{3-x}\text{O}_{12}$. *Materials Research Bulletin* **11**, 173-182 (1976).

23. Kim, J. K., Lim, Y. J., Kim, H., Cho, G. B., Kim, Y. A hybrid solid electrolyte for flexible solid-state sodium batteries. *Energy & Environmental Science* **8**, 3589-3596 (2015).
24. Adelhelm, P., Hartmann, P., Bender, C. L., Busche, M., Eufinger, C., Janek, J. From lithium to sodium: cell chemistry of room temperature sodium-air and sodium-sulfur batteries. *Beilstein Journal of Nanotechnology* **6**, 1016-1055 (2015).
25. Hashimoto, T., Hayashi, K. Aqueous and Nonaqueous Sodium-Air Cells with Nanoporous Gold Cathode. *Electrochimica Acta* **182**, 809-814 (2015).
26. Aono, H., Sugimoto, E., Sadaoka, Y., Imanaka, N., Adachi, G. Y. Ionic conductivity of the lithium titanium phosphate ($\text{Li}_{1-x}\text{M}_x\text{Ti}_2\text{-(PO}_4)_3$, M= Al, Sc, Y, and La) systems. *Journal of The Electrochemical Society* **136**, 590-591 (1989).
27. Li, S. C., Cai, J. Y., Lin, Z. X. Phase-Relationships and Electrical-Conductivity of $\text{Li}_{1-x}\text{Ge}_2\text{XAl}_x\text{P}_3\text{O}_{12}$ and $\text{Li}_{1-x}\text{Ge}_2\text{XCr}_x\text{P}_3\text{O}_{12}$ Systems. *Solid State Ionics* **28**, 1265-1270 (1988).
28. Arbi, K., Bucheli, W., Jimenez, R., Sanz, J. High lithium ion conducting solid electrolytes based on NASICON $\text{Li}_{1+x}\text{Al}_x\text{M}_{2-x}(\text{PO}_4)_3$ materials (M = Ti, Ge and $0 \leq x \leq 0.5$). *Journal of the European Ceramic Society* **35**, 1477-1484 (2015).
29. Wang, C. W., *et al.* Garnet-Type Solid-State Electrolytes: Materials, Interfaces, and Batteries. *Chemical Reviews* **120**, 4257-4300 (2020).
30. Yu, X. H., Bates, J. B., Jellison, G. E., Hart, F. X. A stable thin-film lithium electrolyte: Lithium phosphorus oxynitride. *Journal of The Electrochemical Society* **144**, 524-532 (1997).
31. Li, J. C., Ma, C., Chi, M. F., Liang, C. D., Dudney, N. J. Solid Electrolyte: the Key for High-Voltage Lithium Batteries. *Advanced Energy Materials* **5**, 1401408 (2015).
32. Lu, J. Y., Li, Y. Perovskite-type Li-ion solid electrolytes: a review. *Journal of Materials Science-Materials in Electronics* **32**, 9736-9754 (2021).

33. Deng, Y., *et al.* Crystal Structures, Local Atomic Environments, and Ion Diffusion Mechanisms of Scandium-Substituted Sodium Superionic Conductor (NASICON) Solid Electrolytes. *Chemistry of Materials* **30**, 2618-2630 (2018).
34. Awaka, J., Takashima, A., Kataoka, K., Kijima, N., Idemoto, Y., Akimoto, J. Crystal Structure of Fast Lithium-ion-conducting Cubic $\text{Li}_7\text{La}_3\text{Zr}_2\text{O}_{12}$. *Chemistry Letters* **40**, 60-62 (2011).
35. Lacivita, V., Artrith, N., Ceder, G. Structural and Compositional Factors That Control the Li-Ion Conductivity in LiPON Electrolytes. *Chemistry of Materials* **30**, 7077-7090 (2018).
36. Tatsumisago, M., Hayashi, A. Superionic glasses and glass-ceramics in the Li_2S - P_2S_5 system for all-solid-state lithium secondary batteries. *Solid State Ionics* **225**, 342-345 (2012).
37. Pradel, A., Ribes, M. Electrical-Properties of Lithium Conductive Silicon Sulfide Glasses Prepared by Twin Roller Quenching. *Solid State Ionics* **18-9**, 351-355 (1986).
38. Morimoto, H., Yamashita, H., Tatsumisago, M., Minami, T. Mechanochemical synthesis of new amorphous materials of $60\text{Li}(2)\text{S}$ center dot $40\text{SiS}(2)$ with high lithium ion conductivity. *Journal of the American Ceramic Society* **82**, 1352-1354 (1999).
39. Sakuda, A., Hayashi, A., Tatsumisago, M. Sulfide Solid Electrolyte with Favorable Mechanical Property for All-Solid-State Lithium Battery. *Scientific Reports* **3**, (2013).
40. Kato, A., Yamamoto, M., Sakuda, A., Hayashi, A., Tatsumisago, M. Mechanical Properties of Li_2S - P_2S_5 Glasses with Lithium Halides and Application in All-Solid-State Batteries. *Acs Applied Energy Materials* **1**, 1002-1007 (2018).
41. Mercier, R., Malugani, J. P., Fahys, B., Robert, G. Superionic Conduction in Li_2s - P_2s_5 - Li_i -Glasses. *Solid State Ionics* **5**, 663-666 (1981).
42. Minami, T., Hayashi, A., Tatsumisago, M. Recent progress of glass and glass-ceramics as solid electrolytes for lithium secondary batteries. *Solid State Ionics* **177**, 2715-2720 (2006).

43. Kaup, K., *et al.* A Lithium Oxythioborosilicate Solid Electrolyte Glass with Superionic Conductivity. *Advanced Energy Materials* **10**, 1902783 (2020).
44. Lau, J., DeBlock, R. H., Butts, D. M., Ashby, D. S., Choi, C. S., Dunn, B. S. Sulfide Solid Electrolytes for Lithium Battery Applications. *Advanced Energy Materials* **8**, 1800933 (2018).
45. Deubener, J., *et al.* Updated definition of glass-ceramics. *Journal of Non-Crystalline Solids* **501**, 3-10 (2018).
46. Mizuno, F., Hayashi, A., Tadanaga, K., Tatsumisago, M. New, highly ion-conductive crystals precipitated from Li₂S-P₂S₅ glasses. *Advanced Materials* **17**, 918-921 (2005).
47. Liu, Z. C., *et al.* Anomalous High Ionic Conductivity of Nanoporous beta-Li₃PS₄. *Journal of the American Chemical Society* **135**, 975-978 (2013).
48. Hayashi, A., Noi, K., Sakuda, A., Tatsumisago, M. Superionic glass-ceramic electrolytes for room-temperature rechargeable sodium batteries. *Nature Communications* **3**, 1-5 (2012).
49. Yu, C., Zhao, F. P., Luo, J., Zhang, L., Sun, X. L. Recent development of lithium argyrodite solid-state electrolytes for solid-state batteries: Synthesis, structure, stability and dynamics. *Nano Energy* **83**, 105858 (2021).
50. Zhou, L. D., Minafra, N., Zeier, W. G., Nazar, L. F. Innovative Approaches to Li-Argyrodite Solid Electrolytes for All-Solid-State Lithium Batteries. *Accounts of Chemical Research* **54**, 2717-2728 (2021).
51. Zhou, L. D., Assoud, A., Zhang, Q., Wu, X. H., Nazar, L. F. New Family of Argyrodite Thioantimonate Lithium Superionic Conductors. *Journal of the American Chemical Society* **141**, 19002-19013 (2019).
52. Kamaya, N., *et al.* A lithium superionic conductor. *Nature Materials* **10**, 682-686 (2011).
53. Kato, Y., *et al.* High-power all-solid-state batteries using sulfide superionic conductors. *Nature Energy* **1**, 1-7 (2016).

54. Hayashi, A., *et al.* A sodium-ion sulfide solid electrolyte with unprecedented conductivity at room temperature. *Nature Communications* **10**, 1-6 (2019).
55. Wang, H., *et al.* An Air-Stable Na₃SbS₄ Superionic Conductor Prepared by a Rapid and Economic Synthetic Procedure. *Angewandte Chemie-International Edition* **55**, 8551-8555 (2016).
56. Salyulev, A. B., Khokhlov, V. A., Moskalenko, N. I. Electrical Conductivity of KAlCl₄-ZrCl₄ Molten Mixtures. *Russian Metallurgy*, 95-99 (2017).
57. Plichta, E. J., Behl, W. K., Vujic, D., Chang, W. H. S., Schleich, D. M. The Rechargeable Li₂Ti₂Cl₄/Li_{1-x}CoO₂ Solid-State Cell. *Journal of The Electrochemical Society* **139**, 1509-1513 (1992).
58. Asano, T., Sakai, A., Ouchi, S., Sakaida, M., Miyazaki, A., Hasegawa, S. Solid Halide Electrolytes with High Lithium-Ion Conductivity for Application in 4 V Class Bulk-Type All-Solid-State Batteries. *Advanced Materials* **30**, (2018).
59. Li, X. N., *et al.* Air-stable Li₃InCl₆ electrolyte with high voltage compatibility for all-solid-state batteries. *Energy & Environmental Science* **12**, 2665-2671 (2019).
60. Li, X. N., *et al.* Water-Mediated Synthesis of a Superionic Halide Solid Electrolyte. *Angewandte Chemie-International Edition* **58**, 16427-16432 (2019).
61. Li, X. N., *et al.* Origin of Superionic Li₃Y_{1-x}In_xCl₆ Halide Solid Electrolytes with High Humidity Tolerance. *Nano Letters* **20**, 4384-4392 (2020).
62. Muy, S., *et al.* High-Throughput Screening of Solid-State Li-Ion Conductors Using Lattice-Dynamics Descriptors. *Science* **16**, 270+ (2019).
63. Liang, J. W., Li, X. N., Adair, K. R., Sun, X. L. Metal Halide Superionic Conductors for All-Solid-State Batteries. *Accounts of Chemical Research* **54**, 1023-1033 (2021).
64. Park, K. H., Kaup, K., Assoud, A., Zhang, Q., Wu, X. H., Nazar, L. F. High-Voltage Superionic Halide Solid Electrolytes for All-Solid-State Li-Ion Batteries. *ACS Energy Letters* **5**, 533-539 (2020).

65. Liang, J. W., *et al.* Site-Occupation-Tuned Superionic Li(x)ScCl(3+x)Halide Solid Electrolytes for All-Solid-State Batteries. *Journal of the American Chemical Society* **142**, 7012-7022 (2020).
66. Zhou, L. D., Kwok, C. Y., Shyamsunder, A., Zhang, Q., Wu, X. H., Nazar, L. F. A new halospinel superionic conductor for high-voltage all solid state lithium batteries. *Energy & Environmental Science* **13**, 2056-2063 (2020).
67. Schlem, R., Banik, A., Eckardt, M., Zobel, M., Zeier, W. G. Na_{3-x}Er_{1-x}Zr_xCl₆-A Halide-Based Fast Sodium-Ion Conductor with Vacancy-Driven Ionic Transport. *Acs Applied Energy Materials* **3**, 10164-10173 (2020).
68. Wu, E. A., *et al.* A stable cathode-solid electrolyte composite for high-voltage, long-cycle-life solid-state sodium-ion batteries. *Nat Commun* **12**, (2021).
69. Kwak, H., *et al.* Na₂ZrCl₆ enabling highly stable 3 V all-solid-state Na-ion batteries. *Energy Storage Materials* **37**, 47-54 (2021).
70. Tomita, Y., Fuji-i, A., Ohki, H., Yamada, K., Okuda, T. New lithium ion conductor Li₃InBr₆ studied by Li-7 NMR. *Chemistry Letters*, 223-224 (1998).
71. Li, X. N., *et al.* Progress and perspectives on halide lithium conductors for all-solid-state lithium batteries. *Energy & Environmental Science* **13**, 1429-1461 (2020).
72. Xu, Z. M., Chen, X., Liu, K., Chen, R. H., Zeng, X. Q., Zhu, H. Influence of Anion Charge on Li Ion Diffusion in a New Solid-State Electrolyte, Li₃LaI₆. *Chemistry of Materials* **31**, 7425-7433 (2019).
73. Xie, J., *et al.* Atomic Layer Deposition of Stable LiAlF₄ Lithium Ion Conductive Interfacial Layer for Stable Cathode Cycling. *ACS Nano* **11**, 7019-7027 (2017).
74. Hu, J. L., Yao, Z. G., Chen, K. Y., Li, C. L. High-conductivity open framework fluorinated electrolyte bonded by solidified ionic liquid wires for solid-state Li metal batteries. *Energy Storage Materials* **28**, 37-46 (2020).
75. Goodenough, J. B. Rechargeable batteries: challenges old and new. *Journal of Solid State Electrochemistry* **16**, 2019-2029 (2012).
76. Goodenough, J. B., Kim, Y. Challenges for rechargeable batteries. *Journal of Power Sources* **196**, 6688-6694 (2011).

77. Wang, S., *et al.* Lithium Chlorides and Bromides as Promising Solid-State Chemistries for Fast Ion Conductors with Good Electrochemical Stability. *Angewandte Chemie-International Edition* **58**, 8039-8043 (2019).
78. Banerjee, A., Wang, X. F., Fang, C. C., Wu, E. A., Meng, Y. S. Interfaces and Interphases in All-Solid-State Batteries with Inorganic Solid Electrolytes. *Chemical Reviews* **120**, 6878-6933 (2020).
79. Wolfenstine, J., Allen, J. L., Sakamoto, J., Siegel, D. J., Choe, H. Mechanical behavior of Li-ion-conducting crystalline oxide-based solid electrolytes: a brief review. *Ionics* **24**, 1271-1276 (2018).
80. Zhang, X., Wang, Q. J., Harrison, K. L., Roberts, S. A., Harris, S. J. Pressure-Driven Interface Evolution in Solid-State Lithium Metal Batteries. *Cell Reports Physical Science* **1**, 100012 (2020).
81. Zhu, Y. Z., He, X. F., Mo, Y. F. First principles study on electrochemical and chemical stability of solid electrolyte-electrode interfaces in all-solid-state Li-ion batteries. *Journal of Materials Chemistry A* **4**, 3253-3266 (2016).
82. Chu, I. H., *et al.* Insights into the Performance Limits of the Li₇P₃S₁₁ Superionic Conductor: A Combined First-Principles and Experimental Study (vol 8, pg 7843, 2016). *Acs Applied Materials & Interfaces* **10**, 10598-10598 (2018).
83. Duchene, L., *et al.* A stable 3 V all-solid-state sodium-ion battery based on a closo-borate electrolyte. *Energy & Environmental Science* **10**, 2609-2615 (2017).
84. Zhang, Z. Z., *et al.* New horizons for inorganic solid state ion conductors. *Energy & Environmental Science* **11**, 1945-1976 (2018).
85. Koerver, R., *et al.* Capacity Fade in Solid-State Batteries: Interphase Formation and Chemomechanical Processes in Nickel-Rich Layered Oxide Cathodes and Lithium Thiophosphate Solid Electrolytes. *Chemistry of Materials* **29**, 5574-5582 (2017).
86. Tang, H. M., *et al.* Probing Solid Solid Interfacial Reactions in All-Solid-State Sodium-Ion Batteries with First-Principles Calculations. *Chemistry of Materials* **30**, 163-173 (2018).
87. Tian, Y. S., *et al.* Compatibility issues between electrodes and electrolytes in solid-state batteries. *Energy & Environmental Science* **10**, 1150-1166 (2017).

88. Hartmann, P., *et al.* Degradation of NASICON-Type Materials in Contact with Lithium Metal: Formation of Mixed Conducting Interphases (MCI) on Solid Electrolytes. *Journal of Physical Chemistry C* **117**, 21064-21074 (2013).
89. Wenzel, S., Leichtweiss, T., Kruger, D., Sann, J., Janek, J. Interphase formation on lithium solid electrolytes-An in situ approach to study interfacial reactions by photoelectron spectroscopy. *Solid State Ionics* **278**, 98-105 (2015).
90. Cao, D. X., Sun, X., Li, Q., Natan, A., Xiang, P. Y., Zhu, H. L. Lithium Dendrite in All-Solid-State Batteries: Growth Mechanisms, Suppression Strategies, and Characterizations. *Matter* **3**, 57-94 (2020).
91. Zhao, F. P., *et al.* Ultrastable Anode Interface Achieved by Fluorinating Electrolytes for All-Solid-State Li Metal Batteries. *Acs Energy Letters* **5**, 1035-1043 (2020).
92. Zhao, F. P., *et al.* A Versatile Sn-Substituted Argyrodite Sulfide Electrolyte for All-Solid-State Li Metal Batteries. *Advanced Energy Materials* **10**, 1903422 (2020).
93. Senevirathne, K., Day, C. S., Gross, M. D., Lachgar, A., Holzwarth, N. A. W. A new crystalline LiPON electrolyte: Synthesis, properties, and electronic structure. *Solid State Ionics* **233**, 95-101 (2013).
94. Tian, Y. S., *et al.* Reactivity-Guided Interface Design in Na Metal Solid-State Batteries. *Joule* **3**, 1037-1050 (2019).
95. Si, M. T., *et al.* Local Electric-Field-Driven Fast Li Diffusion Kinetics at the Piezoelectric LiTaO₃ Modified Li-Rich Cathode-Electrolyte Interphase. *Advanced Science* **7**, 1902538 (2020).
96. Ohta, N., *et al.* LiNbO₃-coated LiCoO₂ as cathode material for all solid-state lithium secondary batteries. *Electrochemistry Communications* **9**, 1486-1490 (2007).
97. Chen, D. R., *et al.* Effect of Li₃PO₄ coating of layered lithium -rich oxide on electrochemical performance. *Journal of Power Sources* **341**, 147-155 (2017).
98. Zhu, Y. Z., He, X. F., Mo, Y. F. Origin of Outstanding Stability in the Lithium Solid Electrolyte Materials: Insights from Thermodynamic Analyses Based on

First-Principles Calculations. *Acs Applied Materials & Interfaces* **7**, 23685-23693 (2015).

99. Culver, S. P., Koerver, R., Zeier, W. G., Janek, J. On the Functionality of Coatings for Cathode Active Materials in Thiophosphate-Based All-Solid-State Batteries. *Advanced Energy Materials* **9**, 1900626 (2019).

Chapter 3

3 Experimental apparatus and characterization techniques

In this chapter, the experimental apparatus and main characterization methods are listed with brief introductions.

3.1 Experimental apparatus

Experimental apparatus used to synthesize SEs and coating layers are introduced in this sub-section.

3.1.1 Ball milling machine

High-energy ball mill is an important essential tool to synthesize SEs, which can provide a transformation from mechanical energy to chemical energy. High-energy ball mill is good for the preparation of glassy materials or low-crystallinity materials. As shown in **Figure 3.1**, Planetary PM 200 machine (Produced in Retsch Company, Germany) with two stations is used to prepare SEs in this dissertation.



Figure 3.1 PM200 two-station planetary ball mill produced by Retsch

3.1.2 Ampules

To improve the crystallinity of some ball-milled SE materials, air-sensitive materials are sealed in quartz ampules under vacuum before proceeding to heat treatments. **Figure 3.2a** shows a the nuzzle with controllable inlets of methane fuel gas and oxygen combustion accelerator to achieve high-temperature flames for melting and sealing quartz tubes. The quartz tube was connected to a vacuum pump during sealing. Strict training and protective measures were enforced prior to operating this apparatus. The sealed samples were then transferred in a Muffle furnace for heating procedure (**Figure 3.2b**) at designated temperatures.

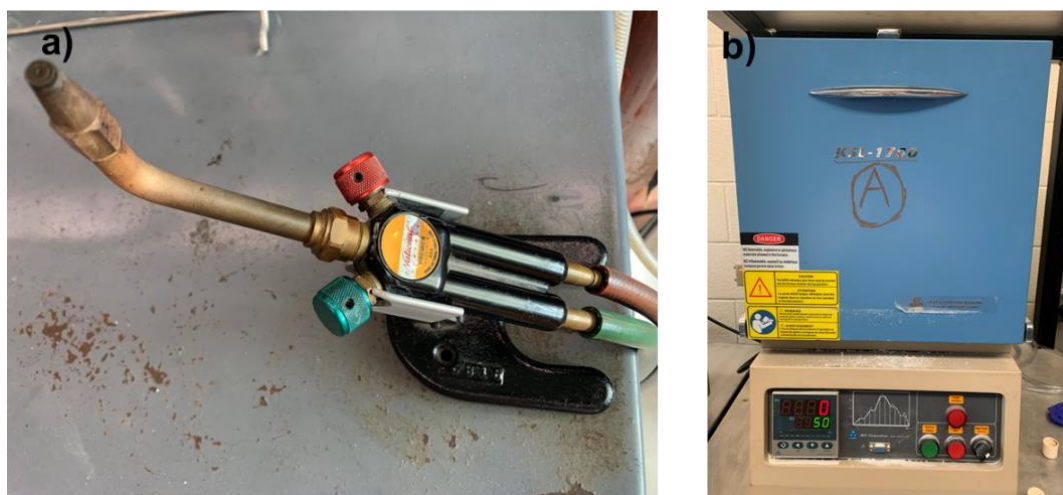


Figure 3.2 (a) The equipment for quartz tube encapsulation. (b) Muffle furnace for heating the ampules

3.1.3 Molecular layer deposition (MLD)

The MLD system (Gemstar-8 ALD system by Arradiance, USA) is connected to an Ar-filled glovebox for handling air sensitive samples (**Figure 3.3**). The active Na foils were placed in the reaction chamber under high vacuum at 85 °C, controlled pulses of trimethylaluminium (TMA) precursor and ethylene glycol (EG) were respectively introduced into the chamber.



Figure 3.3 The Gemstar-8 ALD system as well as the connected glove box.

3.2 Characterization techniques

3.2.1 Scanning electron microscope (SEM)

The morphology of SEs and interface between SE/electrodes can be visualized using a Hitachi S-4800 SEM equipped with energy dispersive spectroscopy (EDS), as shown in **Figure 3.4**. In this dissertation, the SEM images were obtained at an acceleration voltage of 5.0 kV, and the EDS mapping was conducted at 20.0 kV. Air sensitive samples were prepared in an Ar-filled glovebox and transferred to the SEM station using an Ar-filled container to avoid air exposure.



Figure 3.4 The Hitachi S-4800 SEM, equid with EDS.

3.2.2 Time-of-Flight Secondary Ion Mass Spectrometry (ToF-SIMS)

ToF-SIMS is a technique for surface analysis of SE/anode interface, which uses an ion beam to remove small numbers of atoms and molecules from the outermost layer of a surface and analyzes those that are ionized (secondary ions). A short pulse of primary ions (such as Cs^+) strikes the surface and the secondary ions produced in the sputtering process are extracted from the sample surface into a time-of-flight mass spectrometer. These secondary ions are dispersed in time according to their velocities. Assisted with a sputter ion beam, ToF-SIMS can be also used to depth profile both inorganic and organic materials. An area is sputtered for a pre-determined period followed by analyzing the newly generated surface within the sputtered area, which provides a data point in the depth profile. ToF-SIMS can detect ions over a large mass range of 1–10,000 atomic

mass units at a mass resolution of 10,000. The technique can generate an image of lateral distributions of these secondary ions at spatial resolutions of better than 0.15 microns.

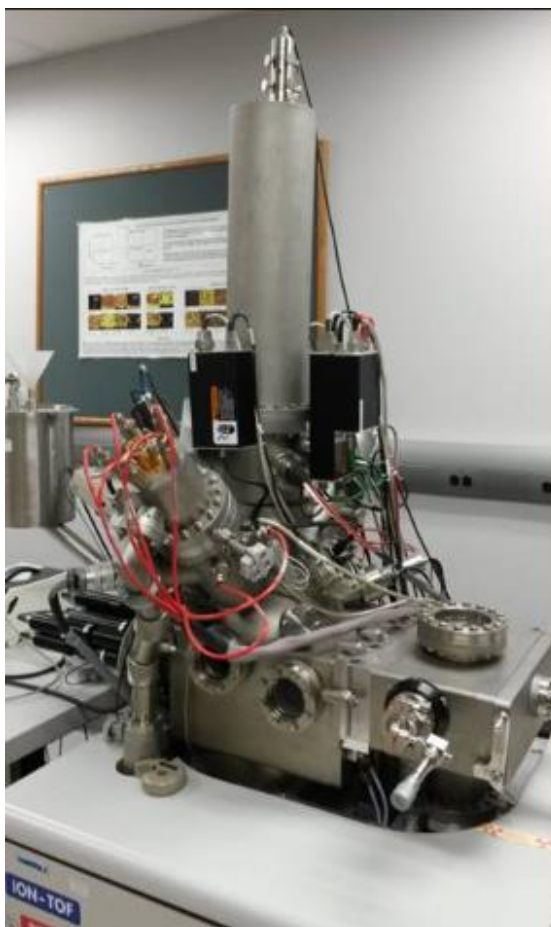


Figure 3.5 The ToF-SIMS station at Surface Science Western¹.

3.2.3 X-ray photoelectron spectroscopy (XPS)

XPS was used to analyze the chemical composition and bonding of samples by probing the photoemission of electrons caused by incident X-rays at different excitation energies. The XPS (Escalab 250 Xi) technique in this dissertation is from Ontario Centre for the Characterization of Advanced Materials at University of Toronto. It shows advantages of firing clusters of argon atoms at the surface, which gently strip away the upper layers and

expose what is underneath without losing molecular information. This is beneficial to get the detailed information at the interfaces between SE/anode.

3.2.4 Lab X-ray diffraction (XRD)

Lab XRD was used phase analysis and crystalline variants of SEs. As shown in **Figure 3.6**, X-ray wavelength provided by the Bruker D8 Advance Diffractometer is 1.5406 \AA ($\text{Cu K}\alpha$). The powder samples were generally put on XRD sample holder and sealed by Kapton film to avoid air exposure. In XRD patterns of this thesis, the broad diffraction peak around $\sim 20^\circ$ is caused by the signals from the Kapton film.



Figure 3.6 The Bruker D8 Advance Diffractometer XRD system.

3.2.5 Raman

Raman is a light scattering technique provides information about chemical structure, phase, crystallinity, and molecular interactions of a SE. A spatial resolution in the order of 0.5-1 micron. In this dissertation, Raman spectra were collected on a HORIBA Scientific LabRAM Raman spectrometer equipped with a 532 nm laser (**Figure 3.7**). The Raman spectra were used frequently to analyze the coordination of polyhedral in SEs.

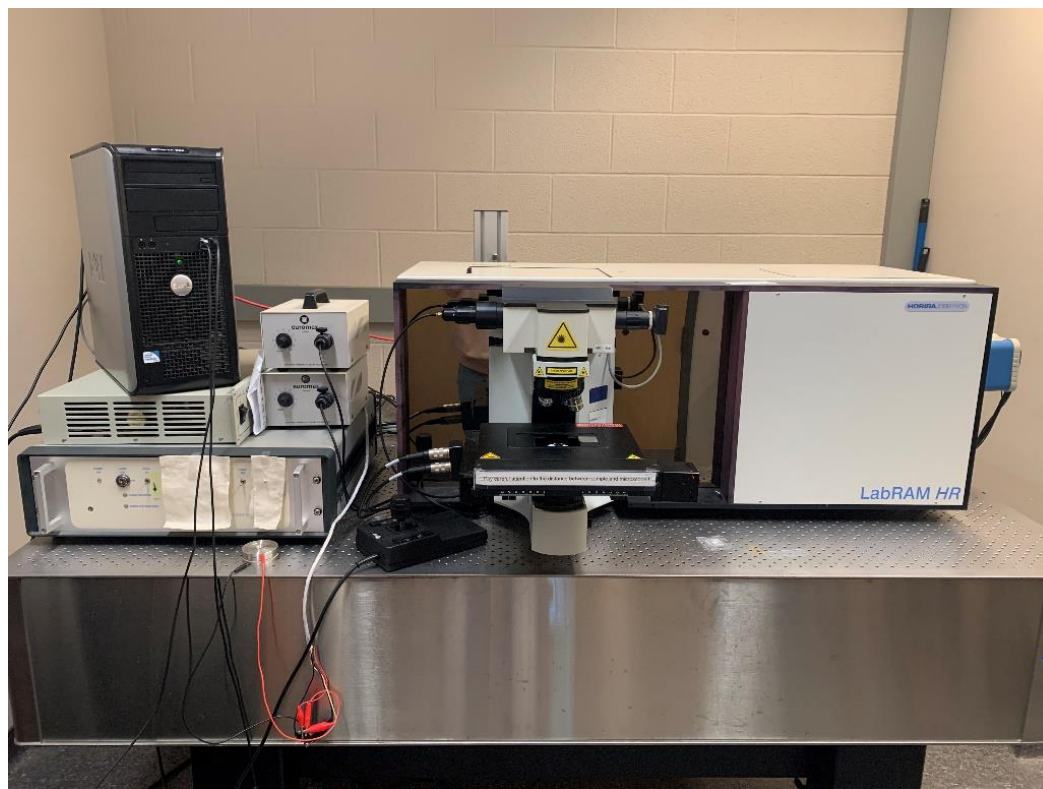


Figure 3.7 The HORIBA Scientific LabRAM HR Raman spectrometer

3.2.6 Solid-state nuclear magnetic resonance (SS-NMR)

The ss-NMR spectroscopy is used for probing the chemical environments of various magnetically active elements. It is ideal to investigate the subtle changes in local structure in SE. In this dissertation, magic angle spinning (MAS) ss-NMR is used

analyze the chemical environment of ${}^6\text{Li}$ in the $\text{Li}_{x-3}\text{YI}_x$ SEs. Besides, ss-NMR is used to precisely analyze the dynamic feature of Li^+ in SEs via designing variable-temperature experiments. It provides a SE sample with the nuclide-specific information on structure and dynamics.

The NMR-related work in this dissertation was collaborated with Prof. Yining Huang's group in the Department of Chemistry at Western University. The ss-NMR spectrometer is shown in **Figure 3.8**.



Figure 3.8 The ss-NMR spectrometer with computers

3.2.7 Synchrotron radiation (SR)

3.2.7.1 Spherical Grating Monochromator (SGM) Beamline at Canadian Light Source (CLS)

The SGM beamline is a soft x-ray beamline located at the CLS, which provides the measurements with the photon energy from 250 to 2000 eV. The beam is focussed to 10 microns in this endstation for x-ray fluorescence mapping of light elements. X-ray absorption spectroscopic measurements (XAS) using transmission, photon in-photon out and photo in-electron out detection can be performed at SGM beamline. There are two in-line endstation areas. Endstation Area 1 is built for performing bulk x-ray absorption and x-ray photoemission studies under ultra high vacuum conditions. Endstation Area 2 is used for micro-focused x-ray absorption and fluorescence mapping experiments under either ambient pressure or high vacuum conditions. In this dissertation, the F K-edge XAS are performed at SGM beamline.

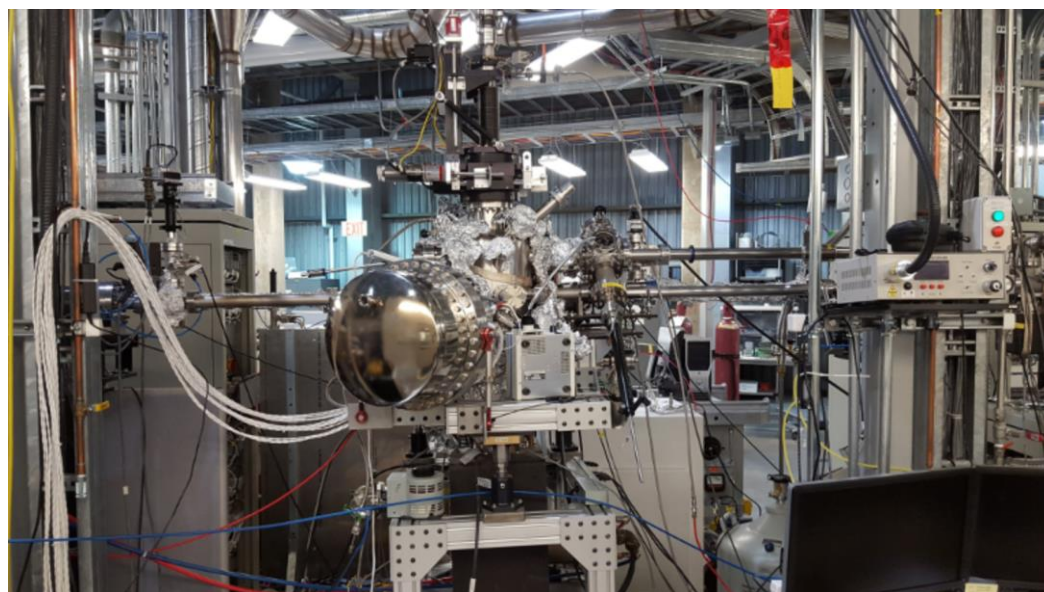


Figure 3.9 One SGM endstation area²

3.2.7.2 Soft X-ray SpectroMicroscopy (SM) facility at CLS

SM beamline provides high brightness and well resolved photons from 130 - 2500 eV. There are two endstations at SM, one is Scanning Transmission X-ray Microscope (STXM) and the other is X-ray Photoemission Electron Microscope (X-PEEM). In this dissertation, our samples were performed at STXM endstation. As shown in **Figure 3.10**,

STXM can provide high quality imaging and spatially resolved spectroscopy with 30 nm spatial resolution. Devices for tomography are also available.

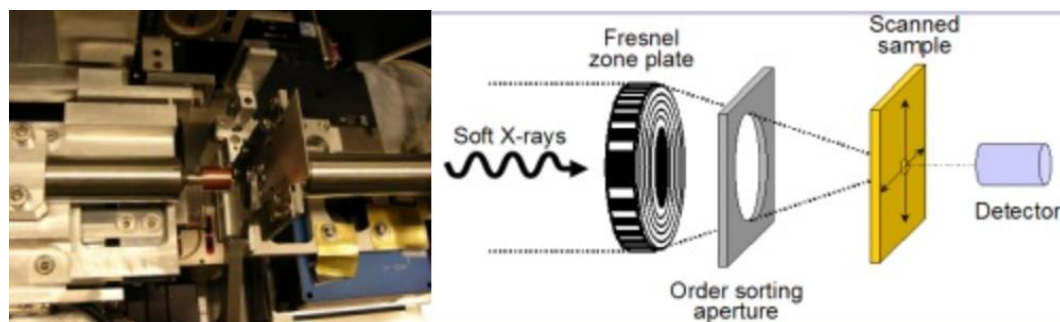


Figure 3.10 STXM endstation at SM beamline³

3.2.7.3 Soft X-Ray Microcharacterization Beamline (SXRMB) at CLS

SXRMB is a medium energy x-ray beamline at CLS, which provides the measurements with the photon energy from 1.7 to 10 keV. There are four endstations available for users: 1) Solid State Endstation for bulk and powder samples under high vacuum. 2) Microprobe Endstation for mapping experiments. 3) Ambient Table for bulk analysis, liquid and solid in-situ experiments and 4) High Energy XPS for depth-profiling analysis. In this dissertation, the I L₂-edge XAS were performed at SXRMB beamline.

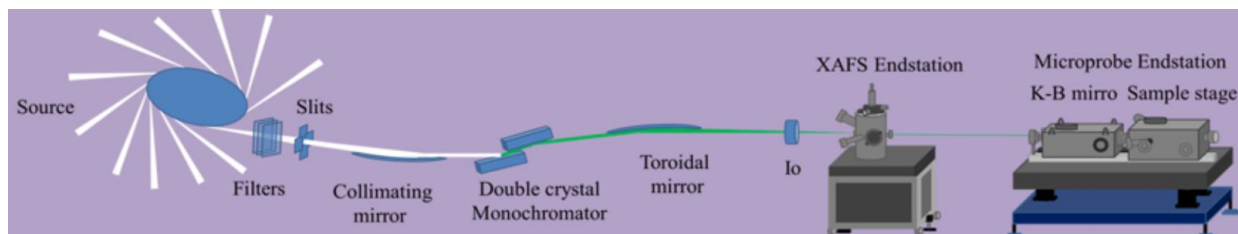


Figure 3.11 The distribution of SXRMB⁴

3.2.7.4 Very Sensitive Elemental and Structural Probe Employing Radiation from a Synchrotron (VESPERS) at CLS

VESPERS is a X-ray microprobe beamline which provides the measurements with the photon energy from 6 to 30 keV. Techniques such as XRD and X-ray fluorescence spectroscopy, as well as XAS can be achieved at VESPERS. In this dissertation, the 2D XRD patterns for SEs were collected at VESPERS.

3.2.7.5 Brockhouse Diffraction Sector Beamlines (BXDS) at CLS

There are three beamlines at Brockhouse, low energy wiggler beamline (7-22 keV), high energy wiggler beamline (20-94 keV), and undulator beamline (5-24 keV). The high energy beamline equips with a Perkin Elmer area detector mounted on a translation table, which can move to follow the Bragg angle of the monochromator as the energy is changed. Any energy within the beamlines range to be easily accessed by using this set up. In this dissertation, PDF were done at this beamline to give the distribution of inter-atomic distances in a material and is an excellent probe of the local and medium range structure. Powder diffraction data were also quickly collected at this beamline with very high counting statistics, which is good for refinement.

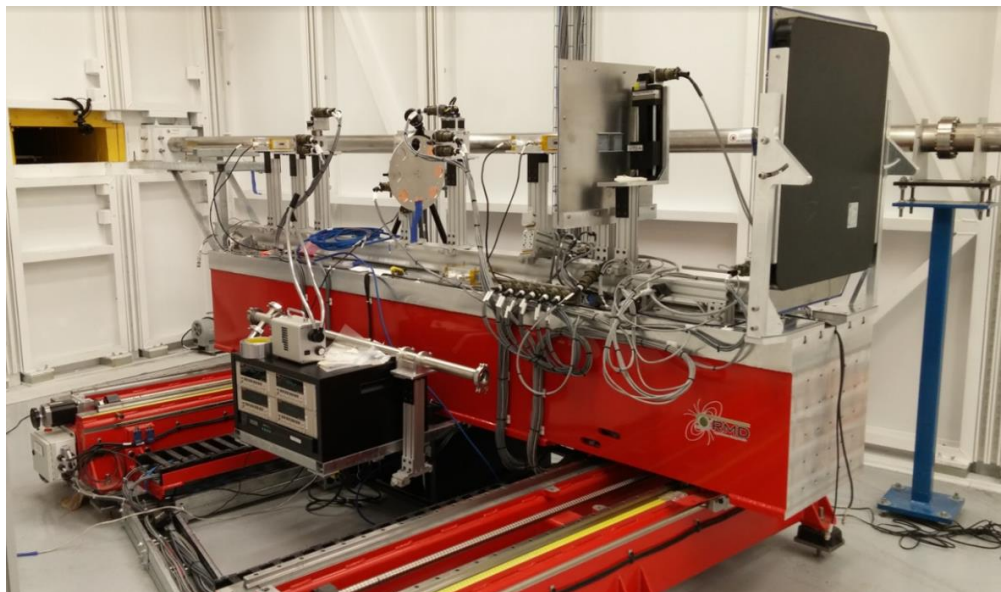


Figure 3.12 The experimental station high energy wiggler beamline at Brockhouse⁵

3.2.7.6 Taiwan Photon Source (TPS) 44A at National Synchrotron Radiation Research Center (NSRRC)

TPS 44A beamline is a hard X-ray beamline which provides the XAFS and XRD measurements with the energy range of 4.5-34 keV. There are several optical devices including a collimating mirror, a quick-scanning monochromator (Q-Mono), a toroidal focusing mirror, and a set of K-B mirrors. The Q-mono has the capability of doing step-by-step scans and quick scans. The EXAFS data in this dissertation were collected at TPS 44A.



Figure 3.13 The XANES/EXAFS experimental station at TPS 44A⁶

3.3 Electrochemical evaluations

3.3.1 Cell configuration

The electrochemical performances (such as cyclic voltammetry, electrochemical impedance spectroscopy, and galvanostatic charge-discharge test) for ASSBs were tested by using model cell in this dissertation. As shown in **Figure 3.14**, a model cell was custom-made to enable the use of powder SSEs. Metal anode, SE powders/pellets, and cathode composite are pressed into the cell layer by layer using stainless-steel terminals and hydraulic press. The cathode composites were prepared by mixing the selective CAM and designated SSE powders at a specific ratio using an agate mortar. The inner diameter of the model cell was 10 mm. Corresponding details related to each project were described in Chapter 4–7.



Figure 3.14 A model cell with the internal parts and the shell

3.3.2 Electrochemical working station

EIS, LSV, and CV tests were completed by using a multichannel potentiostation 3/Z (German VMP3) (**Figure 3.15**). The VMP3 was connected with a programmable thermal test chamber (- 50 °C - 75 °C) for the periodical temperature-dependent EIS test



Figure 3.15 The VMP3 working station with a programmable thermal chamber.

3.3.3 Batter testing system

All the battery performances in this dissertation were measured on the Land 2001A Battery Test System (**Figure 3.16**). Cycling protocols and testing programs can be set differently based on projects. Some channels with extension cords were operated in a low-temperature freezer at $-10\text{ }^{\circ}\text{C}$ to evaluate the battery performances. Galvanstatic charge and discharge tests on the system were used to examine the cycling stability and rater capability. Symmetric cell test on this system was used to check the SE/metal interfacial stability.

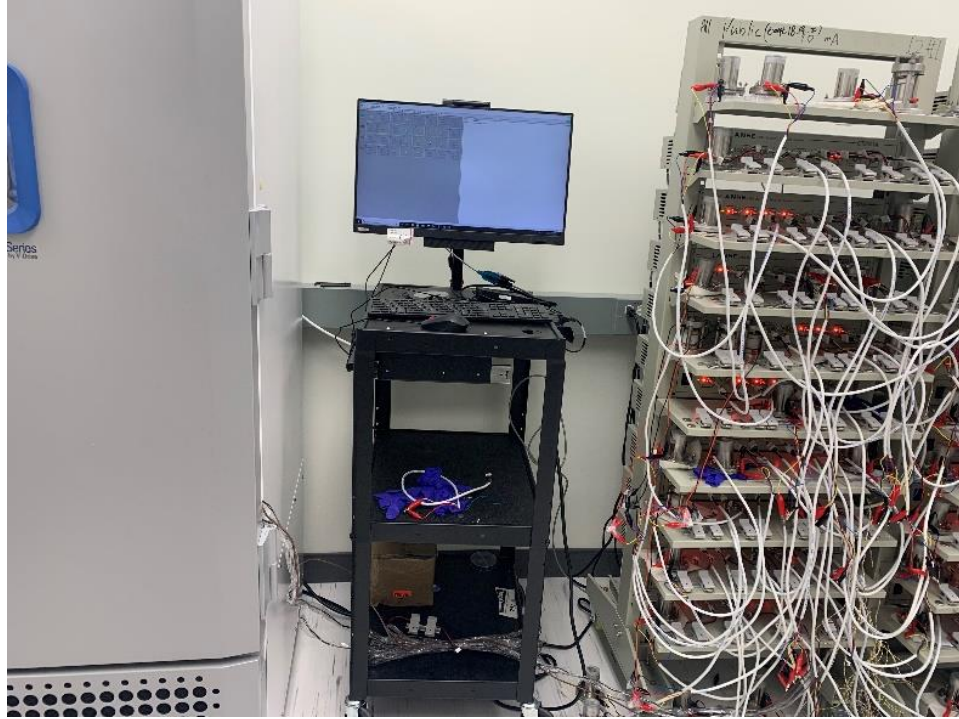


Figure 3.16 The Land 2001A Battery Test System.

Chapter 4

4 Novel Iodide Superionic Conductors: Reviving of $\text{Li}_{x-3}\text{YI}_x$

Solid electrolytes (SEs) are vital to enable high-energy-density all-solid-state lithium batteries (ASSLBs). One key parameter for a SE is ionic conductivity, which can achieve a high value by understanding the underlying mechanisms of ion migration. The classic fundamentals and structural reasons have been guided the rational designs of new SEs materials, opening opportunities for ASSLBs. Herein, we report a new series of iodide-based SEs: $\text{Li}_{x-3}\text{YI}_x$ ($x = 12, 7, 6$ and 5) by doping Y into pristine LiI. The RT ionic conductivity of the optimized Li_4YI_7 reaches up to $1.04 \times 10^{-3} \text{ S cm}^{-1}$. The relation between ionic conductivity and structure of $\text{Li}_{x-3}\text{YI}_x$ is explored from the dimensions of long-range crystalline structures to the local defects. Different from the recent reported halide SEs, $\text{Li}_{x-3}\text{YI}_x$ is a cubic-type Suzuki material with high symmetry. The enlarged diffusion pathway, soft anion, and cation vacancies in $\text{Li}_{x-3}\text{YI}_x$ are combined contributing to the high ionic conductivity. Other than that, the electrochemical performance shows that Li_4YI_7 possesses a low cathodic limit. A stable electrochemical plating/stripping of Li/Li symmetric cell can be achieved for over 1000 h.

*A version of this chapter to be submitted.

4.1 Introduction

With the popularity of electrical vehicles (EVs), all-solid-state lithium batteries (ASSLBs) are promising to be the next-generation power source due to their intrinsic safer property as well as high-energy/power density^{1, 2}. One key component of ASSLBs is solid electrolytes (SEs)^{3, 4, 5}, which replace the conventional flammable liquid electrolytes to improve safety, and at the same time, promisingly contact with Li metal to boost the energy density of ASSLBs. Nevertheless, the problematic Li metal anode still induces the Li dendrite growth that results in the internal short circuit of a battery.^{6, 7} Therefore, high-ionic-conductive SEs that can effectively suppress the Li dendrite growth are expected.

Lithium halide (LiX, such as LiI and LiF, X represents halogen) has been regarded as one of the feasible compounds to suppress the lithium dendrite growth^{8, 9, 10}; yet the binary lithium halides show poor room-temperature (RT) ionic conductivities, in which LiI possesses a relatively higher value but still limited to 10^{-7} S cm⁻¹^{11, 12}. The development of lithium halides then expanded to ternary Li-M-X (M represents metal cation). To date, some of the developed ternary lithium transition metal chlorides and bromides (such as Li₃YBr₆¹³, Li₃InCl₆¹⁴, and Li-Sc-Cl^{15, 16}) show a jumped ionic conductivity reach or close to the benchmark (10^{-3} S cm⁻¹) of the bulk-type ASSLIBs.¹⁷ Compared with the binary LiX, there are two major factors for Li-M-X showing high ionic conductivities. First, the introduction of heterovalent M can create more defects to increase the ion mobility. For example, the substitution of Li⁺ by each trivalent Y³⁺/In³⁺ in LiCl would offer two intrinsic cation vacancies^{18 13}. Second, the change of structural parameters can lower the migration barrier thus accelerating the ion transport. The structural parameters include ion arrangement, phase, ionic radii, and the sublattice dynamics. Li ions in one solid with preferred ion arrangement and phase have lower energy jumps between adjacent sites. For example, the ball-milled α -Li₂ZrCl₆ with a *ccp* anion lattice has an ionic conductivity that is two orders of magnitude higher than that of the annealed β -Li₂ZrCl₆ in a hexagonal-close-packed (*hcp*) anion arrangement^{19, 20}. Li-Sc-Cl analogs with cubic (Li₂Sc_{2/3}Cl₄²¹) or monoclinic structure (Li₃ScCl₆¹⁶) exhibits decent ionic conductivities of 10^{-3} S cm⁻¹. Besides, metal cations and anions with larger radii can help to widen the Li-

ion diffusion pathway. Especially for anions, such as Γ^- with a larger radius of 206 pm, not only have longer bonding length but also higher polarizability to potentially enhance Li-ion conductivity and deformability^{22, 23}. For iodide compounds, the materials that experimentally reported are LiScI_3 ²⁴, Li_3ErI_6 ²², and Li_3HoI_6 ²⁵. They are all in monoclinic phase with different symmetry, while their ionic conductivities are below $10^{-3} \text{ S cm}^{-1}$. Other iodide compounds (Li_3MI_6 ($M = \text{La, Y}$)) predicted to be superionic conductors still belong to monoclinic group, but they are not yet to be experimentally realized. Compared with the reported Li-M-X ($X = \text{F, Cl, Br}$) showing various phases, e.g., spinel, and Suzuki and etc¹⁵, the structural diversity of iodide materials should be well explored to rich the ternary lithium iodides family. At the same time, to make iodide materials superionic conductive and feasible for ASSLIBs, the designing criteria for fast ion conductivity should be applied.

In this work, we experimentally prepared a series of $\text{Li}_{x-3}\text{YI}_x$ via ball milling and annealing methods. The as-prepared materials show a high ionic conductivity over $10^{-4} \text{ S cm}^{-1}$ and the highest value can reach $1.04 \times 10^{-3} \text{ S cm}^{-1}$ for Li_4YI_7 at room temperature (RT). The long-range and local structures of $\text{Li}_{x-3}\text{YI}_x$ were revealed via XRD refinement and X-ray absorption spectroscopy (XAS), respectively. The $\text{Li}_{x-3}\text{YI}_x$ SE is confirmed in Suzuki structure with a space group $Fm-3m$. Y^{3+} partially replaces the Li^+ site and is coordinated by 6 Γ^- ions in YI_6^{3-} octahedra. A large number of vacancies in $\text{Li}_{x-3}\text{YI}_x$ is created, which prompts the Li-ion conductivity. The electrochemical stability of $\text{Li}_{x-3}\text{YI}_x$ is then evaluated, as well as their compatibility with Li metal, which deepens our understanding of iodide SEs and its applications in ASSLIBs.

4.2 Experimental section

Synthesis of $\text{Li}_{x-3}\text{YI}_x$ solid electrolytes:

LiI (Sigma Aldrich, 99.99 %) and YI_3 (Alfa Aesar, 99.5%) were used as the raw materials. The starting materials for each compound were mixed accordingly with a stoichiometric ratio in an argon-filled glovebox (H_2O , $\text{O}_2 < 0.1 \text{ ppm}$). The resulting mixture (~1g) was then placed in a zirconia ball milling pot along with 40 g zirconia

balls. Low-speed ball milling (100 rpm for 5 h) was first run to ensure all the precursors mixed well, followed by a high-speed ball milling process of 400 rpm for 20 h. Next, the ball-milled products were transferred into the glovebox and cold-pressed into pellets. The pellets were then sealed in quartz tubes for annealing under 200 °C for 5 hrs. After naturally cooling down to RT, the SE pellets were transferred into the glovebox and manually ground into powders for further use.

Ionic conductivity measurement

Ionic conductivity of as-prepared SEs was evaluated using electrochemical impedance spectroscopy (EIS) with two stainless steel rods as blocking electrodes. The SE powders (~150 mg) were cold-pressed into pellets under ~400 Mpa. The thickness of each pellet was provided in Nyquist plot figures in supporting information. EIS measurements were performed using a multichannel potentiostat 3/Z (German VMP3). The applied frequency range is 1 Hz ~ 7 MHz and the voltage amplitude is 20 mV.

Characterization methods

Lab-based XRD measurements were performed on Bruker AXS D8 Advance with Cu K α radiation ($\lambda = 1.5406 \text{ \AA}$). Kapton tape was used to cover the sample holder to prevent from the air exposure. Raman spectra were measured with a HORIBA Scientific LabRAM HR. Raman spectrometer operated under laser beam at 532 nm. Electrolyte powders were attached on a carbon tape and covered by a transparent glass for the test.

XAS data were collected at the 44A beamline of Taiwan Photon Source (TPS) of the National Synchrotron Radiation Research Center (NSRRC) in Taiwan. XAS spectra were recorded in transmission mode and the data were processed with Athena and Artemis softwares.

Synchrotron-based XRD patterns and PDF data of the samples were collected at the BXDS-WHE beamline at Canadian Light Source (CLS) in Canada (20 – 94 KeV). GSAS-II and PDFgui softwares were used to process the data.

^7Li MAS NMR measurements were performed on a Varian Infinity Plus wide - bore NMR spectrometer equipped with an Oxford wide-bore magnet (Bo \approx 9.4 T). The ^7Li Larmor frequency was 155.248 MHz. The $\pi/2$ and π pulse length were determined to be 2.3 and 4.5 μs , respectively. Chemical shifts were referenced with respect to a 1.0 M LiCl solution. The electrolyte sample was sealed in custom-made Teflon tubes ($\phi = 4.7$ mm) in an argon-filled glovebox (H_2O , $\text{O}_2 < 0.1$ ppm).

Assembly and electrochemical characterizations of ASSLBs

CV Test: a glassy SE powder was manually mixed well with carbon black (CB) in a weight ratio of 8:2. Then, 80 mg of the Li_4YI_7 SE powder was cold-pressed into a pellet under a pressure of 300 MPa. 10 mg of SE/CB mixture was uniformly placed on one side of the glassy SE pellet as working electrode and compressed again under the same pressure. After that, Li foil (China Energy Lithium Co. LTD) was attached on the other side of the pellet as both counter and reference electrode. In order to avoid the incompatibility between the glassy SE and metallic Li, a thinner layer of Li_3PS_4 sulfide SE (40 mg) was inserted between the glassy SE pellet and Li before Li foil was added. To ensure an intimate contact between layer by layer, the cell was pressed under a pressure of 120 MPa before taking out of the glovebox. The CV electrochemical stability window tests were conducted using versatile multichannel potentiostat 3/Z (VMP 3) with a scan range from open-circuit voltage (OCV) to 5 V (vs Li/Li $^+$, positive scan) and then back to 0 V (vs Li/Li $^+$, negative scan), respectively. The scan rate was 0.1 mV s $^{-1}$.

Symmetric cell Test: 80 mg of Li_4YI_7 SE was pressed by \approx 300 MPa to form solid pellet. Two pieces of Li foil were placed onto both sides of the electrolyte pellet and then pressed. Li plating/stripping experiments were carried out on LAND battery testing stations (CT-2001A, Wuhan Rambo Testing Equipment Co., Ltd.). Current density and cut-off capacity were set at 0.1 mA cm $^{-2}$ and 0.1 mAh cm $^{-2}$.

4.3 Results and discussion

LiI and YI_3 were used as the starting materials to produce a series of $\text{Li}_{x-3}\text{YI}_x$ ($x = 12, 7, 6,$ and 5) SEs, in which x can be regarded as the inverse number of the mole percentage

of YI_3 substituted the corresponding LiI in per mole LiI . Via conventional solid-state method, a mixture of LiI and YI_3 with different stoichiometric ratios was firstly ball-milled and then annealed at a low temperature of 200°C . **Figure 4.1a** shows the XRD patterns of the as-prepared $\text{Li}_{x-3}\text{YI}_x$. All the diffraction peaks in each $\text{Li}_{x-3}\text{YI}_x$ compound can be well indexed to a cubic-structured LiI with a space group of $Fm-3m$ (ICSD No. 04-016-5474)²⁶. However, the corresponding peaks in each $\text{Li}_{x-3}\text{YI}_x$ gradually shift to low 2θ angle along with the decrease of x in $\text{Li}_{x-3}\text{YI}_x$ (see the magnification plots in **Figure 4.1a**). This is related to the radius of dopant element. Y^{3+} (90 pm) shows a larger ionic radius compared to Li^+ (76 pm), which can cause a lattice expansion when Y^{3+} partially substitutes the Li site in LiI . The decrease of x in $\text{Li}_{x-3}\text{YI}_x$ means more Li^+ are replaced by Y^{3+} in $\text{Li}_{x-3}\text{YI}_x$, thus a gradually peak shift can be clearly observed. In this regard, Y substitution widens the lattice of LiI , expectedly resulting in an improvement on Li -ion migrations in $\text{Li}_{x-3}\text{YI}_x$ SEs. Then, the ionic conductivities and activation energies (E_a) of above $\text{Li}_{x-3}\text{YI}_x$ SEs were evaluated by the temperature-dependent measurements. **Figure 4.1b** exhibits the Nyquist plots of different cold-pressed $\text{Li}_{x-3}\text{YI}_x$ pellets at RT. Replacing the Li^+ by Y^{3+} obtains an optimized composition of Li_4YI_7 with a RT ionic conductivity of $1.04 \times 10^{-3} \text{ S cm}^{-1}$. Arrhenius conductivity plots of $\text{Li}_{x-3}\text{YI}_x$ SEs based on the temperature-dependent Nyquist plots (**Figure S4.1**) are plotted in **Figure 4.1c**. The corresponding E_a and ionic conductivity values of $\text{Li}_{x-3}\text{YI}_x$ SEs and LiI are extracted in **Figure 4.1d**. After a small amount of YI_3 (10% mole ratio) doping in LiI , E_a drops from 0.41 eV (LiI) to 0.33 eV ($\text{Li}_9\text{YI}_{12}$), proving that Y substitution allows a larger ‘bottleneck’ size to lower the activation barriers for ion diffusion. As a result, $\text{Li}_9\text{YI}_{12}$ shows an enhanced conductivity of $1.16 \times 10^{-4} \text{ S cm}^{-1}$, 3 orders of magnitude higher than that of the LiI ($10^{-7} \text{ S cm}^{-1}$). Li_4YI_7 is the optimized composition with the highest ionic conductivity and the lowest activation energy (0.26 eV). Y substitution in $\text{Li}_{x-3}\text{YI}_x$ not only expanded the lattice size, but also decrease the Li^+ concentration and simultaneously introduces vacancies. Therefore, the final ionic conductivity is affected by these three factors. Further decreasing x in $\text{Li}_{x-3}\text{YI}_x$ results in a lower ionic conductivity of $7 \times 10^{-4} \text{ S cm}^{-1}$ for Li_3YI_6 and $7 \times 10^{-4} \text{ S cm}^{-1}$ for Li_2YI_5 , respectively. Besides, the electronic conductivity of Li_4YI_7 SE is evaluated by direct current (DC) polarization measurements in the range from 100 to 500 mV. The value is about $2.09 \times$

$10^{-7} \text{ S cm}^{-1}$ (**Figure S4.2**), which can be regarded as almost insulating electron compared to the fast Li^+ conduction.

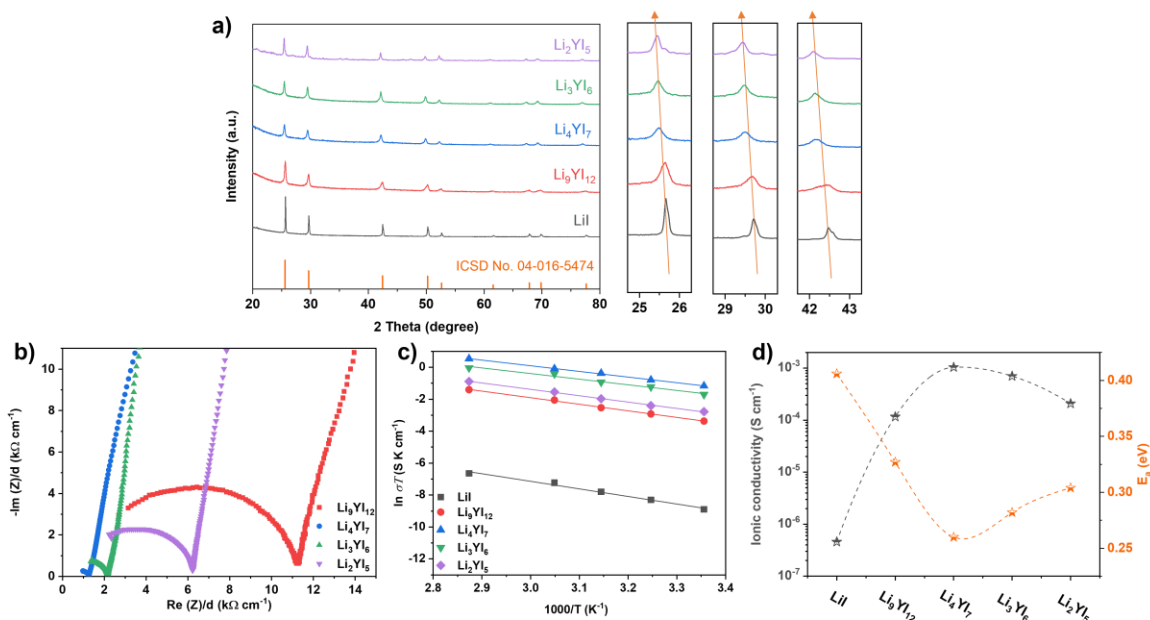


Figure 4.1 (a) Lab-based XRD patterns of the prepared $\text{Li}_{x-3}\text{YI}_x$ powders ($x = 12, 7, 6,$ and 5) and their corresponding magnified regions at 24.7° to 26.3° , 28.7° to 30.3° , and 41.7° to 43.3° ; (b) Normalized impedance spectra of the $\text{Li}_{x-3}\text{YI}_x$ pellets. (c) Arrhenius plots of $\text{Li}_{x-3}\text{YI}_x$ SEs and LiI . (d) Comparison of RT ionic conductivities and activation energies of $\text{Li}_{x-3}\text{YI}_x$ SEs and LiI .

To deeply understand crystallography, local defects, and Li-ion transport kinetics of $\text{Li}_{x-3}\text{YI}_x$ in details, the structures of selected $\text{Li}_9\text{YI}_{12}$ and Li_4YI_7 are firstly determined by Rietveld refinement of the synchrotron-based high-resolution powder X-ray diffraction (SXR) patterns, respectively. As shown in **Figure 4.2a** and **4.2c**, the refined SXR patterns for $\text{Li}_9\text{YI}_{12}$ and Li_4YI_7 (wavelength: 0.3542 \AA) are reasonable with low observation-calculation differences ($R_{wp} \text{Li}_9\text{YI}_{12}$: 2.86%, $R_{wp} \text{Li}_4\text{YI}_7$: 2.26%). Detailed structural and Rietveld refinement information are shown in **Table S4.1 – S4.4** (See **Supporting Information**). The patterns for both compounds are indexed in the cubic

space group ($Fm-3m$). The lattice parameter for $\text{Li}_9\text{YI}_{12}$ is 6.053 Å, larger than that of the LiI in database (ICSD No. 04-016-5474). The lattice for $\text{Li}_{x-3}\text{YI}_x$ is elongated with higher Y substitution content, resulting in a larger lattice parameter of 6.091 Å for Li_4YI_7 . The resultant crystal structures of $\text{Li}_9\text{YI}_{12}$ and Li_4YI_7 are shown in **Figure 4.2b** and **d**, respectively. Different from the recent reported and predicted structures of ternary Li-M-X, both of the two $\text{Li}_{x-3}\text{YI}_x$ compounds show a highly symmetric sublattice that can be regarded as rock-salt derivative. There are only one cation (4a) site and one anion (4b) site in each unit cell, in which Γ ions are cubic-close-packed (*ccp*) to form octahedral voids that are co-occupied by Li^+ , Y^{3+} , and vacancies (V'). Such a structure framework shows high similarities with the predicted Suzuki phase $6\text{NaCl}\cdot\text{CdCl}_2$, while the difference is that in $6\text{NaCl}\cdot\text{CdCl}_2$, there are separate positions for Na^+ (face center), Cd^{2+} (corners) and vacancies (corners)²⁷. Recently, several iodide SEs have been reported (theoretical Li_3LaI_6 ²³, Li_3ErI_6 ²², and Li_3HoI_6 ²⁵) possessing monoclinic phase with space groups $C2/c$, $C2/m$, and $C2$. Here we also fit our experimental $\text{Li}_9\text{YI}_{12}$ and Li_4YI_7 based on the reported lattices and overall symmetry. As shown in **Figure S4.3** and **Figure S4.4**, the resulting fit values and a visual assessment of the profile differences are all show a mismatch of all observed and possible reflection positions. As such, we can generally conclude that $\text{Li}_{x-3}\text{YI}_x$ compounds in this report belong to Suzuki phase with high structural symmetry.

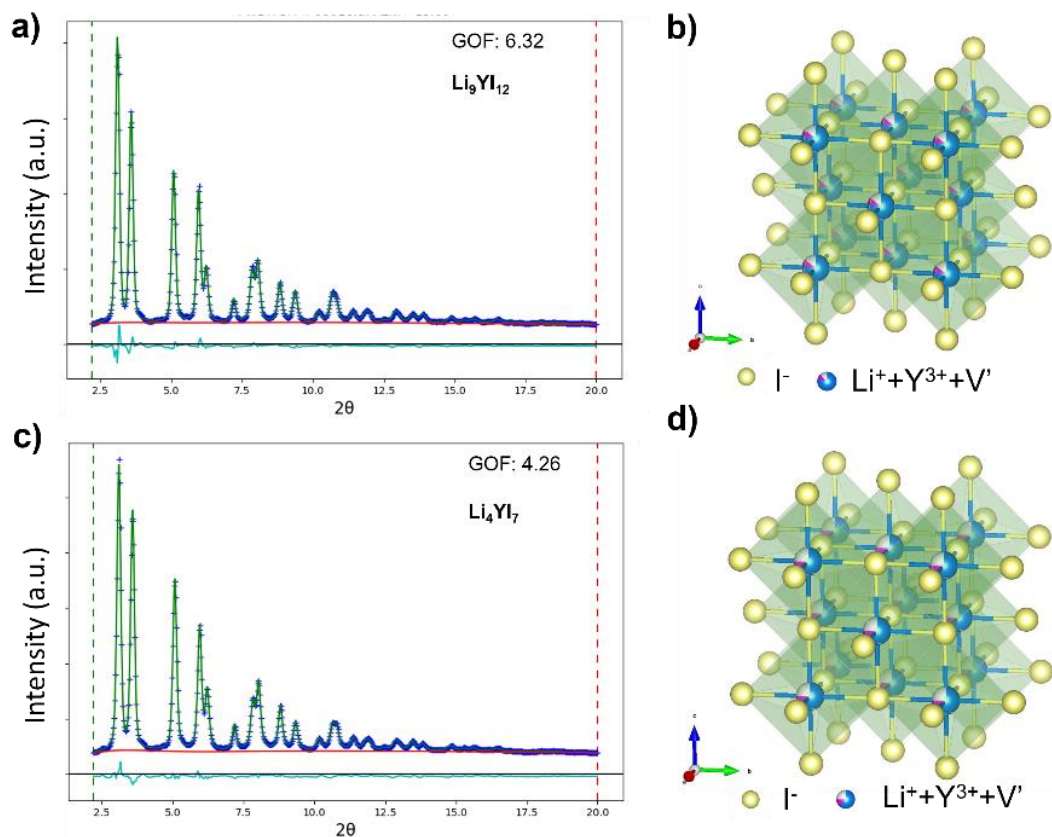


Figure 4.2 Rietveld refinement of the SXR D pattern for (a) $\text{Li}_9\text{YI}_{12}$ and (c) Li_4YI_7 . The experimental profile is shown in blue crosses; the green line denotes the calculated pattern; the difference of profile is shown in cyan, and calculated positions of the Bragg reflections is LiI . Crystal structure of (b) $\text{Li}_9\text{YI}_{12}$ and (d) Li_4YI_7 , respectively.

Based on the design of the substitution effect, one Y^{3+} could replace three Li^+ cations and introduce two intrinsic V' . $\text{Li}_9\text{YI}_{12}$ SE is refined showing 14.8% of V' and Li_4YI_7 possesses 24.8% of V' . Besides, the vacancy existence can be verified from X-ray absorption spectroscopy (XAS) results. **Figure 4.3a** compares the $\text{I } L_2$ -edge X-ray absorption near-edge spectra (XANES) of LiI , $\text{Li}_{x-3}\text{YI}_x$ ($x = 6, 7, \text{ and } 12$), and YI_3 . They are similar with each other in the spectra profile, but there is a small difference for the edge position. The second resonance show increased peak area from $\text{Li}_9\text{YI}_{12}$, Li_4YI_7 , and Li_3YI_6 , in which the corresponding vacancy number increased as well thus causing more

empty orbitals to transit. To fully reveal the effect of local environment changes on Li-ion transport kinetics, the local structure of $\text{Li}_9\text{YI}_{12}$, Li_4YI_7 are studied by X-ray total scattering. The PDF $G(r)$ along with the PDF fit results of Li_4YI_7 are shown in **Figure 4.3b**. The PDF fit result for the r range 2 – 30 Å shows little differences (wR=7.8%) compared with the experimental result, which means the refined average structure is consistent with that of Rietveld refinement of SXRD and the displacements have averaged out in for overall material. The first reasonable peak corresponding to molecular bonds is at 3.034 Å, resulting from the Y(Li) – I contributions. The distance is longer than Li – I interatomic distance in LiI (3.013 Å), further proving Y^{3+} occupies part of the Li site and expand the unit cell. The peak at 4.307 Å is of highest and symmetrical with narrow peak width, which be assigned as the nearest I – I and Y (Li) – Y (Li) interatomic distances. Since Li_4YI_7 crystalizes in rock salt structure and the local Y(Li)I_6^{3-} are regular octahedra, the nearest Y (Li) – Y (Li) and the nearest I – I in Y(Li)I_6^{3-} octahedra show the identical bonding distance. Yttrium K-edge Extended X-ray absorption fine structure is also employed to reveal the detailed structures of the Li_4YI_7 SEs (**Figure S4.5**). Phase-uncorrected radial distribution functions (RDF) after Fourier Transformed (FT) EXAFS for Li_4YI_7 is fitted in **Figure 4.3c**. Intensive signals caused by iodine signal scattering can be found at 2.6 Å. Y – I is fitted with a bonding distance of 3.047 Å and a coordination number of 6.5, which is close to the model we obtained. The Li site in Li_4YI_7 is distinguished by magic angle spinning nuclear magnetic resonance (^6Li MAS NMR), which is a sensitive technique to the atomic and electronic environment at the lithium site²⁸. As shown in **Figure 4.3d**, a single resonance at -3.9 ppm is observed, higher than that in the LiI at -4.6 ppm. This is caused by the lattice expansion of Li_4YI_7 . One Li site in bulk Li_4YI_7 can also be verified from the symmetric peak shape.

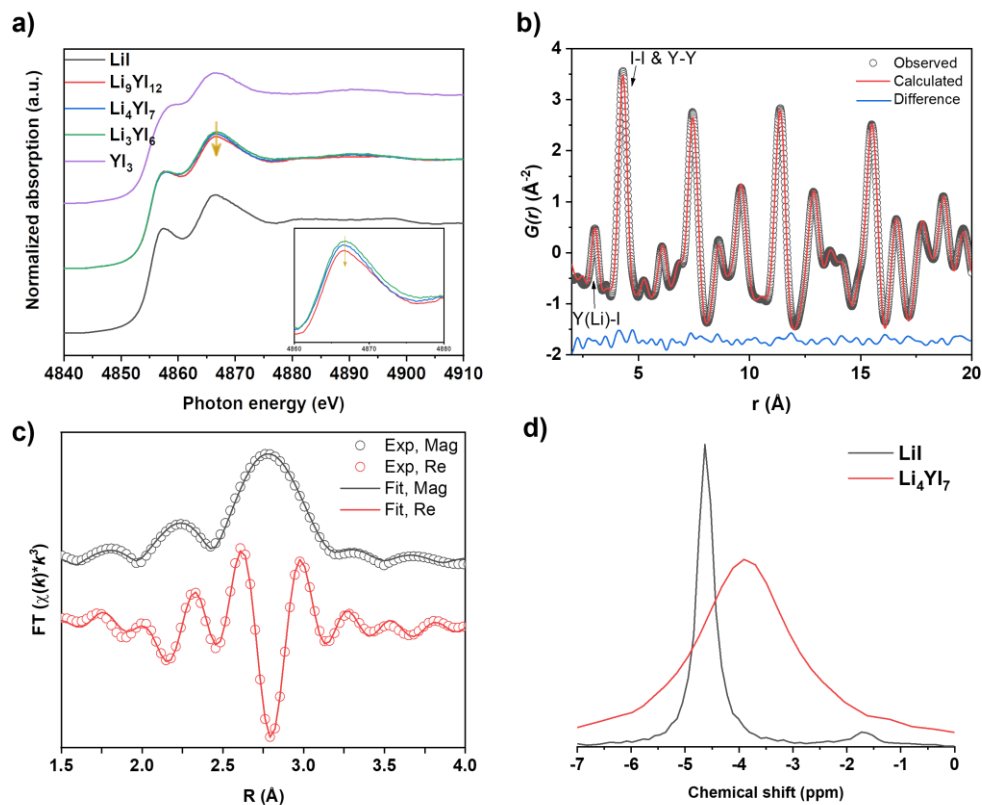


Figure 4.3 (a) I L_2 -edge XANES spectra for LiI, Li_{x-3}YI_x ($x = 6, 7,$ and 12), and YI₃. (b) PDF $G(r)$ and fitting results for Li₄YI₇. (c) Fitting results of the k^3 -weighted FT spectra of Li₄YI₇ at Y K -edge, showing the experimental data (grey circle) and Feff modeling (grey line) in terms of magnitude of FT and the real part of FT experimental data (red circle) and Feff²⁹ modeling (red line) traces. The R factor for this fitting is 0.003 and S_0^2 is set as 0.81. (d) ⁶Li MAS NMR spectra of Li₄YI₇ and LiI.

The chemical stability between Li₄YI₇ and Li metal was examined by testing the impedance evolution of symmetric cells at room temperature. Interval EIS were recorded under open-circuit conditions. As shown in **Figure 4.4a**, after setting for one hour, there are two semi-circles on the spectrum intercepted at 123 Ω (low-frequency impedance) and 163 Ω (medium-frequency impedance). The semi-circles at the low-frequency and medium-frequency represent the impedances of Li₄YI₇ SE and anode/ Li₄YI₇ SE interface³⁰, respectively. Therefore, a spontaneous interface generation between Li₄YI₇

and Li metal is proved. However, there are negligible changes of interface impedance during the rest-time resolved EIS measurement, which means the interface between Li and Li_4YI_7 is chemically stable. This result is consistent with the thermodynamic calculations reported previously²³. Then, we focused on investigating the electrochemical stability of the Li_4YI_7 electrolyte in our studies, in order to pander to the application of this new electrolyte for all-solid-state batteries. Although the oxidation limit of Li-Y-I SEs was inherently restricted by the oxidation of I^- to I_2 at approximately 3.4 V vs. Li/Li^+ , the cathodic stability was decent with negligible reduction current in our LSV measurements (**Figure S4.6** in Supporting information). We further examined the Li metal compatibility of the highly conductive Li_4YI_7 electrolytes via testing Li/ Li_4YI_7 /Li symmetric cells. As shown in **Figure 4.4b**, outstanding Li plating/stripping behavior was achieved under a moderate current density of 0.1 mA cm^{-2} and cut-off capacity of 0.1 mA cm^{-2} , which was able to stand over 1000 hours without any short circuits. It is noted that the decreased overpotential, in the initial stage was the result of the stabilized Li/electrolyte interface accompanied by the reconstruction of electrochemically induced interface composition. Nevertheless, the stable interface was still suggested by a steady overpotential of $\sim 10 \text{ mV}$ shown at $\sim 170 \text{ h}$ and $\sim 900 \text{ h}$, respectively. Even gradually increasing the current density to 1 mA cm^{-2} and cut-off capacity to 1 mAh cm^{-2} , highly reversible Li plating and stripping was performed as displayed in **Figure 4.4c**. XPS measurements were conducted to confirm the stable Li/ Li_4YI_7 interface as shown in **Figures 4.4d to 4.4f**. The Li 1s spectrum was located at the binding energy of $\sim 55.6 \text{ eV}$, which shows a considerable deviation to metallic Li (below 55 eV), indicating there was no Li dendrites at the interface. With regard to Y and I elements, typical 3d spectra were suggested well-defined shape without any additional heterogeneous compositions. Among which, Y 3d spectra at the interface showed reduced binding energy compared with that in the YI_3 reference. This is believed to associate with the electrostatic repulsion of coordinative Li as we discussed previously.

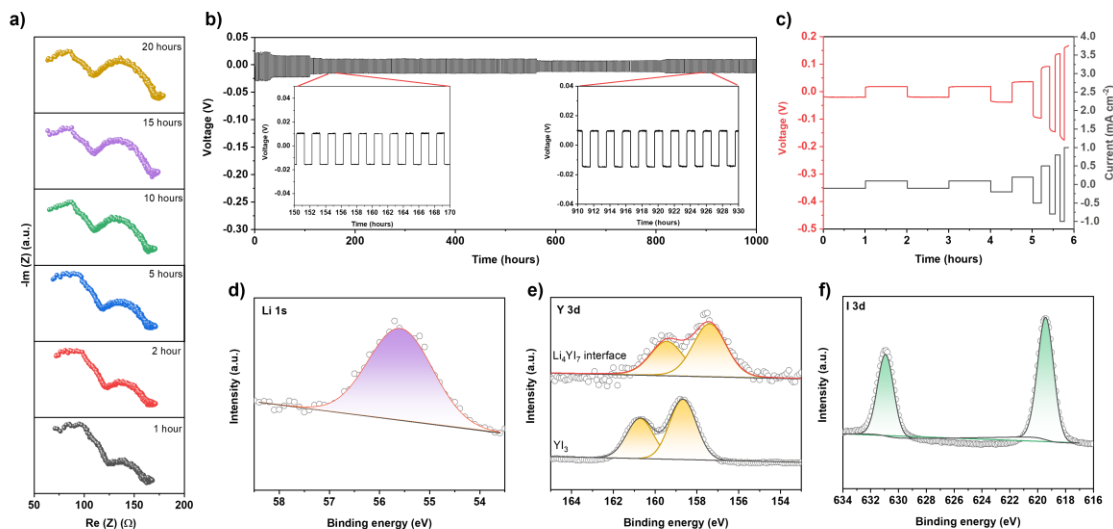


Figure 4.4 (a) Temporal EIS spectra of Li-Li symmetric cells using Li_4YI_7 ; (b) Cycling performance of $\text{Li}/\text{Li}_4\text{YI}_7/\text{Li}$ symmetric cell at 0.1 mA cm^{-2} and 0.1 mAh cm^{-2} ; (c) Critical current density testing from 0.1 to 1.1 mA cm^{-2} ; (d) Li 1s, (e) Y 3d, and (f) I 3d XPS spectrum of the lithium metal side after long cycling.

4.4 Conclusion

In summary, we prepared a series of $\text{Li}_{x-3}\text{YI}_x$ SEs with the room-temperature ionic conductivity up to $1.04 \times 10^{-3} \text{ S/cm}$ at room temperature. The relation between the realization of high ionic conductivity and regulation of average crystal structures as well as local symmetric structures is studied by Rietveld refinement SXRD patterns, PDF, and XAS. The enlarged diffusion pathway, soft anion, and cation vacancies in cubic $\text{Li}_{x-3}\text{YI}_x$ are all the features contribute the high ionic conductivity. Besides, XPS characterization on the cycled interfaces and aging EIS results confirmed a stable interface between Li and Li_4YI_7 . As a result, highly stable cycling performance stable over 1000 hours. This work presents a new superionic conductor with highly symmetric structure, which introduces a new avenue in developing new solid electrolytes for all solid-state batteries.

4.5 Acknowledgments

This research was supported by the Natural Sciences and Engineering Research Council of Canada (NSERC), the Canada Research Chair Program (CRC), the Canada Foundation for Innovation (CFI), Ontario Research Foundation (ORF), and the University of Western Ontario (UWO). The synchrotron research was performed at the Canadian Light Source, a national research facility of the University of Saskatchewan, which was supported by the CFI, NSERC, the National Research Council (NRC), the Canadian Institutes of Health Research (CIHR), the Government of Saskatchewan, and the University of Saskatchewan.

4.6 References

1. Randau, S., *et al.* Benchmarking the performance of all-solid-state lithium batteries. *Nature Energy* **5**, 259-270 (2020).
2. Gong, Y., *et al.* Three-dimensional atomic-scale observation of structural evolution of cathode material in a working all-solid-state battery. *Nature Communications* **9**, 1-8 (2018).
3. Schwietert, T. K., *et al.* Clarifying the relationship between redox activity and electrochemical stability in solid electrolytes. *Nature Materials* **19**, 428-435 (2020).
4. Chen, R. S., Li, Q. H., Yu, X. Q., Chen, L. Q., Li, H. Approaching Practically Accessible Solid-State Batteries: Stability Issues Related to Solid Electrolytes and Interfaces. *Chemical Reviews* **120**, 6820-6877 (2020).
5. Banerjee, A., Wang, X. F., Fang, C. C., Wu, E. A., Meng, Y. S. Interfaces and Interphases in All-Solid-State Batteries with Inorganic Solid Electrolytes. *Chemical Reviews* **120**, 6878-6933 (2020).
6. Cao, D. X., Sun, X., Li, Q., Natan, A., Xiang, P. Y., Zhu, H. L. Lithium Dendrite in All-Solid-State Batteries: Growth Mechanisms, Suppression Strategies, and Characterizations. *Matter* **3**, 57-94 (2020).
7. Krauskopf, T., Richter, F. H., Zeier, W. G., Janek, J. Physicochemical Concepts of the Lithium Metal Anode in Solid-State Batteries. *Chemical Reviews* **120**, 7745-7794 (2020).

8. Rehnlund, D., *et al.* Lithium trapping in alloy forming electrodes and current collectors for lithium based batteries. *Energy & Environmental Science* **10**, 1350-1357 (2017).
9. Han, X. G., *et al.* Negating interfacial impedance in garnet-based solid-state Li metal batteries. *Nature Materials* **16**, 572-579 (2017).
10. Suyama, M., Kato, A., Sakuda, A., Hayashi, A., Tatsumisago, M. Lithium dissolution/deposition behavior with Li₃PS₄-LiI electrolyte for all-solid-state batteries operating at high temperatures. *Electrochimica Acta* **286**, 158-162 (2018).
11. Jackson, B. J. H., Young, D. A. Ionic Conduction in Pure and Doped Single-Crystalline Lithium Iodide. *Journal of Physics and Chemistry of Solids* **30**, 1973-1976 (1969).
12. Schlaikjer, C. R., Liang, C. C. Ionic Conduction in Calcium Doped Polycrystalline Lithium Iodide. *Journal of The Electrochemical Society* **118**, 1447 (1971).
13. Asano, T., Sakai, A., Ouchi, S., Sakaida, M., Miyazaki, A., Hasegawa, S. Solid Halide Electrolytes with High Lithium-Ion Conductivity for Application in 4 V Class Bulk-Type All-Solid-State Batteries. *Advanced Materials* **30**, 1803075 (2018).
14. Li, X. N., *et al.* Water-Mediated Synthesis of a Superionic Halide Solid Electrolyte. *Angewandte Chemie-International Edition* **58**, 16427-16432 (2019).
15. Li, X. N., *et al.* Progress and perspectives on halide lithium conductors for all-solid-state lithium batteries. *Energy & Environmental Science* **13**, 1429-1461 (2020).
16. Liang, J. W., *et al.* Site-Occupation-Tuned Superionic Li_(x)ScCl_(3+x)Halide Solid Electrolytes for All-Solid-State Batteries. *Journal of the American Chemical Society* **142**, 7012-7022 (2020).
17. Kaup, K., *et al.* A Lithium Oxythioborosilicate Solid Electrolyte Glass with Superionic Conductivity. *Advanced Energy Materials* **10**, 1902783 (2020).
18. Li, X. N., *et al.* Air-stable Li₃InCl₆ electrolyte with high voltage compatibility for all-solid-state batteries. *Energy & Environmental Science* **12**, 2665-2671 (2019).

19. Wang, K., *et al.* A cost-effective and humidity-tolerant chloride solid electrolyte for lithium batteries. *Nature Communications* **12**, 1-11 (2021).
20. Kwak, H., *et al.* New Cost-Effective Halide Solid Electrolytes for All-Solid-State Batteries: Mechanochemically Prepared Fe³⁺-Substituted Li₂ZrCl₆. *Advanced Energy Materials* **11**, 2003190 (2021).
21. Zhou, L. D., Kwok, C. Y., Shyamsunder, A., Zhang, Q., Wu, X. H., Nazar, L. F. A new halospinel superionic conductor for high-voltage all solid state lithium batteries. *Energy & Environmental Science* **13**, 2056-2063 (2020).
22. Schlem, R., Bernges, T., Li, C., Kraft, M. A., Minafra, N., Zeier, W. G. Lattice Dynamical Approach for Finding the Lithium Superionic Conductor Li₃ErI₆. *Acs Applied Energy Materials* **3**, 3684-3691 (2020).
23. Xu, Z. M., Chen, X., Liu, K., Chen, R. H., Zeng, X. Q., Zhu, H. Influence of Anion Charge on Li Ion Diffusion in a New Solid-State Electrolyte, Li₃LaI₆. *Chemistry of Materials* **31**, 7425-7433 (2019).
24. Abdessedek Lachgar, D. S. D., Peter K. Dorhout, and John D. Corbett. Synthesis and properties of two novel line phases that contain linear scandium chains, LiScI₃ and Na_{0.5}ScI₃. **30**, 3321-3326 (1991).
25. Plass, M. A., Bette, S., Dinnebier, R. E., Lotsch, B. V. Enhancement of Superionic Conductivity by Halide Substitution in Strongly Stacking Faulted Li₃HoBr_{6-x}I_x Phases. *Chemistry of Materials* **34**, 3227-3235 (2022).
26. Poulsen, F. W. Ionic-Conductivity of Solid Lithium Iodide and Its Monohydrate. *Solid State Ionics* **2**, 53-57 (1981).
27. Chandler, P. J., Lilley, E. Ionic-Conductivity of Single-Crystals of 6nacl . Cdcl₂ Suzuki Phase. *Physica Status Solidi a-Applied Research* **66**, 183-187 (1981).
28. Wang, Y. F., Guo, X. D., Greenbaum, S., Liu, J., Amine, K. Solid electrolyte interphase formation on lithium-ion electrodes - A Li-7 nuclear magnetic resonance study. *Electrochemical and Solid State Letters* **4**, A68-A70 (2001).
29. Ravel, B., Newville, M. ATHENA, ARTEMIS, HEPHAESTUS: data analysis for X-ray absorption spectroscopy using IFEFFIT. *Journal of Synchrotron Radiation* **12**, 537-541 (2005).

30. Riegger, L. M., Schlem, R., Sann, J., Zeier, W. G., Janek, J. Lithium-Metal Anode Instability of the Superionic Halide Solid Electrolytes and the Implications for Solid-State Batteries. *Angewandte Chemie-International Edition* **60**, 6718-6723 (2021).

4.7 Supporting information

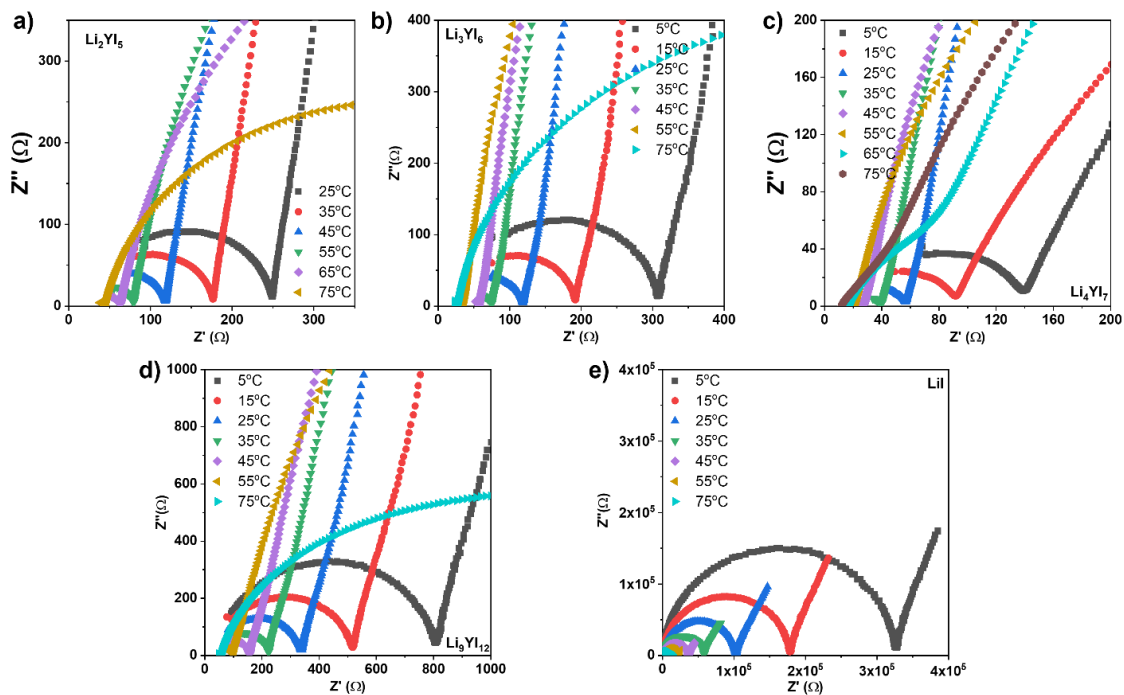


Figure S4.1 Nyquist plots for the $\text{Li}_{x-3}\text{YI}_x$ SEs and LiI at various temperatures.

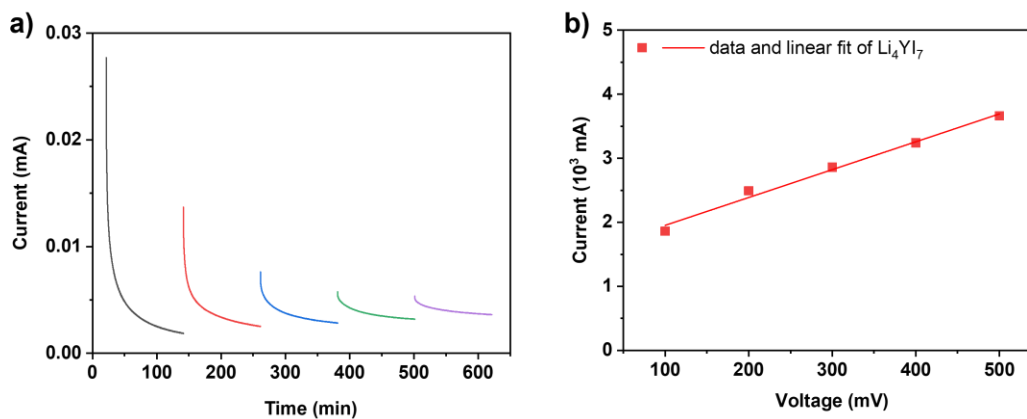


Figure S4.2 (a) DC polarization curves of Li_4YI_7 using symmetric cell configuration at different voltages from 100 to 500 mV. (b) Equilibrium current response of Li_4YI_7 symmetric cell at the corresponding voltages.

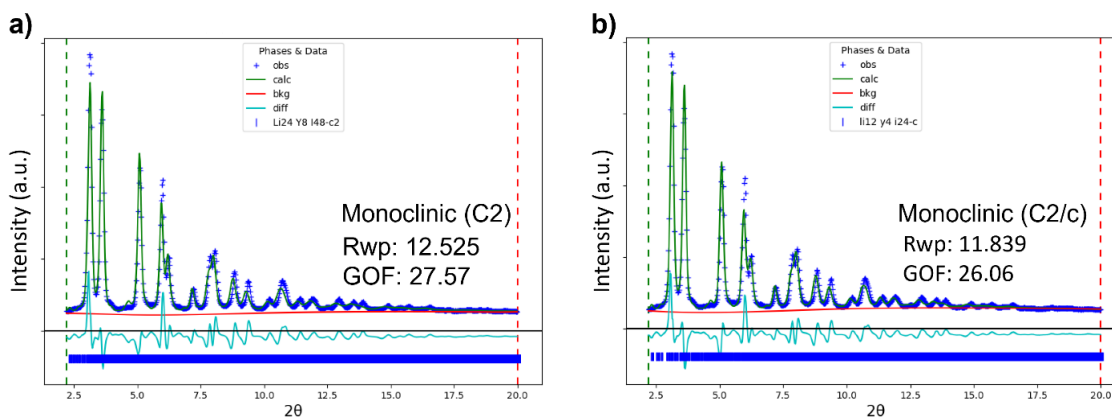


Figure S4.3 Comparison of refinement of $\text{Li}_9\text{YI}_{12}$ against the collected synchrotron X-ray diffraction data using the different possible space groups.

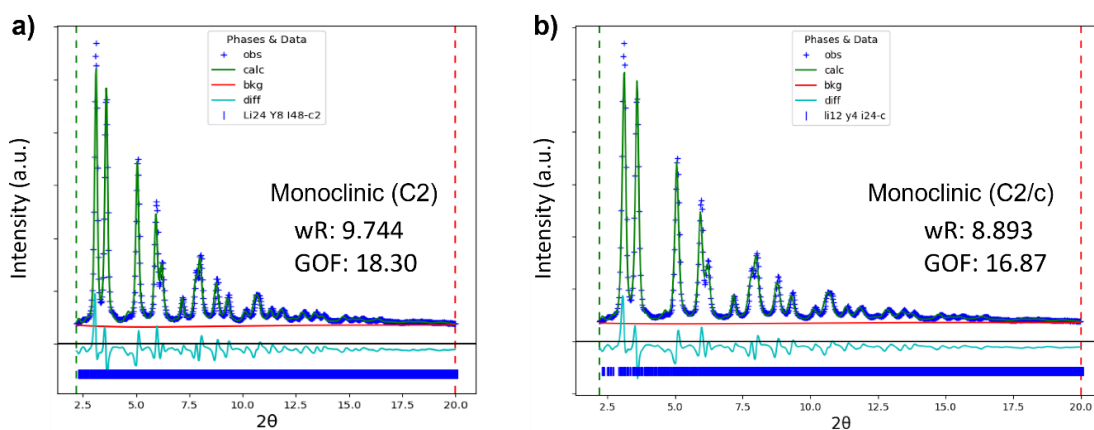


Figure S4.4 Comparison of refinement of Li_4YI_7 against the collected synchrotron X-ray diffraction data using the different possible space groups.

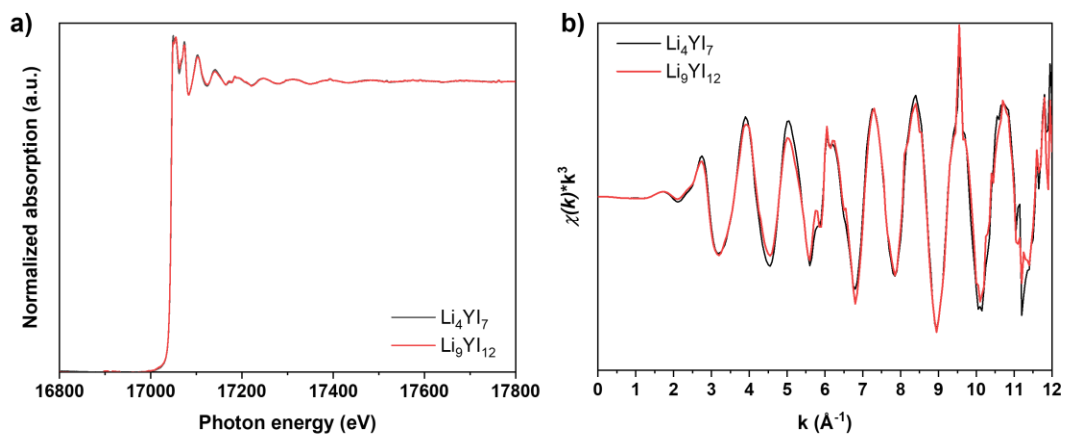


Figure S4.5 (a) XANES and (b) EXAFS of Li_4YI_7 and $\text{Li}_9\text{YI}_{12}$ SEs at Y K-edge.

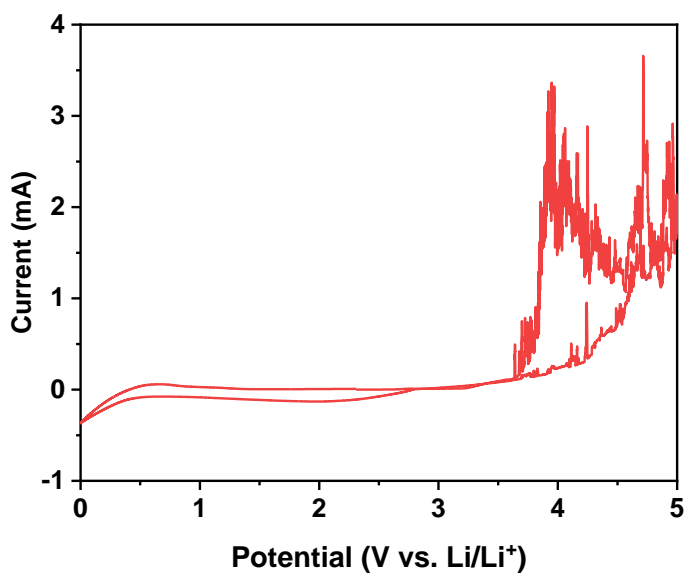


Figure S4.6 LSV analysis of the Li_4YI_7 SE in a configuration of carbon black- $\text{Li}_4\text{YI}_7//\text{Li}_4\text{YI}_7//\text{Li}_3\text{PS}_4//\text{Li}$ from the open-circuit voltage (OCV) $\rightarrow 5\text{ V} \rightarrow 0\text{ V}$.

Table S4.1 Crystallographic data of Li₉YI₁₂ and corresponding refined parameters

Compound	Li ₉ YI ₁₂
Space Group	Fm-3m
a, (Å)	6.053
V, Å ³	221.774708
2θ interval,°	2.5 - 20
Rwp,%	2.86
X-Ray radiation	Photon energy = 35 keV

Table S4.2 Rietveld analysis results for the SXRD pattern of Li₉YI₁₂

Atom	x	y	z	OCC.	B	Site	Sym.
Li	0.00000	0.00000	0.00000	0.778	0.026	4a	m-3m
I	0.50000	0.50000	0.50000	1	0.01	4b	m-3m
Y	0.00000	0.00000	0.00000	0.074	0.026	4a	m-3m

Table S4.3 Crystallographic data of Li₄YI₇ and corresponding refined parameters

Compound	Li ₄ YI ₇
Space Group	Fm-3m
a, (Å)	6.0911
V, Å ³	225.988966
2θ interval, °	2.5 - 20
Rwp, %	2.26
X-Ray radiation	Photon energy = 35 keV

Table S4.4 Rietveld analysis results for the SXRD pattern of Li₄YI₇

Atom	x	y	z	OCC.	B	Site	Sym.
Li	0.00000	0.00000	0.00000	0.629	0.003	4a	m-3m
I	0.50000	0.50000	0.50000	1	0.01	4b	m-3m
Y	0.00000	0.00000	0.00000	0.123	0.003	4a	m-3m

Chapter 5

5 New superionic lithium oxychloride glasses

A high-performance solid electrolyte (SE) is vital to ensure the high energy density, fast charging capability, and a wide operating temperature range for all-solid-state Li-ion batteries (ASSLIBs). Compared to the extensively researched crystalline oxide- and halide-based SEs, the promising possibilities of amorphous SEs with high ionic conductivity and good electrochemical stability are less discussed. Herein, a new family of amorphous SEs, $x\text{Li}_2\text{O-MCl}_y$ ($M = \text{Ta}$ and Hf), synthesized by one-step ball-milling method, are reported. A range of $x\text{Li}_2\text{O-TaCl}_5$ ($x = 1.2\text{--}1.8$) glassy SEs achieved high ionic conductivities above $6.0 \times 10^{-3} \text{ S cm}^{-1}$ and up to $6.6 \times 10^{-3} \text{ S cm}^{-1}$ at room temperature (RT); the $x\text{Li}_2\text{O-HfCl}_4$ analogues also show favorable room-temperature (RT) ionic conductivities up to $1.97 \times 10^{-3} \text{ S cm}^{-1}$. The high ionic conductivity is related to the specific local environment of $x\text{Li}_2\text{O-MCl}_y$ glasses, in which M-centered polyhedrons with abundant terminal Cl form the basic structural units to allow the disordered Li sublattice and fast Li-ion diffusion. Benefiting from the high ionic conductivity and electrochemical stability of the $x\text{Li}_2\text{O-MCl}_y$ glassy SEs, ASSLIBs with $\text{LiNi}_{0.83}\text{Mn}_{0.06}\text{Co}_{0.11}\text{O}$ cathode show excellent RT battery performance over 300 cycles and retain a capacity retention above 80% at 1 C. Moreover, ASSLIBs can also exhibit a long-life of >300 cycles at 0.2 C at a low temperature (-10°C). This work provides a new class of promising SE candidates with an easy synthesis process, high ionic conductivities, good electrochemical stability, and feasibility at different operating temperatures, widening the practical application of ASSLIBs.

*A version of this chapter to be submitted.

5.1 Introduction

Along with the fast growing market of rechargeable electric vehicles (REVs), the development of all-solid-state Li-ion batteries (ASSLIBs) is of high expectations due to their promises of high safety, reliability, and high energy density.^{1,2} A key component for ASSLIBs is solid electrolyte (SE) which replaces the conventional flammable liquid electrolytes and can potentially enable the use of high-voltage cathodes and Li metal anode to boost the energy density.³ One of the essential requirements for a favorable SE is high ionic conductivity. SEs with particular long-range ordered crystalline structures have been shown to allow continuous and fast Li-ion conduction. For example, representative sulfide-based SEs, such as $\text{Li}_{5.5}\text{PS}_{4.5}\text{Cl}_{1.5}$,⁴ $\text{Li}_{6+x}\text{M}_x\text{Sb}_{1-x}\text{S}_5\text{I}$ ($\text{M} = \text{Si}, \text{Ge}, \text{Sn}$),⁵ $\text{Li}_{10}\text{GeP}_2\text{S}_{12}$,⁶ and $\text{Li}_{9.54}\text{Si}_{1.74}\text{P}_{1.44}\text{S}_{11.7}\text{Cl}_{0.3}$,⁷ exhibit attractive ionic conductivities in the order of $10^{-2} \text{ S cm}^{-1}$. Other types of SEs including oxide-based SEs (e.g., perovskite $\text{Li}_x\text{La}_{(2-x)/3}\text{TiO}_3$ ⁸, NASICON $\text{LiTi}_2(\text{PO}_4)_3$ ⁹, and garnet $\text{Li}_7\text{La}_3\text{Zr}_2\text{O}_{12}$ ^{10,11}) and halide-based SEs (e.g., ternary Li-M-Cl system, $\text{M} = \text{Y}, \text{In}, \text{Sc}$ ^{12,13,14,15}) also demonstrate superionic conductivities of 10^{-4} – $10^{-3} \text{ S cm}^{-1}$. While the ion conduction mechanisms of crystalline SEs are widely studied to provide guidance for the search of new superionic conductors, some amorphous SEs also show good potentials.¹⁶

Early researches for glassy SEs have been reported since the 1960s.¹⁷ Glassy/amorphous SEs show the primary advantages of softness, easy fabrication, free of grain boundaries, wider compositional variations, and isotropic ionic conduction,¹⁷ which are expected to compensate the drawbacks of some crystalline SEs with high grain boundary resistance, poor processibility, and high cost. Despite the diligent efforts, the research for glassy SEs has been proceeding slowly. One major challenge is that the ionic conductivities of glassy SEs are much lower than those of the typical crystalline SEs. Another challenge is the lack of long-range periodicity that makes it difficult to understand the long-range ion conduction in glasses. There is no established universal theory for structure modeling and ionic diffusivity prediction for amorphous materials.¹⁸ Therefore, the different types of reported glassy SEs have their own advantages and disadvantages. The sulfide-based glassy SEs, such as $\text{Li}_2\text{S-P}_2\text{S}_5$ ¹⁹ and $\text{Li}_2\text{S-SiS}_2$ ²⁰, show decent ionic conductivities around $10^{-4} \text{ S cm}^{-1}$, but their narrow electrochemical stability window (reduction limit of about

1.5 V vs. Li⁺/Li and oxidation limit of about 2.5 V vs. Li⁺/Li)^{21, 22} and poor electrode compatibility²³ can significantly limit their application in ASSLIBs. Oxide-based glassy SEs (such as Li₂O-MO_x, M = Si, B, P, Ge, *etc.*,^{24, 25, 26, 27} and Lipon²⁸) exhibit improved electrochemical and chemical stabilities compared to the sulfide compounds, but their poor ionic conductivities of 10⁻⁹–10⁻⁶ S cm⁻¹ at room temperature (RT) are far way from the benchmark (10⁻³ S/cm) for bulk-type ASSLIBs²⁹. Nevertheless, if glassy SEs were to be competitive with the crystalline SEs, both superionic conductivity and good compatibility with favorable oxide cathodes are required for use in ASSLIBs.

Herein, we report a family of lithium oxychloride glassy SEs (xLi₂O-MCl_y, M = Ta and Hf) for ASSLIBs. One-step ball-milling method can easily yield the desired products in an amorphous state. The optimized 1.6Li₂O-TaCl₅ glassy SE possessed a high RT ionic conductivity of 6.6 × 10⁻³ S cm⁻¹ surpassing that of all the other developed glassy SEs. Similarly high ionic conductivities can be maintained within the glassy formation region for xLi₂O-TaCl₅ (x = 1.1–1.8). The optimized 1.5Li₂O-HfCl₄ glass also exhibited a good ionic conductivity of 1.97 × 10⁻³ S cm⁻¹ at RT. The local structures of superionic xLi₂O-TaCl₅ glassy SEs are mainly TaCl₄O trigonal bipyramid, and some of the TaCl₃O₂ for xLi₂O-TaCl₅ with more Li₂O content. M–Cl bond is predominant in high ionic conductive xLi₂O-MCl_y glassy SEs, and the ionic conductivity drops for 2Li₂O-MCl_y with more electronegative M–O. In addition, the xLi₂O-MCl_y glasses show good compatibility with different favorable oxide cathodes without any additional cathode coatings. ASSLIBs using xLi₂O-MCl_y glassy SEs showed excellent long-life cycling performance at both -10 °C and RT.

5.2 Experimental section

Synthesis of xLi₂O-MCl_y (M = Ta, Hf, Nb, or Zr) solid electrolytes:

TaCl₅ (Sigma Aldrich, 99.99 %), HfCl₄ (Sigma Aldrich, 98%), and Li₂O (Alfa Aesar, 99.5%) were used as the raw materials. The starting materials for each compound were mixed accordingly with a stoichiometric ratio in an argon-filled glovebox (H₂O, O₂ <0.1 ppm). The resulting mixture (~1g) was then placed in a zirconia ball milling pot along with 40 g zirconia balls. Low-speed ball milling (100 rpm for 5 h) was first run to ensure

all the precursors mixed well, followed by a high-speed ball milling process of 500 rpm for 10 h. Next, the ball-milled products were transferred into the glovebox for further use.

Ionic conductivity measurement

Ionic conductivity of as-prepared SEs was evaluated using electrochemical impedance spectroscopy (EIS) with two stainless steel rods as blocking electrodes. The SE powders (100~150 mg) were cold-pressed into pellets under ~400 Mpa. The thickness of each pellet was provided in Nyquist plot figures in supporting information. EIS measurements were performed using a multichannel potentiostat 3/Z (German VMP3). The applied frequency range is 1 Hz ~ 7 MHz and the voltage amplitude is 20 mV.

Characterization methods

Lab-based XRD measurements were performed on Bruker AXS D8 Advance with Cu K α radiation ($\lambda = 1.5406 \text{ \AA}$). Kapton tape was used to cover the sample holder to prevent from the air exposure. Raman spectra were measured with a HORIBA Scientific LabRAM HR

Raman spectrometer operated under laser beam at 532 nm. Electrolyte powders were attached on a carbon tape and covered by a transparent glass for the test.

XAS data were collected at the 44A beamline of Taiwan Photon Source (TPS) of the National Synchrotron Radiation Research Center (NSRRC) in Taiwan. XAS spectra were recorded in transmission mode and the data were processed with Athena and Artemis softwares.

Synchrotron-based 2D XRD patterns of the samples were collected at the VESPERS beamline at Canadian Light Source (CLS) in Canada (07B2-1, 6 – 30keV). Profex and ALBULA softwares were used to process the data.

^7Li ss-NMR SLR measurements were performed on a Varian Infinity Plus wide - bore NMR spectrometer equipped with an Oxford wide-bore magnet (Bo $\frac{1}{4}$ 9.4 T). The ^7Li Larmor frequency was 155.248 MHz. The $\pi/2$ and π pulse length were determined to be

2.3 and 4.5 μs , respectively. Chemical shifts were referenced with respect to a 1.0 M LiCl solution. The electrolyte sample was sealed in custom-made Teflon tubes ($\phi = 4.7$ mm) in an argon-filled glovebox (H_2O , $\text{O}_2 < 0.1$ ppm). The ^7Li spin-lattice relaxation times (T_1) at different temperatures were determined using an inversion-recovery NMR experiment. The testing temperature ranges from 22 $^\circ\text{C}$ to 180 $^\circ\text{C}$.

Assembly and electrochemical characterizations of ASSLBs

LSV Test: a glassy SE powder was manually mixed well with carbon black (CB) in a weight ratio of 8:2. Then, 60 mg of the glassy SE powder was cold-pressed into a pellet under a pressure of 300 MPa. 10 mg of SE/CB mixture was uniformly placed on one side of the glassy SE pellet as working electrode and compressed again under the same pressure. After that, Li foil (China Energy Lithium Co. LTD) was attached on the other side of the pellet as both counter and reference electrode. In order to avoid the incompatibility between the glassy SE and metallic Li, a thinner layer of $\text{Li}_6\text{PS}_5\text{Cl}$ sulfide SE (40 mg) was inserted between the glassy SE pellet and Li before Li foil was added. To ensure an intimate contact between layer by layer, the cell was pressed under a pressure of 120 MPa before taking out of the glovebox. The LSV electrochemical stability window tests were conducted using versatile multichannel potentiostat 3/Z (VMP 3) with a scan range from open-circuit voltage (OCV) to 6 V (vs Li/Li $^+$, positive scan) and OCV to 0 V (vs Li/Li $^+$, negative scan), respectively. The scan rate was 0.1 mV s $^{-1}$.

Full-cell Test: 60 mg of $1.6\text{Li}_2\text{O-TaCl}_5$ and $1.5\text{Li}_2\text{O-HfCl}_4$ glassy SEs were pressed at ~ 300 MPa to form a solid electrolyte layer (10 mm diameter). 10 mg of glassy SE/LCO composite (3:7 mass ratio) was uniformly spread onto the surface of the one side of electrolyte layer and pressed with ~ 360 MPa for 5 minutes. Subsequently, Li-In alloy was placed on the other side of the electrolyte layer and pressed by ~ 120 MPa for 3 minutes. To prevent the direct contact between glassy SE and Li-In. 40 mg of LGPS pellet was served as the interlayer at the anode side. The LGPS electrolyte was purchased from MSE supplies LLC, showing a high RT ionic conductivity of 6.31×10^{-3} S cm $^{-1}$ with cold-pressed pellet. The obtained internal pellet cell was sandwiched between two

stainless-steel rods as current collectors and sealed in the mold cell for various electrochemical tests. The voltage window was set as 1.9 ~ 3.6 V (vs. Li-In), and various constant current densities were applied to evaluate cycling stability and rate performance. All cell fabrication processes were carried out in an Ar-filled glove box (H_2O , $\text{O}_2 < 0.1$ ppm).

5.3 Results and Discussion

The glassy $x\text{Li}_2\text{O-TaCl}_5$ SEs were prepared by simply ball-milling Li_2O and TaCl_5 at various stoichiometric ratios. Lab-based X-ray diffraction patterns (XRD) of the as-prepared $x\text{Li}_2\text{O-TaCl}_5$ ($1 \leq x \leq 2$) are shown in **Figure 5.1a**. When $x = 1$, the pattern was generally amorphous with a few broad XRD peaks due to impurities (**Figure S5.1a**). Slightly increasing the molar ratio of $\text{Li}_2\text{O/TaCl}_5$ to 1.1 led to the formation of pure $1.1\text{Li}_2\text{O-TaCl}_5$ glass, which shows a smooth diffraction feature without any additional peaks (**Figure S5.1b**). Interestingly, further increase of the Li_2O content ($1.1 \leq x \leq 1.8$) did not change the amorphous nature of $x\text{Li}_2\text{O-TaCl}_5$ glasses. As proved by synchrotron-based 2D diffraction patterns as shown in **Figure 5.1b**, the similarly vague halos were recorded for the selected $1.1\text{Li}_2\text{O-TaCl}_5$, $1.6\text{Li}_2\text{O-TaCl}_5$, and $1.8\text{Li}_2\text{O-TaCl}_5$ samples, indicating mainly amorphous content for the $x\text{Li}_2\text{O-TaCl}_5$ glasses except for few LiCl impurity which can be detected by high-energy XRD. Therefore, the glass formation region for the $x\text{Li}_2\text{O-TaCl}_5$ system ranged from $1.1 \leq x \leq 1.8$. For a higher feeding ratio of Li_2O ($x \geq 1.9$), LiCl impurity appeared and the LiCl content increased along with the increase of Li_2O (**Figure 5.1a**). In addition to the $x\text{Li}_2\text{O-TaCl}_5$ glasses, the lithium oxychloride glasses family can be extended to the other systems involving high-valence transition metal chlorides, for example, using Hf^{4+} instead of Ta^{5+} . **Figure 5.1c** depicts the lab-based XRD patterns for a series of $x\text{Li}_2\text{O-HfCl}_4$ samples. In comparison with the $x\text{Li}_2\text{O-TaCl}_5$ glasses, the formation of amorphous $x\text{Li}_2\text{O-HfCl}_4$ solids was more difficult under the similar ball-milling conditions. Only a ratio of $1.5\text{Li}_2\text{O-HfCl}_4$ exhibited a relatively high amorphous content among all the prepared $x\text{Li}_2\text{O-HfCl}_4$ (**Figure 5.1d**). For other $x\text{Li}_2\text{O-HfCl}_4$ compositions, precipitations of crystalline impurities can be easily observed (**Figure 5.1c**).

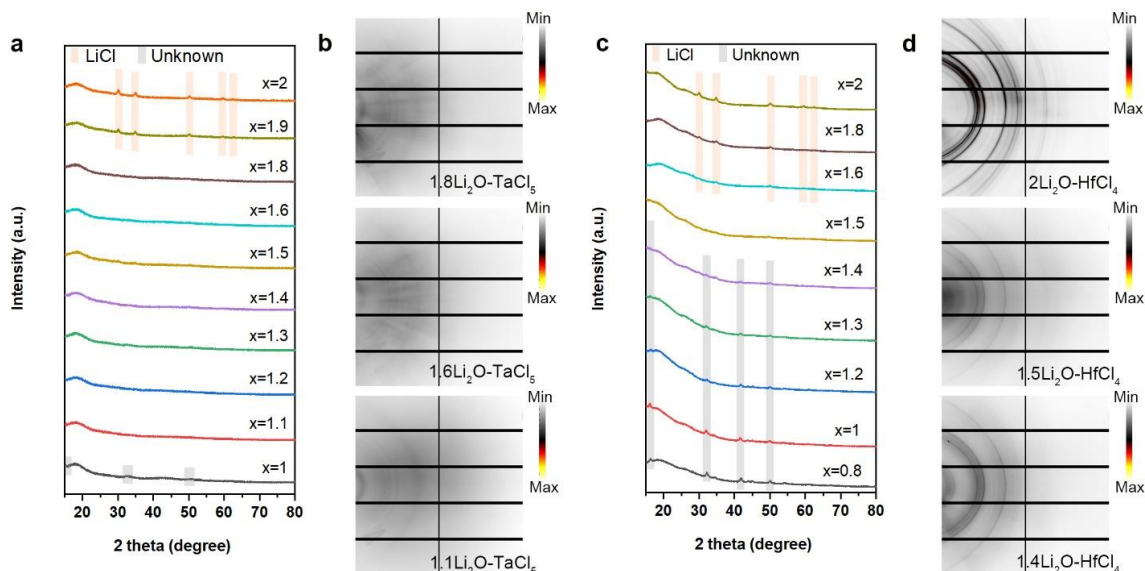


Figure 5.1 Powder XRD diffraction patterns for the as-prepared (a) $x\text{Li}_2\text{O}-\text{TaCl}_5$ ($1 \leq x \leq 2$) and (c) $x\text{Li}_2\text{O}-\text{HfCl}_4$ ($0.8 \leq x \leq 2$) samples. Synchrotron-based 2D diffraction patterns of selected (b) $x\text{Li}_2\text{O}-\text{TaCl}_5$ ($x = 1.8, 1.6,$ and 1.1) and (d) $x\text{Li}_2\text{O}-\text{HfCl}_4$ ($x = 2, 1.5,$ and 1.4) samples. The 2D diffraction data were recorded on a Pilatus 1M detector with a photon energy of 13 keV (0.9537 \AA) at the VESPERS beamline of Canadian Light Source (CLS).

The ionic conductivities of the new glassy SEs were determined by electrochemical impedance spectroscopy (EIS). The $x\text{Li}_2\text{O}-\text{TaCl}_5$ ($x = 1.0, 1.1, 1.2, 1.4, 1.6, 1.8, 1.9,$ and 2.0) powders were cold-pressed into pellets for measurements. Their corresponding temperature-dependent EIS plots are shown in **Figure S5.2**. **Figure 5.2a** shows the extracted conductivity values at RT. When the molar ratio of Li_2O increased from 1 to 1.1, a surge of ionic conductivity (from 0.41 to $5.3 \times 10^{-3} \text{ S cm}^{-1}$) can be observed. Remarkably, the $x\text{Li}_2\text{O}-\text{TaCl}_5$ ($1.1 \leq x \leq 1.8$) glasses retained similarly high ionic conductivities of around $6 \times 10^{-3} \text{ S cm}^{-1}$ which is at the top level among all other developed SEs (**Table S5.1**). The highest RT ionic conductivity was $6.6 \times 10^{-3} \text{ S cm}^{-1}$ for an optimized composition of $1.6\text{Li}_2\text{O}-\text{TaCl}_5$. The high ionic conductivity of the pure $x\text{Li}_2\text{O}-\text{TaCl}_5$ glasses suggested favorable local structures for Li-ion mobility. The activation energies determined from Arrhenius plots of $x\text{Li}_2\text{O}-\text{TaCl}_5$ glasses show lower

values from 0.241 eV to 0.277 eV (**Figure 5.2b** and **Figure S5.3**). Meanwhile, **Figure 5.2c** compares the RT ionic conductivities extracted from the Nyquist plots (**Figure S5.4**) for $x\text{Li}_2\text{O-HfCl}_4$ system ($x = 0.8, 1, 1.2, 1.4, 1.5, 1.6, 1.8, 2$). Similarly, the $1.5\text{Li}_2\text{O-HfCl}_4$ glass in mostly amorphous state showed the highest ionic conductivity ($1.97 \times 10^{-3} \text{ S cm}^{-1}$) and a low activation energy (0.328 eV) among the $x\text{Li}_2\text{O-HfCl}_4$ series (**Figure 5.2d** and **Figure S5.5**).

In order to precisely track the Li-ion mobility in $x\text{Li}_2\text{O-MCl}_y$ glasses, solid-state nuclear magnetic resonance (SSNMR) spectroscopy was adopted to provide a SE sample with the nuclide-specific information on structure and dynamics. First, qualitative information on Li-ion mobility^{30, 31} of the $x\text{Li}_2\text{O-TaCl}_5$ and $x\text{Li}_2\text{O-HfCl}_4$ systems was provided via ^7Li SSNMR temperature-dependent line-shape analyses. The selected ^7Li SSNMR spectra of the $1.6\text{Li}_2\text{O-TaCl}_5$ and $1.5\text{Li}_2\text{O-HfCl}_4$ samples in a temperature range of 293–443 K are displayed in **Figure S5.6a** and **b**, respectively. For both samples, a strong resonance corresponding to the central transition (CT) of ^7Li ($I = 3/2$) was observed in each spectrum. The peaks due to the central transition were narrow. The linewidths (**Figure 5.2e**) were less than 1 kHz (i.e. around 450 Hz for $1.6\text{Li}_2\text{O-TaCl}_5$ and between 520-610 Hz for $1.5\text{Li}_2\text{O-HfCl}_4$) without significant variations in the temperature range of 293–443 K, implying that both systems were in the extreme narrowing regime. Such observation seemed to suggest a narrow distribution of slightly different Li-ion jumping rates and, by extension, a distribution of Li diffusion pathways, which is consistent with the amorphous nature of the materials.

In addition, ^7Li NMR relaxation parameters such as T_1 and spin-lattice relaxation (SLR) time allowed us to quantitatively determine the Li-ion jumping rates and activation energies corresponding to short-range as well as long-range ion diffusions in bulk electrolytes.^{32, 33, 34} **Figure 5.2f** and **g** show the plots of $\ln(1/T_1)$ versus reciprocal temperature ($1/kT$) for $1.6\text{Li}_2\text{O-TaCl}_5$ and $1.5\text{Li}_2\text{O-HfCl}_4$, respectively. A $1/T_1$ maximum was reached for each system, corresponding to 358 and 378 K for $1.6\text{Li}_2\text{O-TaCl}_5$ and for $1.5\text{Li}_2\text{O-HfCl}_4$, respectively. The fact that the peak maximum of $1.6\text{Li}_2\text{O-TaCl}_5$ appeared at a lower temperature than $1.5\text{Li}_2\text{O-HfCl}_4$ suggested higher Li mobility in $1.6\text{Li}_2\text{O-TaCl}_5$.³⁵ Li-ion jump frequency can be deduced from the maximum condition

($\tau \cdot \omega_0 \approx 1$) at the relaxation rate peak.^{31, 33, 36, 37} Since the Larmor frequency of ^7Li at 9.4 T was 155.2 MHz, the Li-ion jump frequency ($1/\tau$) of $9.8 \times 10^8 \text{ s}^{-1}$ occurred at 358 and 378 K for the $1.6\text{Li}_2\text{O-TaCl}_5$ and the $1.5\text{Li}_2\text{O-HfCl}_4$, respectively. The activation energies, E_a^{HT} and E_a^{LT} , derived from the slopes of high- and low-temperature flanks were not equal. Specifically, for the $1.6 \text{Li}_2\text{O-TaCl}_5$ sample, the activation energies were $E_a^{\text{HT}} = 0.138 \text{ eV}$ and $E_a^{\text{LT}} = 0.047 \text{ eV}$, whereas the $E_a^{\text{HT}} = 0.119 \text{ eV}$ and $E_a^{\text{LT}} = 0.081 \text{ eV}$ for $1.5\text{Li}_2\text{O-HfCl}_4$. Generally, the E_a^{HT} and E_a^{LT} are related to by a relationship of $E_a^{\text{LT}} = (\beta - 1) E_a^{\text{HT}}$ where $1 < \beta \leq 2$. For uncorrelated isotropic diffusion described by the BPP (Bloembergen, Purcell and Pound) model, E_a^{HT} and E_a^{LT} are equal, corresponding to $\beta = 2^{16}$. In the present cases, β values were determined to be 1.34 and 1.68 for the $1.6\text{Li}_2\text{O-TaCl}_5$ and the $1.5\text{Li}_2\text{O-HfCl}_4$ samples, respectively, indicating structurally complex Li-ion conduction.^{37, 38, 39} And the native structural disorder of the two glassy samples was the major contributor towards the smaller E_a^{LT} values compared to those of E_a^{HT} .^{30, 39}

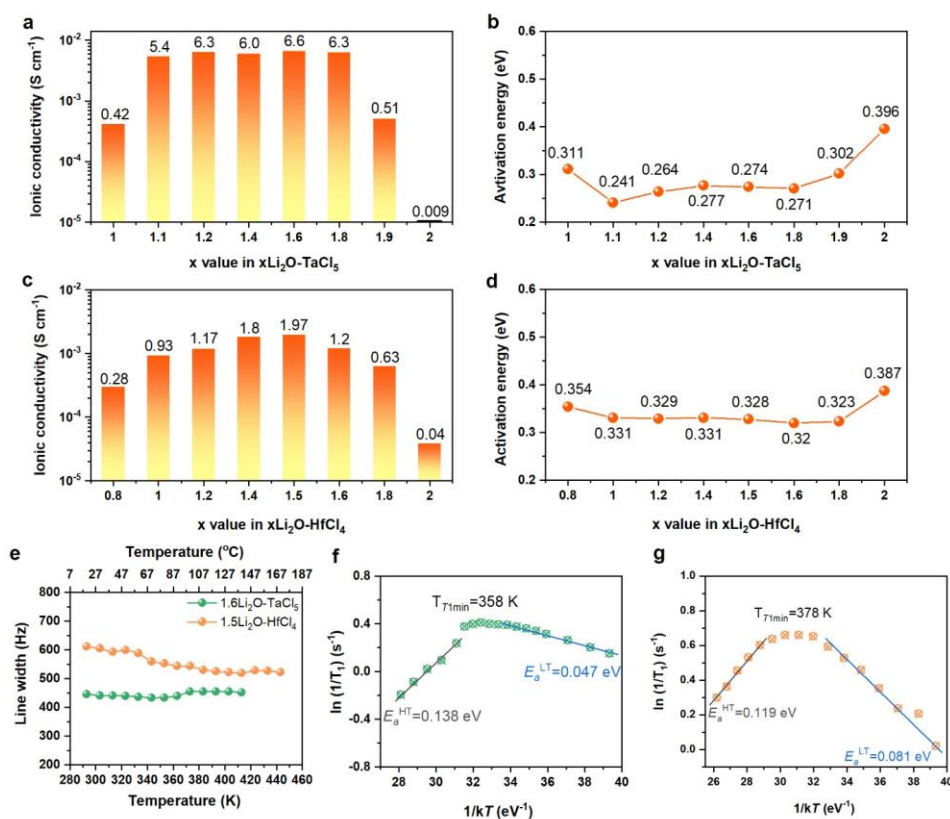


Figure 5.2 Comparison of RT ionic conductivities for selected (a) $x\text{Li}_2\text{O-TaCl}_5$ and (c) $x\text{Li}_2\text{O-HfCl}_4$ samples; extracted activation energy (E_a) from Arrhenius plots for (b)

$x\text{Li}_2\text{O-TaCl}_5$ and (d) $x\text{Li}_2\text{O-HfCl}_4$ samples. (e) Static ^7Li motional narrowing spectra of $1.6\text{Li}_2\text{O-TaCl}_5$ and $1.5\text{Li}_2\text{O-HfCl}_4$ between 293–443 K; temperature-dependent ^7Li SLR NMR rates for (c) $1.6\text{Li}_2\text{O-TaCl}_5$ and (f) $1.5\text{Li}_2\text{O-HfCl}_4$ samples measured in the laboratory frame of the reference. The Larmor frequency was 155.248 MHz.

Raman spectroscopy is used to identify the structural fingerprints by which species in $x\text{Li}_2\text{O-TaCl}_5$ and $x\text{Li}_2\text{O-HfCl}_4$ glasses. **Figure S5.7** depicts the Raman spectra of selected $x\text{Li}_2\text{O-TaCl}_5$ ($x = 1.2, 1.4, 1.6, 1.8, \text{ and } 2$). It is interesting to find that the bands at 180 cm^{-1} and 406 cm^{-1} for $x\text{Li}_2\text{O-TaCl}_5$ ($x = 1.2, 1.4, 1.6 \text{ and } 1.8$) corresponds to Ta–Cl vibrations in trigonal bipyramidal TaCl_5 ^{40, 41}, which implies a decomposition of $\text{Ta}_2\text{Cl}_{10}$ bi-octahedra to TaCl_5 trigonal bipyramid when introducing a moderate amount of Li_2O into TaCl_5 under high-energy ball-milling conditions. Further increasing Li_2O to $x = 2$ cause the disappearance of these Ta–Cl signals. In comparison with noticeable Ta–Cl features, Ta–O fingerprints are more broadened to show representative amorphous features of $x\text{Li}_2\text{O-TaCl}_5$. The fluctuating region from 580 to 890 cm^{-1} corresponds to the vibrational frequencies of Ta–O bonds in amorphous TaO_x .⁴² For Hf compounds, the Raman spectra of $1.5\text{Li}_2\text{O-HfCl}_4$ is flat without obvious peaks (**Figure S5.8**), which is capable of proving the amorphous nature of $1.5\text{Li}_2\text{O-HfCl}_4$ glass.

Then, X-ray absorption near-edge structure (XANES) and extended X-ray absorption fine structure (EXAFS) spectra were employed to investigate the atomic-scale chemical environment of amorphous $x\text{Li}_2\text{O-TaCl}_5$ and $x\text{Li}_2\text{O-HfCl}_4$ glasses. In the XANES spectra, since the white line (WL) at Ta L_3 -edge corresponds to the dipolar transition from 2p core levels to unoccupied Ta 5d states, the WL intensity and peak position increase when the oxidation state of Ta increases, and *vice versa*⁴². As depicted in **Figure 5.3a**, the XANES spectra of $x\text{Li}_2\text{O-TaCl}_5$ ($x = 1.2, 1.4, 1.6, 1.8$) possess a similar feature (9888 to 9898 eV) with that of the TaCl_5 . The absorption energy (E_0) at Ta L_3 -edge for $x\text{Li}_2\text{O-TaCl}_5$ is between 9879.4 eV (ref. Ta_2O_5) and 9877.3 eV (ref. TaCl_5), ascribing to oxidation of TaCl_5 when Li_2O added. EXAFS analyses provide detailed coordination and geometry information for $x\text{Li}_2\text{O-TaCl}_5$ glasses. **Figure 5.3b** shows Ta

L_3 -edge EXAFS of $x\text{Li}_2\text{O-TaCl}_5$ in k -space. The oscillation of four $x\text{Li}_2\text{O-TaCl}_5$ curves is almost identical except for some differences in medium k -range (4 to 8 \AA^{-1} , yellow area). The amplitude of the curves decreases along with the increase of x in $x\text{Li}_2\text{O-TaCl}_5$. At the same time, a gradual phase shift to low k can be observed for 1.4 $\text{Li}_2\text{O-TaCl}_5$, 1.6 $\text{Li}_2\text{O-TaCl}_5$, and 1.8 $\text{Li}_2\text{O-TaCl}_5$. This is a signal for disorder and elongation of Ta–Cl bonds caused by Ta–O bonding. To further resolve the coordination of Ta in $x\text{Li}_2\text{O-TaCl}_5$, phase-uncorrected radial distribution functions (RDF) after Fourier Transformed (FT) EXAFS and wavelet transformed (WT) EXAFS are conducted^{43, 44}. Based on the Ta–O ($k_{max} = 4.5 \text{\AA}^{-1}$) and Ta–Cl ($k_{max} = 7 \text{\AA}^{-1}$) scattering paths in referential TaCl_5 and Ta_2O_5 (**Figure 5.3d**), two distinguished color spots in each $x\text{Li}_2\text{O-TaCl}_5$ can be recognized as Ta–O and Ta–Cl scatterings locating at 1.4 \AA , 1.9 \AA , respectively (**Figure 3e to 3h**). Intensive Ta–O signals can be observed for 1.6 $\text{Li}_2\text{O-TaCl}_5$ and 1.8 $\text{Li}_2\text{O-TaCl}_5$. A gradual increase of Ta–Cl bond length in $x\text{Li}_2\text{O-TaCl}_5$ with larger x can be confirmed in **Figure 5.3c**. EXAFS fitting (**Figure S5.9**) provides a quantitative explanation about these changes in $x\text{Li}_2\text{O-TaCl}_5$ and the results are listed in **Table 5.1**. Consistent with FT-EXAFS and WT-EXAFS results, the nearest coordinated O around Ta increases from 1 in 1.2 $\text{Li}_2\text{O-TaCl}_5$ to almost 2 in 1.8 $\text{Li}_2\text{O-TaCl}_5$. At the same time, the number of nearest Ta–Cl bonds decreases but with longer bond length. More Li_2O in $x\text{Li}_2\text{O-TaCl}_5$ not only changes the O and Cl coordination around Ta, but also brings a structure disorder, which can be confirmed by an increased value of Debye-Waller factor (σ^2)⁴⁵. Despite of that, the overall coordination number (CN) nearest to Ta can be estimated as 5 for each of the $x\text{Li}_2\text{O-TaCl}_5$ compound ($x = 1.2, 1.4, 1.6, 1.8$), consistent with Raman results in **Figure S5.7**. Therefore, we can determine that the local structures in superionic $x\text{Li}_2\text{O-TaCl}_5$ glasses are mainly TaCl_4O trigonal bipyramid, and some of the TaCl_3O_2 for $x\text{Li}_2\text{O-TaCl}_5$ with more Li_2O content (**Figure 5.3i**). Besides, the possible connection of the smallest local structure unit in $x\text{Li}_2\text{O-TaCl}_5$ is also of interest. As shown in **Figure S5.10**, a noticeable Ta–Ta resonance at 12 \AA^{-1} can be found in WT-EXAFS figures for 1.4 $\text{Li}_2\text{O-TaCl}_5$, 1.6 $\text{Li}_2\text{O-TaCl}_5$, and 1.8 $\text{Li}_2\text{O-TaCl}_5$, similar with the Ta–Ta resonance in Ta_2O_5 . Combining with the Raman results, it is highly possible that TaCl_4O and TaCl_3O_2 share O to link with each other (**Figure 5.3j**).

Despite amorphous $x\text{Li}_2\text{O-TaCl}_5$ compounds ($x = 1.2, 1.4, 1.6, 1.8$) show differences in local structures, their ionic conductivity maintains almost the same level. In order to further investigate the relation of ionic conductivity and local structure in $x\text{Li}_2\text{O-TaCl}_5$, the XANES and EXAFS of $2\text{Li}_2\text{O-TaCl}_5$ and high ionic conductive $1.6\text{Li}_2\text{O-TaCl}_5$ and are compared in **Figure S5.11**. E_0 increases from 9878.2 eV ($1.6\text{Li}_2\text{O-TaCl}_5$) to 9878.5 eV ($2\text{Li}_2\text{O-TaCl}_5$). The WL intensity of $2\text{Li}_2\text{O-TaCl}_5$ also higher than that of the $1.6\text{Li}_2\text{O-TaCl}_5$ (**Figure S5.11a**). The effect of Ta-O scattering is distinct in both EXAFS (**Figure S5.11b**) and FT-EXAFS (**Figure S5.11c**) curves. $2\text{Li}_2\text{O-TaCl}_5$ shows a different oscillation feature, similar to that of the Ta_2O_5 before 8 \AA^{-1} . In FT-EXAFS, Ta-Cl bond (1.9 \AA) almost disappear which replaced by intensive Ta-O signals (1.4 \AA). Since this nearest Ta-Cl feature is predominant in high ionic conductive $x\text{Li}_2\text{O-TaCl}_5$ compounds ($x = 1.2, 1.4, 1.6, 1.8$), and the ionic conductivity drops for $2\text{Li}_2\text{O-TaCl}_5$ with more electronegative Ta-O, we can generally deduct that TaCl_4O and TaCl_3O_2 with Ta-Cl bond in amorphous $x\text{Li}_2\text{O-TaCl}_5$ contributes to a high ionic conductivity.

Other than $x\text{Li}_2\text{O-TaCl}_5$ compounds, the local structures of $x\text{Li}_2\text{O-HfCl}_4$ are also explored by XANES and EXAFS. **Figure S5.12** shows the comparison between $2\text{Li}_2\text{O-HfCl}_4$ and high ionic conductive $1.5\text{Li}_2\text{O-HfCl}_4$. Similar to the behaviors in XANES of $x\text{Li}_2\text{O-TaCl}_5$, the E_0 of $1.5\text{Li}_2\text{O-HfCl}_4$ and $2\text{Li}_2\text{O-HfCl}_4$ is between those of the in HfCl_4 and HfO_2 , while Hf in $2\text{Li}_2\text{O-HfCl}_4$ is more oxidized. Combing with the WT-EXAFS spectra (**Figure S5.13**), it is shown that in $1.5\text{Li}_2\text{O-HfCl}_4$, Hf is nearest coordinated by O then Cl (**Figure S5.12b and c**). EXAFS fitting results estimate the CN of Hf in $1.5\text{Li}_2\text{O-HfCl}_4$ is 3.6 for O and 2.3 for Cl (**Figure S5.14 and Table S5.2**). Since there are no other effective techniques to characterize the local structure of $1.5\text{Li}_2\text{O-HfCl}_4$ yet, the polyhedron in $x1.5\text{Li}_2\text{O-HfCl}_4$ cannot be fully revealed. However, local structure changes and the trend of ionic conductivity are consistent with that in $x\text{Li}_2\text{O-TaCl}_5$, which suggests Li-ion conductivity drops in $x\text{Li}_2\text{O-HfCl}_4$ with more Hf-O bonds (**Figure S5.12c**).

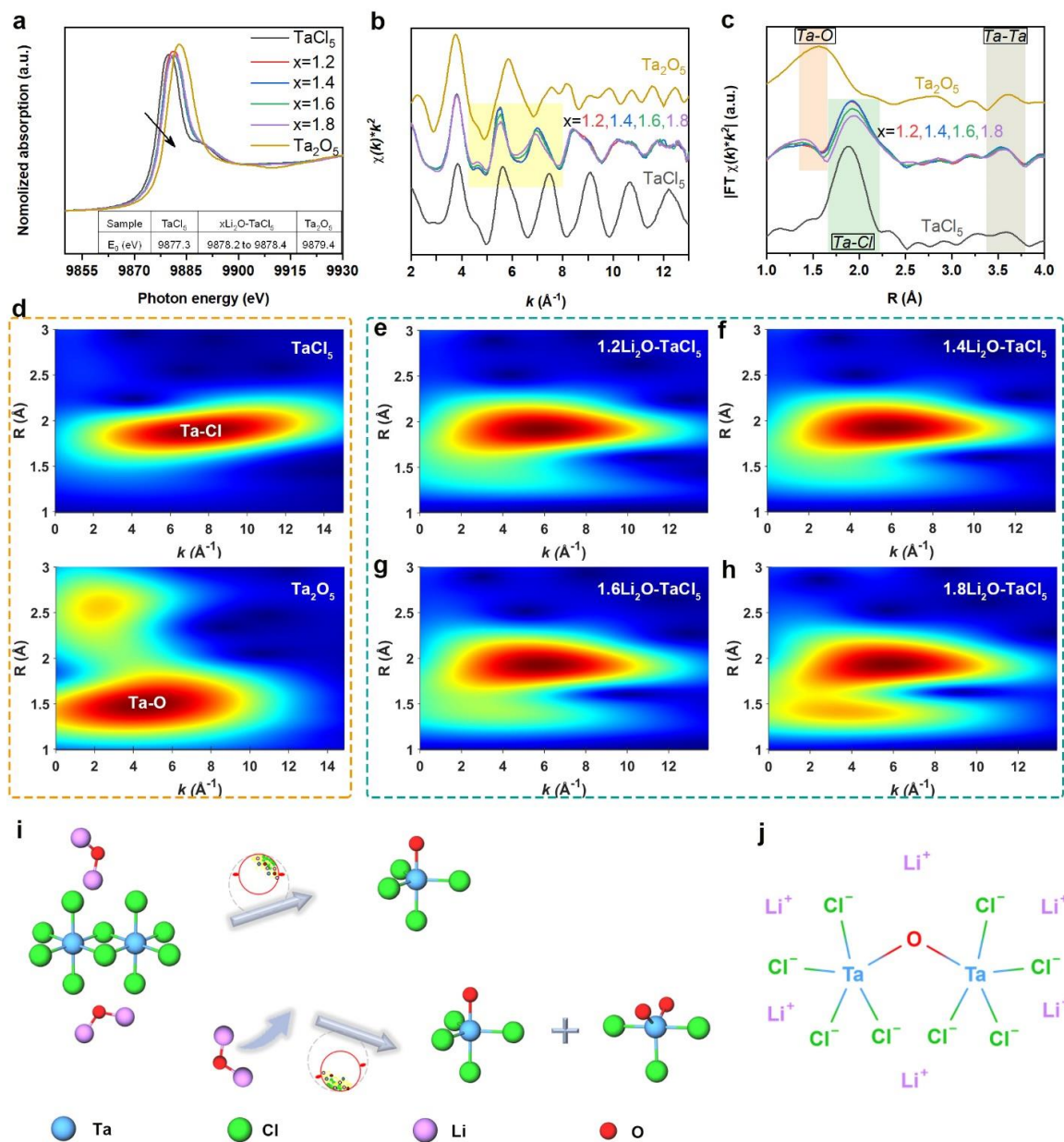


Figure 5.3 (a) XANES, (b) EXAFS, and (c) FT-EXAFS of $x\text{Li}_2\text{O-TaCl}_5$ ($x = 1.2, 1.4, 1.6, 1.8$) glasses, as well as Ta_2O_5 and TaCl_5 referential samples at Ta L_3 -edge. WT spectra of (d) Ta_2O_5 and TaCl_5 , (e) $1.2\text{Li}_2\text{O-TaCl}_5$, (f) $1.4\text{Li}_2\text{O-TaCl}_5$, (g) $1.6\text{Li}_2\text{O-TaCl}_5$, and (h) $1.8\text{Li}_2\text{O-TaCl}_5$ at Ta L_3 -edge with a k^2 weighting. (i) Schematic figure of the reaction route to form superionic $x\text{Li}_2\text{O-TaCl}_5$ glasses. The local structures are also displayed with coordination and possible geometry (bond angle is not accurate). (j) One possible connection of the smallest local structure unit in $x\text{Li}_2\text{O-TaCl}_5$ glasses.

Table 5.1 Structural parameters of $x\text{Li}_2\text{O}-\text{TaCl}_5$ ($x = 1.2, 1.4, 1.6$ and 1.8) glasses extracted from Ta L_3 -edge EXAFS fittings.

		1.2Li ₂ O-TaCl ₅	1.4Li ₂ O-TaCl ₅	1.6Li ₂ O-TaCl ₅	1.8Li ₂ O-TaCl ₅
Ta-O path	CN	0.9 ± 0.2	0.9 ± 0.2	1.4 ± 0.4	1.7 ± 0.4
	d (Å)	1.871 ± 0.023	1.876 ± 0.021	1.866 ± 0.013	1.867 ± 0.010
	σ ² (Å ²)	0.003 ± 0.001	0.003 ± 0.001	0.004 ± 0.003	0.004 ± 0.002
Ta-Cl path	CN	3.5 ± 0.5	3.4 ± 0.5	3.3 ± 0.4	3.0 ± 0.4
	d (Å)	2.334 ± 0.013	2.336 ± 0.011	2.336 ± 0.009	2.345 ± 0.009
	σ ² (Å ²)	0.008 ± 0.002	0.008 ± 0.002	0.009 ± 0.002	0.009 ± 0.002
	ΔE ₀ (eV)	5.08 ± 1.29	5.26 ± 1.23	4.09 ± 1.02	4.25 ± 1.00

*CN, coordination number; d (Å), bonding distance; σ², Debye-Waller factor; ΔE₀ is the inner potential correction. Ta-O path is from the crystal structures of Ta₂O₅ (mp-10390). Ta-Cl path from the crystal structure of TaCl₅ (mp-29831). The fitted k range was set to be 3–13.3 Å⁻¹, and the fitted R range was set to be 1–2.7 Å. A k² weighting was used.

As promising SEs for bulk-type ASSLIBs, the electrochemical performance of 1.6Li₂O-TaCl₅ and 1.5Li₂O-HfCl₄ glassy SEs were evaluated. The electrochemical stability window (ESW) of 1.6Li₂O-TaCl₅ and 1.5Li₂O-HfCl₄ glassy SEs were determined by Linear sweep voltammetry with separate positive and negative scans. As depicted in

Figure S5.14a, the onset redox voltages for the $1.6\text{Li}_2\text{O-TaCl}_5$ glassy SE were the same at both low temperature (LT: $-10\text{ }^\circ\text{C}$) and RT, indicating that the ESW of $1.6\text{Li}_2\text{O-TaCl}_5$ is independent on the testing temperatures. However, slower redox kinetics at LT is expected based on the lower current responses compared to the RT measurements. Similar results were obtained for the $1.5\text{Li}_2\text{O-HfCl}_4$ glassy SE (**Figure S5.14b**). The ESWs of $1.6\text{Li}_2\text{O-TaCl}_5$ and $1.5\text{Li}_2\text{O-HfCl}_4$ were determined as 2.24–4.15 V (vs. Li/Li^+) and 1.95–4.13 V (vs. Li/Li^+), respectively. The reduction limit of the $1.6\text{Li}_2\text{O-TaCl}_5$ and $1.5\text{Li}_2\text{O-HfCl}_4$ glasses are related to the reduction of high valance state Hf and Ta, thus limiting the direct contact between SEs and Li metal; yet the oxidation limit of above 4 V (vs. Li/Li^+) is favorable for the 4-V class cathodes.

$\text{LiNi}_{0.83}\text{Mn}_{0.06}\text{Co}_{0.11}\text{O}$ (NMC83) was selected as an attractive cathode active material for ASSLIBs evaluations to employ the $1.6\text{Li}_2\text{O-TaCl}_5$ and $1.5\text{Li}_2\text{O-HfCl}_4$ glassy SEs. The ASSLIB with $1.6\text{Li}_2\text{O-TaCl}_5$ SE exhibited excellent rate performance from 0.1 C to 3 C ($1\text{ C} = 200\text{ mAh g}^{-1}$) in a voltage range of 1.9 - 3.7 V (vs. Li^+/LiIn). The charge-discharge curves in **Figure 5.4a** depict high reversible capacities of 189.5 mAh g^{-1} , 177.1 mAh g^{-1} , 161.7 mAh g^{-1} , 138 mAh g^{-1} , 105.7 mAh g^{-1} , and 83 mAh g^{-1} at 0.1 C, 0.2 C, 0.5 C, 1 C, 2 C, and 3 C, respectively. As for the ASSLIB with $1.5\text{Li}_2\text{O-HfCl}_4$ SE, the rate performance was comparable with the $1.6\text{Li}_2\text{O-TaCl}_5$ cell at lower rates (191.1 mAh g^{-1} @ 0.1 C, 171.9 mAh g^{-1} @ 0.2 C, 149.2 mAh g^{-1} @ 0.5 C), while the relatively lower conductivity of $1.5\text{Li}_2\text{O-HfCl}_4$ limited the high utilization of NMC83 at higher rates (**Figure 5.4c and d**). Nevertheless, ASSLIBs integrated with either glassy SE showed superior long cycle life at an optimized current density. As shown in **Figure 5.4e**, the ASSLIB with $1.6\text{Li}_2\text{O-TaCl}_5$ SE demonstrated highly stable cycling performance for over 300 cycles with a capacity retention of 92.9% at 1 C. There was even no capacity fading for the $1.6\text{Li}_2\text{O-TaCl}_5$ cell operated at 3 C after 100 cycles (**Figure 5.4b**). The $1.5\text{Li}_2\text{O-HfCl}_4$ ASSLIB also retained 89.6% of its initial reversible capacity after 300 cycles at 0.5 C (**Figure 5.4f**).

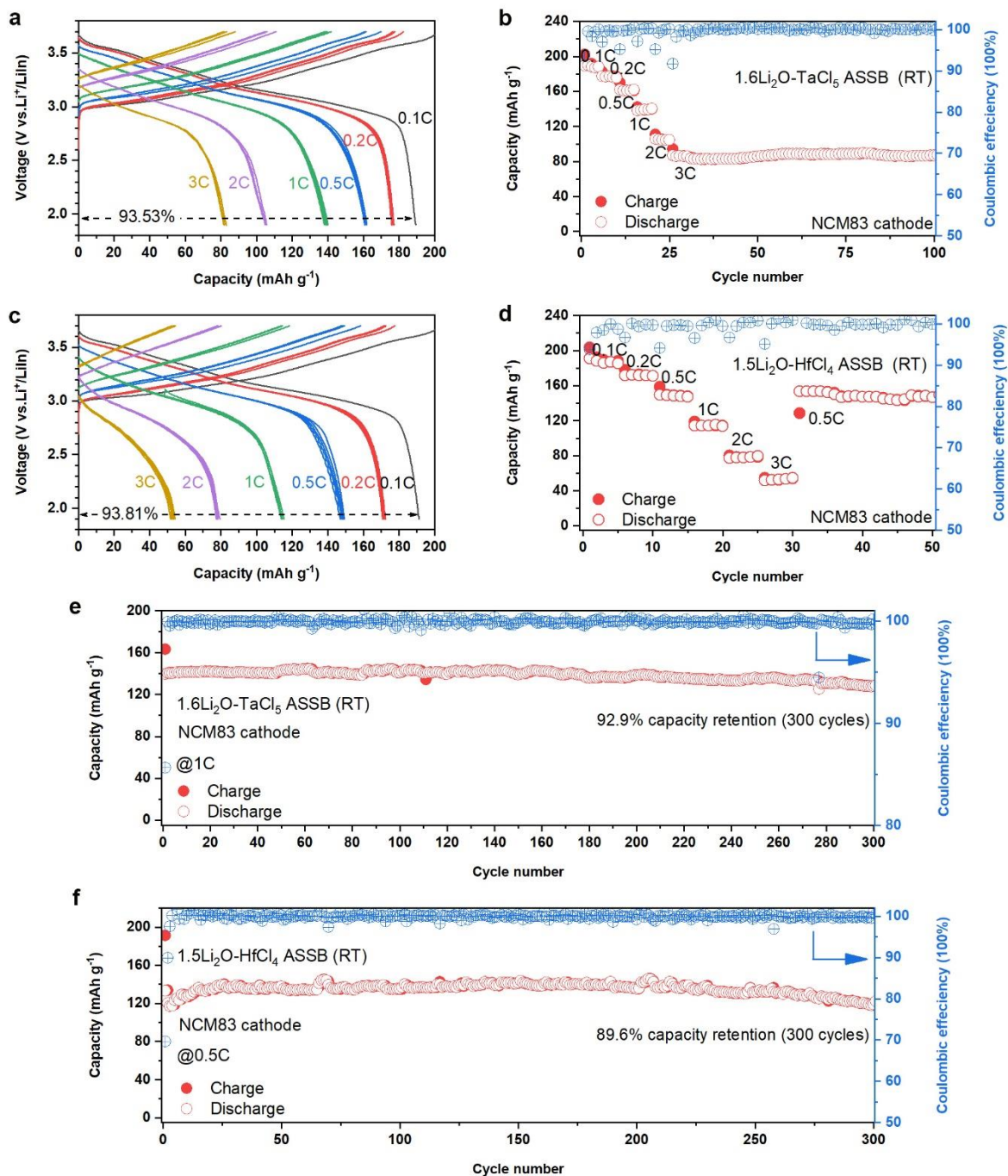


Figure 5.4 Room-temperature electrochemical performance of $\text{Li-In|Li}_3\text{YCl}_6|1.6\text{Li}_2\text{O-TaCl}_5|\text{NMC83}$ and $\text{Li-In|Li}_3\text{YCl}_6|1.5\text{Li}_2\text{O-HfCl}_4|\text{NMC83}$ ASSLIBs: (a) and (c) are charge-discharge curves at different C rates; (b) and (d) are rate performances; (e) and (f) are the long-term cycling performance.

After evaluating the RT battery performance, we also test the ASSLIBs at -10°C . **Figure 5.5a** depicts the rate capability of the cell using $1.6\text{Li}_2\text{O-TaCl}_5$ glassy SE. The reversible capacities of the ASSLIB using LiCoO_2 (LCO) cathode were 119.9, 111.6, 102.3, and 71.2 mAh g^{-1} at rates of 0.05, 0.1, 0.2 and 0.5 C (1 C = 140 mAh g^{-1}), respectively. Further increasing the rate to above 0.5 C led to limited capacity. To test the cycling stability at -10°C , the $1.6\text{Li}_2\text{O-TaCl}_5$ ASSLIB was cycled at 0.2 C (0.25 mA cm^{-2}) in a voltage range of 1.9 - 3.6 V (vs. Li^+/LiIn). As shown in **Figure 5.5b** and **c**, the initial reversible capacity reached 100.6 mAh g^{-1} with a Columbic efficiency (CE) of 94.9%. The cell maintained a high capacity of 93.7 mAh g^{-1} after 100 cycles and stably operated for over 300 cycles with a capacity retention of 79.2% (average CE: 99.94%). Apart from the $1.6\text{Li}_2\text{O-TaCl}_5$ in ASSLIBs, we test the electrochemical performance of $1.5\text{Li}_2\text{O-HfCl}_4$ ASSLIBs. Meanwhile, despite that the $1.5\text{Li}_2\text{O-HfCl}_4$ SE possessed a lower ionic conductivity of $3.4 \times 10^{-4}\text{ S cm}^{-1}$ at -10°C , the cell with $1.5\text{Li}_2\text{O-HfCl}_4$ still exhibited a decent and reversible capacity of 105.6 mAh g^{-1} (0.05 C), 94.5 mAh g^{-1} (0.1 C), and 82 mAh g^{-1} (0.2 C) (**Figure 5.5d**). Moreover, the cell can stably cycle over 300 cycles at 0.2 C and the discharge capacity decreases from 84.1 mAh g^{-1} (1st discharge) to 65.1 mAh g^{-1} (300th discharge), sustaining 77.4% of the useful capacity. (**Figure 5.5e** and **f**).

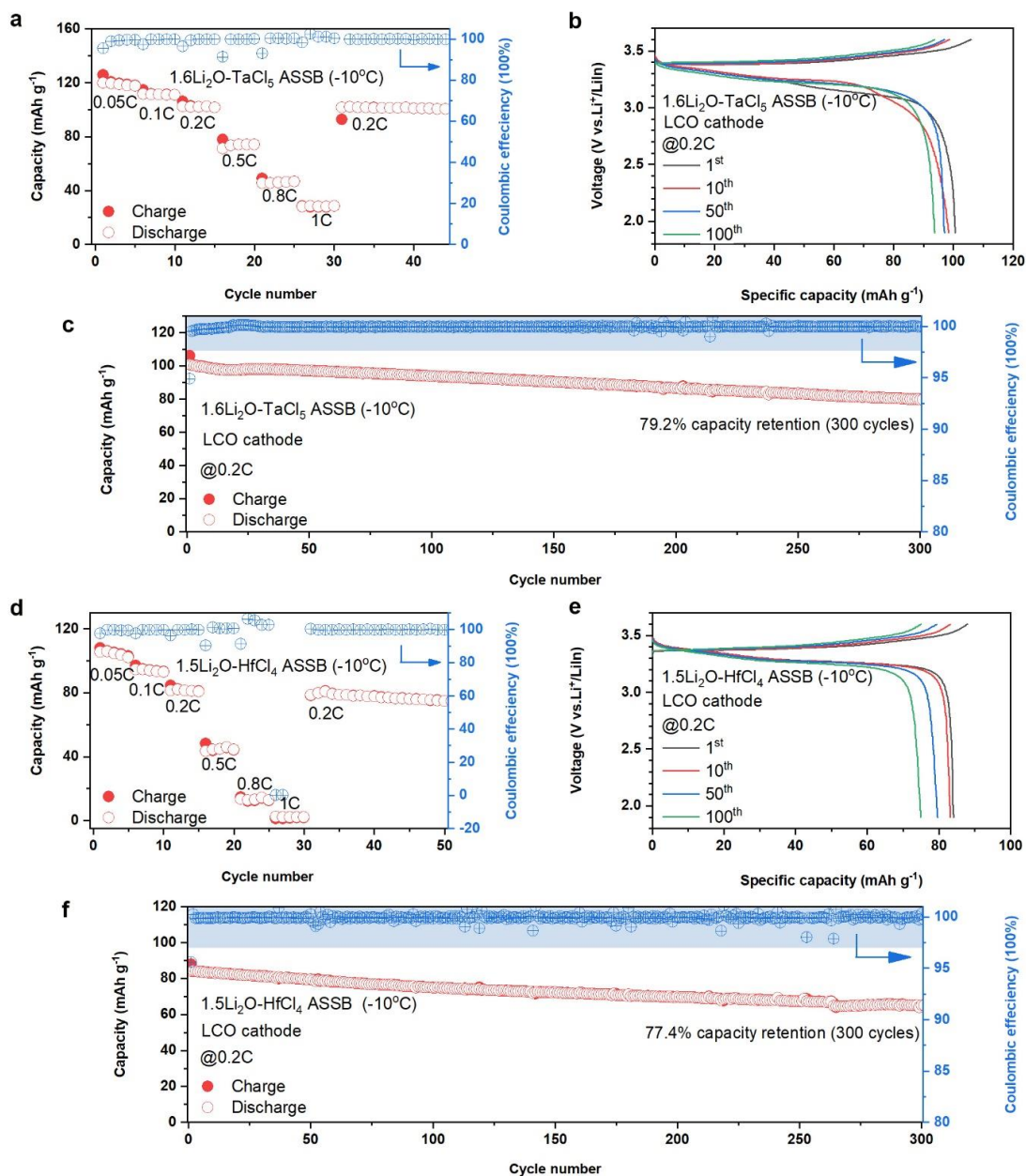


Figure 5.5 Low-temperature electrochemical performance of Li-In|LGPS|1.6Li₂O-TaCl₅|LCO and Li-In/LGPS – 1.5Li₂O-HfCl₄/LCO ASSBs at -10 °C: (a) and (d) are rate performances; (b) and (e) are charge-discharge curves at 1st, 10th, 50th, and 100th; (c) and (f) are long cycling performances at 0.2 C (1 C = 140 mAh g⁻¹).

5.4 Conclusion

In summary, we report a new series of glassy superionic conductors, $x\text{Li}_2\text{O-TaCl}_5$ ($x = 1.1-1.8$) and $x\text{Li}_2\text{O-HfCl}_5$ ($x = 1.5$), which can be prepared via one-step ball-milling method. Among them, the optimized $1.6\text{Li}_2\text{O-TaCl}_5$ and $1.5\text{Li}_2\text{O-HfCl}_4$ glasses possess a high ionic conductivity of $6.6 \times 10^{-3} \text{ S cm}^{-1}$ and $1.97 \times 10^{-3} \text{ S cm}^{-1}$, respectively. The local chemical environment in the representative superionic $x\text{Li}_2\text{O-TaCl}_5$ and $x\text{Li}_2\text{O-HfCl}_5$ was studied by NMR, XAS, and Raman analyses. Disordered Li sublattice and Li-ion diffusion are identified in $1.6\text{Li}_2\text{O-TaCl}_5$ and $1.5\text{Li}_2\text{O-HfCl}_4$. TaCl_4O is the main local structure in $x\text{Li}_2\text{O-TaCl}_5$ followed by TaCl_3O_2 only with enough Li_2O feeding content. In $1.5\text{Li}_2\text{O-HfCl}_5$, Hf is closely surrounded by O then Cl with a totally CN of 6. The ionic conductivity of either $x\text{Li}_2\text{O-TaCl}_5$ or $x\text{Li}_2\text{O-HfCl}_4$ drops when the feeding content of Li_2O exceeded to form more electronegative Ta-O or Hf-O bonds. Benefiting from the electrochemical stability and high ionic conductivity of the $1.6\text{Li}_2\text{O-TaCl}_5$ and $1.5\text{Li}_2\text{O-HfCl}_4$ glassy SEs, the ASSLIBs with these SEs showed excellent electrochemical performance. At -10°C , ASSLIBs with $1.6\text{Li}_2\text{O-TaCl}_5$ SE can stably cycle for over 300 cycles at a current density of 28 mA g^{-1} (0.2 C). The cell with $1.5\text{Li}_2\text{O-HfCl}_4$ can also perform decent cycling for over 300 cycles. At room temperature, ASSLIBs with $1.6\text{Li}_2\text{O-TaCl}_5$ SE showed superior performance at different C-rates and long cycles. This study shall provide insights into the design principles of glassy SEs and lead to a key advancement for ASSLIBs.

5.5 Acknowledgements

This research was supported by the Natural Sciences and Engineering Research Council of Canada (NSERC), the Canada Research Chair Program (CRC), the Canada Foundation for Innovation (CFI), Ontario Research Foundation (ORF), and the University of Western Ontario (UWO). The synchrotron research was performed at the Canadian Light Source, a national research facility of the University of Saskatchewan, which was supported by the CFI, NSERC, the National Research Council (NRC), the Canadian Institutes of Health Research (CIHR), the Government of Saskatchewan, and the University of Saskatchewan.

5.6 References

1. Janek, J., Zeier, W. G. A solid future for battery development. *Nature Energy* **1**, (2016).
2. Schmich, R., Wagner, R., Horpel, G., Placke, T., Winter, M. Performance and cost of materials for lithium-based rechargeable automotive batteries. *Nature Energy* **3**, 267-278 (2018).
3. Manthiram, A., Yu, X. W., Wang, S. F. Lithium battery chemistries enabled by solid-state electrolytes. *Nature Reviews Materials* **2**, 1-16 (2017).
4. Adeli, P., *et al.* Boosting Solid-State Diffusivity and Conductivity in Lithium Superionic Argyrodites by Halide Substitution. *Angewandte Chemie-International Edition* **58**, 8681-8686 (2019).
5. Zhou, L. D., Assoud, A., Zhang, Q., Wu, X. H., Nazar, L. F. New Family of Argyrodite Thioantimonate Lithium Superionic Conductors. *Journal of the American Chemical Society* **141**, 19002-19013 (2019).
6. Kamaya, N., *et al.* A lithium superionic conductor. *Nature Materials* **10**, 682-686 (2011).
7. Kato, Y., *et al.* High-power all-solid-state batteries using sulfide superionic conductors. *Nature Energy* **1**, 1-7 (2016).
8. Inaguma, Y., *et al.* High Ionic-Conductivity in Lithium Lanthanum Titanate. *Solid State Communications* **86**, 689-693 (1993).
9. Luo, J. Y., Xia, Y. Y. Aqueous lithium-ion battery $\text{LiTi}_2(\text{PO}_4)_3/\text{LiMn}_2\text{O}_4$ with high power and energy densities as well as superior cycling stability. *Advanced Functional Materials* **17**, 3877-3884 (2007).
10. Wu, J. F., *et al.* Gallium-Doped $\text{Li}_7\text{La}_3\text{Zr}_2\text{O}_{12}$ Garnet-Type Electrolytes with High Lithium-Ion Conductivity. *Acs Applied Materials & Interfaces* **9**, 1542-1552 (2017).
11. Bernuy-Lopez, C., Manalastas, W., del Amo, J. M. L., Aguadero, A., Aguesse, F., Kilner, J. A. Atmosphere Controlled Processing of Ga-Substituted Garnets for High Li-Ion Conductivity Ceramics. *Chemistry of Materials* **26**, 3610-3617 (2014).

12. Asano, T., Sakai, A., Ouchi, S., Sakaida, M., Miyazaki, A., Hasegawa, S. Solid Halide Electrolytes with High Lithium-Ion Conductivity for Application in 4 V Class Bulk-Type All-Solid-State Batteries. *Advanced Materials* **30**, 1803075 (2018).
13. Li, X. N., *et al.* Water-Mediated Synthesis of a Superionic Halide Solid Electrolyte. *Angewandte Chemie-International Edition* **58**, 16427-16432 (2019).
14. Zhou, L. D., Kwok, C. Y., Shyamsunder, A., Zhang, Q., Wu, X. H., Nazar, L. F. A new halospinel superionic conductor for high-voltage all solid state lithium batteries. *Energy & Environmental Science* **13**, 2056-2063 (2020).
15. Zhou, L. D., *et al.* High areal capacity, long cycle life 4 V ceramic all-solid-state Li-ion batteries enabled by chloride solid electrolytes. *Nature Energy* **7**, 83-93 (2022).
16. Grady, Z. A., Wilkinson, C. J., Randall, C. A., Mauro, J. C. Emerging Role of Non-crystalline Electrolytes in Solid-State Battery Research. *Frontiers in Energy Research* **8**, (2020).
17. Chandra, A., Bhatt, A., Chandra, A. Ion Conduction in Superionic Glassy Electrolytes: An Overview. *Journal of Materials Science & Technology* **29**, 193-208 (2013).
18. Bunde, A., Funke, K., Ingram, M. D. Ionic glasses: History and challenges. *Solid State Ionics* **105**, 1-13 (1998).
19. Mizuno, F., Hayashi, A., Tadanaga, K., Tatsumisago, M. New, highly ion-conductive crystals precipitated from Li₂S-P₂S₅ glasses. *Advanced Materials* **17**, 918-921 (2005).
20. Kondo, S., Takada, K., Yamamura, Y. New Lithium Ion Conductors Based on Li₂S-Si₂ System. *Solid State Ionics* **53**, 1183-1186 (1992).
21. Zhu, Y. Z., He, X. F., Mo, Y. F. Origin of Outstanding Stability in the Lithium Solid Electrolyte Materials: Insights from Thermodynamic Analyses Based on First-Principles Calculations. *Acs Applied Materials & Interfaces* **7**, 23685-23693 (2015).

22. Nolan, A. M., Zhu, Y. Z., He, X. F., Bai, Q., Mo, Y. F. Computation-Accelerated Design of Materials and Interfaces for All-Solid-State Lithium-Ion Batteries. *Joule* **2**, 2016-2046 (2018).
23. Lau, J., DeBlock, R. H., Butts, D. M., Ashby, D. S., Choi, C. S., Dunn, B. S. Sulfide Solid Electrolytes for Lithium Battery Applications. *Advanced Energy Materials* **8**, 1800933 (2018).
24. Charles, R. J. Some Structural and Electrical Properties of Lithium Silicate Glasses. *Journal of the American Ceramic Society* **46**, 235-243 (1963).
25. Ehrt, D. Structure, properties and applications of borate glasses. *Glass Technology* **41**, 182-185 (2000).
26. Martin, S. W. Ionic-Conduction in Phosphate-Glasses. *Journal of the American Ceramic Society* **74**, 1767-1784 (1991).
27. Murthy, M. K., Ip, J. Studies in Germanium Oxide Systems .1. Phase Equilibria in the System $\text{Li}_2\text{O-GeO}_2$. *Journal of the American Ceramic Society* **47**, 328-331 (1964).
28. Kozen, A. C., Pearse, A. J., Lin, C. F., Noked, M., Rubloff, G. W. Atomic Layer Deposition of the Solid Electrolyte LiPON. *Chemistry of Materials* **27**, 5324-5331 (2015).
29. Kaup, K., *et al.* A Lithium Oxythioborosilicate Solid Electrolyte Glass with Superionic Conductivity. *Advanced Energy Materials* **10**, 1902783 (2020).
30. Wilkening, M., Heitjans, P. From Micro to Macro: Access to Long-Range Li^+ Diffusion Parameters in Solids via Microscopic Li-6, Li-7 Spin-Alignment Echo NMR Spectroscopy. *Chemphyschem* **13**, 53-65 (2012).
31. Uitz, M., Epp, V., Bottke, P., Wilkening, M. Ion dynamics in solid electrolytes for lithium batteries. *Journal of Electroceramics* **38**, 142-156 (2017).
32. Grey, C. P., Greenbaum, S. G. Nuclear magnetic resonance studies of lithium-ion battery materials. *MRS Bulletin* **27**, 613-618 (2002).
33. Heitjans, P., Wilkening, M. Ion Dynamics at Interfaces: Nuclear Magnetic Resonance Studies. *MRS Bulletin* **34**, 915-922 (2009).

34. Yu, C., *et al.* Unravelling Li-Ion Transport from Picoseconds to Seconds: Bulk versus Interfaces in an Argyrodite Li₆PS₅Cl-Li₂S All-Solid-State Li-Ion Battery. *Journal of the American Chemical Society* **138**, 11192-11201 (2016).
35. Yu, C., *et al.* Superionic conductivity in lithium argyrodite solid-state electrolyte by controlled Cl-doping. *Nano Energy* **69**, 104396 (2020).
36. Yu, C., *et al.* Revealing the relation between the structure, Li-ion conductivity and solid-state battery performance of the argyrodite Li₆PS₅Br solid electrolyte. *Journal of Materials Chemistry A* **5**, 21178-21188 (2017).
37. Yu, C., *et al.* Facile Synthesis toward the Optimal Structure-Conductivity Characteristics of the Argyrodite Li₆PS₅Cl Solid-State Electrolyte. *Acs Applied Materials & Interfaces* **10**, 33296-33306 (2018).
38. Epp, V., Gun, O., Deiseroth, H. J., Wilkening, M. Highly Mobile Ions: Low-Temperature NMR Directly Probes Extremely Fast Li⁺ Hopping in Argyrodite-Type Li₆PS₅Br. *Journal of Physical Chemistry Letters* **4**, 2118-2123 (2013).
39. Hanghofer, I., *et al.* Substitutional disorder: structure and ion dynamics of the argyrodites Li₆PS₅Cl, Li₆PS₅Br and Li₆PS₅I. *Physical Chemistry Chemical Physics* **21**, 8489-8507 (2019).
40. Huglen, R., Poulsen, F. W., Mamantov, G., Begun, G. M. Characterization of Tantalum Pentachloride Containing Melts by Raman-Spectroscopy. *Inorganic Chemistry* **18**, 2551-2555 (1979).
41. Beattie, I. R., Ozin, G. A. Gas-Phase Raman Spectroscopy of Trigonal Bipyramidal Pentachlorides and Pentabromides. *Journal of the Chemical Society a -Inorganic Physical Theoretical*, 1691-1693 (1969).
42. Tsuchiya, T., Imai, H., Miyoshi, S., Glans, P. A., Guo, J. H., Yamaguchi, S. X-Ray absorption, photoemission spectroscopy, and Raman scattering analysis of amorphous tantalum oxide with a large extent of oxygen nonstoichiometry. *Physical Chemistry Chemical Physics* **13**, 17013-17018 (2011).
43. Xia, Z. M., Zhang, H., Shen, K. C., Qu, Y. Q., Jiang, Z. Wavelet analysis of extended X-ray absorption fine structure data: Theory, application. *Physica B-Condensed Matter* **542**, 12-19 (2018).

44. Munoz, M., Argoul, P., Farges, F. Continuous Cauchy wavelet transform analyses of EXAFS spectra: A qualitative approach. *American Mineralogist* **88**, 694-700 (2003).
45. Dalba, G., Fornasini, P. EXAFS Debye-Waller factor and thermal vibrations of crystals. *Journal of Synchrotron Radiation* **4**, 243-255 (1997).

5.7 Supporting information

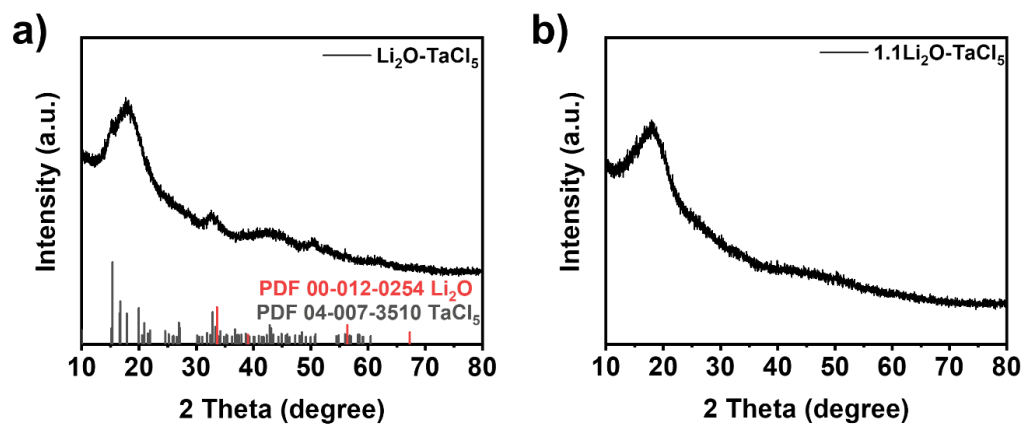


Figure S5.1 Lab-based XRD patterns for (a) $\text{Li}_2\text{O-TaCl}_5$ and (b) $1.1\text{Li}_2\text{O-TaCl}_5$.

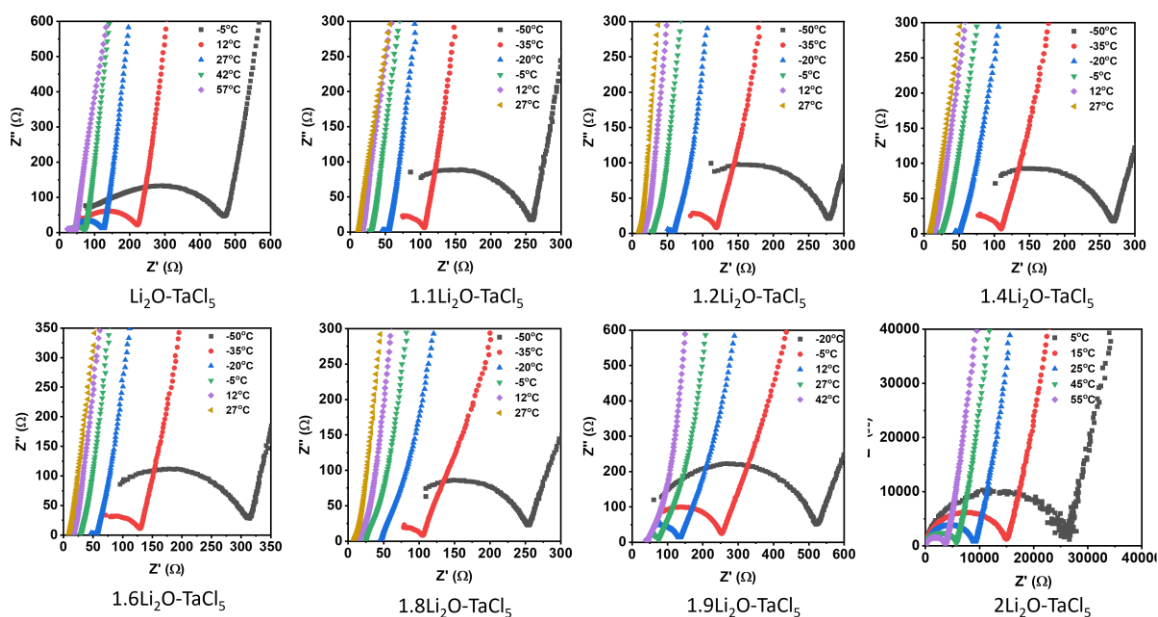


Figure S5.2 Nyquist plots for the $x\text{Li}_2\text{O-TaCl}_5$ SEs at various temperatures.

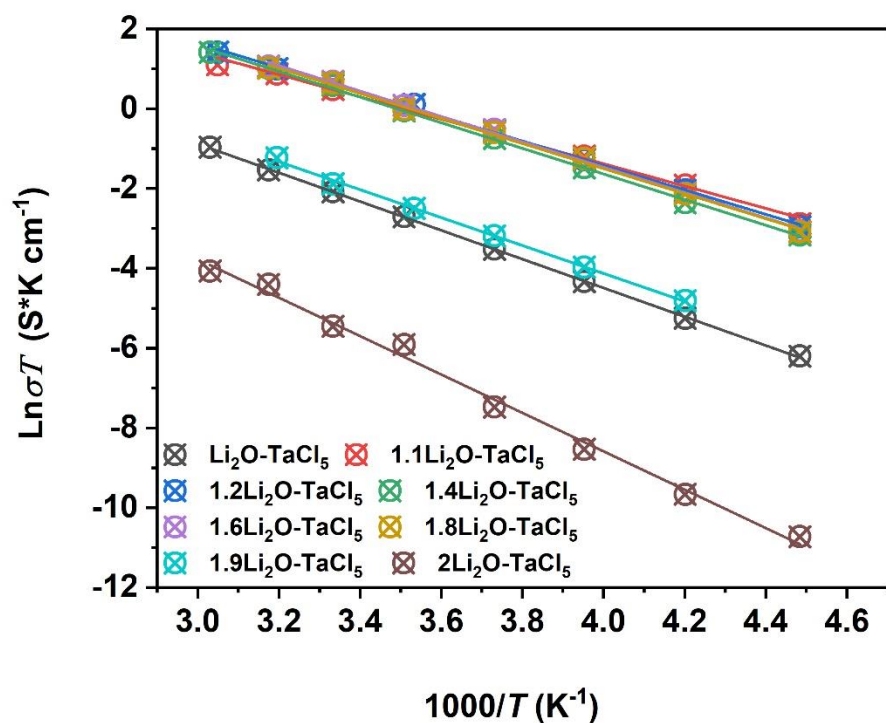


Figure S5.3 Arrhenius plots of $x\text{Li}_2\text{O}-\text{TaCl}_5$ SEs.

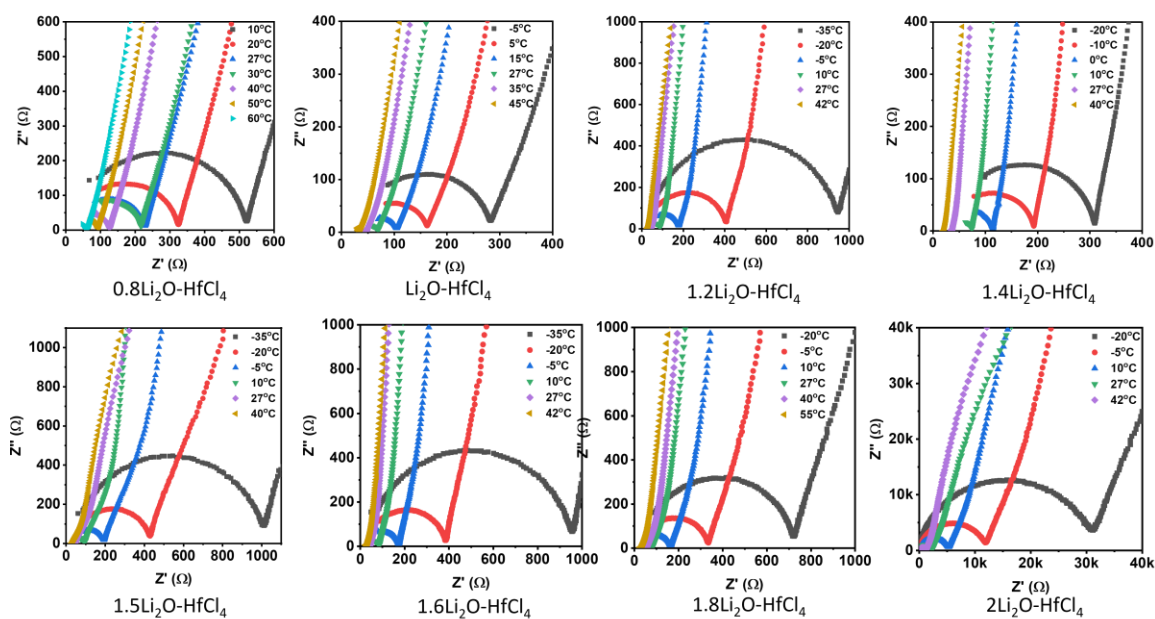


Figure S5.4 Nyquist plots of the $x\text{Li}_2\text{O-HfCl}_4$ SEs at various temperatures to determine the ionic conductivity and activation energy.

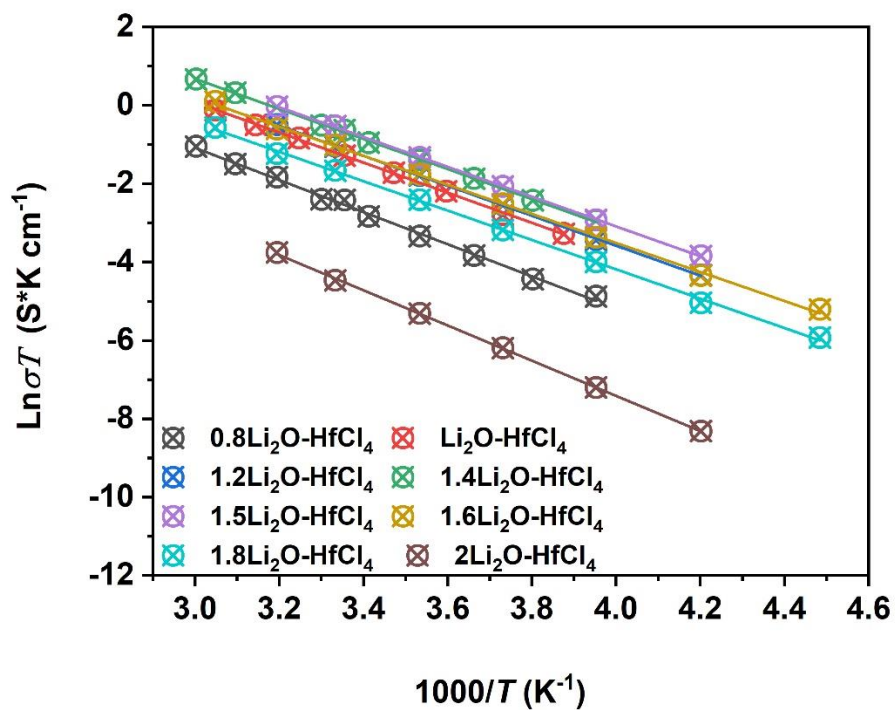


Figure S5.5 Arrhenius plots of the $x\text{Li}_2\text{O-HfCl}_4$ SEs.

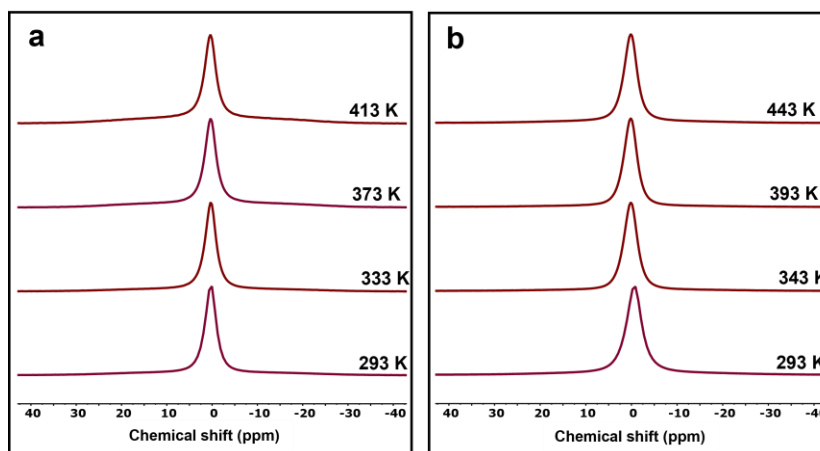


Figure S5.6 ^7Li SSNMR spectra of (a) $1.6\text{Li}_2\text{O}\text{-TaCl}_5$ and (b) $1.5\text{Li}_2\text{O}\text{-HfCl}_4$ at designated temperatures.

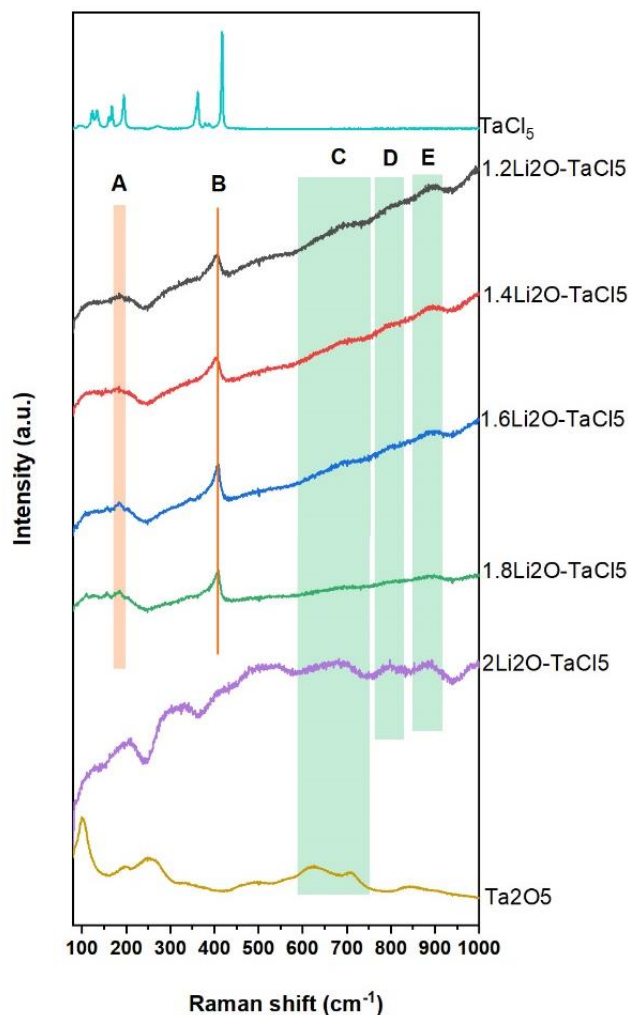


Figure S5.7 Raman spectra of the selected $x\text{Li}_2\text{O}\text{-TaCl}_5$ glasses ($x = 1.2, 1.4, 1.6, 1.8$ and 2), reference Ta_2O_5 , and TaCl_5 .

The peaks in TaCl_5 can be well assigned as Ta–Cl vibrations in the $\text{Ta}_2\text{Cl}_{10}$ with edge-sharing TaCl_6 octahedra¹. In $x\text{Li}_2\text{O}\text{-TaCl}_5$ ($x = 1.2, 1.4, 1.6, 1.8$), the strong peak B (406 cm^{-1}) and broaden feature A ($\sim 180\text{ cm}^{-1}$) are commonly observed as Ta–Cl vibrations in trigonal bipyramidal TaCl_5 ². Feature C (from around 585 cm^{-1} to 780 cm^{-1}) and E (around

885 cm^{-1}) can be assigned as the Ta–O vibrations in TaO_6 ³. Feature D (around 800 cm^{-1}) is the vibrations for Ta–O in pyramid TaO_5 ^{3,4}.

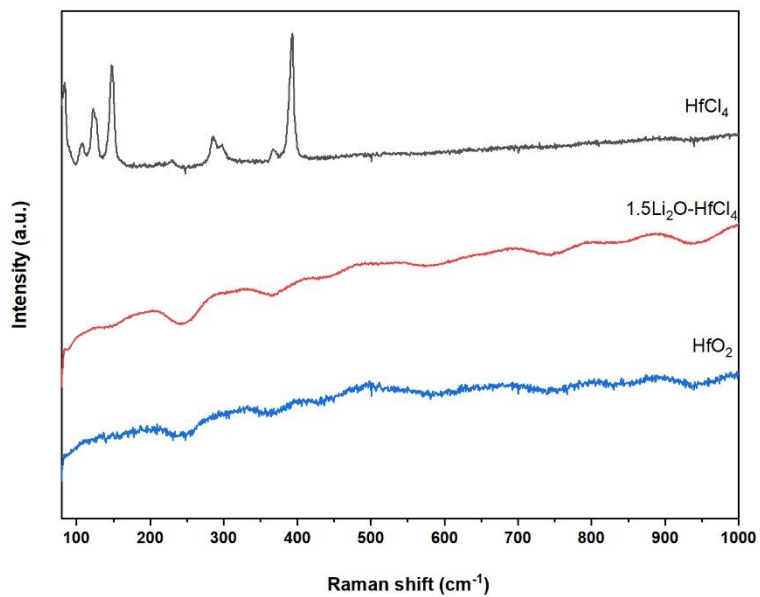


Figure S5.8 Raman spectra of 1.5Li₂O-HfCl₄ glass, reference HfCl₄, and HfO₂.

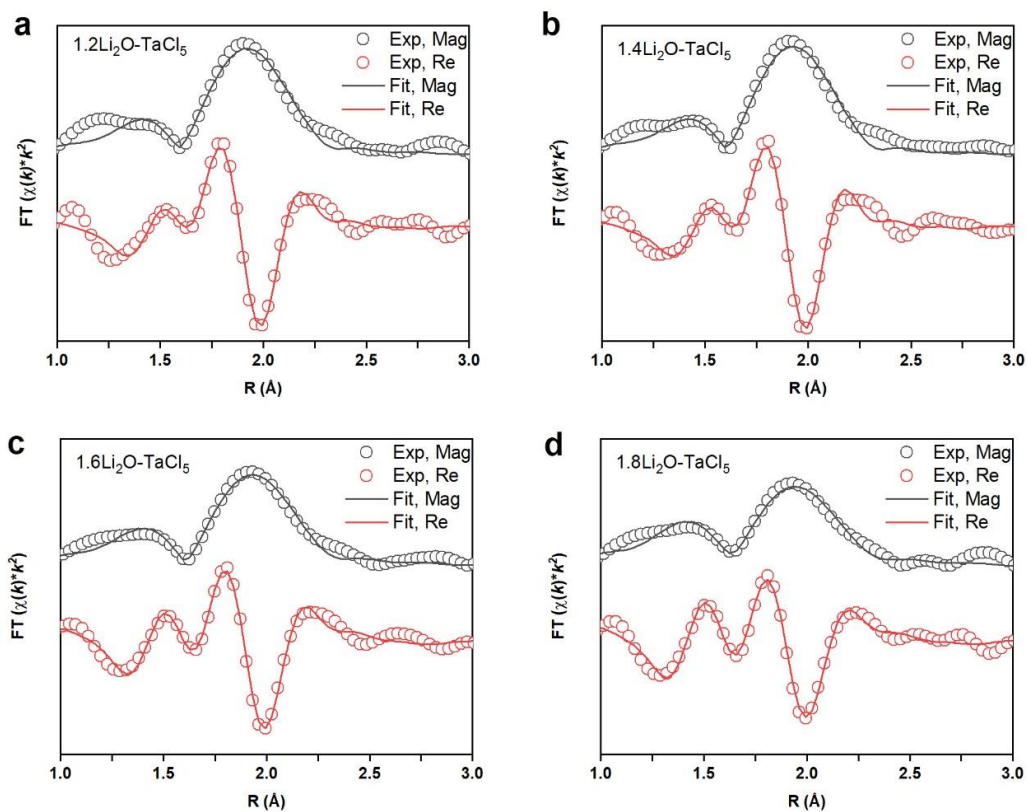


Figure S5.9 Fitting results of the k^2 -weighted FT spectra of (a) $1.2\text{Li}_2\text{O-TaCl}_5$, (b) $1.4\text{Li}_2\text{O-TaCl}_5$, (c) $1.6\text{Li}_2\text{O-TaCl}_5$, and (d) $1.8\text{Li}_2\text{O-TaCl}_5$ at Ta L_3 -edge, showing the experimental data (grey circle) and Feff modeling (grey line) in terms of magnitude of FT and the real part of FT experimental data (red circle) and Feff⁵ modeling (red line) traces. The R factor for each fitting is 0.026, 0.023, 0.014, and 0.013, respectively. In each fitting, S_0^2 is set as 0.9114.

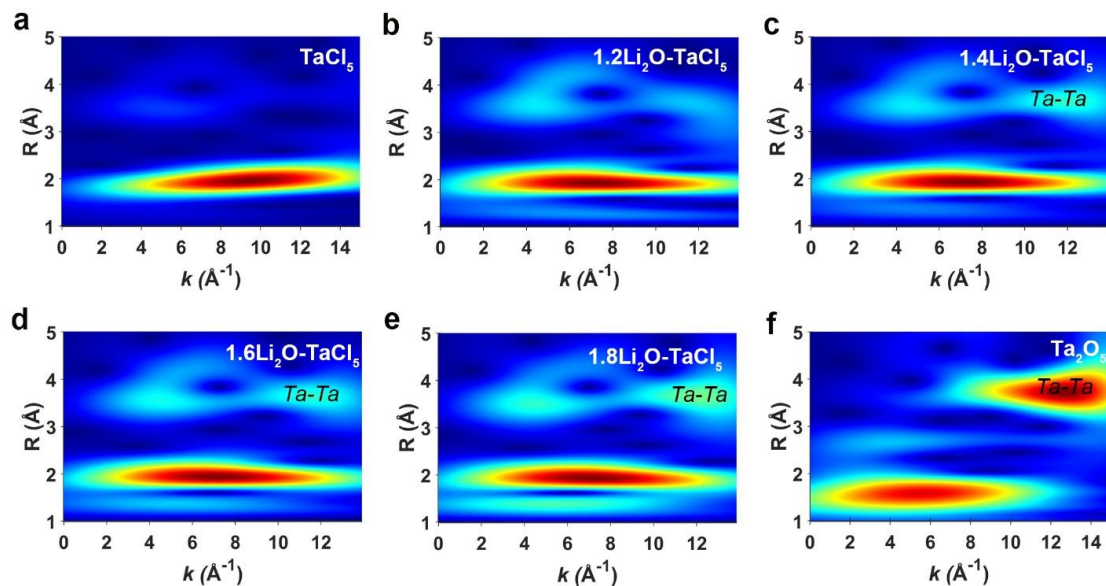


Figure S5.10 wavelet transformed Ta L_3 -EXAFS for (a) TaCl_5 , (b) $1.2\text{Li}_2\text{O-TaCl}_5$, (c) $1.4\text{Li}_2\text{O-TaCl}_5$, (d) $1.6\text{Li}_2\text{O-TaCl}_5$, (e) $1.8\text{Li}_2\text{O-TaCl}_5$, and (f) Ta_2O_5 with a k^3 weighting.

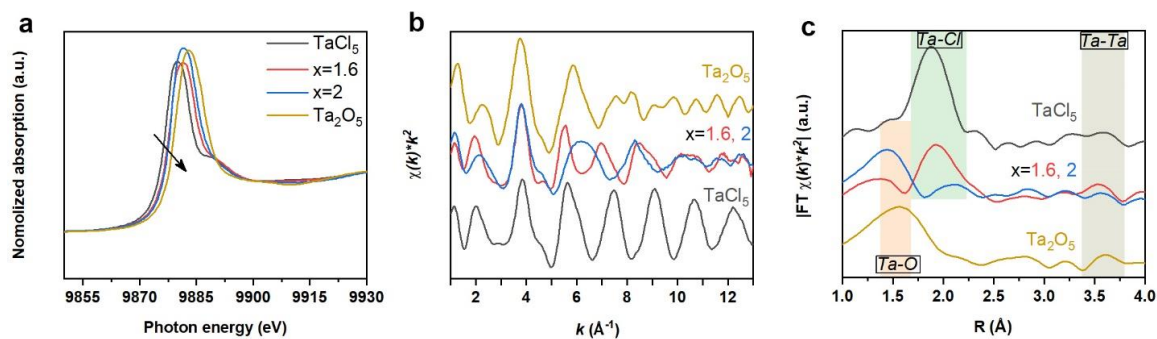


Figure S5.11 (a) XANES, (b) EXAFS, and (c) FT-EXAFS of $x\text{Li}_2\text{O-TaCl}_5$ ($x = 1.6$ and 2) glasses, as well as Ta_2O_5 and TaCl_5 referential samples at Ta L_3 -edge.

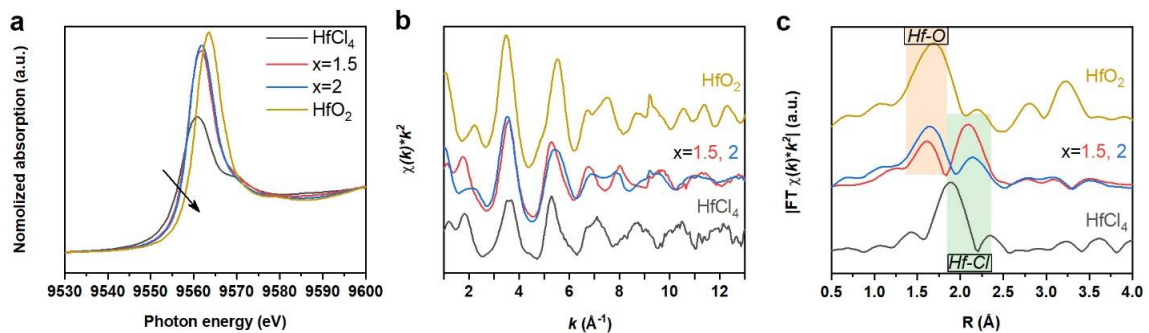


Figure S5.12 (a) XANES, (b) EXAFS, and (c) FT-EXAFS of $x\text{Li}_2\text{O-HfCl}_4$ ($x = 1.5$ and 2) glasses, as well as HfO_2 and HfCl_4 referential samples at Hf L_3 -edge.

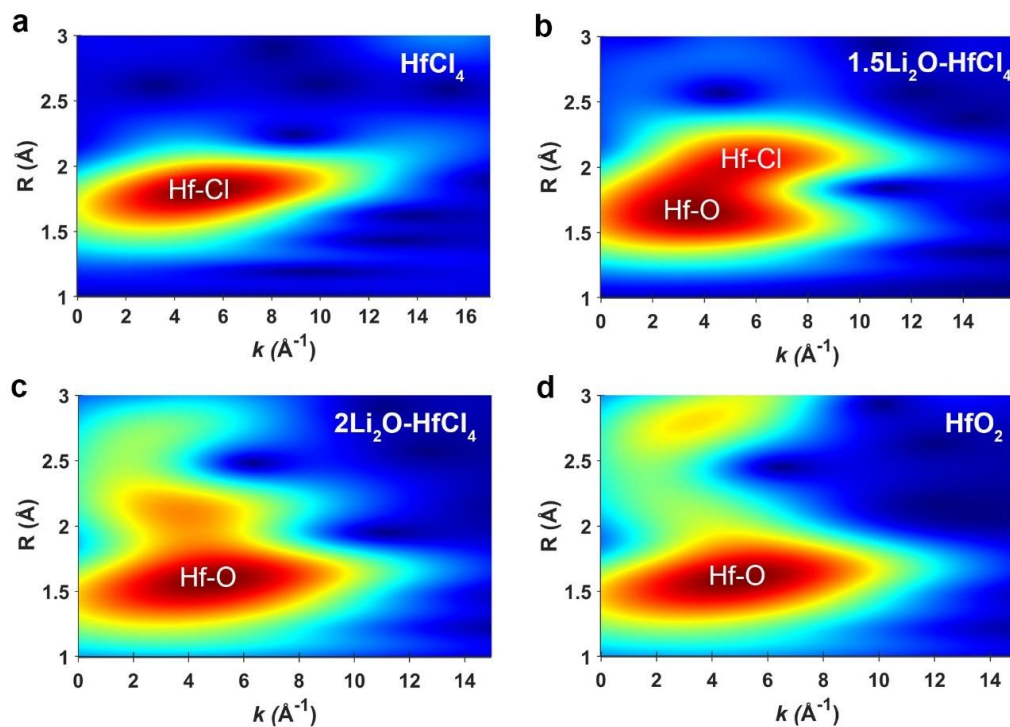


Figure S5.13 wavelet transformed Hf L_3 -EXAFS for (a) HfCl_4 , (b) $1.5\text{Li}_2\text{O-HfCl}_4$, (c) $2\text{Li}_2\text{O-HfCl}_4$, and (d) HfO_2 with a k^2 weighting.

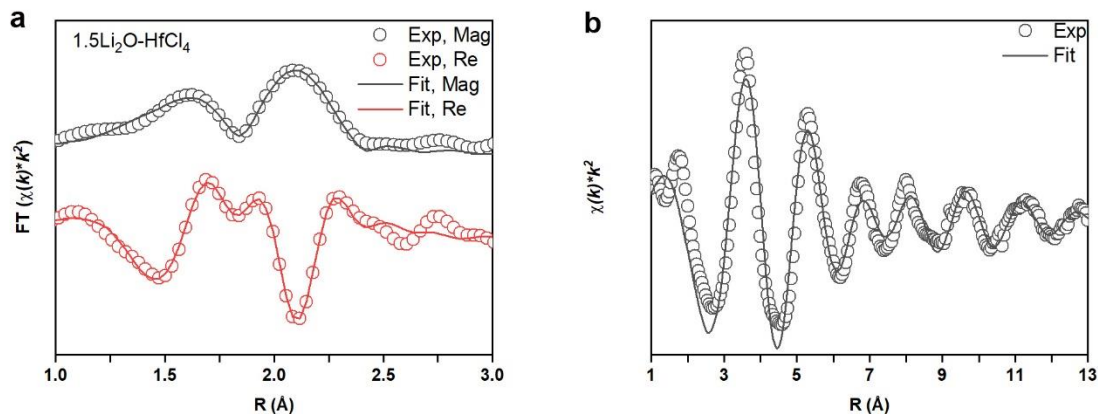


Figure S5.14 (a) Fitting results of k^2 -weighted FT spectra of $1.5\text{Li}_2\text{O-HfCl}_4$ at Hf L_3 -edge, showing the experimental data (grey circle) and Feff modeling (grey line) in terms of magnitude of FT and the real part of FT experimental data (red circle) and Feff⁵ modeling (red line) traces. (b) Hf L_3 -edge EXAFS and fit curve for $1.5\text{Li}_2\text{O-HfCl}_4$ in k -space. R factor for each fitting is 0.008. S_0^2 is set as 0.9114.

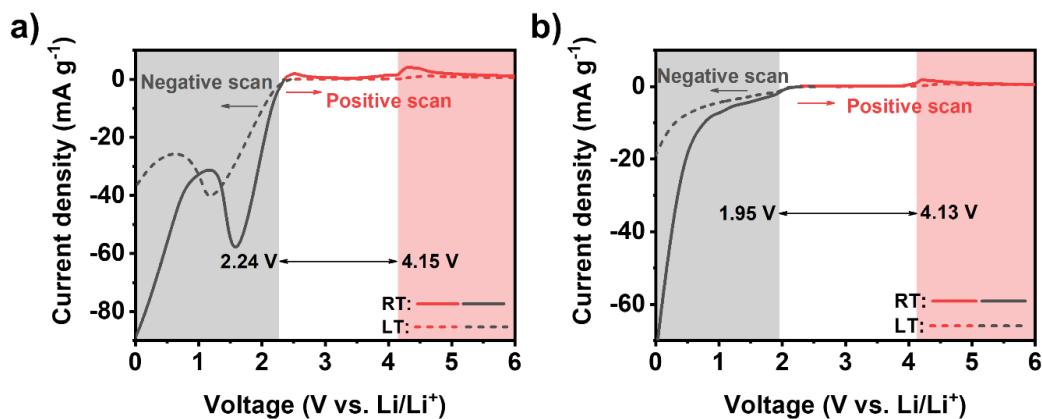


Figure S5.15 Linear sweep voltammetry (LSV) profile comparison between RT and LT for (a) $1.6\text{Li}_2\text{O-TaCl}_5$ and (b) $1.5\text{Li}_2\text{O-HfCl}_4$ using a configuration of $\text{Li}|\text{Li}_6\text{PS}_5\text{Cl}|\text{glassy SE}|\text{glassy SE} + \text{carbon black}$ (the working electrode consisted of 80 wt.% SE and 20 wt.% carbon black).

Table S5.1 Summary of the ionic conductivity and activation energy of the representative SEs

Inorganic SSE category	Materials	Ionic conductivity at 25°C (S cm ⁻¹)	Ref.
Sulfide	Li _{9.54} Si _{1.74} P _{1.44} S _{11.7} Cl _{0.3}	2.5 × 10 ⁻²	Nat. Energy 2016, 1 (4), 16030.
	Li ₁₀ GeP ₂ S ₁₂	1.2 × 10 ⁻²	Nat. Mater. 2011, 10 (9), 682-686.
	Li _{6.6} Si _{0.6} Sb _{0.4} S ₅ I	1.5 × 10 ⁻²	J. Am. Chem. Soc. 2019, 141 (48), 19002-19013.
	Li _{6.6} P _{0.4} Ge _{0.6} S ₅ I	5.4 × 10 ⁻³	J. Am. Chem. Soc. 2018, 140 (47), 16330-16339
	Li ₆ PS ₅ X (X = Cl, Br)	1.0 × 10 ⁻³	Angew. Chem. Int. Ed. 2008, 47 (4), 755-758.
	Li _{5.5} PS _{4.5} Cl _{1.5}	9.4 × 10 ⁻³	Angew. Chem. Int. Ed. 2019, 58 (26), 8681-8686
	Glass-ceramic Li ₇ P ₃ S ₁₁	3.2 × 10 ⁻³	Adv. Mater. 2005, 17 (7), 918-921.
	Li ₂ ZrCl ₆	8.1 × 10 ⁻⁴	Nat. Commun. 2021, 12(1), 1-11

Halide	$\text{Li}_2\text{In}_x\text{Sc}_{0.666-x}\text{Cl}_4$	2×10^{-3}	Nat. Energy, 2022, https://doi.org/10.1038/s41560-021-00952-0
	Li_3YCl_6	5.1×10^{-4}	Adv. Mater. 2018, 30 (44), 1803075
	Li_3YBr_6	1.7×10^{-3}	Adv. Mater. 2018, 30 (44), 1803075
	Li_3InCl_6	2.0×10^{-3}	Angew. Chem. Int. Ed. 2019, 58 (46), 16427-16432
	Li_3ScCl_6	3.0×10^{-3}	J. Am. Chem. Soc. 2020, 142 (15), 7012-7022
	$\text{Li}_2\text{Sc}_{2/3}\text{Cl}_4$	1.5×10^{-3}	Energy Environ. Sci. 2020, 13 (7), 2056-2063
Oxide	$\text{Li}_7\text{La}_3\text{Zr}_2\text{O}_{12}$ system	$10^{-4} \sim 10^{-3}$	Angew. Chem. Int. Ed. 2007, 46, 7778–7781; Chem. Mater. 2014, 26, 3610–3617; Chem. Mater. 2016, 28, 2384–2392; ACS Appl. Mater. Interfaces 2017, 9, 1542–1552; Chem. Mater. 2017, 29, 1769–1778;
	$\text{LiTi}_2(\text{PO}_4)_3$ system	$\sim 10^{-4}$	J. Electrochem. Soc. 1990, 137, 1023-1027; Acc. Chem. Res. 1994, 27, 265–270.

	LiGe ₂ (PO ₄) ₃ system	~10 ⁻³	J. Electrochem. Soc. 2008, 155, A915–A920; Solid State Ionics 2016, 289, 180–187.
	Li _{3x} La _{2/3-x} TiO ₃	~10 ⁻⁴	Solid State Commun. 1993, 86, 10, 689-693
	100[Li _{1.5} Cr _{0.5} Ti _{1.5} (PO ₄) ₃]-5SiO ₂	2.14 × 10 ⁻²	J. Non-Cryst. Solids 2015, 409, 120–125

Table S5.2 EXAFS fitting of 1.5Li₂O-HfCl₄, giving the information of bonding distance and coordination numbers

		1.5Li ₂ O-HfCl ₄
Hf-O path	CN	3.6 ± 0.7
	d (Å)	2.056 ± 0.017
	σ ²	0.009 ± 0.002
Hf-Cl path	CN	2.3 ± 0.5
	d (Å)	2.457 ± 0.009
	σ ²	0.006 ± 0.002
	ΔE ₀	3.74 ± 0.83

*CN, coordination number; d (Å), bonding distance; σ², Debye-Waller factor; ΔE₀ is the inner potential correction. The distance for Hf-O is from the crystal structures of HfO₂ (mp-776097). The distance for Hf-

Cl from the crystal structure of HfCl₄ (mp-29422). The fitted k range was set to be 3–14.035 Å⁻¹, and the fitted R range was set to be 1–2.6 Å. A *k*² weighting was used.

References for the supporting information of Chapter 5

1. Huglen, R., Poulsen, F. W., Mamantov, G., Begun, G. M. Characterization of Tantalum Pentachloride Containing Melts by Raman-Spectroscopy. *Inorganic Chemistry* **18**, 2551-2555 (1979).
2. Beattie, I. R., Ozin, G. A. Gas-Phase Raman Spectroscopy of Trigonal Bipyramidal Pentachlorides and Pentabromides. *Journal of the Chemical Society a -Inorganic Physical Theoretical*, 1691-& (1969).
3. Tsuchiya, T., Imai, H., Miyoshi, S., Glans, P. A., Guo, J. H., Yamaguchi, S. X-Ray absorption, photoemission spectroscopy, and Raman scattering analysis of amorphous tantalum oxide with a large extent of oxygen nonstoichiometry. *Physical Chemistry Chemical Physics* **13**, 17013-17018 (2011).
4. Krishnan, R. R., Nissamudeen, K. M., Gopchandran, K. G., Pillai, V. P. M., Ganesan, V. Effect of doping and substrate temperature on the structural and optical properties of reactive pulsed laser ablated tin oxide doped tantalum oxide thin films. *Vacuum* **84**, 1204-1211 (2010).
5. Ravel, B., Newville, M. ATHENA, ARTEMIS, HEPHAESTUS: data analysis for X-ray absorption spectroscopy using IFEFFIT. *Journal of Synchrotron Radiation* **12**, 537-541 (2005).

Chapter 6

6 Advanced high-voltage all-solid-state Li-ion batteries enabled by a dual-halogen solid electrolyte

Solid-state electrolytes (SEs) with high anodic (oxidation) stability are essential for achieving all-solid-state Li-ion batteries (ASSLIBs) operating at high voltages. Until now, halide-based SEs have been one of the most promising candidates due to the compatibility with cathodes and fast ionic conductivity. However, the developed chloride and bromide SEs still show limited electrochemical stability that is inadequate for ultrahigh voltage operation. Herein, this challenge is addressed by designing a dual-halogen Li-ion conductor: $\text{Li}_3\text{InCl}_{4.8}\text{F}_{1.2}$. F is demonstrated to selectively occupy a specific lattice site (Cl-8j) in a solid Li-ion superionic conductor (Li_3InCl_6) to form a new dual-halogen solid electrolyte (DHSE). With the incorporation of F, the $\text{Li}_3\text{InCl}_{4.8}\text{F}_{1.2}$ DHSE becomes dense and maintains a room-temperature ionic conductivity over $10^{-4} \text{ S cm}^{-1}$, which is higher than that of the reported fluoride compounds that are expected showing wide electrochemical windows. Moreover, the $\text{Li}_3\text{InCl}_{4.8}\text{F}_{1.2}$ DHSE exhibits a practical anodic limit over 6 V (vs. Li/Li^+), which can enable high-voltage ASSLIBs with decent cycling performance. Spectroscopic, computational, and electrochemical characterizations are combined to identify that a rich F-containing passivating cathode-electrolyte interface (CEI) is generated in-situ during electrochemical reactions, thus expanding the electrochemical window of $\text{Li}_3\text{InCl}_{4.8}\text{F}_{1.2}$ DHSE and preventing the detrimental interfacial reactions associated with the LiCoO_2 cathode at high applied voltages. This work provides a new design strategy for fast Li-ion conductors to achieve oxidation stability and show great potential in the application of ultrahigh-voltage ASSLIBs.

*One version of this chapter has been published in *Advanced Energy Materials* 2021, 11 (35), 2100836.

6.1 Introduction

All-solid-state Li-ion batteries (ASSLIBs) have been of significant interest due to the use of solid-state electrolytes (SEs) which replace the conventional flammable liquid electrolytes and possess improved safety.^[1] Many SEs are also predicted to be excellent for high-voltage applications where conventional liquid electrolytes decompose.^[2] In the early stages of development, several sulfide compounds^[3] were reported to possess high ionic conductivity that is comparable to those of the conventional liquid electrolytes. Nevertheless, it is still challenging for them to be used directly in commercialized batteries due to the compatibility issues between SEs and electrode materials, air sensitivity (H_2S generation), as well as their limited electrochemical windows.^[4] Recently, apart from the sulfide and oxide SEs with divalent anions, halide SEs have emerged as attractive alternatives due to the monovalent halogen anions having Coulombic interactions with Li ions, which facilitates Li-ion conduction.^[5] The other advantage of halide materials is their high theoretical anodic limits, as exemplified by ~ 4 V (vs. Li/Li^+) for chloride compounds and over 6 V for fluoride compounds.^[6] While fluoride SEs may have higher voltage stability, they have been shown to possess relatively lower Li-ion conductivity due to the strong electronegativity of fluorine.^[7] Moreover, a series of advanced chloride SEs (Li_3InCl_6 ^[5b, 6a], Li_3ErCl_6 ^[8], Li-Sc-Cl ^[5c, 5d], and etc.) have been reported not only possessing high ionic conductivity over 1 mS cm^{-1} , but also having excellent cathode compatibility to realize good battery performance without any additional protection coatings on the cathode materials.^[9] The very recently developed $\text{Li}_{3-x}\text{Y}_{1-x}\text{Zr}_x\text{Cl}_6$ ^[10] and $\text{Li}_{2+x}\text{Zr}_{1-x}\text{Fe}_x\text{Cl}_6$ ^[11] using earth-abundant and low-cost elements make chloride SEs commercially important. Despite chloride SEs being able to support ASSLIBs cycling up to a cut-off voltage around 4.5 V, these compounds are still inadequate for LIBs operating at higher voltages. This downside originates from the oxidation of Cl^- above 4.3 V in chloride SEs along with the formation of other Li-deficient metal-chloride products (ErCl_3 , InCl_3 , etc.), which lacks sufficient Li-ion conductive paths and continuously consumes SEs to deteriorate the performance of full cells.^[12] Therefore, the problems associated with the SE/cathode interface should be solved for the development of high-voltage ASSLIBs.

Previous research for improving the compatibility of the SE/cathode interface has mainly relied protective coatings.^[13] In general, various artificial coatings are utilized to modify the cathode materials, which physically protect the SEs from oxidation by the electroactive cathode materials.^[13a] A perfect coating layer featuring Li-ion conduction, electronic insulation, and (electro)chemical stability not only prolongs the cycle life of ASSLIBs at high applied potentials, but also acts as an additional SE to extend the anodic limit of the SE itself.^[14] However, compared with the direct use of a well-rounded SE, the processing of additional artificial coatings adds complication, is time consuming, and can be costly.^[13] As such, it is highly desired to develop SEs which can adopt the additional benefits of artificial coatings.

Herein, we propose a strategy to design a novel SE to enable high-voltage ASSLIBs. The in-situ generation of passivating interphases with favorable Li-ion diffusion pathways is expected to suppress the SEs degradation and continuous interfacial reactions. Guided by this, a dual-halogen solid electrolyte (DHSE) is demonstrated where fluorine (F) is employed to selectively occupy a specific lattice site (Cl-8j) in Li_3InCl_6 SE to form a new SE: $\text{Li}_3\text{InCl}_{4.8}\text{F}_{1.2}$. With the incorporation of F, the practical oxidation limit of DHSE is enhanced to over 6 V. Both experimental and computational results identify that the F-containing passivating interphases are generated in-situ, contributing to the enhanced anodic (oxidation) stability of $\text{Li}_3\text{InCl}_{4.8}\text{F}_{1.2}$ and stabilization on the surface of cathodes at high cut-off voltages. As a proof of concept, this $\text{Li}_3\text{InCl}_{4.8}\text{F}_{1.2}$ DHSE is directly matched with bare high-voltage LiCoO_2 (LCO), enabling ASSLIBs to stably operate at room temperature at a cut-off voltage of 4.8 V (vs. Li/Li^+). Scanning transmission X-ray microscope (STXM) combined with advanced ptychography technique visualizes a F-rich cathode-electrolyte interface (CEI), which is further analyzed by X-ray absorption spectroscopy (XAS) showing LiF is the major interfacial component. This work presents a SE design strategy exemplified through the $\text{Li}_3\text{InCl}_{4.8}\text{F}_{1.2}$ DHSE with high practical anodic stability derived from the formation of a fluorinated interface, opening up new opportunities for the wide application of ultrahigh-voltage ASSLIBs.

6.2 Experimental Section

Synthesis of Li_3InCl_6 and $\text{Li}_3\text{InCl}_{4.8}\text{F}_{1.2}$ Solid Electrolytes

All raw materials were purchased and used directly as received. LiCl (Sigma-Aldrich, \geq 99.98% trace metals basis), InCl₃ (Sigma-Aldrich, 98%), and InF₃ (Alfa Aesar™ anhydrous, 99.95% (metals basis)) were used as precursors and they were mixed with a stoichiometric amount in an argon-filled glovebox. The resulting mixture (~1 g) was then placed in a zirconia ball milling pot along with 40 g zirconia balls. Low-speed ball milling (150 rpm for 2 h) was first run to ensure all the precursors mixed well, followed by a high-speed ball milling process of 550 rpm for 20 h. Next, the ball-milled product was pelletized and sealed in quartz tubes for annealing under 260 °C. After naturally cooling down to room temperature, the SE pellets were transferred into the glovebox and manually ground into powders for further use.

Ionic Conductivity and Porosity Measurements

The porosity measurement as a function of applied pressure is similar with previous reports.^[11, 32] Ionic conductivity of as-prepared SEs was evaluated by using electrochemical impedance spectroscopy (EIS) with two stainless steel rods as blocking electrodes at room temperature (RT). The SE powders are cold-pressed into pellets under ~400 Mpa. EIS measurements are performed using a multichannel potentiostation 3/Z (German VMP3). The applied frequency range is 1 Hz ~ 7 MHz and the amplitude is 20 mV. Direct current (DC) polarization measurements are conducted on a pellet with applied voltages of 0.1 V, 0.2 V, 0.3 V, 0.4 V, and 0.5 V for 60 min each to determine the electronic conductivity of Li₃InCl_{4.8}F_{1.2} DHSE.

Cell Assembly and Electrochemical Measurements

LSV testing cells: Two kinds of SE powders (Li₃InCl₆ and Li₃InCl_{4.8}F_{1.2}) was first manually mixed well with carbon black (CB) at a ratio of 8:2, respectively. Then, 80 mg of Li₃InCl₆ powder was cold pressed into a pellet under a pressure of 300 MPa. 10 mg of SE/CB mixture was uniformly placed on one side of the Li₃InCl₆ pellet as working electrode and compressed again under the same pressure. After that, Li foil (China Energy Lithium Co. LTD) was attached on the other side of the pellet as both counter and reference electrode. In order to avoid the incompatibility between Li₃InCl₆ and metallic Li, a thinner layer of sulfide SE (Li₆PS₅Cl: ~40 mg)^[33] was inserted between the Li₃InCl₆

pellet and Li before Li foil was added. To ensure an intimate contact between layer by layer, the cell was pressed under a pressure of ~ 120 MPa before taking out of the glovebox. The LSV electrochemical stability window tests were conducted using versatile multichannel potentiostat 3/Z (VMP3) with a scan range from open-circuit voltage to 7 V (vs. Li/Li⁺). The scan rate was 0.1 mV s⁻¹.

ASSLIBs: For the cathode composite, two kinds of SE powders (Li₃InCl₆ and Li₃InCl_{4.8}F_{1.2}) were manually mixed for over 15 minutes with high-voltage lithium cobalt oxide (LCO) at a ratio of 3:7, respectively. The high-voltage LCO is supplied from China Automotive Battery Research Institute. The powder has a PSD-D50 of ~ 16 μm and a BET specific surface area of 0.190 m²/g. The particles are neither agglomerated nor coagulated. The total procedure was similar to above for LSV testing but Li foil was changed to In foil (99.99%, Φ 10 mm, thickness 0.1 mm). Typically, 80 mg of Li₃InCl₆ powder was cold pressed into a pellet under a pressure of 300 MPa. 10 mg of the cathode composite was uniformly placed on one side of the Li₃InCl₆ pellet and compressed again under the same pressure. After that, In foil was attached on the other side before adding a thinner layer of sulfide SE (Li₆PS₅Cl: ~ 40 mg) between Li₃InCl₆ pellet and In to avoid the possible influence of redox conversion between In³⁺ and In foil. The cell was pressed under a pressure of ~ 120 MPa before taking out of the glovebox. Galvanostatic charge-discharge was conducted on a LAND battery test system. The voltage window was set as 2.6 - 4.47 and 4.8 V (vs. Li/Li⁺) to evaluate the cycling stability and the rate performance. Cyclic voltammetry (CV) measurements were conducted using versatile multichannel potentiostat 3/Z (VMP3) under a voltage profile of 2.6 – 4.47 V (vs. Li/Li⁺) at a scan rate of 0.1 mV s⁻¹. The galvanostatic intermittent titration technique (GITT) was employed to analyze the apparent chemical reactions between electrolyte and electrode. The batteries were charge/discharge 1 cycle at a current of 0.05 C for 30 min and followed by 4 h relaxation until the voltage reached upper or lower limits.

Characterization Methods

Synchrotron X-ray diffraction (SXRD) measurements were performed at beamline 33-BM-C at the Advanced Photon Source (APS) of Argonne National Laboratory using a

constant wavelength of 0.729293 Å. The use of high-energy X-rays ($E = 21$ keV) minimizes absorption effects. The Rietveld refinements were performed using the TOPAS 5.0 software package (Bruker). The powder samples were packed and sealed into Kapton tape to avoid air exposure. SEM images and element mapping were obtained by using a Hitachi S-4800 field-emission scanning electron microscope (FE-SEM, acceleration voltage 5 kV) equipped with energy dispersive spectroscopy (EDS). X-ray absorption spectroscopy (XAS) measurements were conducted at the SGM beamline (11ID-1, 250-2000 eV) of Canadian Light Source (CLS). For LiF and InF_3 standard samples, absorption is measured using drain current in total electron yield (TEY) mode. The absorption of all the experimental samples is collected in fluorescence yield (FLY) mode. Scanning transmission X-ray microscopy (STXM) was carried out on the soft X-ray spectromicroscopy (SM, 130 ~ 2700 eV) beamline at CLS. The LCO/ $\text{Li}_3\text{InCl}_{4.8}\text{F}_{1.2}$ cathode composite powder (after 50 cycles) was ultrasonic dispersed in heptane for over one hour. SGM and STXM data were processed with Athena and aXis2000 software.

Density Functional Theory Methods

Sites occupancy ordering: The $\text{Li}_3\text{InCl}_{4.8}\text{F}_{1.2}$ sample can be indexed well with a distorted monoclinic rock-salt structure with the C2/m space group as Li_3InCl_6 (ICSD No. 89617), which has the partial occupancy of In at 4g/2a sites and F at 8j sites. To determine the sites occupancy, we employed the same ordering procedure as in previous studies.^[12, 34] Based on the structure and site occupancies from XRD refinement results, we enumerate all the possible structures in a primitive cell at composition of $\text{Li}_3\text{InCl}_5\text{F}$ using the pymatgen package.^[35] And then all the 69 symmetry independent structures were statically relaxed in the DFT calculations. The lowest energy structure is identified as ground state for other further calculations. The In ions tend to have a uniform distribution to have further distances to reduce Coulomb repulsion as the In-In pair correlation function for several low-energy structures in Figure 2c.

Electrochemical stability: The phase diagram was constructed to evaluate the stability of a material in equilibrium against external environment.^[36] To study the electrochemical stability, we identified the grand phase equilibria of solid electrolyte in equilibrium with

Li reservoir at chemical potential μ_{Li} referenced to Li metal. As in previous studies,^[37] the decomposition reaction energy at a given chemical potential μ_{Li} of element Li is calculated as:

$$\Delta E_{\text{D}}^{\text{open}}(\text{phase}, \mu_{\text{Li}}) = E_{\text{eq}}(C_{\text{eq}}(C, \mu_{\text{Li}})) - E(\text{phase}) - \Delta n_{\text{Li}} \cdot \mu_{\text{Li}}$$

Where $C_{\text{eq}}(C, \mu_{\text{Li}})$ is the phase equilibria of a given phase composition C at the given chemical potential of μ_{Li} . The electrochemical window of the phase was estimated as the range of μ_{Li} , where the phase is neither oxidized nor reduced.

Interface stability: The interface is considered as a pseudo binary of the solid electrolyte and the electrode as in previous study.^[14b, 37] The interface phase equilibria were evaluated along the energy minimum using the decomposition energy ΔE_{D} in the previous studies:

$$\Delta E_{\text{D}}(\text{SSE}, \text{electrode}, x) = E_{\text{eq}}(C_{\text{interface}}(C_{\text{SE}}, C_{\text{electrode}}, x)) - E_{\text{interface}}(\text{SE}, \text{electrode}, x)$$

where C_{SE} and $C_{\text{electrode}}$ are the compositions of SSE and electrode materials at the interface, normalized to one atom per formula. The x is the molar fraction of the SSE, since the phase equilibria and the reaction energies vary with the pseudo-binary composition, we identified the minimum of the reaction energy ($\Delta E_{\text{D},\text{min}}$) at molar fraction of x_{m} in the study. The $\Delta E_{\text{D},\text{min},\text{mutual}}$ and $\Delta E_{\text{D},\text{min},\text{total}}$ represent minimum interface decomposition energy excluding and including the decomposition energy of the SE and electrode, respectively. The energies of decomposed materials were obtained from MP database, and more details can be found in previous studies.^[14b, 37] We considered LiCoO_2 and $\text{Li}_{0.5}\text{CoO}_2$ as the discharged and charged states of the cathode material, respectively.^[14b]

Ab initio molecular dynamics simulation (AIMD): We performed AIMD simulation as our previous scheme.^[36b] The supercells with lattice parameters larger than 10 Å in each direction, non-spin mode and Γ -centered $1 \times 1 \times 1$ k-point grid were used. The initial temperature of simulations was set to 100 K and then the structures were heated to the target temperatures at a constant rate by velocity scaling during a period of 2 ps. All

simulations adopted the NVT ensemble with Nosé-Hoover thermostat.^[38] The lithium ionic conductivity was calculated following the Nernst–Einstein relation as:

$$\sigma = \frac{N q^2}{V k_B T} D = \frac{q^2}{V k_B T} \frac{\text{TMSD}(\Delta t)}{2d\Delta t}$$

where N is the number of the mobile carriers and d is the diffusion dimensionality which is 3 in our simulation, V is the volume of the model, q is the charge of the carrier, k_B is the Boltzmann constant, and T is the temperature, total mean square displacement (TMSD) represents the total diffusion of all lithium ions in the material. Arrhenius relation is used to get diffusion barrier and to evaluate the ionic conductivity at desired temperature

$$\sigma T = \sigma_0 \exp\left(\frac{-E_a}{k_B T}\right)$$

where E_a is activation energy, σ_0 is the pre-exponential factor. Given that the ion hopping is a stochastic process, the statistical deviations of the diffusivities were evaluated according to the values of TMSD in our previous report.^[39] The total time duration of AIMD simulations were within the range of 100 to 300 ps until the ionic diffusivity converged with relative standard deviation is from 20% to 30%.

Nudged Elastic Band Calculations (NEB): We performed NEB^[40] calculation for Li hopping between two adjacent octahedral sites through the intermediate tetrahedral sites, the only diffusion pathway observed in the AIMD. A Li ion was removed from the original structure to create a vacancy for Li-ion hopping with a background electron for charge compensation. We did static relaxation for initial and final structures with the same supercell, the energy convergence criterion was set to 10^{-7} eV and a force convergence criterion was set to $0.01 \text{ eV } \text{\AA}^{-1}$. And then five images were linearly interpolated between the initial and final structure for NEB calculation. The energy convergence criterion in NEB calculation was adjusted to 10^{-5} eV and the force convergence criterion was set to $0.05 \text{ eV } \text{\AA}^{-1}$. The energy barrier ΔE_b was calculated by the difference between the maximum and minimum energies along the entire oct-tet-oct migration pathway.

6.3 Results and discussion

6.3.1 Synthesis and Characterizations of $\text{Li}_3\text{InCl}_{4.8}\text{F}_{1.2}$ DHSE

$\text{Li}_3\text{InCl}_{4.8}\text{F}_{1.2}$ DHSE was obtained via a two-step solid reaction method. The first ball milling step was employed to mix the precursors, which is accompanied by the formation of partially crystallized products. Subsequently, a post annealing step at a relatively low temperature can improve the crystallinity and ionic conductivity.^[5b] Synchrotron X-ray diffraction (SXRD) ($\lambda = 0.729293 \text{ \AA}$) was used to study the phase composition of the products at different stages. As shown in **Figure 6.1a-1**, the diffraction peaks of the $\text{Li}_3\text{InCl}_{4.8}\text{F}_{1.2}$ DHSE obtained after annealing become obviously sharper than the ball milling sample (denoted as $\text{Li}_3\text{InCl}_{4.8}\text{F}_{1.2}$ BM), indicating improved crystallinity in the final product. Compared with the diffraction pattern of annealed Li_3InCl_6 without F incorporation, the peaks of $\text{Li}_3\text{InCl}_{4.8}\text{F}_{1.2}$ DHSE shift to higher 2θ angle (see the magnified regions in **Figures 6.1a-2 and 6.1a-3**), but are still assigned to a monoclinic phase (ICSD No. 04-009-9027). This suggests that the lattice space of $\text{Li}_3\text{InCl}_{4.8}\text{F}_{1.2}$ DHSE becomes contracted due to the partial replacement of Cl by F with a smaller ionic radius (F: 133 pm < Cl: 181 pm). SEM images depict a pelletized $\text{Li}_3\text{InCl}_{4.8}\text{F}_{1.2}$ with dense and compact morphology from the top-view observation (**Figure 6.1b-1** and **Figure S6.1**, Supporting Information). In sharp contrast, without the incorporation of F, the electrolyte particles are disconnected and there are several obvious cracks on the surface of the pelletized Li_3InCl_6 (**Figure 6.1b-2**). Such a morphological difference can also be verified in **Figure S6.2**, which depicts the porosity of $\text{Li}_3\text{InCl}_{4.8}\text{F}_{1.2}$ pellet is much lower than that of Li_3InCl_6 under various pressures. Therefore, $\text{Li}_3\text{InCl}_{4.8}\text{F}_{1.2}$ DHSE has an advantage over Li_3InCl_6 SE due to its intimate contact and confined effect with the cathode material.^[15] The energy dispersive X-ray spectroscopy (EDS) mapping of the $\text{Li}_3\text{InCl}_{4.8}\text{F}_{1.2}$ DHSE shows the most homogeneous dispersion of In, Cl, and F elements (**Figure 6.1c**), indicating the complete reaction of various precursors. The ionic conductivity of $\text{Li}_3\text{InCl}_{4.8}\text{F}_{1.2}$ DHSE is measured to be $5.1 \times 10^{-4} \text{ S cm}^{-1}$ at room temperature (**Figure 6.1d**), which is lower than that of the Li_3InCl_6 ($1.3 \times 10^{-3} \text{ S cm}^{-1}$), coordinating with their Li-ion diffusivity trend from AIMD simulations^[16] (**Figure S6.3**, Supporting Information). The Li-ion diffusion mechanism of the lower conductive

$\text{Li}_3\text{InCl}_{4.8}\text{F}_{1.2}$ DHSE is understood by Nudged Elastic Band (NEB) calculations. Compared with Li_3InCl_6 , F^- in $\text{Li}_3\text{InCl}_{4.8}\text{F}_{1.2}$ has shorter and stronger bonds with lithium, and induces local distortion in local Li coordination environment (**Figure 6.1e**). As a result, the changes in Li site energy with different Cl^-/F^- coordination increases the barriers for Li-ion migration (**Figure 6.1f**). Reduced ionic conductivity of the F-introduced electrolyte is also observed in the reported F-doped sulfide SEs.^[17] However, it is noted that the ionic conductivity of the $\text{Li}_3\text{InCl}_{4.8}\text{F}_{1.2}$ DHSE is significantly higher than that of all other reported fluoride-based SEs.^[6b] The electronic conductivity of the $\text{Li}_3\text{InCl}_{4.8}\text{F}_{1.2}$ was measured by a direct current (DC) polarization measurement (**Figure S6.4**, Supporting Information), which is $1.02 \times 10^{-9} \text{ S cm}^{-1}$. Combining the advantages of chloride and fluoride SEs, it is anticipated that the $\text{Li}_3\text{InCl}_{4.8}\text{F}_{1.2}$ DHSE can serve as an essential component in cathode composite, which can not only provide enough Li-ion flux for essential electrochemical reactions, but also increase the practical anodic stability with the assistant of fluorinating components at the interface.

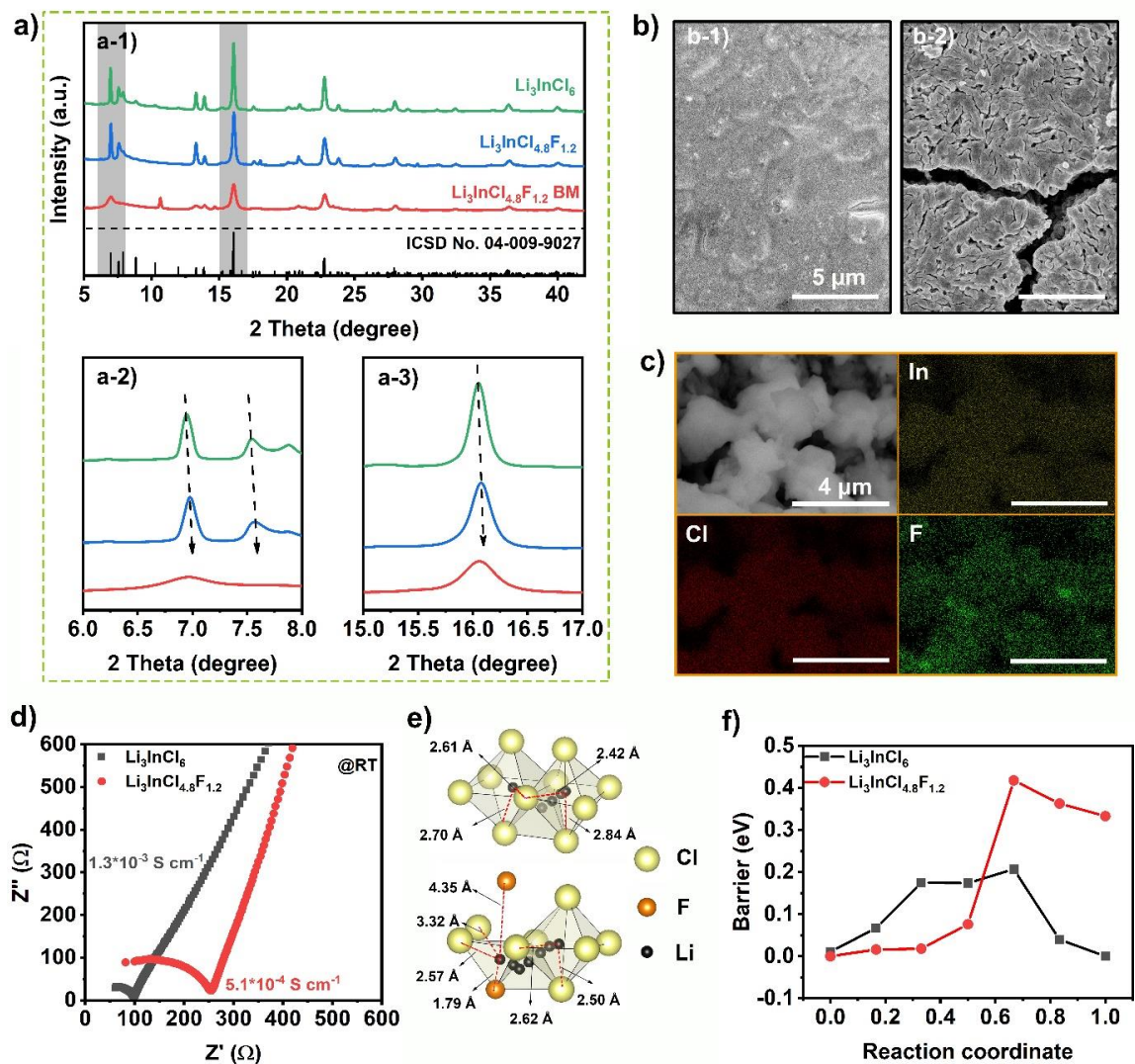


Figure 6.1 (a-1) SXRD ($\lambda=0.729293\text{\AA}$) patterns of the prepared $\text{Li}_3\text{InCl}_{4.8}\text{F}_{1.2}$ BM, $\text{Li}_3\text{InCl}_{4.8}\text{F}_{1.2}$, and Li_3InCl_6 powders and their corresponding magnified regions ((a-2) 6° to 8° and (a-3) 15° to 17°). (b) SEM images of pelletized (b-1) $\text{Li}_3\text{InCl}_{4.8}\text{F}_{1.2}$ DHSE and (b-2) Li_3InCl_6 SE, scale bar: 5 μm . (c) EDS elemental mapping of In, Cl, and F in the powder $\text{Li}_3\text{InCl}_{4.8}\text{F}_{1.2}$ sample, scale bar: 4 μm . (d) Nyquist plots of Li_3InCl_6 and $\text{Li}_3\text{InCl}_{4.8}\text{F}_{1.2}$ SEs at room temperature (RT). (e) The Li-ion migration pathways in the anion sublattice of Li_3InCl_6 (upper) and $\text{Li}_3\text{InCl}_{4.8}\text{F}_{1.2}$ (lower) structure, and (f) corresponding energy profiles of Li-ion migration.

To understand the structure of $\text{Li}_3\text{InCl}_{4.8}\text{F}_{1.2}$ DHSE, Rietveld refinement was conducted using the SXRD pattern in **Figure S6.5** and the corresponding crystal structure is shown in **Figure 6.2a**. A distorted rock-salt structure belonging to the monoclinic group ($C2/m$) is observed. Anions (Cl^- and F^-) are packed layer-by-layer to form edge-sharing octahedrons, where cation/vacancy fills each octahedral hole that is coordinated to six packing anion atoms. There are two symmetrically distinct Cl sites in $\text{Li}_3\text{InCl}_{4.8}\text{F}_{1.2}$, Cl3 (4i) and Cl6 (8j), and F is found to selectively occupy 16.2 % of the Cl6 site. The detailed crystallographic data and atom occupation results are displayed in **Table S6.1** and **S6.2**, respectively. Due to the participation of F and its small radius, the unit cell parameters of $\text{Li}_3\text{InCl}_{4.8}\text{F}_{1.2}$ ($a = 6.42009 \text{ \AA}$, $b = 11.07660 \text{ \AA}$, $c = 6.37873 \text{ \AA}$) reduce and the corresponding cell volume shrinks to 427.32 \AA^3 . The doping of F was also confirmed by F K-edge XAS. The spectrum arise from the photo-excited transitions of $\text{F } 1s \rightarrow 2p^{[18]}$, reflecting the local structure and bonding environment of F with the neighboring atoms. The corresponding changes can be determined by the shift of edge jump or the position of the first resonance (known as the whiteline^[19]). As shown in **Figure 6.2b**, multiple scattering features of F K-edge XAS of $\text{Li}_3\text{InCl}_{4.8}\text{F}_{1.2}$ resemble those for LiF, indicating F in the DHSE exists in a similar octahedral environment to that of LiF.^[20] However, compared to the spectra of LiF in the zoom-in figure, the whiteline of $\text{Li}_3\text{InCl}_{4.8}\text{F}_{1.2}$ shifts slightly to low energy ($\sim 0.4 \text{ eV}$) due to F bonding contribution with indium, which can be further confirmed by their derivative absorption spectrum in **Figure S6.6**. Therefore, co-existence of Li-F and In-F bonding is verified in the structure of $\text{Li}_3\text{InCl}_{4.8}\text{F}_{1.2}$. In addition, the structural stability of $\text{Li}_3\text{InCl}_{4.8}\text{F}_{1.2}$ was identified via first-principles calculations (see **Table S6.3** and **S6.4**, Supporting Information). Based on the XRD refinement results of $\text{Li}_3\text{InCl}_{4.8}\text{F}_{1.2}$, all the possible structures and site occupations in a primitive cell were enumerated and evaluated using DFT calculations. Uniform and sparse In^{3+} distribution to reduce Coulombic repulsion are observed in low-energy structures as shown in **Figure 6.2c-e**, which would benefit lithium diffusion by minimizing the effect of cation repulsion and blocking.^[5c, 21] The low-energy structures also have F ions occupy the diagonal 8j sites of In-centered octahedron, which agrees with the structures determined by the experiments in $\text{Li}_3\text{InCl}_{4.8}\text{F}_{1.2}$. These results provide

systematical information that F successfully substitutes partly of Cl to form $\text{Li}_3\text{InCl}_{4.8}\text{F}_{1.2}$ DHSE.

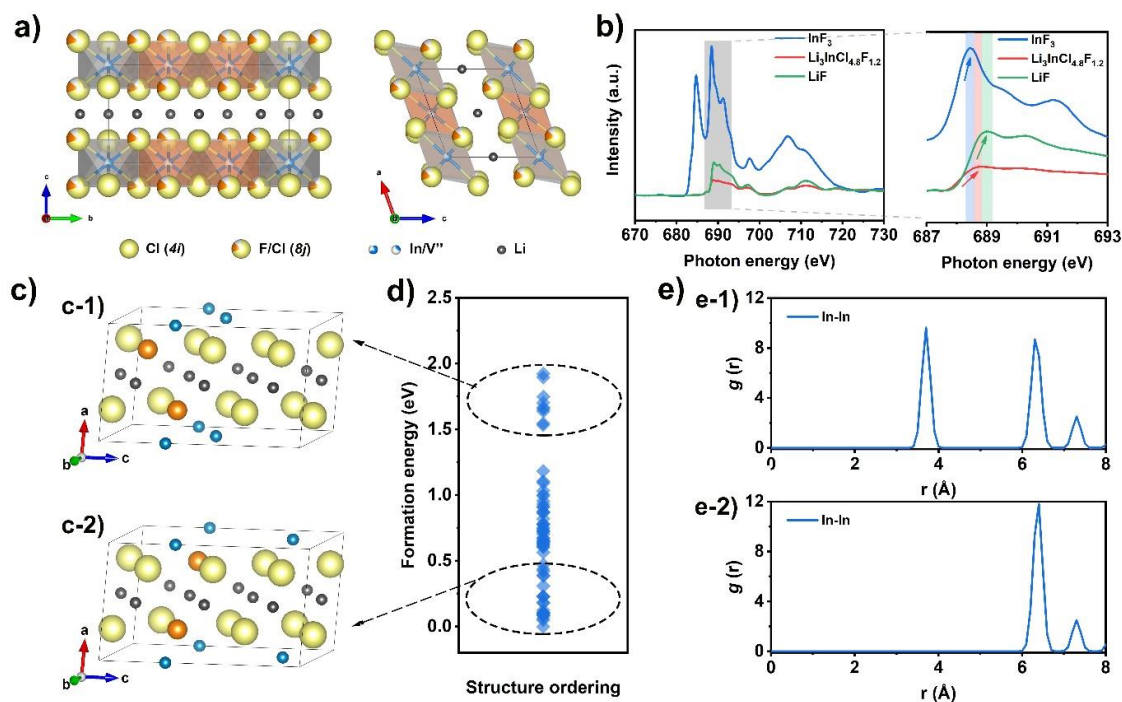


Figure 6.2 (a) Crystal structure of $\text{Li}_3\text{InCl}_{4.8}\text{F}_{1.2}$ from the view that is parallel to a axis and b axis, respectively. (b) F K-edge XAS spectra at $\text{Li}_3\text{InCl}_{4.8}\text{F}_{1.2}$ and standard samples (LiF and InF_3). First-principles calculations results: (c) $\text{Li}_3\text{InCl}_{4.8}\text{F}_{1.2}$ unit cells with (c-1) high-energy and (c-2) low-energy In-F sublattice. (d) Calculated formation energy of two In-F disordering in $\text{Li}_3\text{InCl}_{4.8}\text{F}_{1.2}$ versus the structure ordering which is referenced to the lowest-energy structure unit cell. (e) In-In pair correlation function $g(r)$ for (e-1) high-energy and (e-2) low-energy structures.

6.3.2 Electrochemical Stability

The electrochemical stability of SEs is evaluated by the linear sweep voltammetry (LSV) with asymmetric cell using carbon black (CB)/SE composites as the working electrode and lithium metal as the counter/reference electrode. The introduced CB in the working electrode can provide sufficient electron transport, thus precisely monitoring the reaction

potentials.^[22] **Figure 6.3a** shows the anodic (positive) scan curve (scan rate: 0.1 mV s⁻¹) of the cells with CB/Li₃InCl_{4.8}F_{1.2} and CB/Li₃InCl₆ working electrodes. For the Li₃InCl_{4.8}F_{1.2} cell, the anodic potential is defined^[23] to be ~4.3 V, from which a negligible Faradaic current appears due to the oxidation reaction at the electrode. Notably, the LSV curve exhibits a plateau with the anodic current as small as 0.6 mA g⁻¹ in the following potential range (~4.3 V – 7 V). This constant small current is probably due to the Nonfaradaic current which is caused by the passivating interface established at the electrode.^[24] In the subsequent second anodic scan, the I-V curve is linear and no oxidation peaks are found (**Figure S6.7**, Supporting Information), further verifying that the in-situ generation of a passivating interface during the first LSV process is stable and can prevent the further interfacial reactions between the Li₃InCl_{4.8}F_{1.2} DHSE and CB. In sharp contrast, the onset potential of the Li₃InCl₆ cell occurs prior to that of the Li₃InCl_{4.8}F_{1.2} cell and the oxidation of Li₃InCl₆ becomes increasingly serious from ~4.3 V to 7 V, suggesting continuous and severe degradation of the Li₃InCl₆ SE. Moreover, the anodic stability difference is quantified by integrating the current density from 2.6 V – 7 V. The integrated current of Li₃InCl_{4.8}F_{1.2} is 1.726 mA V g⁻¹, which is one fifth smaller than that of Li₃InCl₆, indicating significantly improved anodic stability of the Li₃InCl_{4.8}F_{1.2} DHSE.

First principles computation was employed to understand the enhanced electrochemical stability of Li₃InCl_{4.8}F_{1.2} DHSE again CB at varying applied voltages. Based on the thermodynamic equilibrium voltage profile (**Figure S6.8**, Supporting Information), the calculated anodic potential of Li₃InCl_{4.8}F_{1.2} DHSE is 4.42 V, which is close to the experimental value where oxidation begin to happen in **Figure 6.3a**. Despite the oxidation potential of the Li₃InCl_{4.8}F_{1.2} DHSE itself depends on the redox of Cl (-1)/Cl (0) at 4.42 V, its practical anodic limit and the practical electrochemical window are dominated by the in-situ derived passivating interface. **Figure 6.3b** depicts the calculated phase equilibria of Li₃InCl_{4.8}F_{1.2} DHSE at different Li/Li⁺ potentials. The pre-stored F in Li₃InCl_{4.8}F_{1.2} DHSE near the interface contribute to the formation of fluorinating interphase.^[25] Specifically, LiF is expected to firstly generate once the oxidation of DHSE occurs, followed by LiInF₄ and InF₃ at around 4.43 V and 4.54 V, respectively. The thermodynamic electrochemical stability window and anodic limit of F-containing

compounds (such as LiF , LiInF_4 , and LiInF_6) are calculated in **Figure 6.3c**. All of them feature wide electrochemical stability window with ultrahigh anodic limits $> 6 \text{ V}$, thus these F-containing compounds are key components for passivating interphase layers. Together, these reaction products enable an extended electrochemical stability window to compensate for the thermodynamic intrinsic anodic limit of $\text{Li}_3\text{InCl}_{4.8}\text{F}_{1.2}$ DHSE to achieve an ultrahigh anodic limit over 6 V . In consistency with the LSV observations, the formation of F-containing passivating interphases protects $\text{Li}_3\text{InCl}_{4.8}\text{F}_{1.2}$ DHSE from further decomposition and strengthen its oxidation stability.

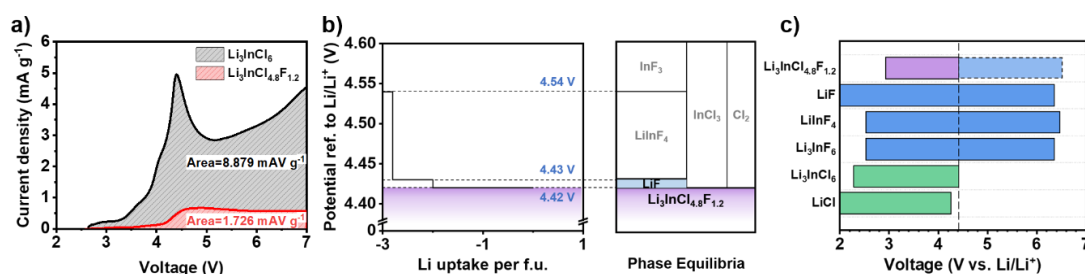


Figure 6.3 (a) LSV analysis of the Li_3InCl_6 SE and $\text{Li}_3\text{InCl}_{4.8}\text{F}_{1.2}$ DHSE from open circuit voltage (OCV) to 7 V. The dashed area represents the integral spectrum intensity of each material. (b) Phase equilibria of $\text{Li}_3\text{InCl}_{4.8}\text{F}_{1.2}$ DHSE at different Li/Li^+ potentials based on the first principles computation. (c) The calculated thermodynamics electrochemical stability windows of $\text{Li}_3\text{InCl}_{4.8}\text{F}_{1.2}$, LiF , LiInF_4 , In_3InF_6 , Li_3InCl_6 , and LiCl .

6.3.3. Full Battery Performance

To demonstrate the applicability of the $\text{Li}_3\text{InCl}_{4.8}\text{F}_{1.2}$ DHSE in high-voltage ASSLIBs, we utilized $\text{Li}_3\text{InCl}_{4.8}\text{F}_{1.2}$ as cathode electrolyte, matching a commercialized high-voltage LCO (designed cut-off voltage: 4.47 V) to fabricate bulk-type halide-based ASSLIBs. It is noted that the liquid-electrolyte half-cell using the high-voltage LCO as the cathode material was firstly assembled, and the cycling stability was evaluated as shown in **Figure S6.9**. The negligible capacity decay during 100 cycles indicates the good structural stability of the high-voltage LCO cathode material. Room-temperature

galvanostatic measurements were conducted on the In//Li₃InCl₆//Li₃InCl_{4.8}F_{1.2}/LCO all-solid-state full cells in the voltage range of 2.6 – 4.47 V (vs. Li/Li⁺). **Figure 6.4a** depicts the charge and discharge profiles of the full cell in the first three cycles at a low current density of 0.063 mA cm⁻². An initial reversible specific capacity of 160.6 mAh g⁻¹ is achieved with a high Coulombic efficiency of 92%. The cyclic voltammetry (CV) test for the ASSLIB was conducted to exhibit the highly reversible lithiation and de-lithiation process (**Figure S6.10**, Supporting Information). Additionally, the cycling performance of ASSLIBs with different cathode electrolytes is depicted in **Figure 6.4b**. It is obvious to find that the cycling stability of the cell with Li₃InCl_{4.8}F_{1.2} is remarkably improved in comparison with the full cell using Li₃InCl₆ as the electrolyte in the cathode composite. The reversible specific capacity slightly drops to 140.0 mAh g⁻¹ after the initial five cycles and a value of 102 mAh g⁻¹ can be retained after 70 cycles. Notably, the average Coulombic efficiency reaches 99.5% during this long cycling process, confirming highly reversible Li-ion intercalation/de-intercalation behavior once the stabilized and Li-ion conductive passivation layer forms. Furthermore, Galvanostatic intermittent titration technique (GITT) was employed to verify the low polarization of Li-ion (de)intercalation toward the LCO cathode materials in the presence of Li₃InCl_{4.8}F_{1.2} DHSE (**Figure S6.11a**, Supporting Information). The Coulombic efficiency of the GITT charge-discharge process reaches as high as 89%, suggesting a good charge/discharge reversibility of the full cells.^[26] The cathode composite with Li₃InCl_{4.8}F_{1.2} shows lower polarization than that with Li₃InCl₆ during the discharging process, which indicates the interfacial stability between Li₃InCl_{4.8}F_{1.2} and LCO. (**Figure S6.11b**, Supporting Information). To fully utilize the high practical anodic stability of Li₃InCl_{4.8}F_{1.2} DHSE, a rigorous charging protocol with a cut-off voltage of 4.8 V (vs. Li/Li⁺) was applied to the Li₃InCl_{4.8}F_{1.2} cell. The comparison of charge-discharge behaviors between Li₃InCl_{4.8}F_{1.2} and Li₃InCl₆ cells is exhibited in **Figure 6.4c**. Li₃InCl_{4.8}F_{1.2} cell delivers a reversible capacity of 203.7 mAh g⁻¹ with the initial Coulombic efficiency of 89.2%, higher than that of the Li₃InCl₆ cell. After a low-rate activation process, the capacity of Li₃InCl₆ cell drops and the polarization dramatically increases at 10th and 20th cycles, while the Li₃InCl_{4.8}F_{1.2} cell maintains a decent cycling performance over 70 cycles (**Figure 6.4d**) despite the capacity decay possibly caused by the structural instability of LCO materials

over 4.47 V. These results further prove the excellent interfacial stability between LCO and $\text{Li}_3\text{InCl}_{4.8}\text{F}_{1.2}$, which evokes the high capacity of LCO cathode materials at high voltages. To the best of our knowledge, the aforementioned high cut-off voltage is higher than any reported charging protocols previously reported with LCO-based cathode materials, and the delivered capacity as well as the durability both are among the best reported performances in high-voltage ASSLBs field (Table S6.5, Supporting Information).

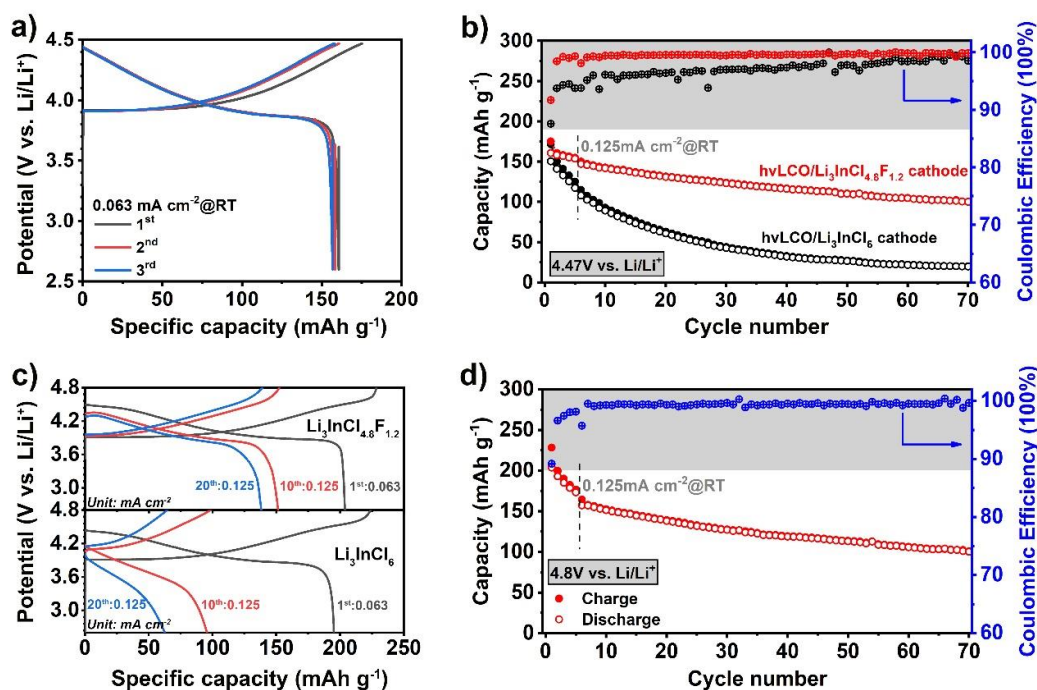


Figure 6.4 Electrochemical performance of the full cells using $\text{Li}_3\text{InCl}_{4.8}\text{F}_{1.2}$ and Li_3InCl_6 cathode SE. (a) the first three discharge/charge curves of $\text{Li}_3\text{InCl}_{4.8}\text{F}_{1.2}$ cathode SE cell. (b) Cycling performance of $\text{Li}_3\text{InCl}_{4.8}\text{F}_{1.2}$ and Li_3InCl_6 cathode SE cells in the voltage range of 2.6 – 4.47 V (vs. Li/Li^+) (first 5 cycles at 0.063 mA cm^{-2}). (c) Charge-discharge profiles of $\text{Li}_3\text{InCl}_{4.8}\text{F}_{1.2}$ (upper) and Li_3InCl_6 (lower) cathode SE cells at 1st, 10th, and 20th cycles in the voltage range of 2.6 – 4.8 V (vs. Li/Li^+). (d) Cycling performance of $\text{Li}_3\text{InCl}_{4.8}\text{F}_{1.2}$ cathode SE cell charged at 4.8 V (vs. Li/Li^+) (first 5 cycles at 0.063 mA cm^{-2}).

6.3.4. Mechanism behind high-voltage stability

A fundamental understanding behind the nature of the high-voltage-stable passivation layer was achieved via various spectroscopic, thermodynamic, and electrochemical characterizations. **Figure 6.5a** depicts the F K-edge XAS of the cycled LCO/Li₃InCl_{4.8}F_{1.2} cathode composites (after 1 cycle and 10 cycles) in fluorescence yield (FLY) mode. They show similar six-coordinating features in the extended spectral region compared with the pristine Li₃InCl_{4.8}F_{1.2} DHSE. Precise identification is shown in a magnified plot in **Figure S6.12**. The 1-cycle and 10-cycle LCO/Li₃InCl_{4.8}F_{1.2} samples have the same absorption threshold (E_0) and whiteline position, but blue-shift compared with the F K-edge spectrum of the pristine Li₃InCl_{4.8}F_{1.2} DHSE. This suggests that a passivating CEI is electrochemically generated after the first cycle and maintains stable in the subsequent cycles. In comparison with the standard LiF (E_0 is marked by black vertical line)^[27], both two cycled samples (1-cycle and 10-cycle) show a low-energy-shift (red shift) absorption edge, which can be tracked in the first derivative XAS plot (**Figure 6.5b**) and quantified as 0.25 eV, providing further evidence that a considerable amount of LiF is probably generated as the component of the CEI layer. The flat F K-pre-edge feature also suggests the existence of rather weak metal-ligand bonds, excluding the generation of LiInF₄ and InF₃.^[28] In order to further identify the distribution and composition of the CEI, synchrotron-based STXM was utilized to measure the transmitted intensity at 50-cycle LCO particles.^[29] As shown in **Figure S6.13**, A single LCO particle (dark area) was firstly screened in conventional STXM at the photon energy of 780 eV (the energy of Co L-edge). Then, STXM-ptychography technique^[30] is adopted, which demonstrates high-resolution transmission images of the single LCO particle in the photon energy between 681.5 and 691.5 eV (**Figure S6.14**, Supporting Information). A reconstructed image at the photon energy of 688.5 eV (close to the absorption energy of F K-edge) is picked and displayed in **Figure 6.5c**. STXM mapping of F shown in **Figure 6.5d** visualizes the CEI layer in-situ formed on one single LCO particle, which displays a relatively homogenous distribution of F on the cathode surface. Such distributions proceed from F K-edge absorption spectra via conventional STXM mode, which provide detailed information for the CEI composition. Various positions (marked from a to g in **Figure 6.5c**) were selected around the LCO particle and the

corresponding spectra of F K-edge are plotted in **Figure 6.5e**. It is found that the seven spectra have same E_0 as that of the standard LiF, revealing that LiF is the major compound of the in-situ generated CEI layer. In addition, thermodynamic analyses based on first principles computation^[12, 14b] were applied to study the LCO/Li₃InCl_{4.8}F_{1.2} interface at charged and discharged states. As shown in **Table 6.1**, the minimum mutual reaction energies ($\Delta E_{D, \text{min, mutual}}$) of Li₃InCl_{4.8}F_{1.2} against LCO are as small as -15 meV at discharged (lithiation) state and -7 meV at charged (delithiation) state, respectively. The calculated phase equilibria components of LCO/Li₃InCl_{4.8}F_{1.2} are largely similar with those of the LCO/Li₃InCl₆ interface; however, the major difference is that the side-reaction products of LCO/Li₃InCl_{4.8}F_{1.2} contain LiF. The excellent stability of LiF against LCO can be quantified as 0 meV decomposition energy both in charged and discharged states, thus leading to the enhanced interfacial stability of LCO/Li₃InCl_{4.8}F_{1.2}, especially under ultrahigh-voltage status.

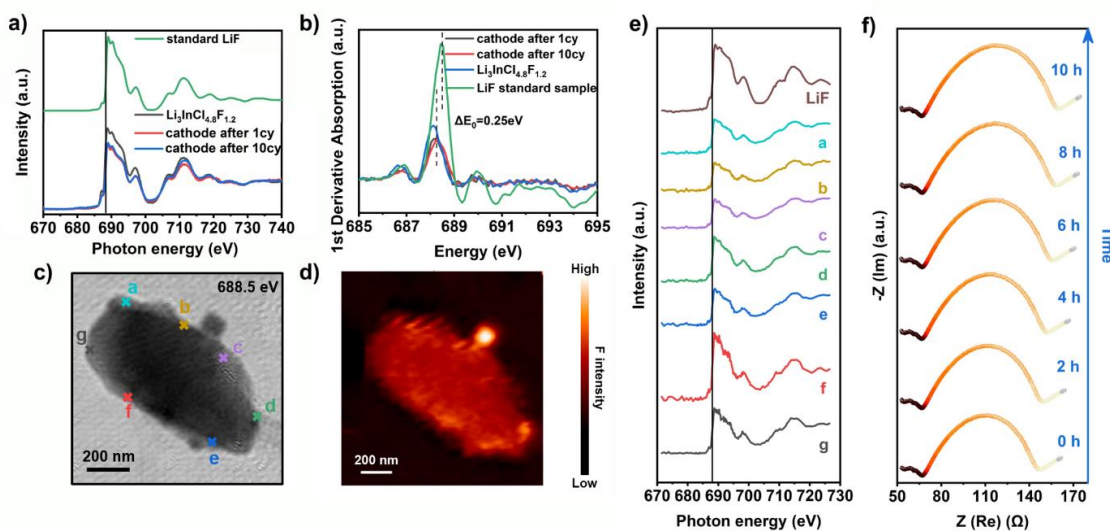


Figure 6.5 Synchrotron spectroscopic analyses for standard LiF, Li₃InCl_{4.8}F_{1.2}, LCO/Li₃InCl_{4.8}F_{1.2} cathode composites after 1st, 10th, and 50th cycling processes: (a) F K-edge XAS (the E_0 of standard LiF is marked by the black vertical line) and (b) first derivative absorption spectra. (c) X-ray ptychography and (d) STXM mapping images of a single 50-cycle LCO particle at 688.5 eV, pixel size: 5.7 nm. (e) F K-edge XAS at 7 marked positions (a-g) in (c) compared with that of the standard LiF. (f) The periodic

EIS results during a constant-voltage charging (CVC) test process at 4.47 V, time scale indicates the time of CVC processes.

Table 6.1 Phase equilibria and minimum decomposition energies of the $\text{Li}_3\text{InCl}_{4.8}\text{F}_{1.2}$, Li_3InCl_6 , LiF , LiInF_4 , and Li_3InF_6 materials at the interface with LiCoO_2 cathode materials under charged and discharged status.

C_{SE}	LCO		Phase equilibria at x_m	$\Delta E_{\text{D, min, mutual}}$ (meV/atom)
	cathode status	x_m		
$\text{Li}_3\text{InCl}_{4.8}\text{F}_{1.2}$	discharged	0.83	$\text{Li}(\text{CoO}_2)_2$, InClO , Co_3O_4 , Li_3InCl_6 , LiF	-15
	charged	0.77	$\text{Li}(\text{CoO}_2)_2$, InClO , Co_3O_4 , Li_3InCl_6 , LiF	-7
Li_3InCl_6	discharged	0.5	$\text{Li}(\text{CoO}_2)_2$, InClO , Co_3O_4 , LiCl	-4
	charged	--	$\text{Li}(\text{CoO}_2)_2$, Li_3InCl_6 (stable)	0
LiF	discharged	--	LiCoO_2 , LiF (stable)	0
	charged	--	$\text{Li}(\text{CoO}_2)_2$, LiF (stable)	0
LiInF_4	discharged	0.29	In_2O_3 , Co_3O_4 , $\text{Li}(\text{CoO}_2)_2$, LiF	-51
	charged	--	$\text{Li}(\text{CoO}_2)_2$, LiInF_4 (stable)	0
Li_3InF_6	discharged	0.40	In_2O_3 , Co_3O_4 , $\text{Li}(\text{CoO}_2)_2$, LiF	-61

charged	--	LiCoO ₂ , Li ₃ InF ₆ (stable)	0
---------	----	--	---

To further demonstrate the high-voltage stability of Li₃InCl_{4.8}F_{1.2} DHSE in ASSLIBs, we designed a constant-voltage protocol to monitor the impedance change of a full cell during an aging process at high-voltage status. Once the full cell was charged to 4.47 V (vs. Li/Li⁺), a periodic 2-hour constant-voltage charging (CVC) and 2-hour rest (to equilibrium state) were applied then followed by EIS measurements. The according EIS plots after the periodic rests are displayed in **Figure 6.5f**. The total impedance in each period shows negligible changes and almost keeps the same value of ~150 Ω, indicating the F-rich CEI layer formed in the initial charging process effectively prevents further interfacial reactions between the Li₃InCl_{4.8}F_{1.2} DHSE and fully charged LCO cathode. Combining the findings from the abovementioned discussions, Li₃InCl_{4.8}F_{1.2} DHSE is demonstrated showing great potential in ultrahigh-voltage ASSLIBs, which can be achieved by transforming the contact surface of Li₃InCl_{4.8}F_{1.2} DHSE into F-rich CEI layer to stabilize the cathode material/DHSE interface at high operating voltages.^[31]

6.4 Conclusion

In summary, we developed a strategy to design a DHSE that can enable ultrahigh-voltage ASSLIBs. F is introduced in a halide SE and selectively occupies part of the Cl sites to form a morphologically dense Li₃InCl_{4.8}F_{1.2} DHSE, which shows a good ionic conductivity of $5.1 \times 10^{-4} \text{ S cm}^{-1}$ at room temperature and high practical anodic stability over 6 V. Both experimental and computational results identify that F-containing passivating components are generated from Li₃InCl_{4.8}F_{1.2} DHSE at an applied potential, protecting the Li₃InCl_{4.8}F_{1.2} from further decomposition and extending its anodic stability window. As a proof of concept, this Li₃InCl_{4.8}F_{1.2} DHSE is demonstrated in high-voltage ASSLIBs, performing good cycling stability at room temperature. Spectroscopic, computational, and electrochemical characterizations are utilized to deeply understand the practical electrochemical stability of Li₃InCl_{4.8}F_{1.2} and high-voltage stability of full cells. Rich F-containing passivating interphases are proved to generate in-situ on the

cathode interface and prevent further interfacial reactions at high-voltages, contributing to promising cycling stability in full cells. This work presents a new DHSE with outstanding practical anodic stability, paving the way for rapid development and wide application of all-solid-state batteries at ultrahigh operational voltages.

6.5 Acknowledgments

This research was supported by the Natural Sciences and Engineering Research Council of Canada (NSERC), the Canada Research Chair Program (CRC), the Canada Foundation for Innovation (CFI), Ontario Research Foundation (ORF), China Automotive Battery Research Institute Co., Ltd., Glatat Solid-State Battery Inc., and the University of Western Ontario (UWO). The synchrotron research was performed at the SGM and SM beamlines of the Canadian Light Source, a national research facility of the University of Saskatchewan, which is supported by the CFI, NSERC, the National Research Council (NRC), the Canadian Institutes of Health Research (CIHR), the Government of Saskatchewan, and the University of Saskatchewan. Synchrotron XRD data were collected at the X-ray Science Division Beamline 33 BM-C at the Advanced Photon Source, Argonne National Laboratory. Y.M acknowledges the support from National Science Foundation under award No. 1550423 and the computational facilities from the University of Maryland supercomputing resources, the Maryland Advanced Research Computing Center (MARCC). The authors also appreciate the great help from the SGM beamline scientists at Canadian Light Source.

6.6 References

- [1]a) Q. Zhao, S. Stalin, C. Z. Zhao, L. A. Archer, *Nat. Rev. Mater.* 2020, 5, 229; b) R. S. Chen, Q. H. Li, X. Q. Yu, L. Q. Chen, H. Li, *Chem. Rev.* 2020, 120, 6820.
- [2]a) M. Li, C. S. Wang, Z. W. Chen, K. Xu, J. Lu, *Chem. Rev.* 2020, 120, 6783; b) W. Zhao, J. Yi, P. He, H. Zhou, *Electrochem. Energ. Rev.* 2019, 2, 574.
- [3]a) Q. Zhang, D. X. Cao, Y. Ma, A. Natan, P. Aurora, H. L. Zhu, *Adv. Mater.* 2019, 31, 1901131; b) N. Kamaya, K. Homma, Y. Yamakawa, M. Hirayama, R. Kanno, M. Yonemura, T. Kamiyama, Y. Kato, S. Hama, K. Kawamoto, A. Mitsui, *Nat. Mater.* 2011, 10, 682; c) Y. Kato, S. Hori, T. Saito, K. Suzuki, M. Hirayama, A. Mitsui, M. Yonemura, H. Iba, R. Kanno, *Nat. Energy* 2016, 1, 16030.
- [4]a) A. Manthiram, X. W. Yu, S. F. Wang, *Nat. Rev. Mater.* 2017, 2, 1; b) Y. H. Xiao, Y. Wang, S. H. Bo, J. C. Kim, L. J. Miara, G. Ceder, *Nat. Rev. Mater.* 2020, 5, 105.

- [5]a) T. Asano, A. Sakai, S. Ouchi, M. Sakaida, A. Miyazaki, S. Hasegawa, *Adv. Mater.* 2018, 30, 1803075; b) X. N. Li, J. W. Liang, J. Luo, M. N. Banis, C. H. Wang, W. H. Li, S. X. Deng, C. Yu, F. P. Zhao, Y. F. Hu, T. K. Sham, L. Zhang, S. Q. Zhao, S. G. Lu, H. Huang, R. Y. Li, K. R. Adair, X. L. Sun, *Energy Environ. Sci.* 2019, 12, 2665; c) J. Liang, X. Li, S. Wang, K. R. Adair, W. Li, Y. Zhao, C. Wang, Y. Hu, L. Zhang, S. Zhao, S. Lu, H. Huang, R. Li, Y. Mo, X. Sun, *J. Am. Chem. Soc.* 2020, 142, 7012; d) L. D. Zhou, C. Y. Kwok, A. Shyamsunder, Q. Zhang, X. H. Wu, L. F. Nazar, *Energy Environ. Sci.* 2020, 13, 2056.
- [6]a) X. N. Li, J. W. Liang, N. Chen, J. Luo, K. R. Adair, C. H. Wang, M. N. Banis, T. K. Sham, L. Zhang, S. Q. Zhao, S. G. Lu, H. Huang, R. Y. Li, X. L. Sun, *Angew. Chem. Int. Ed.* 2019, 58, 16427; b) J. L. Hu, Z. G. Yao, K. Y. Chen, C. L. Li, *Energy Stor. Mater.* 2020, 28, 37.
- [7]M. Feinauer, H. Euchner, M. Fichtner, M. A. Reddy, *ACS Appl. Energy Mater.* 2019, 2, 7196.
- [8]R. Schlem, S. Muy, N. Prinz, A. Banik, Y. Shao-Horn, M. Zobel, W. G. Zeier, *Adv. Energy Mater.* 2020, 10, 1903719.
- [9]X. N. Li, J. W. Liang, X. F. Yang, K. R. Adair, C. H. Wang, F. P. Zhao, X. L. Sun, *Energy Environ. Sci.* 2020, 13, 1429.
- [10]K. H. Park, K. Kaup, A. Assoud, Q. Zhang, X. H. Wu, L. F. Nazar, *ACS Energy Lett.* 2020, 5, 533.
- [11]H. Kwak, D. Han, J. Lyoo, J. Park, S. H. Jung, Y. Han, G. Kwon, H. Kim, S. T. Hong, K. W. Nam, Y. S. Jung, *Adv. Energy Mater.* 2021, 11, 2003190.
- [12]S. Wang, Q. Bai, A. M. Nolan, Y. Liu, S. Gong, Q. Sun, Y. Mo, *Angew. Chem. Int. Ed.* 2019, 58, 8039.
- [13]a) S. P. Culver, R. Koerver, W. G. Zeier, J. Janek, *Adv. Energy Mater.* 2019, 9, 1900626; b) Y. H. Xiao, L. J. Miara, Y. Wang, G. Ceder, *Joule* 2019, 3, 1252.
- [14]a) Y. Zhao, K. Zheng, X. L. Sun, *Joule* 2018, 2, 2583; b) Y. Z. Zhu, X. F. He, Y. F. Mo, *J. Mater. Chem. A* 2016, 4, 3253.
- [15]F. Mo, J. Ruan, S. Sun, Z. Lian, S. Yang, X. Yue, Y. Song, Y. N. Zhou, F. Fang, G. Sun, S. Peng, D. Sun, *Adv. Energy Mater.* 2019, 9, 1902123.
- [16]a) J. Kang, B. Han, *J. Phys. Chem. Lett* 2016, 7, 2671; b) K. Nam, H. Chun, J. Hwang, B. Han, *ACS Sustainable Chem. Eng.* 2020, 8, 3321.
- [17]F. P. Zhao, Q. Sun, C. Yu, S. M. Zhang, K. Adair, S. Z. Wang, Y. L. Liu, Y. Zhao, J. W. Liang, C. H. Wang, X. N. Li, X. Li, W. Xia, R. Y. Li, H. Huang, L. Zhang, S. Q. Zhao, S. G. Lu, X. L. Sun, *ACS Energy Lett.* 2020, 5, 1035.
- [18]Y. Gao, T. Tiedje, P. C. Wong, K. A. R. Mitchell, *Phys. Rev. B* 1993, 48, 15578.
- [19]T. K. Sham, *Acc. Chem. Res.* 1986, 19, 99.

- [20]B. Q. Wang, J. Liu, M. N. Banis, Q. Sun, Y. Zhao, R. Y. Li, T. K. Sham, X. L. Sun, *ACS Appl. Mater. Interfaces* 2017, 9, 31786.
- [21]Y. S. Liu, S. Wang, A. M. Nolan, C. Ling, Y. F. Mo, *Adv. Energy Mater.* 2020, 10, 2002356.
- [22]G. F. Dewald, S. Ohno, M. A. Kraft, R. Koerver, P. Till, N. M. Vargas-Barbosa, J. Janek, W. G. Zeier, *Chem. Mater.* 2019, 31, 8328.
- [23]F. Wu, W. Fitzhugh, L. H. Ye, J. X. Ning, X. Li, *Nat. Commun.* 2018, 9, 1.
- [24]G. B. Qu, T. Xia, W. H. Zhou, X. Zhang, H. Y. Zhang, L. G. Hu, J. B. Shi, X. F. Yu, G. B. Jiang, *Chem. Rev.* 2020, 120, 2288.
- [25]X. L. Fan, L. Chen, X. Ji, T. Deng, S. Y. Hou, J. Chen, J. Zheng, F. Wang, J. J. Jiang, K. Xu, C. S. Wang, *Chem* 2018, 4, 174.
- [26]Y. Yang, X. Qu, X. Zhang, Y. Liu, J. Hu, J. Chen, M. Gao, H. Pan, *Adv. Mater.* 2020, 32, 1908285.
- [27]R. M. Qiao, I. T. Lucas, A. Karim, J. Syzdek, X. S. Liu, W. Chen, K. Persson, R. Kostecki, W. L. Yang, *Adv. Mater. Interfaces* 2014, 1, 1300115.
- [28]P. Olalde-Velasco, J. Jimenez-Mier, J. Denlinger, W. L. Yang, *Phys. Rev. B* 2013, 87, 245136.
- [29]J. Wang, J. Zhou, Y. F. Hu, T. Regier, *Energy Environ. Sci.* 2013, 6, 926.
- [30]a) D. A. Shapiro, Y. S. Yu, T. Tyliczszak, J. Cabana, R. Celestre, W. L. Chao, K. Kaznatcheev, A. L. D. Kilcoyne, F. Maia, S. Marchesini, Y. S. Meng, T. Warwick, L. L. Yang, H. A. Padmore, *Nat. Photonics* 2014, 8, 765; b) Y. S. Yu, C. Kim, D. A. Shapiro, M. Farmand, D. Qian, T. Tyliczszak, A. L. D. Kilcoyne, R. Celestre, S. Marchesini, J. Joseph, P. Denes, T. Warwick, F. C. Strobridge, C. P. Grey, H. Padmore, Y. S. Meng, R. Kostecki, J. Cabana, *Nano Lett.* 2015, 15, 4282.
- [31]a) C. S. Wang, Y. S. Meng, K. Xu, *J. Electrochem. Soc.* 2018, 166, A5184; b) X. L. Fan, X. Ji, L. Chen, J. Chen, T. Deng, F. D. Han, J. Yue, N. Piao, R. X. Wang, X. Q. Zhou, X. Z. Xiao, L. X. Chen, C. S. Wang, *Nat. Energy* 2019, 4, 882.
- [32]K. H. Park, D. Y. Oh, Y. E. Choi, Y. J. Nam, L. L. Han, J. Y. Kim, H. L. Xin, F. Lin, S. M. Oh, Y. S. Jung, *Adv. Mater.* 2016, 28, 1874.
- [33]F. Zhao, Y. Zhao, J. Wang, Q. Sun, K. Adair, S. Zhang, J. Luo, J. Li, W. Li, Y. Sun, X. Li, J. Liang, C. Wang, R. Li, H. Huang, L. Zhang, S. Zhao, S. Lu, X. Sun, *Energy Stor. Mater.* 2020, 33, 139.
- [34]X. F. He, Y. F. Mo, *Phys. Chem. Chem. Phys.* 2015, 17, 18035.
- [35]S. P. Ong, W. D. Richards, A. Jain, G. Hautier, M. Kocher, S. Cholia, D. Gunter, V. L. Chevrier, K. A. Persson, G. Ceder, *Comp. Mater. Sci.* 2013, 68, 314.
- [36]a) H. Tang, Z. Deng, Z. Lin, Z. Wang, I.-H. Chu, C. Chen, Z. Zhu, C. Zheng, S. P. Ong, *Chem. Mater.* 2017, 30, 163; b) Y. F. Mo, S. P. Ong, G. Ceder, *Chem. Mater.* 2012, 24, 15.

- [37]Y. Z. Zhu, X. F. He, Y. F. Mo, ACS Appl. Mater. Interfaces 2015, 7, 23685.
[38]S. Nose, Prog. Theor. Phys. Supp. 1991, 103, 1.
[39]X. F. He, Y. Z. Zhu, A. Epstein, Y. F. Mo, npj Comput. Mater. 2018, 4, 18.
[40]G. Henkelman, H. Jonsson, J. Chem. Phys. 2000, 113, 9978.

6.7 Supporting Information

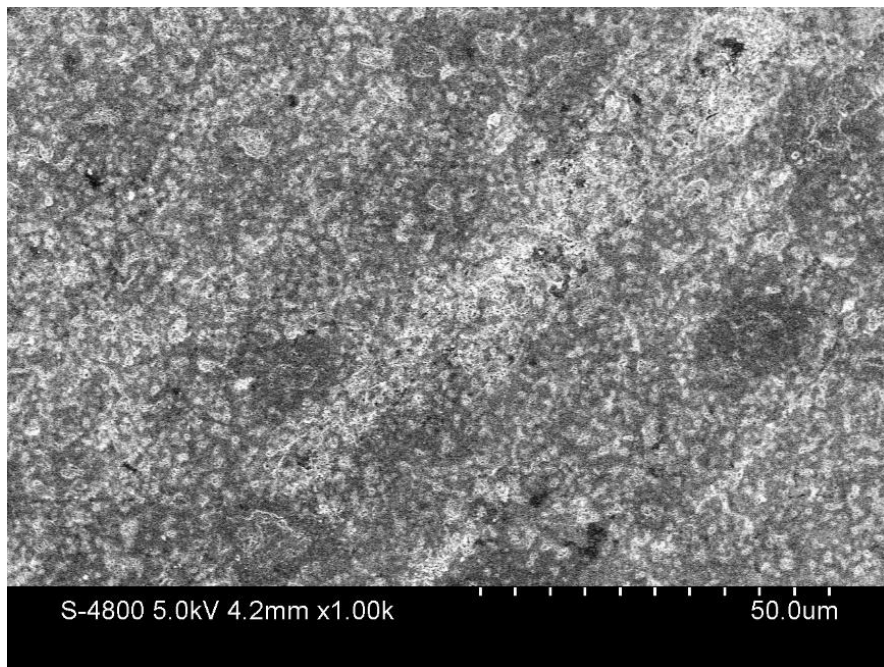


Figure S6.1 SEM image of pelletized $\text{Li}_3\text{InCl}_{4.8}\text{F}_{1.2}$ DHSE at a larger area.

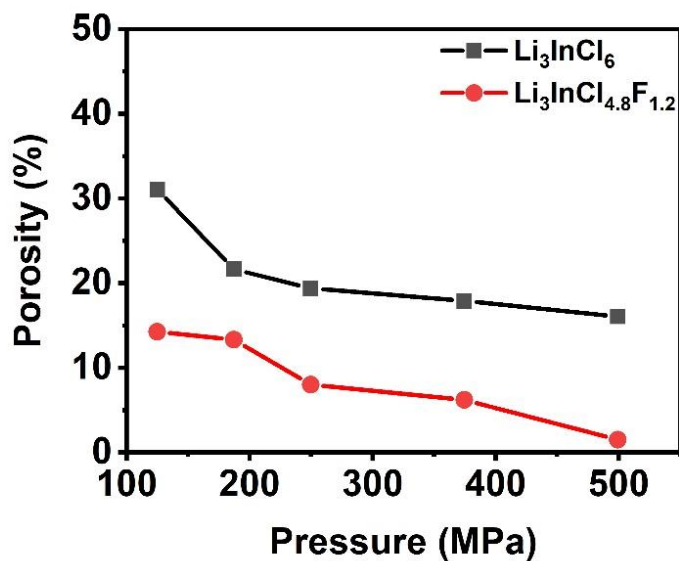


Figure S6.2 Porosities comparison as a function of applied pressure for the pellets of Li_3InCl_6 and $\text{Li}_3\text{InCl}_{4.8}\text{F}_{1.2}$.

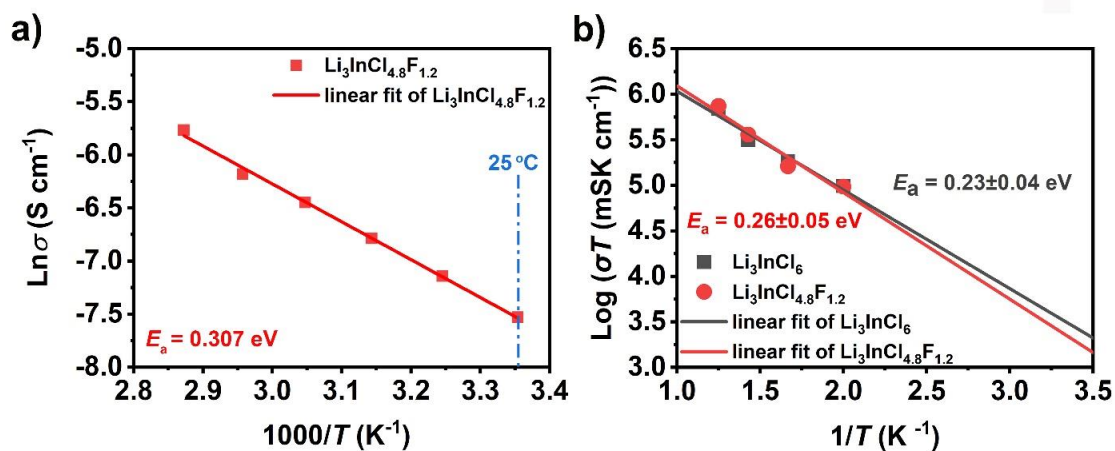


Figure S6.3 (a) Experimental Arrhenius plot of $\text{Li}_3\text{InCl}_{4.8}\text{F}_{1.2}$ DHSE. (b) Arrhenius plot of Li-ion diffusivity in Li_3InCl_6 and $\text{Li}_3\text{InCl}_{4.8}\text{F}_{1.2}$ from AIMD simulations.

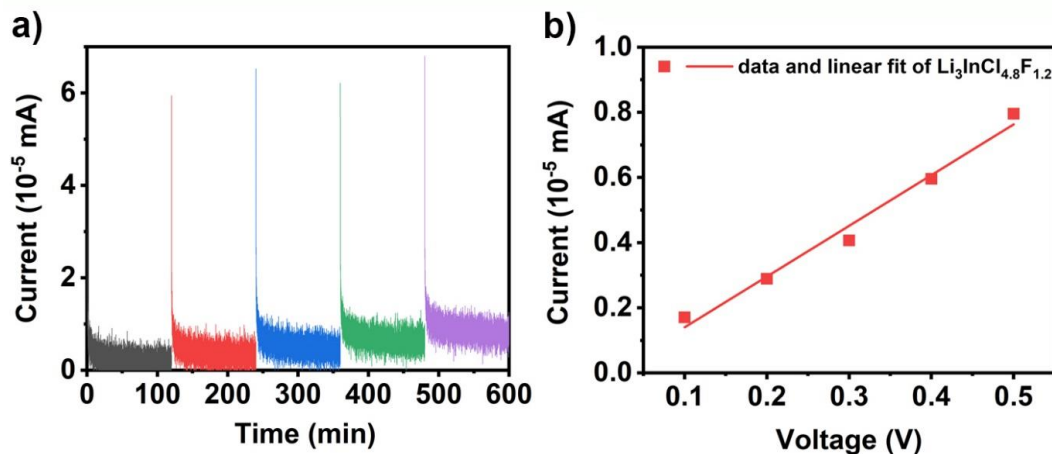


Figure S6.4 (a) DC polarization curves of Li₃InCl_{4.8}F_{1.2} using symmetric cell configuration at different voltages from 0.1-0.5 V. (b) Equilibrium current response of Li₃InCl_{4.8}F_{1.2} symmetric cell at different voltages.

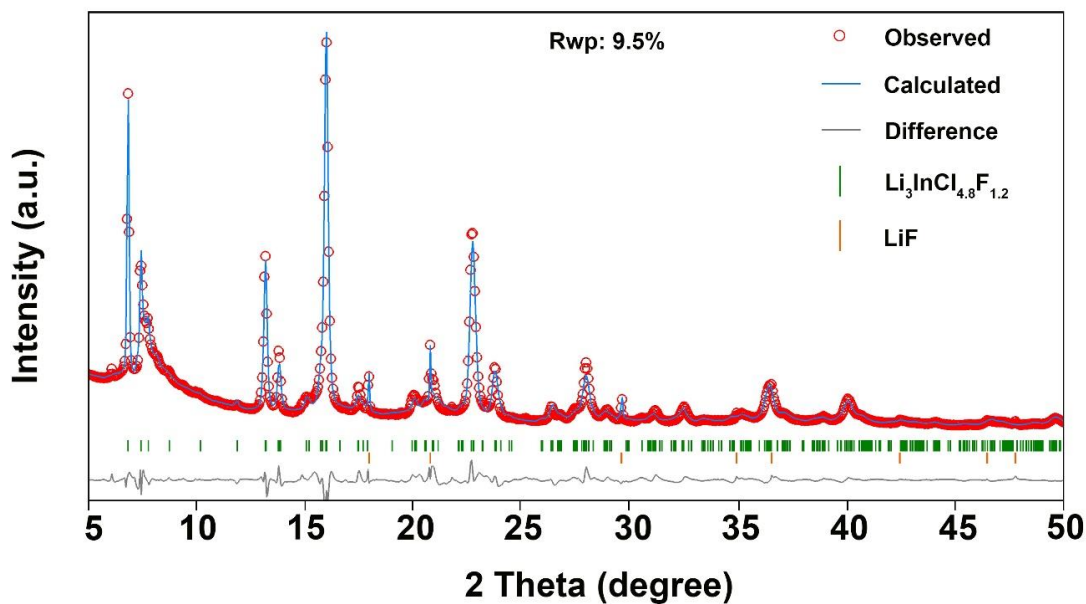


Figure S6.5 Rietveld refinement of the SXRD pattern for Li₃InCl_{4.8}F_{1.2} DHSE. The experimental profile is shown in red crosses; the blue line denotes the calculated pattern; the difference of profile is shown in grey, and calculated positions of the Bragg reflections are shown in green (Li₃InCl_{4.8}F_{1.2}) and orange (LiF). $\lambda=0.729293\text{ \AA}$.

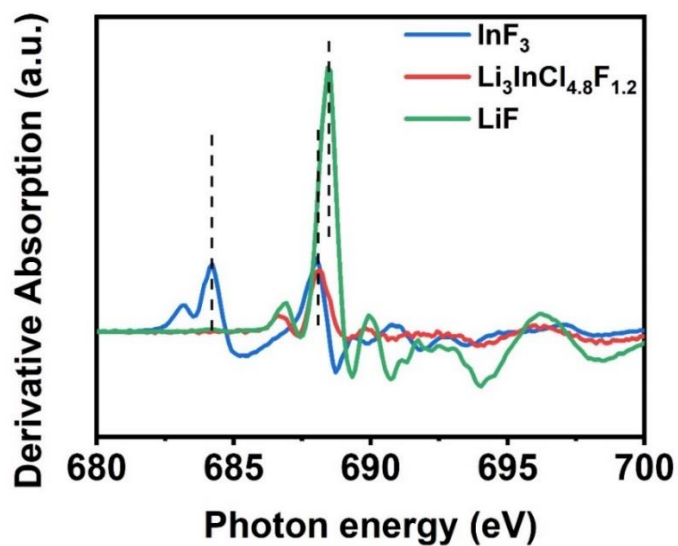


Figure S6.6 The first derivative F K-edge XAS spectra for standard LiF, InF₃ and Li₃InCl_{4.8}F_{1.2} SEs.

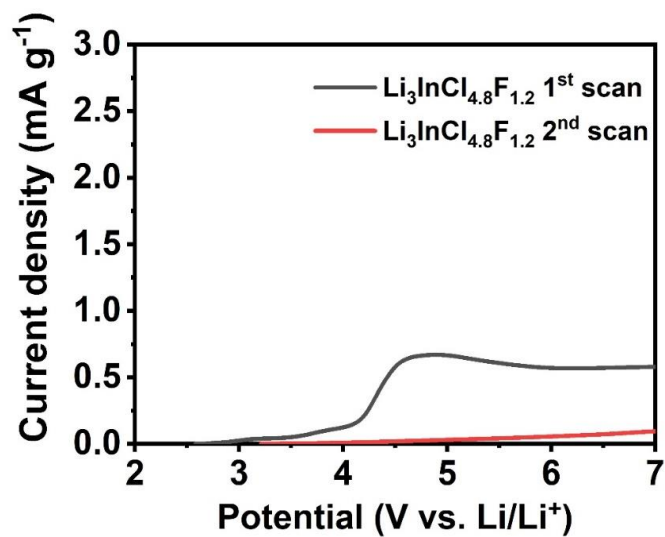


Figure S6.7 First and second positive scans of the Li₃InCl_{4.8}F_{1.2} DHSE from open circuit voltage (OCV) to 7 V (vs. Li/Li⁺).

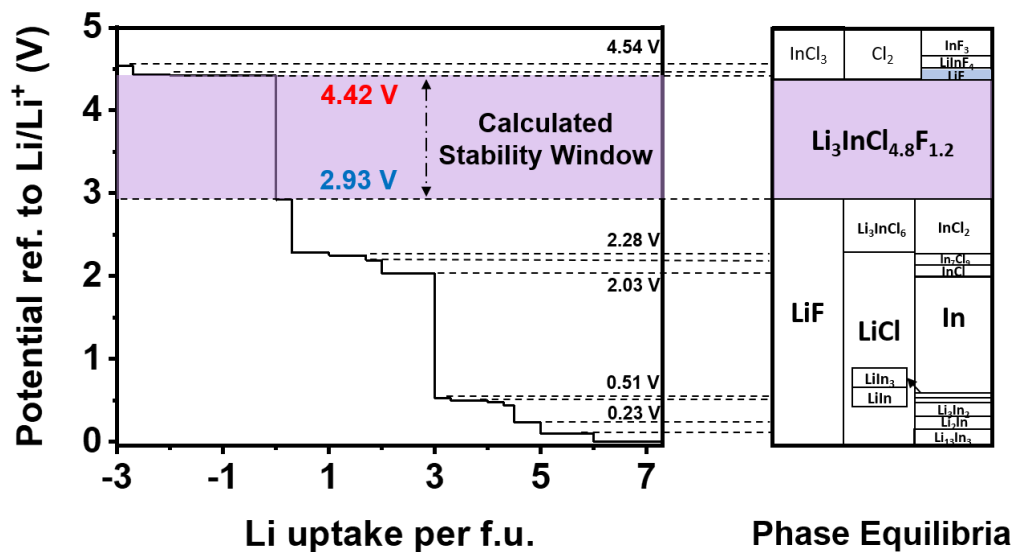


Figure S6.8 First principles computation results of the thermodynamic equilibrium voltage profile and phase equilibria of $\text{Li}_3\text{InCl}_{4.8}\text{F}_{1.2}$.

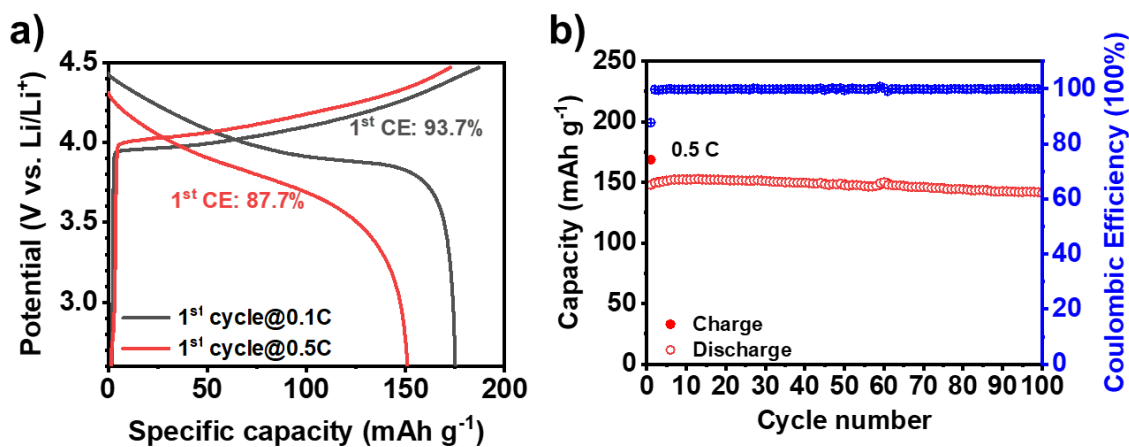


Figure S6.9 (a) 1st cycle charge-discharge curves of the liquid-electrolyte LCO half-cells at 0.1C and 0.5C. (b) Cycling stability and coulombic efficiency of the liquid-electrolyte LCO cells at 0.5 C. (Voltage range: 2.6~ 4.47 V (vs. Li/Li^+))

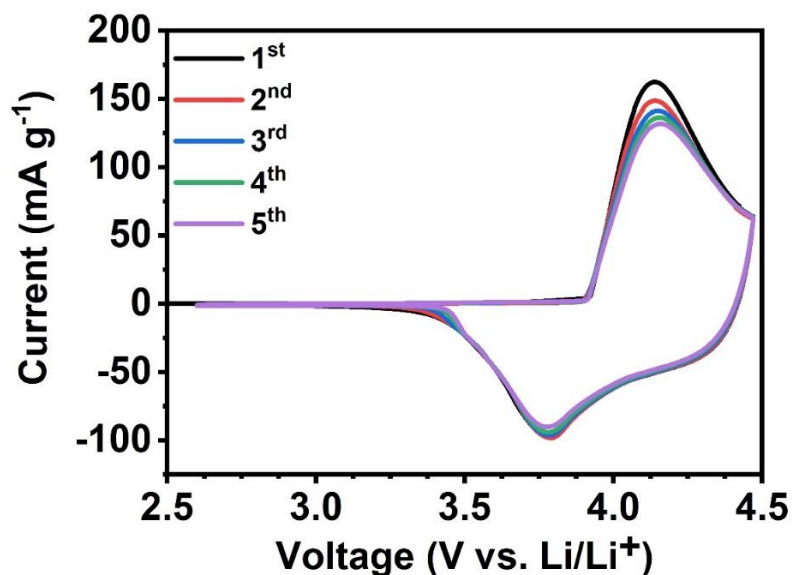


Figure S6.10 CV profiles of the In//Li₃InCl₆//Li₃InCl_{4.8}F_{1.2}/LCO solid full cell at a scan rate of 0.1 mV s⁻¹.

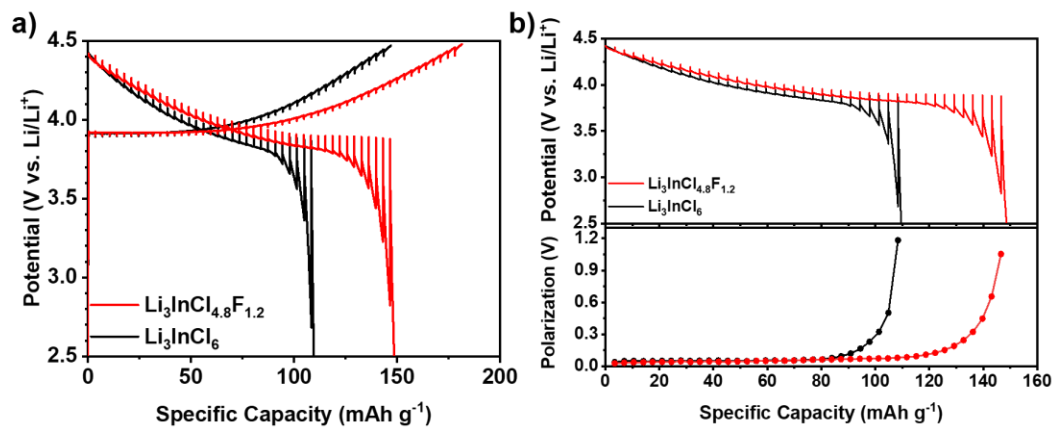


Figure S6.11 Galvanostatic intermittent titration technique (GITT) curves of (a) Li₃InCl_{4.8}F_{1.2} and Li₃InCl₆ SEs serving as cathode SEs and (b) their corresponding discharge profile and polarization.

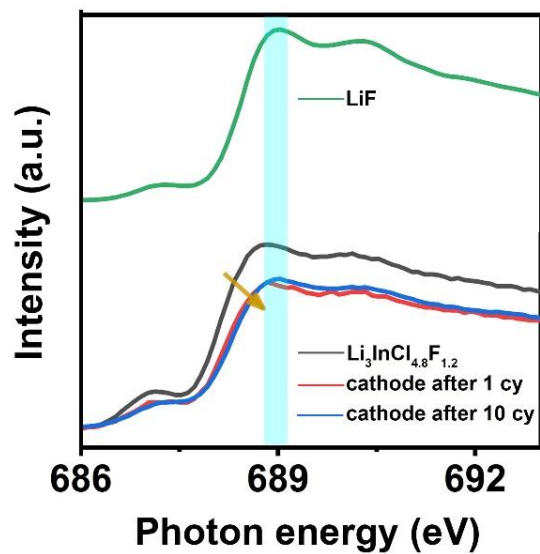


Figure S6.12 Zoomed-in figure (from 686 eV to 693 eV) of F K-edge XAS in Figure 6.5a.

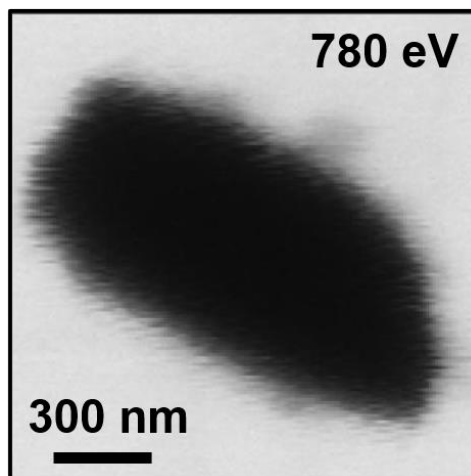


Figure S6.13 STXM optical image of a single 50-cycle LCO particle at the absorption energy of 780 eV (Co L-edge) via conducting the conventional STXM mode.

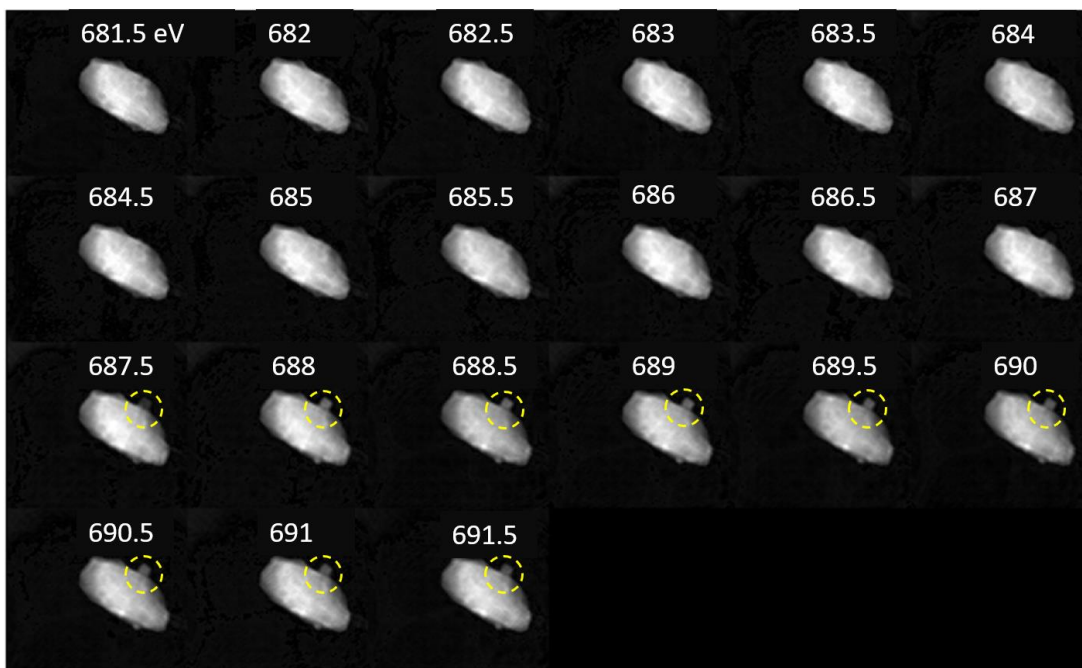


Figure S6.14 Reconstructed images of a single 50-cycle LCO particle in the photon-energy range from 681.5 to 691.5 eV (0.5 eV/step) via conducting the STXM-ptychography measurement. The species indicated in yellow circles after 687.5 eV is the residual $\text{Li}_3\text{InCl}_{4.8}\text{F}_{1.2}$ particle connecting with the LCO particle.

Chapter 7

7 Gradiently Sodiated Alucone as an Interfacial Stabilizing Strategy for Solid-State Na Metal Batteries

All-solid-state metal batteries (ASSMBs) are attracting much attention due to their cost effectiveness, enhanced safety, room-temperature performance and high theoretical specific capacity. However, the alkali metal anodes (such as Li and Na) are active enough to react with most solid-state electrolytes (SSEs), leading to detrimental reactions at the metal-SSE interface. In this work, a molecular layer deposition (MLD) alucone film is employed to stabilize the active Na anode/electrolyte interface in the ASSMBs, limiting the decomposition of the sulfide-based electrolytes (Na_3SbS_4 and Na_3PS_4) and Na dendrite growth. Such a strategy effectively improves the room-temperature full battery performance as well as cycling stability for over 475 hours in Na-Na symmetric cells. The modified interface is further characterized by X-ray photoelectron spectroscopy (XPS) depth profiling, which provides spatially resolved evidence of the synergistic effect between the dendrite-suppressed sodiated alucone and the insulating unsodiated alucone. The coupled layers reinforce the protection of the Na metal/electrolyte interface. Therefore, alucone is identified as an effective and bi-functional coating material for the enhancement of the metal/electrolyte interfacial stability, paving the way for rapid development and wide application of high-energy ASSMBs.

*One version of this chapter has been published in *Advanced Functional Materials* 2020, 30 (22), 2001118

7.1 Introduction

With a high demand on advanced energy storage systems, all-solid-state metal batteries (ASSMBs) are believed to be an emerging and competitive candidate due to their enhanced safety as well as high energy and power density.^[1] Among those, all-solid-state sodium (Na) metal batteries (ASSSMBs) are particularly promising for the high natural abundance and low cost of sodium, as well as the comparative performance with that of the all-solid-state lithium metal batteries (ASSLMBs).^[2] The essence of ASSSMBs is to develop excellent solid-state electrolytes (SSEs) which not only possess a high ionic conductivity at room temperature (RT) but also show good compatibility with the Na anode and cathode materials.^[3] In recent years, some SSEs have been reported to exhibit ionic conductivity as high as 10^{-3} S cm⁻¹, such as β -Alumina,^[4] NASICONs, polymer-based electrolytes,^[5] and sulfide-based electrolytes.^[3b, 3c, 6] Generally, the oxide-based SSEs (including both β -Alumina and NASICONs) show unfavorable thermodynamic stability, the rigid instinct and high grain boundary resistance, which severely limit their applications. For polymer-based electrolytes, it is still challenging to obtain decent ionic conductivity at RT despite their flexibility and low interfacial contact resistance. In contrast, sulfide-based electrolytes are the most promising candidates and meet most of the criteria of solid-state electrolytes in high-performance ASSSMBs. Compared with analogous oxides, the sulfide SSEs consist of highly polarizable S atoms which can weaken the electrostatic interactions with Na ions, thus facilitating Na-ion migration and exhibiting considerable ionic conductivity at RT.^[7] Furthermore, the intimate electrolyte/electrode contact can reduce the interfacial resistance, boosting the Na-ion mobility at the interface and enabling high-performance ASSSMBs.^[8]

However, the interfacial issues are the most serious challenges to hinder the development of sulfide-based ASSSMBs, especially on the Na anode/SSE interface. One of the problems is that sodium metal can thermodynamically react with most sulfide SSEs to form a poor interface with the reduced products (Na₃Sb, Na₂S, Na₂Se and *etc.*),^[9] continuously depleting both the SSE and Na metal. Meanwhile, the resultant large polarization can lead to high interfacial resistances and deterioration of battery performance. Another downside is that uneven Na deposition occurring at the Na/sulfide

SSE interface is capable to cause the formation of Na dendrites which penetrate along the grain boundary of the SSE, resulting in short circuits of the batteries.^[10] As such, the interfacial stability is the key to realize the high-performance sulfide-based ASSSMBs. Up to now, some effective approaches have been reported to address these issues. For example, Tian *et al.* reported a reactivity-driven hydrated interface showing the improved stability between Na₃SbS₄ SSE and Na metal.^[11] Nevertheless, the developments of ASSSMBs is still in its infancy, particularly interfacial studies.^[11] Inspired from the ASSLMBs, interfacial engineering, including surface coatings and interlayer-strategies, is the most facile and effective way to achieve a stable interface between the metal anode and SSE. Various coating- and interlayer-strategies (LiF-based functional interfaces^[12], organic polymer^[5], Al₂O₃^[13], and etc.) have been adopted to realize the integration of sulfide SSEs and Li anodes,^[14] which can be applied to the Na counterparts and guide the research for ASSSMBs.

Herein, for the first time, we employ molecular layer deposition (MLD) technique in ASSSMBs to stabilize the Na anode/electrolyte interface. This is achieved by coating a 150-cycle alucone film on Na foil, alleviating the decomposition of sulfide-based electrolytes (Na₃SbS₄ and Na₃PS₄) and suppressing Na dendrite growth. The protection mechanism of alucone is further investigated. Benefiting from an initial activation process, the pristine coating layer can be partly sodiated resulting in a sodiation gradient in the alucone which strengthens interfacial protection, thus enabling enhanced battery performance and cycling stability at RT. Due to the ability of stabilizing the Na metal/electrolyte interface in ASSSMBs, the MLD alucone deposition strategy presents enormous potential to be applied in high-energy-density ASSMBs.

7.2 Experimental section

Preparation of Na₃SbS₄ solid-state electrolyte: Na₂S (Sigma Aldrich), Sb₂S₃ (Sigma Aldrich, > 99 %) and Sulfur (Sigma Aldrich, 99.99 %, trace metals basis) were purchased for using without further purification. An appropriate ratios of powder precursors (total 1 g) were sealed in zirconia ball milling pots in an Ar-filled glovebox. The mass ratio between the mixture and the zirconia ball is 1:40. After that, low-speed ball milling (150

rpm for 2 h) was firstly carried out to fully mix the starting materials, followed by a high-speed ball-milling process (510 rpm) for 20 hours. Then, a certain amount of the ball-milled product was cold-pressed into pellet, and sealed in quartz tubes for annealing treatment. After heating at 550 °C for 5 h in the muffle furnace, the sample naturally cooled down to room temperature and was grinded to powder for further use.

Preparation of Na₃PS₄ solid-state electrolyte: c-Na₃PS₄ electrolyte was synthesized following the reported literature. Typically, a stoichiometric mixture of Na₂S (Sigma Aldrich) and P₂S₅ (Sigma Aldrich, >99%,) were mechanochemical milled at 510 rpm for 1.5 h in Ar-filled zirconia ball milling pots, followed by a heat treatment at 270 °C for 2 hours in Ar atmosphere. The products were then ground into fine powders for further use.

Preparation of alucone film on Na foils: As the previously reported method from our group, molecular layer deposition (MLD) was used to prepare alucone coating layer fresh Na foils. Typically, fresh Na foils with a diameter of 3/8 inch was prepared by pressing a piece of sodium (Sigma Aldrich, 99.9% trace metals basis) using a homemade press machine in an argon-filled glovebox. These fresh foils were then transferred into a Gemstar-8 ALD system without overlap. Two of organic precursors, trimethylaluminium (TMA) and ethylene glycol (EG), were alternatively deposited on the surface of Na foils at 85°C to form alucone thin films. The MLD process used is as follows: 0.01 s/40 s/0.01 s/70 s TMA pulse/purge/EG pulse/purge. Different cycle numbers (50, 150 and 300) of alucone coating on Na foils are named as Na@mld50C, Na@mld150C and Na@mld300C, respectively.

Ionic conductivity measurements: Ionic conductivity of prepared Na₃PS₄ and Na₃SbS₄ electrolytes were measured by electrochemical impedance spectroscopy (EIS) and corresponding fitting. This was completed on a multichannel potentiostation 3/Z (German VMP3). The applied frequency range is 1 Hz ~ 7 MHz and the amplitude is 20 mV. The test cell was fabricated as follows: 80 mg of the electrolyte was pressed into a pellet (diameter 1 cm, thickness 0.7 mm) with a pressure of ~ 300 MPa. Successively, two pieces of indium (In) foil serving as the current collector were pressed on both sides of

the electrolyte pellet in a model cell. To gain the Arrhenius plot, variable-temperature EIS was measured from -15 °C to 35 °C with an interval of 10 °C.

Na/Na₃SbS₄ (Na₃PS₄)/Na symmetric cells assembly and electrochemical measurements: 80 mg of electrolyte (Na₃SbS₄ or Na₃PS₄) was pressed by ~300 MPa to form solid pellet. Two pieces of Na foil were placed onto both sides of the electrolyte pellet and then pressed. The alucone-coated Na symmetric cells were assembled in the same way. Na plating/stripping experiments were carried out on LAND battery testing stations (CT-2001A, Wuhan Rambo Testing Equipment Co., Ltd.). Current density and cut-off capacity were set at 0.1 mA cm⁻² and 0.1 mAh cm⁻².

Na@mld150C/Na₃SbS₄/TiS₂ ASSSMBs: Using Na₃SbS₄ as the electrolyte, prepared Na₃SbS₄/TiS₂ as the cathode composite, Na@mld150C as anode. 120 mg of the Na₃SbS₄ electrolyte was pressed under ~300 MPa to form a solid pellet (10 mm of diameter). 10 mg of Na₃SbS₄/TiS₂ powder was uniformly spread onto one side of Na₃SbS₄ pellet and pressed under ~360 MPa for 5 minutes. Finally, Na@mld150C foil was attached on the other surface of Na₃SbS₄ pellet and pressed gently. The as prepared cell was sandwiched between two stainless-steel rods as current collectors and sealed in the model cell. Galvanostatic charge-discharge was conducted on the LAND battery test system. The voltage window was set as 1.0~2.8 V (vs. Na/Na⁺). All cell fabrication processes were conducted in an Ar-filled glove box.

Characterization methods: Scanning electron microscope (SEM) images and element mapping were obtained by using a Hitachi S-4800 field-emission scanning electron microscope (FE-SEM, acceleration voltage 5 kV) equipped with energy dispersive spectroscopy (EDS). X-ray diffraction (XRD) measurements were performed on Bruker AXS D8 Advance with Cu K α radiation ($\lambda = 1.54178 \text{ \AA}$). Capton tape was covered on the XRD holder to prevent from the air exposure. X-ray photoelectron spectroscopy (XPS) spectra were obtain by using Krotos AXIS Ultra Spectrometer system using a monochromatic Al K(alpha) X-ray source (3kV, high current). The Kratos charge neutralizer system was used for all analyses. High resolution analyses were carried out with an analysis area of 200 microns and a pass energy of 100 eV. The energy step size

is 0.2 eV. For depth profiling, the same beam gun with a raster of 1 mm was used. These conditions have a calculated sputter rate of ~ 1.94 nm per second based on Ta_2O_5 . Multiple signal collections (50 times in total) were conducted after sputtering for 30 min at intervals. Time-of-Flight (ToF-SIMS) measurements were conducted using an ION-TOF (GmbH, Germany) ToF-SIMS IV with a bismuth liquid metal ion source at Surface Science Western. The base pressure of the analysis chamber was $\sim 10^{-8}$ mbar. The action of the primary ion beam bombardment on the sample surface induces the emission of negative secondary ions. Sputtering with a Cs^+ ion beam (3 keV) was used for depth profiling analysis.

7.3 Results and Discussion

One remarkable advantage of sulfide-based SSEs is their softness, and this flexibility makes it possible to reversibly deform at the metal/SSE interface as the metal expands, maintaining performance during cycling.^[15] However, these electrolytes are air sensitive enough to evolve gas during oxidation. Another intrinsic problem is that Na metal thermodynamically reacts with most thiophosphates to form poor ion-conducting products (e.g., Na_2S).^[9a] Even though substitution of the P can improve the electrochemical performance, those elements (As, Sb, and *etc.*) contributing to high ionic conductivity and chemical stability are redox-active, thus directly resulting in the decomposition of electrolytes in ASSSMBs (as shown in **Figure 7.1a**). Herein, we utilize alucone thin film deposited on Na foil to separate the Na metal and sulfide electrolytes. Typically, trimethylaluminum (TMA) and ethylene glycol (EG) are alternately sputtered on Na foil in a vacuum chamber at 85°C, similar to our previous reports.^[16] X-ray photoelectron spectroscopy (XPS) was carried out to study the surface composition of the 150-cycle alucone coated Na sample, denoted as Na@mld150C. The XPS spectra show the existence of Al, C, and O. The peak positions of Al 2p and C 1s are in agreement with Al-O, C-H, and C-C references, confirming the successful deposition of MLD alucone (**Figure S7.1**). To identify the appearance and depth information of that deposited layer, Time-of-Flight Secondary Ion Mass Spectrometry (ToF-SIMS) is used to characterize the Na@mld150C anode. With the Cs^+ ion beam etching, the secondary ions, including C_2Al^- and AlO^- , are removed and measured by the

detector, while few Na^- signals are detected, indicating that the Na surface is fully covered with alucone film (**Figure 7.1b**). Depth profiling records the intensity changes of secondary ions along with the sputtering time. The trends of these ions remain stable during the first 260 s whereas the curves of C_2Al^- and AlO^- gradually decrease accompanied by the growth of Na^- intensity (**Figure S7.2**). Based on the sputtering rate (0.15 nm s^{-1} on the Si substrate), the thickness of 150-cycle alucone layer could be estimated for over 50 nm, which is consistent with the growth rate of alucone.^[16a] As shown in **Figure 7.1c**, ToF-SIMS 3D rendering models further demonstrate the elemental distribution of Na@mld150C according to the mass spectrometric data. For the x-y plane, the upper portion of the matrix models shows uniformly dispersed C_2Al^- and AlO^- , which is attributed to the formation of a good coating layer on the Na foil. Due to the longitudinal distribution from alucone to Na and their close connection between each other, the signals of C_2Al^- and AlO^- are gradually faded accompanied by the appearance of Na^- along the z axis.

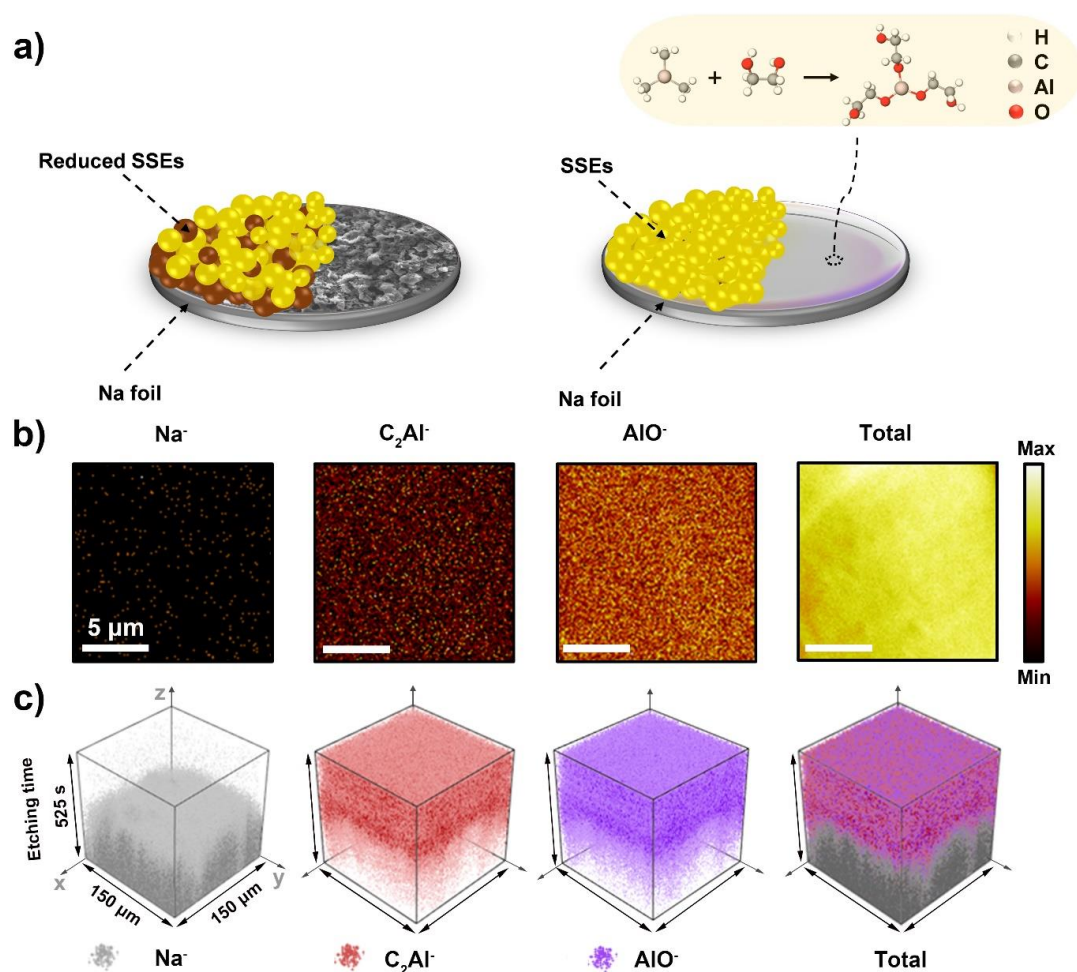


Figure 7.1 (a) Schematic diagram of the reactive Na/sulfide-based SSEs interface and stable Na@alucone/sulfide-based SSEs interface; (b) ToF-SIMS secondary ion images of Na@alucone anode before Cs⁺ consecutive sputtering; (c) 3D rendering models based on the depth scan of Na@mld150C anode by ToF-SIMS.

The effect of the above coating layer is evaluated by comparing the interfacial stability of Na (Na@alucone)/SSEs/ Na (Na@alucone) symmetric cells. Two kinds of representative sulfide electrolytes, Na₃SbS₄ and Na₃PS₄, are chosen because of their high ionic conductivities and relatively wide electrochemical stability windows. The synthesis procedures can be found in previous works.^[3a, 17] **Figure S7.3** shows the powder X-ray

diffraction patterns (XRD) of the prepared Na_3SbS_4 and Na_3PS_4 , whose diffraction peaks are consistent with those of previously published Na_3SbS_4 (t- Na_3SbS_4 : ICSD no. 01-085-8198) and cubic Na_3PS_4 (c- Na_3PS_4 : mp-985584). Additionally, the room-temperature ionic conductivity is measured as $1.1 \times 10^{-3} \text{ S cm}^{-1}$ and $8 \times 10^{-5} \text{ S cm}^{-1}$ for Na_3SbS_4 and Na_3PS_4 SSEs, respectively. (**Figure S7.4**). Even though Na_3SbS_4 is an air stable superionic conductor, calculated and experimental results show it has a higher reaction energy with Na metal compared to other solid electrolytes and the interfacial products lead to continuous decomposition of Na_3SbS_4 .^[18] Therefore, the chemical stability between Na_3SbS_4 and (modified)-Na can be examined by observing the impedance evolution of symmetric cells at room temperature. The effect of alucone coatings with various thickness, such as 50-cycle alucone and 300-cycle alucone (denote as Na@mld50C and Na@mld300C, respectively), are also examined. Electrochemical impedance spectroscopy (EIS) was recorded every four hours under open-circuit conditions. In **Figure S7.5a**, Nyquist plots of EIS shows the growth of impedance from $620 \text{ } \Omega$ to $1240 \text{ } \Omega$ during the first 24 hours, suggesting that Na_3SbS_4 and bare Na are highly unstable even through contact at open circuit. In sharp contrast, those Na foils coated with alucone exhibit good compatibility with Na_3SbS_4 , which can be concluded from the negligible changes of total impedance in each group of Nyquist plots (**Figure S7.5b, c, and d**). Notably, the as-prepared Na@mld50C and Na@mld150C symmetric cells have little difference in overall resistance, whose initial impedance is $100 \text{ } \Omega$, larger than that of as-prepared bare Na symmetric cell, indicating that alucone has lower ionic conductivity. It should be mentioned that fresh alucone coating with 100 cycles is loosely packed and soft,^[19] which is easily compressed between the solid anode and electrolyte during the battery assembly process, thus leading to a similar time-resolved EIS performance of Na@mld50C and Na@mld150C symmetric cells. However, too many MLD cycles produce a denser and thicker layer (Na@mld300C), causing an increased interfacial impedance of $1080 \text{ } \Omega$. These results suggest that as-deposited thinner alucone coatings are insulating enough to restrain the interfacial reaction between Na and sulfide-based electrolytes, resulting from marginal increases to the initial interfacial impedance.

Next, the electrochemical stability of the Na-Na symmetric cells with and without MLD alucone assistance is investigated at room temperature. After resting for 2 hours, the cells were charged and discharged under a current density of 0.1 mA cm^{-2} and a cut-off areal capacity of 0.1 mAh cm^{-2} . As shown in **Figure 7.2**, the over-potential of Na plating/stripping in the bare Na symmetric cell dramatically increases from 56 mV to 1.2 V, which is caused by the detrimental side reactions between Na metal and Na_3SbS_4 . Furthermore, there is a sudden drop of the potential after 269 hours, which is a signal of cell short caused by Na dendrites. To optimize the thicknesses of the protective layers, the symmetric cells using Na@mld50C, 150C, and 300C were also investigated. From **Figure 7.2a**, the over-potential of the Na@mld50C symmetric cell grows slowly and levels off around 350 mV (vs. Na^+/Na) after a 160-hour Na plating/stripping process. Corresponding with the above EIS data, this result also indicates that alucone can effectively prevent the side reactions between Na and Na_3SbS_4 , leading to improved interfacial stability. However, the cell survives only slightly longer, experiencing an internal short circuit after a 320h cycling, indicating that 50 cycles of alucone are still insufficient to totally prevent Na dendrite penetration. Remarkably, the cell with 150-cycle alucone showed a small increase in polarization during the initial activation process and then stably cycled at around 450 mV for 475 hours (**Figure 7.2b**). Compared with the Na@mld50C, compressed Na@mld150C is much compact to suppress the growth of Na dendrite, leading to outstandingly stable Na plating/stripping behavior. Its performance also surpasses other reported results with various Na sulfide SSEs (see the performance comparison in **Supplementary Table S7.1**). However, increasing coating cycles from 150 to 300 gives rise a large over-potential at the beginning (see in **Figure 7.2c**), revealing that the thick and dense coating layer hinders Na^+ migration through the interface. Moreover, the same experiments conducted in the Na_3PS_4 system (**Figure S7.6**) with Na@mld150C symmetric cells also show the best performance. These results consistently demonstrate the effectiveness of alucone coating in suppressing the interfacial reactions between Na metal and sulfide-based SSEs as well as Na dendrite growth.

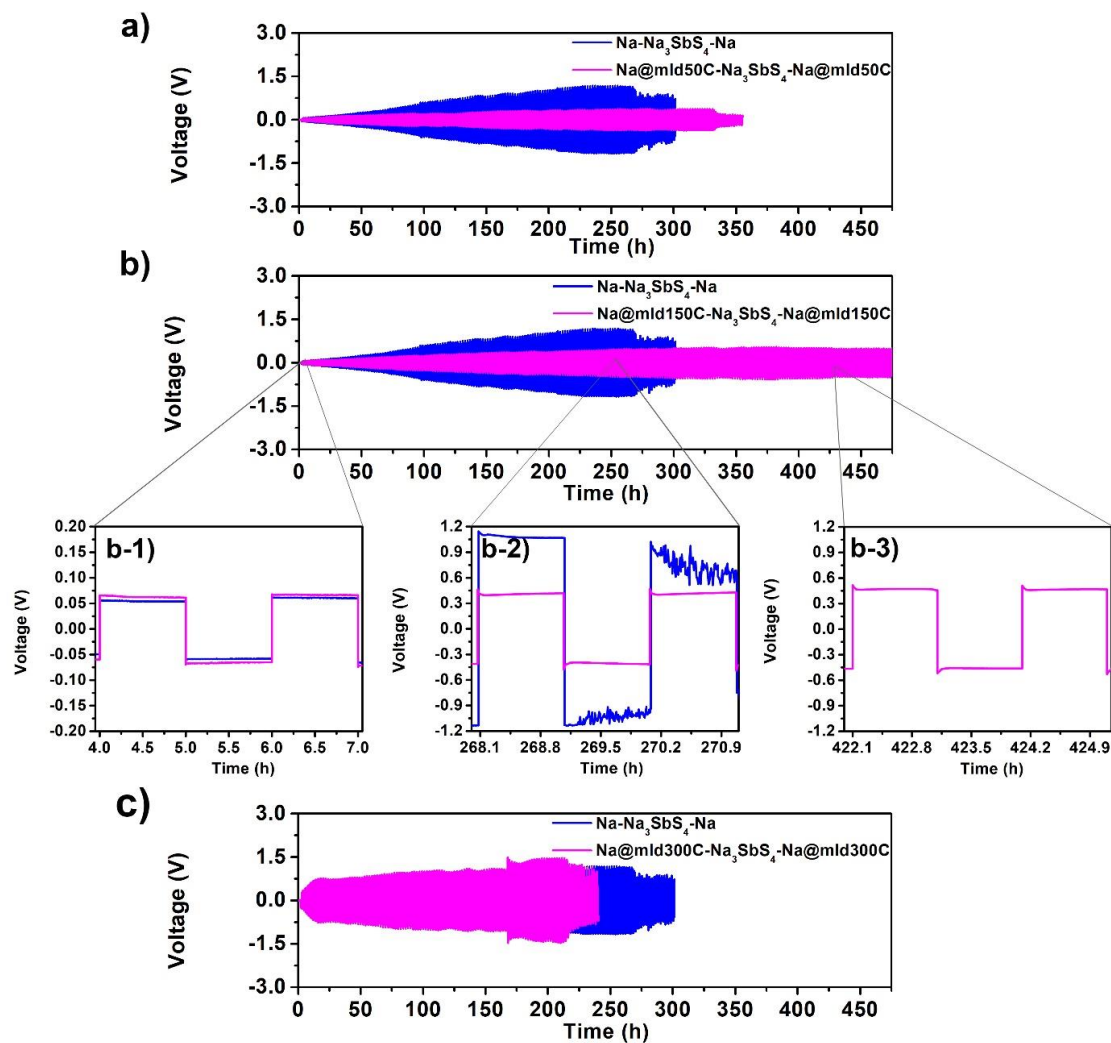


Figure 7.2 Comparison of Na plating/stripping behavior of Na symmetric cells at a current density of 0.1 mA cm^{-2} with an areal capacity of 0.1 mAh cm^{-2} : a) 50 cycles alucone (mld50C) versus bare Na; b) 150 cycles alucone (mld150C) versus bare Na; c) 300 cycles alucone (mld300C) versus bare Na

As alucone coating has been demonstrated to show a positive effect on the Na/SSEs interfacial issues, it is worth exploring how this protective layer works. Bare Na and Na@mld150C symmetric cells were disassembled after being cycled for 10 times. The interface between bare Na and Na_3SbS_4 is rough with large black areas (as shown in

Figure S7.7a), indicating the formation of Na dendrites due to unstable interface of Na/Na₃SbS₄.^[20] In comparison, the interface with alucone protection is much flatter and does not show any observable color changes after cycling (**Figure S7.7b**). Then, the surface morphology of the above two buried-electrodes is investigated by scanning electron microscope (SEM). As shown in **Figure 7.3a**, in the absence of MLD coating, continuously protruding particles on the rough surface are observed for the bare Na metal electrode, indicating the growth of Na dendrites.^[13] In contrast, the surface of Na@mld150C appears flat and smooth (**Figure 7.3b**), showing the evidence of restricting Na dendrite and providing intimate contact with Na₃SbS₄ electrolyte. Alucone molecular layer are soft and flexible, thus such morphological differences are more capable to be caused by the sodiation of alucone forming a smooth and strong surface to reduce the Na dendrite. An analysis of the surface composition by Energy-dispersive X-ray spectroscopy (EDS) reveals that the surface of Na@mld150C contains carbon, oxygen, sodium, aluminum, sulfur and antimony, originating from both the electrolyte and coated electrode. (**Figure S7.7**) In order to deeply understand the nature of the cycled interface between Na and Na₃SbS₄, ToF-SIMS depth profiling is employed to analyze the specific chemical species as a function of time. With Cs⁺ ions sputtering, the characteristic fragments for bare Na/Na₃SbS₄ interface, including Na⁻ and SbS⁻, are monitored (**Figure 7.3c**). The SbS⁻ signal remains stable with fluctuations while Na⁻ intensity decreases slowly after reaching an initial maximum. This trend difference suggests the decomposition of Na₃SbS₄ during the electrochemical cycling process. In **Figure 7.3d**, the signal intensity of SbS⁻ dropped after first 180 seconds, indicating there were few electrolyte particles left on the cycled Na@mld150C surface. Notably, the alucone fragments (AlO₂⁻ and AlO⁻) also had a maximum signal at the same sputtering period, but then showed a similar climbed trend with that of Na⁻ species. Such in-depth variations in concentration are highly possible to attribute to the generation of two separate alucone-contained layers during Na plating/stripping.

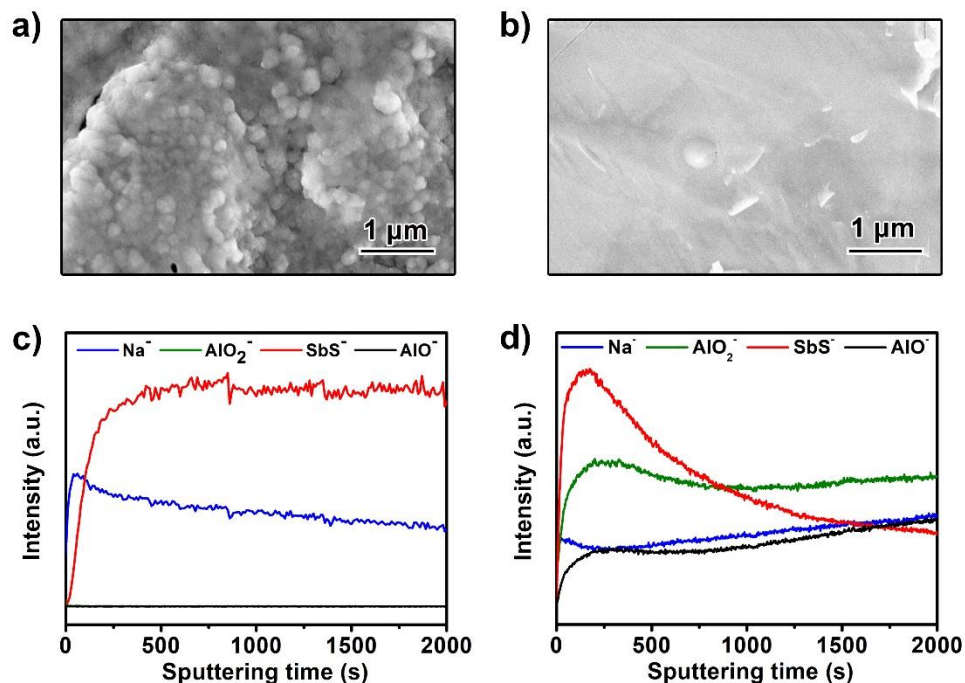


Figure 7.3 Top-side SEM images of the cycled Na|Na₃SbS₄|Na using (a) bare Na and (b) Na@mld150C electrodes; ToF-SIMS depth profile of the cycled (c) bare Na electrode and (d) Na@mld150C electrode, respectively.

As depicted above, the expected model of cycled Na@mld150C electrode can be divided roughly into top interlayer 1, interlayer 2 and Na foil at the bottom. (**Figure 7.4a**) To further confirm this result and find out the chemical composition of each layer, XPS depth profiling is adopted to analyze chemical environments at the cycled electrolyte/metal interface. We totally collected 50 levels of elemental signals sputtering with an Al K Alpha beam gun in an 8-hour timeslot. Figure 4b shows the spectra of etching level 3. The presence of no reduced Na₃SbS₄ electrolyte is evidenced by the Sb 3d spectra which can be fitted as a Sb-S bond in the SbS₄³⁻ tetrahedron.^[20] Meanwhile, the peak positions of S 2p spectra (the S 2p_{3/2} peaks at 163.3 and 161.5 eV and the respective S 2p_{1/2} peaks at 164.5 and 162.7 eV) can be assigned to Sb=S and Sb-S-Na bonds, respectively.^[20] At this etching level, the signals of Al and C are also detected, whose characteristic peaks are the same as that of as-prepared Na@mld150C anode.

These results not only prove no decomposition of Na_3SbS_4 at the $\text{Na}_3\text{SbS}_4/\text{Na@mld150C}$ interface, but also support the existence of a $\text{Na}_3\text{SbS}_4/\text{alucone}$ hybrid interlayer. As shown in **Figure 7.4c** and **4d**, the overall evolution was summarized as representative Na and Al spectrum profiles (8-times signal collections after interval sputtering). Curves 1 and 2 at the top are assigned to interlayer 1 for the Na 1s and Al 2p indicating Na^{1+} and Al^{3+} , respectively, further proving the composition of interlayer 1 (Na_3SbS_4 and alucone). It is worth noting that the peak positions of Al 2p shift to low energy from curve 3 to curve 7, suggesting that the sodiation of alucone forms Na-Al-C-O structure at a second interlayer (interlayer 2). For Na 1s curves (3 - 7, green color), the peaks at around 1070.4 eV are assigned to Na-O bond in Na-Al-C-O interlayer. Via a Na-O bond breaking/making process, the Na ion diffusivity can be accelerated.^[21] During the formation of interlayer 2, the surface is gradually flattened for homogenous Na ion deposition, coinciding well with the above SEM images. Besides, the as-formed Na-Al-C-O structure is ductile and shows mechanical constraint to Na dendrites.^[22] Finally, the intensity of Al 2p becomes weak and ultimately vanishes at the bottom level (Na foil layer), where the peak of Na 1s (indexed at 1070 eV) is assigned to metallic Na. The synergistic effect between dendrite-suppressed sodiated alucone and the insulating unsodiated alucone reinforces the protection of the Na metal/electrolyte interface, benefiting the electrochemical performance of ASSSMBs.

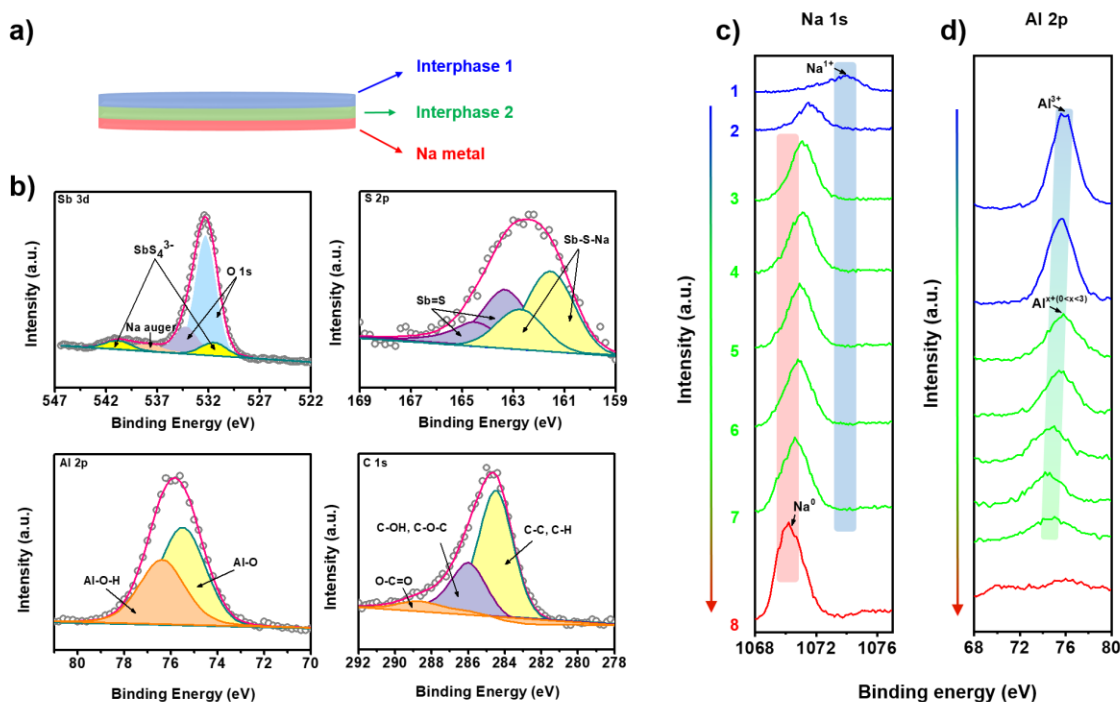


Figure 7.4 (a) Presumed schematic diagram of Na@mld150C/Na₃SbS₄ interface after symmetric cell cycles; (b) High-resolution XPS spectra of S 2p, Sb 3d, Al 2p and C 1s. The Sb 3d spectra indicate Sb⁵⁺. The peaks of Al 2p and C 1s represent the existence of alucone; XPS depth profile of Na 1s (c) and Al 2p (d) of the cycled Na@mld150C/Na₃SbS₄ interface. The metallic Na (bottom curve) and interlayer 1 (top two curves) were identified in different sputtering depths, and the interlayer 2 was identified by the chemical valence changes of Na and Al.

In order to demonstrate the potential application of the coated Na anode, we construct solid-state Na@mld150C/Na₃SbS₄/TiS₂ ASSSMBs. The loading mass of the TiS₂ cathode is 8.92 mg cm⁻². **Figure 7.5a** shows the cyclic voltammetry (CV) curves of this battery within the potential region of 1–2.8 V (vs. Na/Na⁺) at a scan rate of 0.1 mV s⁻¹. During the first cycle, redox peaks at 1.85 V and 2.4 V imply the reversible phase change between TiS₂ to Na_xTiS₂.^[23] In the subsequent 2nd and 3rd cycles, highly overlapping CV curves indicate good cycling stability. **Figure 7.5b** depicts the galvanostatic

charge/discharge profiles of Na@mld150C/Na₃SbS₄/TiS₂ battery at a constant current density of 0.11 mA cm⁻². Its discharge plateau at 1.85 V in the initial discharge curve shifts to 1.9 V in the second cycle onward, which is in accordance with the previously analyzed CV results. The discharge capacity initially reaches 200 mAh g⁻¹ and then reversibly maintains at 140 mAh g⁻¹ in the following cycles. A stable cycling at room temperature over 30 cycles and a high coulombic efficiency of ~100% are demonstrated in **Figure 7.5c**, in sharp contrast to the performance when bare Na anode is used. The full cell performance with Na₃PS₄ SSE is also tested, while the intrinsically poor ionic conductivity of Na₃PS₄ leads to a large polarization and limited specific capacity. These results prove that the full cell addresses the interfacial instability issues and shows comparable performance with other reported sulfide-based ASSSMBs.^[24]

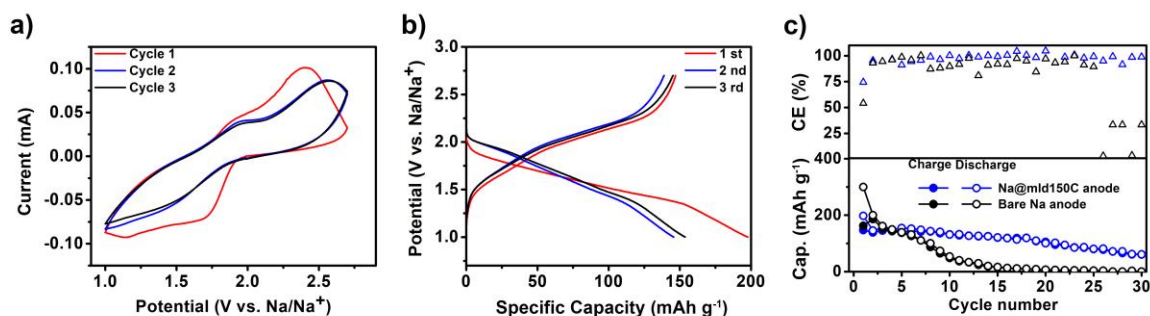


Figure 7.5 (a) CV curves of all-solid-state Na@mld150C/Na₃SbS₄/TiS₂ battery. (b) The charge and discharge profiles of Na@mld150C/Na₃SbS₄/TiS₂ cell performed at room temperature with a current density of 0.11 mA cm⁻² (c) cycling stability and coulombic efficiency of Na/Na₃SbS₄/TiS₂ and Na@mld150C/Na₃SbS₄/TiS₂ cells.

7.4 Conclusion

In summary, for the first time, an MLD alucone coated-Na foil is successfully applied in ASSSMBs as this coating film passivates the active metal anode, thus enabling a stable and long-life battery performance at room temperature. The optimized 150-MLD cycle alucone coating layer can effectively stabilize the reactive Na₃SbS₄ and Na metal interface, leading to enhanced room-temperature full batteries performance as well as excellent cycling stability for over 475 hours in Na-Na symmetric cells. Moreover, we use XPS depth profiling analysis to illustrate the protection mechanism of coating layer at

the Na/ sulfide-based SSEs interface: the insulating pristine alucone layer (Al-C-O) is partly sodiated upon electrochemical cycling, and this sodiated alucone (Na-Al-C-O) layer is beneficial for Na deposition as well as Na dendrite suppression. Such coupled interlayers synergistically stabilize the interface between Na metal and sulfide-based SSEs while suppressing dendrite growth, thus successfully realizing the ASSMBs with superb electrochemical performance. Our work identifies alucone as an effective and bi-functional coating material as its derivatives can stabilize the metal/electrolyte interface of solid-state batteries, paving the way for rapid development and wide utilization of high-energy ASSMBs.

7.5 Acknowledgments

This research was supported by the Natural Science and Engineering Research Council of Canada (NSERC), the Canada Research Chair Program (CRC), the Canada Foundation for Innovation (CFI), Ontario Research Fund (ORF), China Automotive Battery Research Institute Co., Ltd., Glabat Solid-State Battery Inc., and the University of Western Ontario (UWO). Y. Z. appreciated the funding support of Mitac Elevate Postdoctoral Fellowship.

7.6 References

- [1]a) X. G. Han, Y. H. Gong, K. Fu, X. F. He, G. T. Hitz, J. Q. Dai, A. Pearse, B. Y. Liu, H. Wang, G. Rublo, Y. F. Mo, V. Thangadurai, E. D. Wachsman, L. B. Hu, *Nat. Mater.* 2017, 16, 572; b) K. K. Fu, Y. H. Gong, B. Y. Liu, Y. Z. Zhu, S. M. Xu, Y. G. Yao, W. Luo, C. W. Wang, S. D. Lacey, J. Q. Dai, Y. N. Chen, Y. F. Mo, E. Wachsman, L. B. Hu, *Sci. Adv.* 2017, 3, 1601659; c) H. Lee, P. Oh, J. Kim, H. Cha, S. Chae, S. Lee, J. Cho, *Adv. Mater.* 2019, 31, 1900376; d) H. Li, D. Chao, B. Chen, X. Chen, C. Chuah, Y. Tang, Y. Jiao, M. Jaroniec, S. Z. Qiao, *J. Am. Chem. Soc.* 2020, 142, 2012.
- [2]a) R. Bouchet, S. Maria, R. Meziane, A. Aboulaich, L. Lienafa, J. P. Bonnet, T. N. T. Phan, D. Bertin, D. Gimes, D. Devaux, R. Denoyel, M. Armand, *Nat. Mater.* 2013, 12, 452; b) B. Lee, E. Paek, D. Mitlin, S. W. Lee, *Chem. Rev.* 2019, 119, 5416; c) J.-J. Kim, K. Yoon, I. Park, K. Kang, *Small Methods* 2017, 1, 1700219; d) C. Ye, Y. Jiao, D. Chao, T. Ling, J. Shan, B. Zhang, Q. Gu, K. Davey, H. Wang, S. Z. Qiao, *Adv. Mater.* 2020, 1907557; e) C. Ye, D. Chao, J. Shan, H. Li, K. Davey, S. Z. Qiao, *Matter* 2020, 2, 323.
- [3]a) A. Banerjee, K. H. Park, J. W. Heo, Y. J. Nam, C. K. Moon, S. M. Oh, S. T. Hong, Y. S. Jung, *Angew. Chem. Int. Edit.* 2016, 128, 9786; b) W. D. Richards, T. Tsujimura, L. J. Miara, Y. Wang, J. C. Kim, S. P. Ong, I. Uechi, N. Suzuki, G. Ceder, *Nat. Commun.* 2016, 7, 11009; c) H. Wang, Y. Chen, Z. D. Hood, G. Sahu, A. S. Pandian, J. K. Keum, K. An, C. Liang, *Angew. Chem. Int. Edit.* 2016, 55, 8551; d) L. Zhang, D. C. Zhang, K. Yang,

X. L. Yan, L. M. Wang, J. L. Mi, B. Xu, Y. M. Li, *Adv. Sci.* 2016, 3, 1600089; e) Z. Zhang, E. Ramos, F. Lalere, A. Assoud, K. Kaup, P. Hartman, L. F. Nazar, *Energy Environ. Sci.* 2018, 11, 87; f) C. Zhao, L. Liu, X. Qi, Y. Lu, F. Wu, J. Zhao, Y. Yu, Y.-S. Hu, L. Chen, *Adv. Energy Mater.* 2018, 8, 1703012.

[4]a) X. C. Lu, G. G. Xia, J. P. Lemmon, Z. G. Yang, *J. Power Sources* 2010, 195, 2431; b) Z. Y. Wen, Y. Y. Hu, X. W. Wu, J. D. Han, Z. H. Gu, *Adv. Funct. Mater.* 2013, 23, 1005.

[5]Z. Q. Zhu, M. L. Hong, D. S. Guo, J. F. Shi, Z. L. Tao, J. Chen, *J. Am. Chem. Soc.* 2014, 136, 16461.

[6]a) D. C. Zhang, X. T. Cao, D. Xu, N. Wang, C. Yu, W. T. Hu, X. L. Yan, J. L. Mi, B. Wen, L. M. Wang, L. Zhang, *Electrochim. Acta* 2018, 259, 100; b) F. Zhao, J. Liang, C. Yu, Q. Sun, X. Li, K. Adair, C. Wang, Y. Zhao, S. Zhang, W. Li, S. Deng, R. Li, Y. Huang, H. Huang, L. Zhang, S. Zhao, S. Lu, X. Sun, *Adv. Energy Mater.* 2020, 10, 1903422.

[7]a) S. L. Shang, Z. X. Yu, Y. Wang, D. H. Wang, Z. K. Liu, *Acs Appl. Mater. Interfaces* 2017, 9, 16261; b) Y. Wang, W. D. Richards, S. H. Bo, L. J. Miara, G. Ceder, *Chem. Mater.* 2017, 29, 7475.

[8]a) A. Hayashi, K. Noi, A. Sakuda, M. Tatsumisago, *Nat. Commun.* 2012, 3, 856; b) C. Zeng, F. X. Xie, X. F. Yang, M. Jaroniec, L. Zhang, S. Z. Qiao, *Angew. Chem. Int. Edit.* 2018, 57, 8540.

[9]a) H. M. Tang, Z. Deng, Z. N. Lin, Z. B. Wang, I. H. Chu, C. Chen, Z. Y. Zhu, C. Zheng, S. P. Onets, *Chem. Mater.* 2018, 30, 163; b) Y. Tian, T. Shi, W. D. Richards, J. Li, J. C. Kim, S. H. Bo, G. Ceder, *Energy Environ. Sci.* 2017, 10, 1150.

[10]Y. S. Hong, N. Li, H. S. Chen, P. Wang, W. L. Song, D. N. Fang, *Energy Storage Mater.* 2018, 11, 118.

[11]Y. S. Tian, Y. Z. Sun, D. C. Hannah, Y. H. Xiao, H. Liu, K. W. Chapman, S. H. Bo, G. Ceder, *Joule* 2019, 3, 1037.

[12]Y. Gao, D. W. Wang, Y. G. C. Li, Z. X. Yu, T. E. Mallouk, D. H. Wang, *Angew. Chem. Int. Edit.* 2018, 57, 13608.

[13]Y. Zhao, K. R. Adair, X. L. Sun, *Energy Environ. Sci.* 2018, 11, 2673.

[14]a) Z. Shen, W. Zhang, G. Zhu, Y. Huang, Q. Feng, Y. Lu, *Small Methods* 2019, 4, 1900592; b) C. Ye, Y. Jiao, H. Jin, A. D. Slattery, K. Davey, H. Wang, S. Z. Qiao, *Angew. Chem. Int. Edit.* 2018, 57, 16703.

[15]Q. Zhang, D. X. Cao, Y. Ma, A. Natan, P. Aurora, H. L. Zhu, *Adv. Mater.* 2019, 31, 1901131.

[16]a) Y. Zhao, L. V. Goncharova, Q. Zhang, P. Kaghazchi, Q. Sun, A. Lushington, B. Q. Wang, R. Y. Li, X. L. Sun, *Nano Lett.* 2017, 17, 5653; b) C. H. Wang, Y. Zhao, Q. Sun, X. Li, Y. L. Liu, J. W. Liang, X. N. Li, X. T. Lin, R. Y. Li, K. R. Adair, L. Zhang, R. Yang, S. G. Lu, X. L. Sun, *Nano Energy* 2018, 53, 168.

- [17]A. Hayashi, K. Noi, N. Tanibata, M. Nagao, M. Tatsumisago, J. Power Sources 2014, 258, 420.
- [18]E. A. Wu, C. S. Kompella, Z. Y. Zhu, J. Z. Lee, S. C. Lee, I. H. Chu, H. Nguyen, S. P. Ong, A. Banerjee, Y. S. Meng, ACS Appl. Mater. Interfaces 2018, 10, 10076.
- [19]Y. Zhao, X. L. Sun, ACS Energy Lett. 2018, 3, 899.
- [20]P. Hu, Y. Zhang, X. W. Chi, K. K. Rao, F. Hao, H. Dong, F. M. Guo, Y. Ren, L. C. Grabow, Y. Yao, ACS Appl. Mater. Interfaces 2019, 11, 9672.
- [21]S. C. Jung, H. J. Kim, J. W. Choi, Y. K. Han, Nano Lett. 2014, 14, 6559.
- [22]X. G. Han, Y. Liu, Z. Jia, Y. C. Chen, J. Y. Wan, N. Weadock, K. J. Gaskell, T. Li, L. B. Hu, Nano Lett. 2014, 14, 139.
- [23]Y. P. Liu, H. T. Wang, L. Cheng, N. Han, F. P. Zhao, P. R. Li, C. H. Jin, Y. G. Li, Nano Energy 2016, 20, 168.
- [24]a) X. Y. Feng, P. H. Chien, Z. Y. Zhu, I. H. Chu, P. B. Wang, M. Immediato-Scuotto, H. Arabzadeh, S. P. Ong, Y. Y. Hu, Adv. Funct. Mater. 2019, 29, 1807951; b) I. H. Chu, C. S. Kompella, H. Nguyen, Z. Y. Zhu, S. Hy, Z. Deng, Y. S. Meng, S. P. Ong, Sci. Rep. 2016, 6, 33733.

7.7 Supporting information

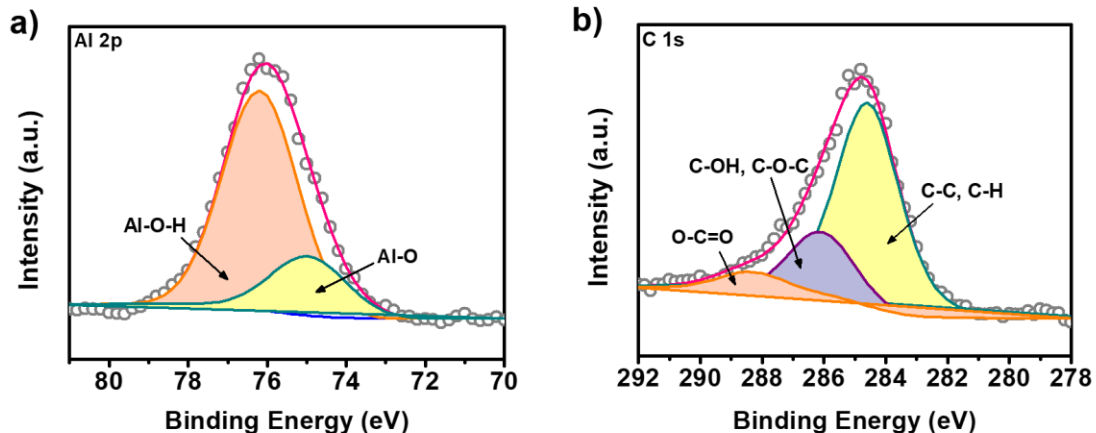


Figure S7.1. High-resolution XPS spectra of Al 2p and C 1s in as-prepared Na@mld150C.

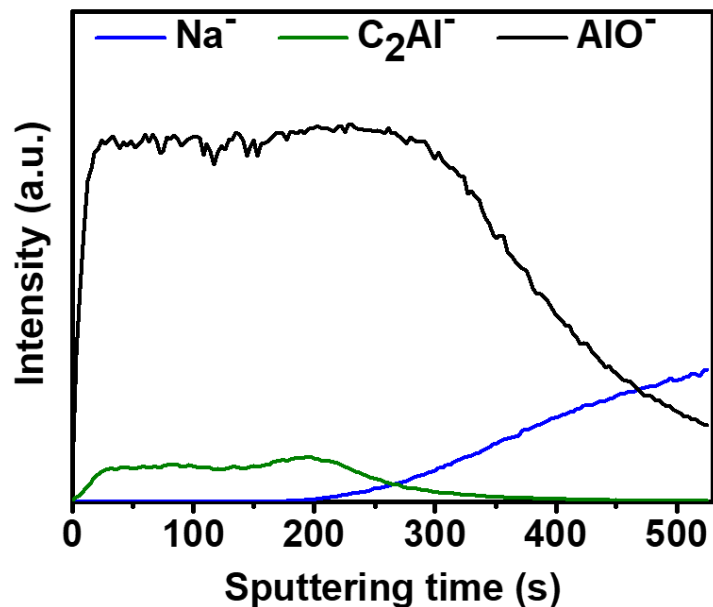


Figure S7.2 ToF-SIMS depth profile of various secondary ion species obtained by sputtering the surface of as-prepared Na@mld150C.

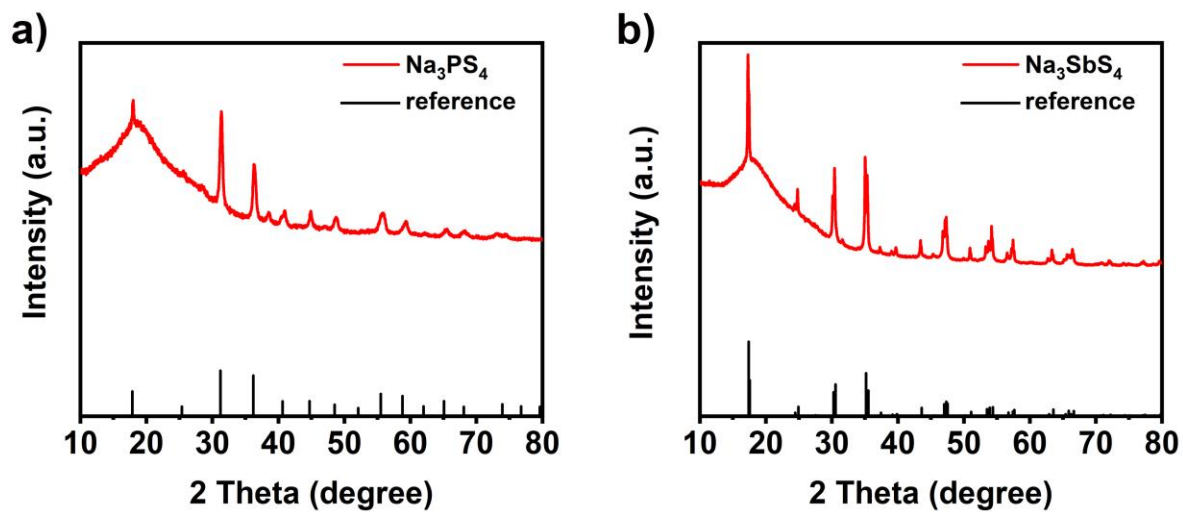


Figure S7.3 XRD patterns of the prepared (a) c- Na_3PS_4 and (b) t- Na_3SbS_4 sulfide-based electrolytes.

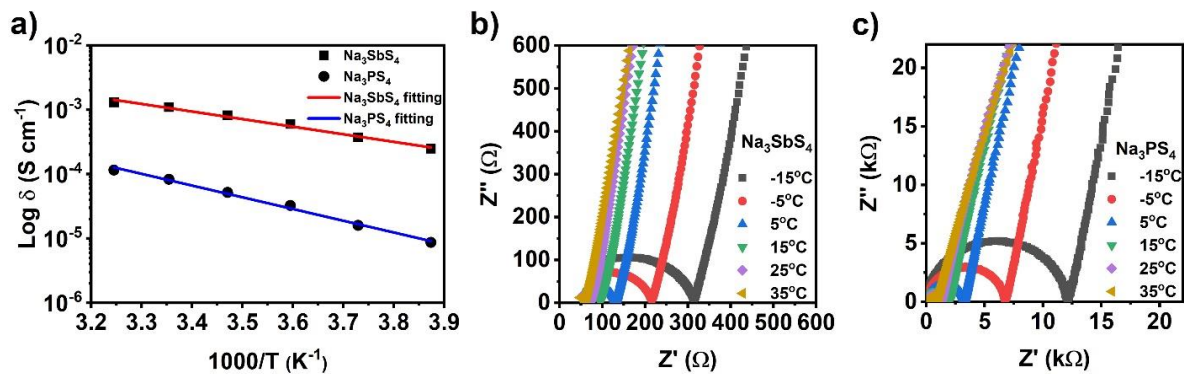


Figure S7.4 (a) Arrhenius plots of the t- Na_3SbS_4 and c- Na_3PS_4 sulfide-based electrolytes; Nyquist EIS plots of (b) t- Na_3SbS_4 and (c) c- Na_3PS_4 under different testing temperatures (from -15°C to 35°C).

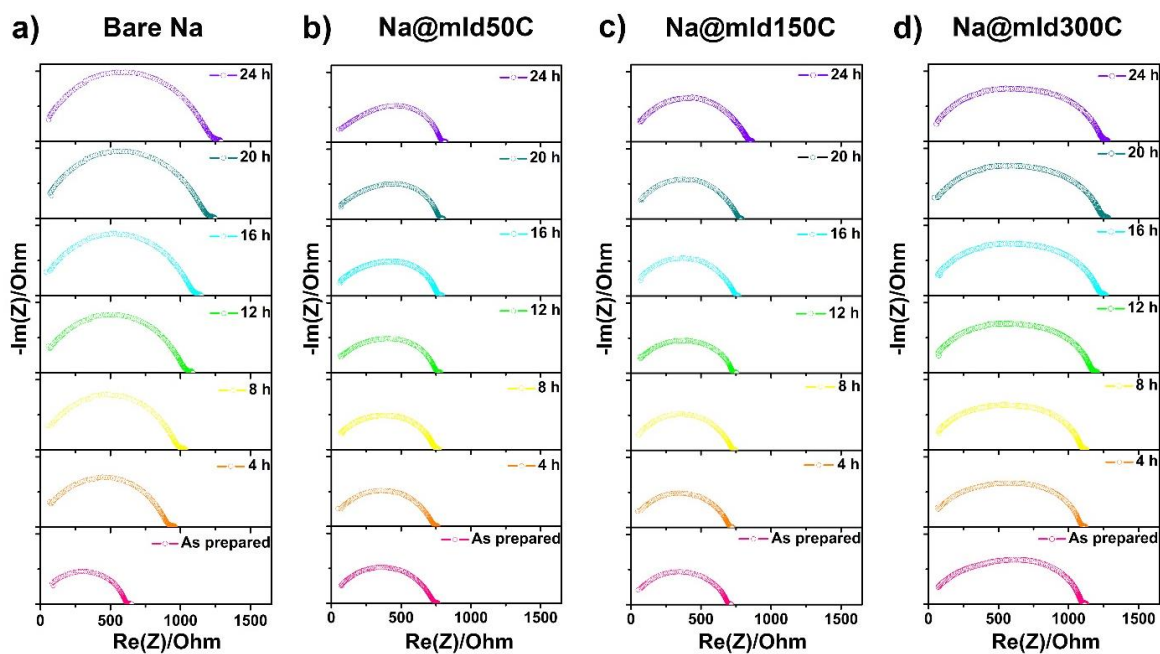


Figure S7.5 Time-resolved EIS spectrum of Na symmetric cell: a) bare Na- Na_3SbS_4 -Na; b) Na@mld50C- Na_3SbS_4 -Na@mld50C; c) Na@mld150C- Na_3SbS_4 -Na@mld150C; d) Na@mld300C- Na_3SbS_4 -Na@mld300C.

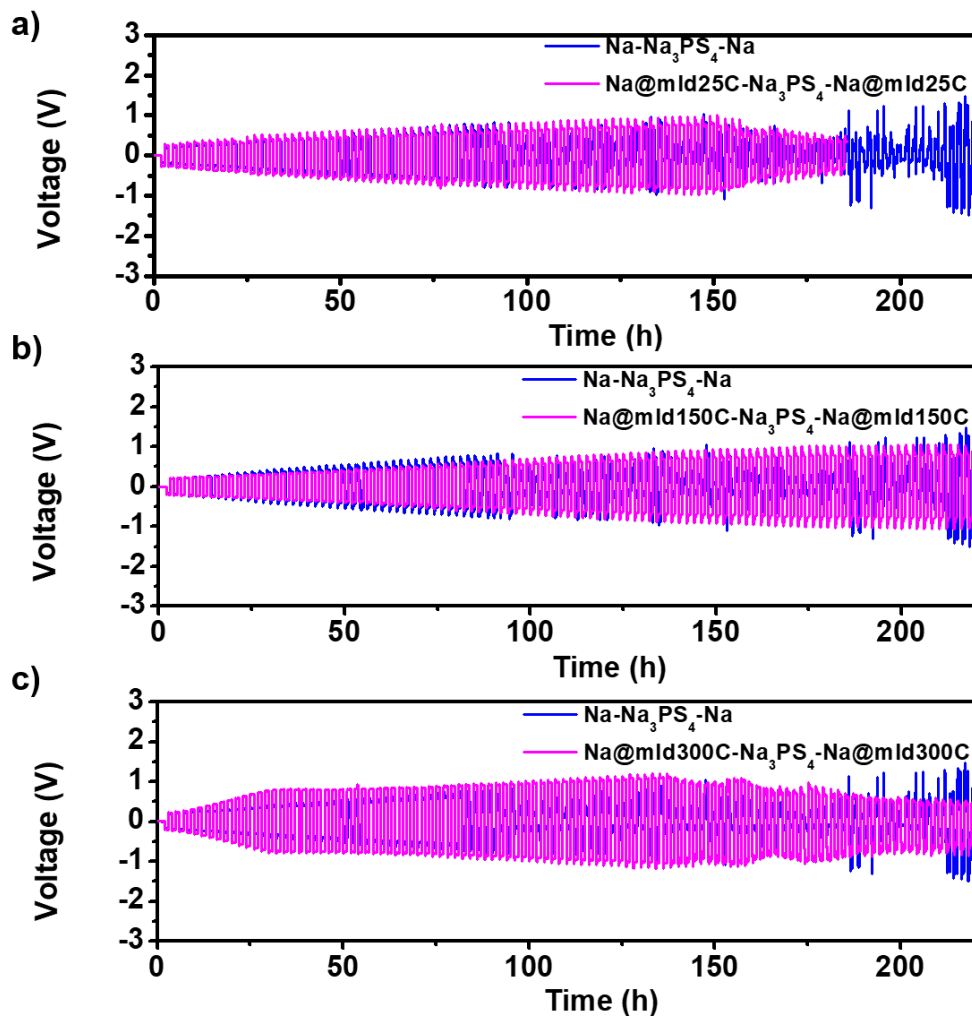


Figure S7.6 Comparison of Na plating/stripping behavior of Na/Na₃PS₄/Na symmetric cells at a current density of 0.1 mA cm⁻² with an areal capacity of 0.1 mAh cm⁻²: a) 50 cycles alucone (mld50C) versus bare Na; b) 150 cycles alucone (mld150C) versus bare Na; c) 300 cycles alucone (mld300C) versus bare Na

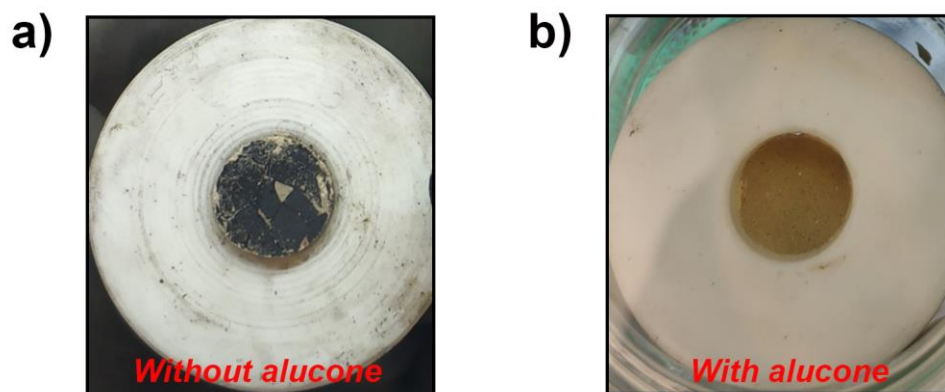


Figure S7.7 Comparison of the interface of symmetric cells after 10 plating/stripping cycles: (a) the interface between Na and Na₃SbS₄ SSE; (b) the interface between Na@mld150C and Na₃SbS₄ SSE.

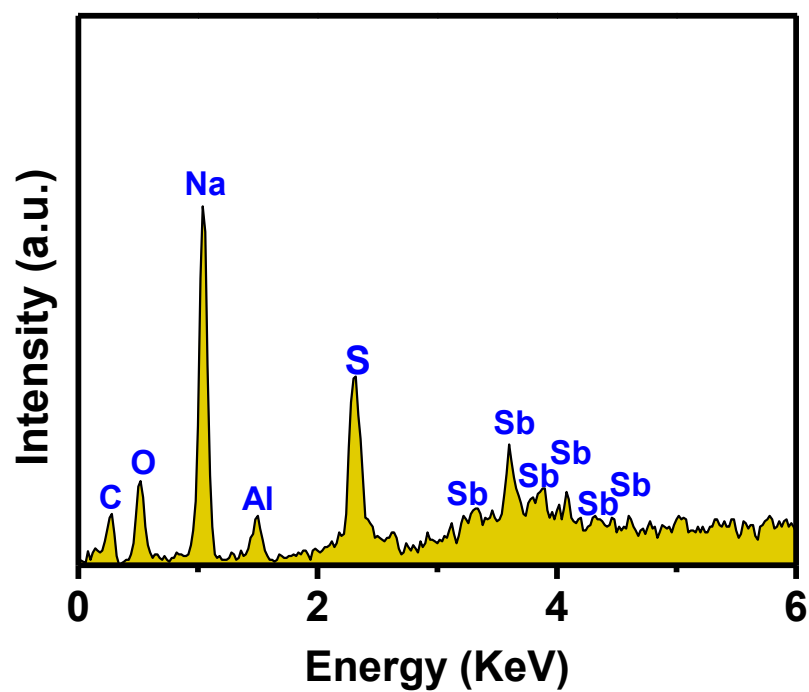


Figure S7.8 Energy dispersive spectroscopy (EDS) shows the chemical composition of Na@mld150C after cycling 10 times.

Table S7.1 Summary of the sulfide electrolyte-based Na-Na symmetric cells performance

Symmetric cell type	T (°C)	Current density (mA cm ⁻²)	Per cycle areal capacity (mAh cm ⁻²)	Cumulative Na capacity plated (mAh cm ⁻²)	Reference
Na Na ₃ PS ₄ Na	RT	0.1	0.1	10	[1]
Na Na _{2.9375} PS _{3.9375} Cl _{0.0625} Na	RT	0.05	*	1.25	[1]
Na Na ₃ PSe ₄ Na	RT	0.1	*	1.2	[2]
Na CPEO Na ₃ SbS ₄ CPEO Na	60	0.1	0.05	80	[3]
Na@mld150C Na ₃ SbS ₄ Na@mld150C	RT	0.1	0.1	47.5	<u>This work</u>
Na@mld150C Na ₃ PS ₄ Na@mld150C	RT	0.1	0.1	22.5	

References for the supporting information of Chapter 5

- [1] E. A. Wu, C. S. Kompella, Z. Zhu, J. Z. Lee, S. C. Lee, I. H. Chu, H. Nguyen, S. P. Ong, A. Banerjee, Y. S. Meng, *ACS Appl. Mater. Interfaces* **2018**, *10*, 10076-10086.
- [2] Y. Tian, T. Shi, W. D. Richards, J. Li, J. C. Kim, S. H. Bo, G. Ceder, *Energy Environ. Sci.* **2017**, *10*, 1150-1166;
- [3] P. Hu, Y. Zhang, X. W. Chi, K. K. Rao, F. Hao, H. Dong, F. M. Guo, Y. Ren, L. C. Grabow, Y. Yao, *Acs Appl. Mater. Interfaces* **2019**, *11*, 9672-9678.

Chapter 8

8 Conclusions and Perspectives

8.1 Conclusions

All-solid-state batteries (ASSBs) are regarded as one of the future energy storage devices that can compete with the state-of-the-art LIBs. Owing to the use of non-flammable solid electrolytes (SEs), ASSBs can effectively eliminate safety concerns in electric vehicles and airline industry in urban environments. Generally, a desired SE should possess high ionic conductivity and good electrochemical compatibility with electrodes (cathode and Li/Na anode). In this dissertation, based on fundamental theories, different types of inorganic SEs are developed showing high ionic conductivities over 10^{-3} S cm⁻¹. Besides, for those promising developed SEs but with insufficient electrode compatibility, their interfacial instabilities are addressed by either modifying the existing SE or adding insulating layers. This thesis devoted efforts to solving some important challenges for the development of ASSBs from designing SEs to building stable interfaces. The detailed strategies and conclusions are demonstrated as following:

Development of superionic conductive lithium iodide SEs: $\text{Li}_{x-3}\text{YI}_x$

A series of $\text{Li}_{x-3}\text{YI}_x$ SEs were prepared via conventional mechanochemical methods, which shows a room-temperature ionic conductivity up to 1.04×10^{-3} S/cm. The relation between the realization of high ionic conductivity and regulation of average crystal structures and local symmetric structures is studied by Rietveld refinement against SXRD patterns, PDF, and XAS. The representative Li_4YI_7 shows cubic structure belonging to rock salt phases. XPS characterization on the cycled interfaces and aging EIS results confirmed the stable interface between Li and Li_4YI_7 . As a result, highly stable cycling performance can be achieved over 1000 hours. This work presents a new superionic conductor with highly symmetric structure, which introduces a new avenue in developing new SEs for ASSBs.

Development of new superionic lithium oxychloride glasses: $x\text{Li}_2\text{O}-\text{MCl}_y$ (M = Ta and Hf)

A new series of glassy superionic conductors, $x\text{Li}_2\text{O}-\text{TaCl}_5$ ($x = 1.1-1.8$) and $x\text{Li}_2\text{O}-\text{HfCl}_5$ ($x = 1.5$), can be prepared via one-step ball-milling method. Among them, the optimized $1.6\text{Li}_2\text{O}-\text{TaCl}_5$ and $1.5\text{Li}_2\text{O}-\text{HfCl}_4$ glasses possess a high ionic conductivity of $6.6 \times 10^{-3} \text{ S cm}^{-1}$ and $1.97 \times 10^{-3} \text{ S cm}^{-1}$, respectively. The local chemical environment in the representative superionic $x\text{Li}_2\text{O}-\text{TaCl}_5$ and $x\text{Li}_2\text{O}-\text{HfCl}_5$ was studied by NMR, XAS, and Raman analyses. Disordered Li sublattice and Li-ion diffusion are identified in $1.6\text{Li}_2\text{O}-\text{TaCl}_5$ and $1.5\text{Li}_2\text{O}-\text{HfCl}_4$. TaCl_4O is the main local structure in $x\text{Li}_2\text{O}-\text{TaCl}_5$ followed by TaCl_3O_2 only with enough Li_2O feeding content. In $1.5\text{Li}_2\text{O}-\text{HfCl}_5$, Hf is closely surrounded by O then Cl with a totally CN of 6. The ionic conductivity of either $x\text{Li}_2\text{O}-\text{TaCl}_5$ or $x\text{Li}_2\text{O}-\text{HfCl}_4$ drops when the feeding content of Li_2O exceeded to form more electronegative Ta-O or Hf-O bonds. Benefiting from the electrochemical stability and high ionic conductivity of the $1.6\text{Li}_2\text{O}-\text{TaCl}_5$ and $1.5\text{Li}_2\text{O}-\text{HfCl}_4$ glassy SEs, ASSLIBs with these SEs showed excellent electrochemical performance. At -10°C , ASSLIBs with $1.6\text{Li}_2\text{O}-\text{TaCl}_5$ SE can stably cycle for over 300 cycles at a current density of 28 mA g^{-1} (0.2 C). The cell with $1.5\text{Li}_2\text{O}-\text{HfCl}_4$ can also perform decent cycling for over 300 cycles. At room temperature, ASSLIBs with $1.6\text{Li}_2\text{O}-\text{TaCl}_5$ SE showed superior performance at different C-rates and long cycles. This study shall provide insights into the design principles of glassy SEs and lead to a key advancement for ASSLIBs.

Expand practical electrochemical stability window of SEs to enable high-voltage ASSBs

We developed a strategy to design a dual-halogen solid electrolyte (DHSE) that can enable ultrahigh-voltage ASSLIBs. F is introduced in a halide SE and selectively occupies part of the Cl sites to form a morphologically dense $\text{Li}_3\text{InCl}_{4.8}\text{F}_{1.2}$ DHSE, which shows a good ionic conductivity of $5.1 \times 10^{-4} \text{ S cm}^{-1}$ at room temperature and high practical anodic stability over 6 V. Both experimental and computational results identify that F-containing passivating components are generated from $\text{Li}_3\text{InCl}_{4.8}\text{F}_{1.2}$ DHSE at an applied potential, protecting the $\text{Li}_3\text{InCl}_{4.8}\text{F}_{1.2}$ from further decomposition and extending its anodic stability window. As a proof of concept, this $\text{Li}_3\text{InCl}_{4.8}\text{F}_{1.2}$ DHSE is demonstrated in high-voltage ASSLIBs, performing good cycling stability at room temperature. Spectroscopic, computational, and electrochemical characterizations are

utilized to deeply understand the practical electrochemical stability of $\text{Li}_3\text{InCl}_{4.8}\text{F}_{1.2}$ and high-voltage stability of full cells. Rich F-containing passivating interphases are proved to generate in-situ on the cathode interface and prevent further interfacial reactions at high-voltages, contributing to promising cycling stability in full cells. This work presents a new DHSE with outstanding practical anodic stability, paving the way for rapid development and wide application of ASSBs at ultrahigh operational voltages.

Constructing favorable Na metal anode/sulfide interface via molecular-layer-deposition coating

A alucone coated-Na foil is successfully applied in ASSSMBs as this coating film passivates the active metal anode, enabling a stable and long-life battery performance at room temperature. The optimized 150-cycle alucone coating layer can effectively stabilize the reactive Na_3SbS_4 and Na metal interface, leading to enhanced room-temperature full batteries performance as well as excellent cycling stability for over 475 hours in Na-Na symmetric cells. Moreover, we use XPS depth profiling analysis to illustrate the protection mechanism of coating layer at the Na/ sulfide-based SSEs interface: the insulating pristine alucone layer (Al-C-O) is partly sodiated upon electrochemical cycling, and this sodiated alucone (Na-Al-C-O) layer is beneficial for Na deposition as well as Na dendrite suppression. Such coupled interlayers synergistically stabilize the interface between Na metal and sulfide-based SSEs while suppressing dendrite growth, thus successfully realizing the all-solid-state Na metal batteries with superb electrochemical performance. Our work identifies alucone as an effective and bi-functional coating material as its derivatives can stabilize the metal/electrolyte interface of solid-state batteries, paving the way for rapid development and wide utilization of high-energy all-solid-state metal batteries.

8.2 Contributions to this field

The key challenges for ASSBs are designing superionic conductors and building stable interfaces between SEs and electrodes. This thesis has addressed some important challenges of halide-based and sulfide-based SEs involving materials synthesis, interfacial engineering, electrochemical performances, and mechanism studies. New

insights provided in this thesis shall contribute to the further development of practical ASSBs.

(1) Rational design of superionic conductors is vital to improve the ionic conductivity, particularly through changing crystallography and compositions, creating defects, and etc. Solids with highly symmetric cubic structures (rock salt phases, Suzuki phases) are predicted to be good candidates for SEs since ions can conduct through 3-dimensional paths. The choice of ligand also matters due to different polarization and radius of anions. $\text{Li}_{x-3}\text{YI}_x$ in this dissertation achieves 4 orders of magnitude higher ionic conductivity than LiI. At the same time, different from all the reported ternary halide SEs, $\text{Li}_{x-3}\text{YI}_x$ maintains the similar cubic structure with that of the LiI. We firstly found a material with desired symmetric phases. The concepts (cubic phases, anion effects, and local defects) in this report can be applied to other existing SEs to develop new SEs for ASSBs.

(2) Other than crystalline SEs, glassy materials are also important to be SE candidates due to free of grain boundaries, easy fabrications, and favorable mechanical properties. The $x\text{Li}_2\text{O-TaCl}_5$ glassy SEs in this dissertation possess higher ionic conductivities up to $6.6 \times 10^{-3} \text{ S cm}^{-1}$, which is the highest value among all the developed glassy materials. The local structures of the $x\text{Li}_2\text{O-TaCl}_5$ glasses are also fully revealed, providing fundamental guidance for designing other high ionic conductive glasses and understanding Li-ion transport kinetics.

(3) Many SEs are reported showing wide ESWs, while in practical they are inadequate to enable high-voltage or metal anode ASSBs. This is caused by a poor understanding of the practical ESWs of SEs. Rational design of SEs can make ESWs of SEs notably larger than predicted for direct decomposition. F is introduced in a halide-based SE (Li_3InCl_6) to form a $\text{Li}_3\text{InCl}_{4.8}\text{F}_{1.2}$, which shows excellent electrochemical stability with a high anodic limit over 6 V (vs. Li/Li⁺). The extrinsic ESW brought by F-containing interphases compensate for the ESW of $\text{Li}_3\text{InCl}_{4.8}\text{F}_{1.2}$ SE itself, making the $\text{Li}_3\text{InCl}_{4.8}\text{F}_{1.2}$ SE comparable to the highly stable lithium fluoride compounds. The $\text{Li}_3\text{InCl}_{4.8}\text{F}_{1.2}$ SE is matched with high-voltage LiCoO_2 (LCO), enabling ultrahigh-voltage ASSLIBs (charged

to 4.8 V) with stable cycling. The design of $\text{Li}_3\text{InCl}_{4.8}\text{F}_{1.2}$ SE achieves outstanding oxidation stability, paving the way for rapid development and wide application of ASSBs at ultrahigh operational voltages.

(4) All-solid-state Na-metal batteries are considered as one of the most promising energy storage technologies due to the improved safety and high energy densities. However, Na metal anode is active enough to react with most SEs, leading to detrimental reactions at the metal/SE interface. In the dissertation, for the first time, we employ molecular layer deposition technique in All-solid-state Na-metal batteries to stabilize the Na anode/electrolyte interface. This is achieved by coating optimized alucone film on Na foil, alleviating the decomposition of sulfide-based electrolytes (Na_3SbS_4 and Na_3PS_4) and suppressing Na dendrite growth. Most importantly, the protection mechanism of alucone is further investigated. Benefiting from an initial activation process, the pristine alucone layer can be partly sodiated resulting in a sodiation gradient in the alucone to strengthen interfacial protection, thus enabling enhanced battery performance and cycling stability at room temperature. Due to the ability of stabilizing the Na metal/electrolyte interface in all-solid-state Na metal batteries, the MLD alucone deposition strategy presents enormous potential to be applied in high-energy-density ASSMBs.

8.3 Perspectives

All-solid-state Li/Na-ion batteries are promising to be the next-generation power sources due to their high energy and powder density, long cycle life, low cost, and safety.

Despite there have been considerable progresses for developing all-solid-state Li/Na-ion batteries in academic research area, they are still unlikely to meet all the requirements for practical energy storage.

All-solid-state Li-ion batteries are the most researched system. At anode side, using Li metal as anode can obtain high energy density ASSBs for EV applications due to its high theoretical capacity (3860mAh g^{-1}) and low electrochemical potential (-3.04 V vs. standard hydrogen electrode). At cathode side, NMC CAMs can provide long life cycle, lower cost, and high energy density, which already achieved in commercialized liquid

LIBs. Therefore, a perfect SE which can directly manufacturing with Li metal and commercialized CAMs in bulk-type ASSBs should be urgently proposed.

It is desired to realize high ionic conductivity, soft nature, wide practical ESW, air stability, and electrodes compatibility in a SE. Specifically, since oxide- or halide-based superionic conductors show wide electrochemical stability window and can match with Li metal (e.g. LLZO) or NMC CAMs (e.g. Li_3InCl_6) without additional coatings, their ionic conductivities achieve $10^{-2} \text{ S cm}^{-1}$ are firstly expected. At the same time, for oxide-based SEs, eliminating grain boundaries and gaining soft nature are also vital to be used in ASSBs. Strategies such as developing hybrid SEs to combine oxide-based SEs and polymer SEs or developing oxide-based glassy SEs are expected to offset the weakness of oxide SEs. For halide-based SEs, achieving Li metal compatibility becomes an urgent issue. Elemental substitution or insert buffer layer may help to address it. For sulfide-based superionic conductors ($10^{-2} \text{ S cm}^{-1}$ level materials), despite limited from the intrinsic drawbacks of S^{2-} , strategies such as modifying existing SEs to expand practical ESW and improve moisture stability are expected. LiPON is the only material that is reported to directly match Li metal and a 5 V-class cathode to fabricate thin-film ASSBs. Improving the ionic conductivity of LiPON or other nitride-based SEs is also desired.

However, the natural sources of lithium, cobalt, and nickel are not available all the time. With growing concerns about the resource exhaustion, searching the alternative chemistries for the next-generation large-scale batteries should be motivated. All-solid-state Na-ion batteries relying on naturally abundant sodium possibly provide a significant advantage in terms of cost efficiency. Besides, all-solid-state Mg-ion batteries are potentially to be alternative choices since the use of Mg metal as an anode is less prone to dendritic growth than Li and leads to higher energy densities with less safety concerns. All these beyond lithium technologies are at the very start stages, the established knowledge for ASSLIBs industry can be applied to develop All-solid-state Na-ion batteries or all-solid-state Mg-ion batteries.

Fundamental understanding for ASSLIBs can not only solve the scientific issues in ASSLIBs, but also provide guidance for developing other materials or batteries.

Advanced characterizations, such as, synchrotron radiation, Neutron, PDF, and solid-state NMR, should be well developed to understand the structural and chemical factors governing the ion diffusion in solids. Therefore, strategies to reduce migration barriers, such as anion substitution with larger and more polarizable anions to promote Li-ion diffusion, can be applied in the search for both fast Na/Mg-ion conductors.

Appendices

Appendix A: Permission from John Wiley and Sons for Published Article on *Advanced Energy Materials*



Advanced High-Voltage All-Solid-State Li-Ion Batteries Enabled by a Dual-Halogen Solid Electrolyte

Author: Xueliang Sun, Yifei Mo, Tsun-Kong Sham, et al

Publication: Advanced Energy Materials

Publisher: John Wiley and Sons

Date: Jul 4, 2021

© 2021 Wiley-VCH GmbH

Order Completed

Thank you for your order.

This Agreement between University of Western Ontario -- Shumin Zhang ("You") and John Wiley and Sons ("John Wiley and Sons") consists of your license details and the terms and conditions provided by John Wiley and Sons and Copyright Clearance Center.

Your confirmation email will contain your order number for future reference.

License Number 5306550985056

[Printable Details](#)

License date May 12, 2022

Licensed Content

Licensed Content Publisher	John Wiley and Sons
Licensed Content Publication	Advanced Energy Materials
Licensed Content Title	Advanced High-Voltage All-Solid-State Li-Ion Batteries Enabled by a Dual-Halogen Solid Electrolyte
Licensed Content Author	Xueliang Sun, Yifei Mo, Tsun-Kong Sham, et al
Licensed Content Date	Jul 4, 2021
Licensed Content Volume	11
Licensed Content Issue	32
Licensed Content Pages	10

Order Details

Type of use	Dissertation/Thesis
Requestor type	Author of this Wiley article
Format	Electronic
Portion	Full article
Will you be translating?	No

Published paper: **Zhang, S.**, Zhao, F., Wang, S., Liang, J., Wang, J., Wang, C., Zhang, H., Adair, K., Li, W., Li, M. and Duan, H., 2021. Advanced High-Voltage All-Solid-State Li-Ion Batteries Enabled by a Dual-Halogen Solid Electrolyte. *Advanced Energy Materials*, **2021**, *11*, 2100836

Appendix B: Permission from John Wiley and Sons for Published Article on *Advanced Functional Materials*



Gradiently Sodiated Alucone as an Interfacial Stabilizing Strategy for Solid-State Na Metal Batteries

Author: Xueliang Sun, Tsun-Kong Sham, Ruying Li, et al

Publication: Advanced Functional Materials

Publisher: John Wiley and Sons

Date: Apr 6, 2020

© 2020 WILEY-VCH Verlag GmbH & Co. KGaA, Weinheim

Order Completed

Thank you for your order.

This Agreement between University of Western Ontario -- Shumin Zhang ("You") and John Wiley and Sons ("John Wiley and Sons") consists of your license details and the terms and conditions provided by John Wiley and Sons and Copyright Clearance Center.

Your confirmation email will contain your order number for future reference.

License Number 5306551296353

[Printable Details](#)

License date May 12, 2022

Licensed Content

Licensed Content Publisher	John Wiley and Sons
Licensed Content Publication	Advanced Functional Materials
Licensed Content Title	Gradiently Sodiated Alucone as an Interfacial Stabilizing Strategy for Solid-State Na Metal Batteries
Licensed Content Author	Xueliang Sun, Tsun-Kong Sham, Ruying Li, et al
Licensed Content Date	Apr 6, 2020
Licensed Content Volume	30
Licensed Content Issue	22
Licensed Content Pages	9

Order Details

Type of use	Dissertation/Thesis
Requestor type	Author of this Wiley article
Format	Electronic
Portion	Full article
Will you be translating?	No

Published paper: **Zhang, S.**, Zhao, Y., Zhao, F., Zhang, L., Wang, C., Li, X., Liang, J., Li, W., Sun, Q., Yu, C. and Luo, J., 2020. Gradiently Sodiated Alucone as an Interfacial Stabilizing Strategy for Solid - State Na Metal Batteries. *Advanced Functional Materials*, **2020**, *30*, 20011

Curriculum Vitae

Name: Shumin Zhang

Post-secondary Education and Degrees: Soochow University
Suzhou, Jiangsu, China
2012-2016 B.A.

Soochow University
Suzhou, Jiangsu, China
2016-2019 M.A.

The University of Western Ontario
London, Ontario, Canada
2018-2022 Ph.D.

Honors and Awards: Student Award of Merit at Soochow University
2015-2018

Outstanding Award for Academic Science and Technology
2015

Related Work Experience

Teaching Assistant
The University of Western Ontario
2021-2022

Research Assistant
The University of Western Ontario
2018-2022

Teaching Assistant
Soochow University
2016-2017

Research Assistant
Soochow University
2016-2018

Publications:
(A) Peer-reviewed journal papers based on this Thesis (First Author and co-first author)

1. **Zhang, S.**, Zhao, F., Liang, J., Fu, J., Li, M., Alahakoon, S., ... & Sun, X. (2022). Novel Iodide Superionic Conductors: Reviving of $\text{Li}_{x-3}\text{YI}_x$. *To be submitted*.
2. **Zhang, S.**, Zhao, F., Chen, J., Fu, J., Luo, J., Alahakoon, S., ... & Sun, X. (2022). New superionic lithium oxychloride glasses. *To be submitted*.
3. **Zhang, S.**, Zhao, F., Wang, S., Liang, J., Wang, J., Wang, C., ... & Sun, X. (2021). Advanced High-Voltage All-Solid-State Li-Ion Batteries Enabled by a Dual-Halogen Solid Electrolyte. *Advanced Energy Materials*, 11(32), 2100836.
4. **Zhang, S.**, Zhao, Y., Zhao, F., Zhang, L., Wang, C., Li, X., ... & Sun, X. (2020). Gradiently Sodiated Alucone as an Interfacial Stabilizing Strategy for Solid-State Na Metal Batteries. *Advanced Functional Materials*, 30(22), 2001118.
5. Zhao, F., **Zhang, S.**, Li, Y., & Sun, X. (2021). Emerging Characterization Techniques for Electrode Interfaces in Sulfide-Based All-Solid-State Lithium Batteries. *Small Structures*, 3(1), 2100146 (**First co-author**)

(B) Peer-reviewed journal papers related to this Thesis (Co-author)

6. Zhao, F., Sun, Q., Yu, C., **Zhang, S.**, Adair, K., Wang, S., ... & Sun, X. (2020). Ultrastable anode interface achieved by fluorinating electrolytes for all-solid-state Li metal batteries. *ACS Energy Letters*, 5(4), 1035-1043.
7. Zhao, F., Alahakoon, S. H., Adair, K., **Zhang, S.**, Xia, W., Li, W., ... & Sun, X. (2021). An Air-Stable and Li-Metal-Compatible Glass-Ceramic Electrolyte enabling High-Performance All-Solid-State Li Metal Batteries. *Advanced Materials*, 33(8), 2006577.
8. Zhao, F., Zhao, Y., Wang, J., Sun, Q., Adair, K., **Zhang, S.**, ... & Sun, X. (2020). Tuning bifunctional interface for advanced sulfide-based all-solid-state batteries. *Energy Storage Materials*, 33, 139-146.

(c) Publications before joining UWO

9. **Zhang, S.**, Li, C., Yu, Y., Zhu, Z., Zhang, W., Tang, R., ... & Zhang, X. (2018). A general and mild route to highly dispersible anisotropic magnetic colloids for sensing weak magnetic fields. *Journal of Materials Chemistry C*, 6(20), 5528-5535.
10. **Zhang, S.**, Liu, P., Yin, Y., Wang, X., Tang, W., Chen, R., & He, J. (2015). Electricity from Nanoparticles on a Nanomembrane. *Thermal Science*, 19(1), 351-352.
11. Zhu, Z., **Zhang, S.**, Li, C., Zhang, J., Yu, J., Du, X., ... & Zhang, X. (2018). A mechanistic study of silica-etching by hot water. *Physical Chemistry Chemical Physics*, 20(3), 1440-1446. (**First co-author**)
12. Li, C., **Zhang, S.**, Zhang, B., Liu, J., Zhang, W., Solovev, A. A., ... & Zhang, X. (2018). Local-Curvature-Controlled Non-Epitaxial Growth of Hierarchical Nanostructures. *Angewandte Chemie*, 130(14), 3834-3838.

13. Yang, P., Li, H., **Zhang, S.**, Chen, L., Zhou, H., Tang, R., ... & Zhang, X. (2016). Gram-scale synthesis of superparamagnetic Fe₃O₄ nanocrystal clusters with long-term charge stability for highly stable magnetically responsive photonic crystals. *Nanoscale*, 8(45), 19036-19042.
14. Li, C., Yu, Y., Wang, L., **Zhang, S.**, Liu, J., Zhang, J., ... & He, L. (2019). A Step-by-Step Strategy for Controlled Preparations of Complex Heterostructured Colloids. *Chemistry of Materials*, 31(22), 9513-9521.
15. Wu, L., Yu, J., Chen, L., Yang, D., **Zhang, S.**, Han, L., ... & Zhang, Q. (2017). A general and facile approach to disperse hydrophobic nanocrystals in water with enhanced long-term stability. *Journal of Materials Chemistry C*, 5(12), 3065-3071.
16. Li, H., Li, C., Sun, W., Wang, Y., Hua, W., Liu, J., **Zhang, S.**, ... & Zhang, X. (2019). Single-Stimulus-Induced Modulation of Multiple Optical Properties. *Advanced Materials*, 31(23), 1900388.

(D) Patents

17. **Zhang, S.**, Yin, Y., Wang, X., He, J., Chen, R. (2015) Device and method for measuring PM_{2.5} concentration based on nonwoven fabric resistance method. CN104535468A
18. Yin, Z., Lu, S., Ren, J., **Zhang, S.**, Wang, X., Xia, T. (2015) Hollow fibroin albumen micropin delivery system of swelling type and preparation method. CN104888284B
19. Xun, X., **Zhang, S.**, Zhao, F., Wang, J., Zhao, S., Yang, R., Xu, G., Huang, H., Huang, Z. (2020) Fluorine-containing solid electrolyte for high-voltage all-solid-state battery and preparation method and application of fluorine-containing solid electrolyte. (CN 202010693709.X)
20. Xun, X., Zhao, F., **Zhang, S.**, Liang, J., Lu, S., Zhang, L., Zhao, S., Huang, H. (2020) Synthesis and applications of glass-ceramic sulfide-based electrolytes. (CN 202010693709.X)

(E) Conference presentation and abstract

21. **Zhang, S.**; Zhao, F.; Sun, X., Interface Engineering by Fluorinated Solid Electrolytes for All-Solid-State Li Batteries, the 241st ECS Meeting, 2022. (Abstract and Oral)
22. **Zhang, S.**; Sun, X., Advanced High-Voltage All-Solid-State Li-Ion Batteries Enabled by a Dual-Halogen Solid Electrolyte, 2021 Western University ECS Student Chapter Symposium (Virtual Oral)
23. **Zhang, S.**; Zhao, Y.; Sun, X., Na Metal Batteries: Interface Design from Liquid to Solid Systems, the 237th ECS Meeting Abstracts, 2020. (Abstract)

24. **Zhang, S.**; Sun, X., Gradiently Sodiated Alucone as an Interfacial Stabilizing Strategy for Solid-State Na Metal Batteries, 2020 Western University ECS Student Chapter Symposium (Virtual Oral)
25. **Zhang, S.**; Sun, X., Advanced High-voltage All-Solid-State Li-ion Batteries Boosted by Dual-Halogen Solid Electrolytes, 2020 International Forum on Functional Materials of China, America and Canada. (Virtual Oral)
26. **Zhang, S.**; Zhu, Z. ; He, L. A Mechanistic Study of Silica-Etching by Hot Water and Their Application for Highly Dispersible Anisotropic Magnetic Colloids, The 8th International Colloids Conference (10th June - 13th June 2018), Shanghai, China (Poster)